CARBON NANOTUBE BEARINGS IN THEORY AND PRACTICE

by

Eugene Hightower Cook

Scientiæ Magister in Aeronautics and Astronautics, 2008
Massachusetts Institute of Technology, Cambridge, Massachusetts

Baccalaureus Scientiæ in Aerospace Engineering, 2006
University of Maryland, College Park, Maryland

Submitted to the Department of Aeronautics and Astronautics
in partial fulfillment of the requirements for the degree of

Philosophiæ Doctor in Aeronautics and Astronautics
at the

MASSACHVSETTS INSTITVTE OF TECHNOLOGY

September 2011

Author

Department of Aeronautics and Astronautics
15 July 2011

Certified by

Prof. Zoltán S. Spakovszky
Associate Professor of Aeronautics and Astronautics

Certified by

Dr. David J. D. Carter
Distinguished Member of the Technical Staff
The Charles Stark Draper Laboratory, Inc.

Certified by

Prof. Markus J. Buehler
Associate Professor of Civil and Environmental Engineering

Certified by

Dr. Marc Weinberg
Laboratory Technical Staff
The Charles Stark Draper Laboratory, Inc.

Certified by

Prof. Jeffrey H. Lang
Professor of Electrical Engineering

Accepted by

Prof. Eytan H. Modiano
Professor of Aeronautics and Astronautics
Chairman, Graduate Program Committee

[This page intentionally left blank.]

Carbon Nanotube Bearings in Theory and Practice

by

Eugene H. Cook

Submitted to the Department of Aeronautics and Astronautics on 15 July 2011 in partial fulfillment of the requirements for the degree of Doctor of Philosophy in Aeronautics and Astronautics

Abstract

Carbon Nanotubes (CNTs) are attractive elements for bearings in Micro-Electro-Mechanical Systems (MEMS), because their structure comprises nested shells with no bonding and sub-nanometer spacing between them, enabling relative motion with low friction and wear. A few demonstrations of CNT bearings have been reported in the literature, and atomistic simulations have been used to probe the properties of these bearings. This thesis extends the state of knowledge about these bearing systems, by building on these prior works in both the experimental and simulation domains.

The prototype CNT rotor device presented in this thesis, and accompanying fabrication process, improve on existing CNT bearing demonstrators by establishing a vertical bearing orientation (enabling superior rotor balance and speed, and flexibility of placement for drive mechanisms) and a more manufacturable process (employing CNTs grown in place by chemical vapor deposition, and evaluating trade-offs in growth parameters). The device consists of a silicon rotor, supported on a cantilevered CNT shaft, and actuated by impingement of air jets on blades around its perimeter. For the fabrication development, extensive and consistent studies on the compatibility of CNTs with a suite of standard MEMS process were conducted, yielding valuable information for future CNT-based device designers on the effects of these processes on CNTs. Additionally, manual manipulation and placement of loose CNTs into the required vertical alignment was demonstrated, providing an alternate fabrication route, as well as a useful research technique for development of CNT devices.

Simulation of friction in a CNT bearing system has been a popular topic, yet many questions remain open. For example, the quantitative estimates of this friction reported to date range by as much as eight orders of magnitude, and simulation techniques employ a variety of disparate simulation paradigms and parameters. This thesis presents a new suite of consistently implemented but complementary and independent simulations, which span the approaches reported to date, yet agree quantitatively within the error margin. Furthermore, the quantitative relationships between friction and sliding speed, temperature, geometry, and simulation implementation parameters are determined, and a description of the causes of friction based on phonon analyses is offered.

Technical Supervisor: Dr. David J. D. Carter
Distinguished Member of the Technical Staff
The Charles Stark Draper Laboratory, Inc.

Thesis Advisor: Prof. Zoltán S. Spakovszky
Associate Professor of Aeronautics and Astronautics
Massachusetts Institute of Technology

An electronic PDF version of this thesis, with color figures and hyperlinks, is available at http://dspace.mit.edu.

[This page intentionally left blank.]

Acknowledgments

I would never have been able to complete this thesis without the help and support of many people; I am very grateful for all of their efforts.

First, I must thank my Draper Laboratory mentor, Dr. David Carter. Not only did he create this project, but he has nurtured it and me through five years of tough work. He has shared so much good advice, optimistic thinking, and also responsibility and trust that I must acknowledge, and I look forward to working for him at my first "real job."

Many thanks are also due my MIT faculty advisor, Prof. Zoltán Spakovszky. He has always had time to help me in any way that I needed, and I very much appreciate his enthusiasm, new insights, and especially his persistence in helping me to mine for "nuggets." Thanks to him as well for shepherding me through the perilous Ph.D. exams, and for giving me the opportunity to serve as a teaching assistant.

Committee Member Dr. Marc Weinberg, of Draper Laboratory, has been helping me from the beginning of the project, and I am very grateful to him. He has provided many useful thoughts for the project, and has always been available for talking with me about all manner of technical and other concerns.

I wish also to thank Committee Member Prof. Markus Buehler; when I needed to learn MD from scratch, Prof. Buehler welcomed me to his research group and was very enthusiastic about the project. He contributed many great ideas for implementing and getting the most out of the simulations.

Committee Member Prof. Jeff Lang was also instrumental in this research. His knowledge of MEMS and willingness to furnish that knowledge, as well as his generosity in providing time for the numerous committee meetings are very much appreciated.

I would also like to thank Prof. Carol Livermore and Prof. Carl Thompson for graciously agreeing to review the thesis, offering advice for improvement.

I must thank all of the folks at Boston College who helped make this work possible. Thanks to Prof. Zhifeng Ren and Trilochan Paudel for all of the CNT growth work. Thanks to Dr. Dezhi Wang and Dr. Yucheng Lan for assistance with the TEM facility at BC. Thanks as well to Dr. Greg McMahon for spending so much time with me and the BC SEM/FIB tool.

I am grateful to the members of Prof. Buehler's research group, in particular Steve Cranford and Zhiping Xu; they were happy to help me get started with MD, by showing me the tools and providing other helpful implementation tips and research ideas.

There are many people at Draper Laboratory who have helped me along the way. I am especially grateful to Parshant Kumar and Bill Teynor, who contributed their own efforts directly to the Project. I must also thank the numerous other staff who provided advice, consultation, and support throughout the work: Mark April, Janis Aten, Mirela Bancu, Connie Beauregard, Jon Bernstein, Connie Cardoso, Dick Caruso, Jim Cousens, Amy Duwel, Jason Fiering, Dan Frigon, Biga Ganesh, Doug Gauthier, Manuela Healy, Tom Langdo, John Le Blanc, Cheryl Major, Mark Mescher, Pete Miraglia, Tony Monteiro, Andy

Mueller, Tenzin Nyinjee, Erin Pararas, Elaine Pereira, Rich Poillucci, Mert Prince, Livia Racz, Henry Raczkowski, Ricky Soong, Rachel St. Hillaire, and Dan Traviglia.

I would also like to thank the Education office at Draper, comprising Linda Fuhrman and Gail DiDonato. They have spent a lot of effort guiding me through all the requirements of the Draper Fellow program, and making sure I have what need. I am grateful. I must also thank Beth Marois and Marie Stuppard in the Aeronautics and Astronautics Office, for guiding me through the graduate program at MIT.

I wish also to thank several folks at the gas turbine laboratory. Thanks to Prof. Ed Greitzer for his participation in my general examination, and for teaching several excellent classes. Thanks as well to Dr. Choon Tan for his admirable teaching. Thanks to Holly Anderson and Robin Courchesne-Sato for their support and friendliness.

Finally, I have a few personal thanks to offer. I must thank Jon Varsanik, for being such a pleasant officemate, for weathering the office move with me, and for a most indispensable refrigerator. I also wish to thank Yong-yi Zhu. He is just so much fun, and has been there whenever I needed it.

Thanks to my brother Gordon, who spirited me away to Appalachia, Azeroth, Columbus, or the Koprulu Sector, giving my brain some much-needed respites and recharges. Thanks to my parents; the older I get the more I appreciate the unfathomable dedication they exercised in raising me. I am truly privileged. Thanks to my son Alex, who smiles at me when I come home, no matter what; that simple act melts the thickest ice. Last, I thank my wife, and love of my life, Kyra. The entire volume of this thesis is not enough to describe my debt to her. She makes me better in every way.

This thesis was prepared at The Charles Stark Draper Laboratory, Inc., under Internal Research and Development projects 23027-001, 23949-001, and 25150-001.

Publication of this thesis does not constitute approval by Draper or the sponsoring agency of the findings or conclusions contained herein. It is published for the exchange and stimulation of ideas.

Eugene H. Cook
15 July 2011

CONTENTS

[This page intentionally left blank.]

LIST OF FIGURES

LIST OF TABLES

[This page intentionally left blank.]

NOMENCLATURE

Symbol	Meaning
a	Unit cell length
$a_{\text{C-C}}$	Carbon-carbon bond length
A, A_1, A_2, B	Fitting constants
d	Diameter of a carbon nanotube
E	Energy in the system
E_{T}	Thermal energy
ΔE_{Q}	Total energy transferred via thermostat
F^*	Non-dimensional friction force per atom
F_{f}	Friction force
$\vec{F}_i$	Force on atom i
F_{LJ}	Lennard-Jones force
F_{solvent}	Force due to interaction with fictitious “solvent” particles
g	Number of degrees of freedom
h	Inter-wall spacing between carbon nanotubes
I_{yy}	Second moment of area of the carbon nanotube
I	Moment of inertia of the carbon nanotube
I_1	Moment of inertia of inner nanotube
I_2	Moment of inertia of outer nanotube
k	Wave number
k_{B}	Boltzmann constant
ℓ	Length of a carbon nanotube
ℓ_{p}	Persistence length
L	Angular momentum of a carbon nanotube
L_0	Initial angular momentum of the system
L_1	Angular momentum of inner nanotube
L_2	Angular momentum of outer nanotube
m	Chiral index
m_{C}	Mass of one carbon atom
m_i	Mass of atom i
n	Chiral index
N	Number of atoms
N_1	Number of atoms in inner nanotube
N_2	Number of atoms in outer nanotube
P	Energy transfer or accumulation rate
δP	Energy transfer or accumulation per revolution

q	Nosé-Hoover parameter
$\dot{Q}$	Heat transfer rate (via thermostat)

Symbol	**Meaning**
r	Radius of a carbon nanotube
r_1	Radius of inner nanotube
r_2	Radius of outer nanotube
$\bar{r}$	Interface radius between two carbon nanotubes
$\vec{r}_i$	Position of atom i
s	Nosé-Hoover reservoir
t	Time
t_{steady}	Timescale of steady behavior
t_{unsteady}	Timescale of unsteady behavior
δt	Simulation timestep
T	Temperature
T_0	Desired temperature
U	Potential energy in the system, from an empirical potential function
v	Velocity
v^*	Non-dimensional sliding velocity
v_{LJ}	Lennard-Jones velocity
$\bar{v}_{\text{T}}$	Average thermal velocity of the atoms
Y	Young's Modulus
α	Thermostat timescale parameter
β	Reduced Frequency
ε	Lennard-Jones energy parameter
θ	Angle of rotation of the carbon nanotube
λ	Scale parameter for Berendsen thermostat
μ_{k}	Kinetic friction coefficient
ρ_{S}	Surface atomic density (atoms per area)
ρ_{I}	Interface atomic density
σ	Lennard-Jones distance parameter
τ_{f}	Friction torque
ω	Angular speed of a carbon nanotube
ω_0	Initial angular speed
ω_1	Angular speed of inner nanotube
ω_2	Angular speed of outer nanotube
ω_∞	Final angular speed

Acronyms

Acronym	Meaning
a-Si	Amorphous Silicon
AFM	Atomic Force Microscopy, Microscope, Micrograph
AIREBO	Adaptive Intermolecular Reactive Empirical Bond Order
ASTM	American Society for Testing and Materials
CNT	Carbon Nanotube
BC	Boston College
BOE	Buffered Oxide Etch
CVD	Chemical Vapor Deposition
DC	Direct Current
DI	De-Ionized
DRIE	Deep Reactive Ion Etching
DWNT	Double-Wall Nanotube
e-beam	Electron Beam
EDX	Energy Dispersive X-ray Spectroscopy
FIB	Focused Ion Beam
FTIR	Fourier Transform Infrared Spectroscopy
GULP	General Utility Lattice Program
ICP	Inductively Coupled Plasma
JEOL	Japan Electron Optics Laboratory
LAMMPS	Large-scale Atomic/Molecular Massively Parallel Simulator
LPCVD	Low-Pressure Chemical Vapor Deposition
MD	Molecular Dynamics
MEMS	Micro-Electro-Mechanical Systems
MIT	Massachusetts Institute of Technology
MWNT	Multi-Wall Nanotube
NEMS	Nano-Electro-Mechanical Systems
p-Si	Polycrystalline Silicon
PECVD	Plasma-Enhanced Chemical Vapor Deposition
PEEK	Polyetheretherketone
PMMA	Polymethyl Methacrylate
RCA	Radio Corporation of America
RIE	Reactive Ion Etching
SC1	Standard Clean 1
SEBL	Scanning Electron Beam lithography
SEM	Scanning Electron Microscopy, Microscope, Micrograph

Acronym	Meaning
STS	Surface Technology Systems
SWNT	Single-Wall Nanotube
TEM	Transmission Electron Microscopy, Microscope, Micrograph

1 Overview

The purpose of this thesis is to advance the state of knowledge about Carbon Nanotube (CNT) based rotary bearings for Micro-Electro-Mechanical Systems (MEMS) and Nano-Electro-Mechanical Systems (NEMS). The CNT bearing, which had been demonstrated in simple devices [1, 2] and which was further developed in part during the precursor to this thesis [3], relies on the structure of the CNT to enable rotation with low friction and minimal wear, or potentially even "anti-wear" or "self-healing." Multiwall carbon nanotubes (MWNTs) are characterized by strong shells, comprising cylindrical tubes of covalently bonded carbon one atom thick. These shells nest inside each other, analogously to the manner in which graphene sheets stack to form graphite. While the strong shells provide a mechanically robust framework to leverage in building devices, the lack of covalent bonding between shells enable adjacent shells to slide relative to each other with extremely low resistance. The CNT system is therefore attractive as a bearing.

1.1 Motivation

MEMS and NEMS have proven effective at providing functionality similar to their larger-scale counterparts, with significant savings in cost, weight, size, and power consumption. Examples of commercially successful devices include pressure sensors, accelerometers, inkjet printer heads, and mirror arrays. However, a significant limitation restricts the diversity of successful devices, which is well described by the taxonomy of Romig *et al.* [4]. Almost all current commercially successful devices are Class I (no moving parts) or Class II (moving but not contacting parts). The only exception is the micro-mirror array, which falls into Class III (contacting but not rubbing parts). A wealth of possibilities exists for Class IV (rubbing parts) MEMS, but despite plentiful laboratory demonstrations and prototypes, none of these possibilities have been realized in a commercially successful device.

The tribological phenomena of interfacial friction and wear are recognized [4, 5] as a leading cause of failure in Class IV MEMS, and are largely responsible for the absence of any commercially successful devices requiring such sliding motion. To improve the reliability of Class IV MEMS, it will be necessary to reduce friction at these interfaces, and especially to control the mechanisms that cause friction to increase over the device lifetime, by developing bearing technologies that counteract or mitigate these issues.

Recognizing the critical importance of bearing development for the future of MEMS, many have invested substantially in bearing research (see section 2.1). From simple bushings, consisting of parts rubbing directly on each other, to macro-inspired designs such as ball-bearings, to more complex systems such as gas or liquid film bearings, a diverse array of approaches has arisen. While most of these solutions offer greatly improved performance over bearing-less designs, often it comes at the cost of fabrication complexity or design restrictions, and further performance improvements are sometimes desirable. The landscape of micro bearing research is still ripe for novel concepts that offer strong performance with relatively straightforward implementation.

One promising approach would be the incorporation of CNT-based bearings. CNTs have long been known to exhibit low sliding resistance between adjacent walls [6], and several experimental demonstrations have been accomplished [1, 2, 7-11]. Other experimental work has shown that friction performance can remain constant over 10^4 cycles, and even decrease after "self-repair" of the CNT

undergoing motion [12]. These encouraging properties can be attributed to the energetically favorable and chemically stable structure of CNTs, and the inability of debris to accumulate in the 0.34 nm gap between adjacent walls. Because of these properties, CNTs, and graphene, their planar analogue, are attractive as elements for constructing high reliability rotary and translational bearings, and thus reliable Class IV MEMS devices.

However, despite existing demonstrations and some attempts to measure friction in CNT devices, a clear understanding not only of the quantitative value of friction, but of the mechanisms that govern this friction, remains elusive. Because this question has yet to be resolved, and because of the relatively simple molecular structure of CNTs, simulation of CNTs for the purpose of measuring the friction has become popular [10, 13-27]. However, the tremendous interest has so far done little to resolve the question; in fact, considering all the friction estimates reported throughout the literature, the spread amongst these estimates is as much as eight orders of magnitude. More details on the discrepancies among the existing literature are provided in section 2.2.2.3 and section 5.1. It is of vital importance to the utility of these simulations that they be credible, which cannot occur until the variations in results between them have been explained. A large portion of this work (chapter 5) has therefore been devoted to a thorough investigation of all of the simulation methods employed to date, with the goal of identifying the causes of and resolving the discrepancies.

In order to truly advance the reliability of Class IV MEMS, it is also vital to understand those processes that lead to failure over time. Therefore, measurement of the time-history of friction performance in CNT and graphene bearings will be necessary to enable real world devices that take advantage of the bearing technology. Furthermore, an accurate picture of the wear processes, obtained by morphological examination of operating bearings, will contribute to this understanding. The development of a manufacturable, robust test article, such as the CNT bearing prototype of this work, will enable measurement of the friction performance and wear characteristics of these bearings over time. The resulting bearing prototypes and accompanying qualitative and quantitative understanding will be critically important to future MEMS device designers, by providing a method for reducing device failures due to friction and wear in a predictable way.

1.2 Challenges

CNT bearings are a difficult problem, and there have been many challenges with which to contend. Some challenges are still outstanding, and more research work will need to be done to bring the concept of a CNT bearing to the state where it can be leveraged by applications.

One of the biggest challenges has been knowing how to fabricate MEMS devices which incorporate CNTs. The patchwork of data that exists in the literature is not readily accessible in the way that data on most established MEMS materials is. The work performed as a part of this thesis partially mitigates that issue, by providing a consistent reference on whether CNTs will have significant issues with any given process. However, much work remains to determine the precise variations in properties that these processes can cause, before CNTs can be considered a “standard” MEMS material.

In fabricating the prototype device, the largest challenge continues to be achieving an isolated, vertically aligned CNT with sufficient crystalline quality. Section 4.2.1 explains the details of why this is so difficult. Of the two options, each has different limitations. CVD grown tubes can be grown in the desired location with good control on orientation, but this becomes more difficult when single, isolated CNTs are required as opposed to CNT “forests.” A trade-off between control of location and tube crystalline quality exists, and a suitable optimum has yet to be found. For manipulation of CNTs into

place, arbitrary tube quality can be obtained, since tubes can come from any source, including arc-discharge synthesis. However, the process is extraordinarily tedious and time consuming, and control over tube orientation is limited by the available degrees of freedom and viewing angles in the manipulation system. With more work, an effective protocol for consistently manipulating tubes into place may be developed, but the process will still require manual action for each CNT. At present, the lack of availability of isolated, vertically-oriented CNTs of sufficient quality is the reason that the prototype device described here has not successfully rotated.

Challenges also remain in understanding the friction in the CNT system. Surveying the existing literature on simulation of CNTs via Molecular Dynamics (MD) demonstrates that wildly different predictions of friction are possible, and without carefully considering the validity of the simulation and its relation to reality, the numbers cannot be taken at face value. When coupled with the paucity of experimental friction measurements, it becomes clear that extensive work remains to be done in validating these simulations. While the work here in unifying the disparate methods is a good start, experimental data is the only real way to ensure that the simulations are accurate. The prototype, when completed with a sufficiently high quality CNT, can provide this desperately needed data.

The simulations can also be extended to more closely describe the CNTs used in the experiments. One outstanding issue is scale: while real tubes used thus far comprise millions to billions of atoms, simulations are difficult with more than a few or tens of thousands. Increasing computational resources will mitigate this issue in time. There is also a schism between the characteristic timescales of the experiment and the simulations. The speed of available processors forces rotation rates in excess of GHz for the simulations; furthermore lower rates have higher noise relative to the thermal motion, so even longer running times or multiple parallel simulations are required to get an accurate result. Experimental data thus far collected has been constrained to mere Hz, and the model predicts that prototype device described here cannot exceed a few tens of MHz. Advanced time-lengthening techniques for MD, such as temperature accelerated dynamics, might be able to bridge the inaccessible region in the future.

Finally, a major difference between simulated and real tubes is defects. As illustrated in section 4.2.1.1, real CNTs can have extremely high defect densities, and at times can seem to be more defect than proper tube. Simulations including defects have yet to be reported, partly because the description of defective geometry is much more complex than ideal CNTs. An initial way to include defects might be to introduce point defects such as vacancies or interstitials, randomly distributed throughout the structure. Further work could implement procedures to design tubes with larger-scale defects. As real CNT quality improves, this gap will hopefully close from both ends in the future.

1.3 Goals of the Project

One major goal of the project is to demonstrate a prototype CNT bearing device that can be useful for applications. While the possibility of utilizing a CNT as a bearing has already been shown, in a few bold demonstrations [1, 2] (discussed in more detail in section 2.2.1), to be feasible, further work is necessary to incorporate them into useful devices. One possible extension of those technologies would be to transition from a horizontally oriented CNT to a vertically oriented CNT. The benefits of this orientation change are discussed in section 1.4. Additionally, it is hoped that a more manufacturable process for constructing CNT based rotors can be developed, which can eliminate some of the time consuming manual process steps employed in demonstrations to date. Construction of the prototype device will demonstrate that such improvements on the existing state of the art are feasible, and will also provide a baseline fabrication process that will be critical to the development of application devices.

Further, testing of the prototype will eventually provide some of the first ever experimental data on the behavior of the CNT bearing system, and specifically on the friction in the bearing. Prototype construction is detailed in chapter 4.

In the process of developing the prototype device, an additional goal was set to establish some guidelines for the incorporation of CNTs in to MEMS devices, using the standard toolbox of available MEMS processes and techniques. CNTs have begun to be incorporated into various micro-electronic [28-34], micro-mechanical [1, 2, 35, 36], and micro-fluidic [37-40] devices. Before using established MEMS fabrication procedures on CNTs, it is important to know what effects these procedures will have. Researchers have investigated the effects of the processes that make up their fabrication procedures, and hence, as a result of the development of fabrication processes for these devices, a patchwork of knowledge about the effects of various processes on the CNT is beginning to emerge. However, a comprehensive reference describing the compatibility of CNTs with a broad range of processes in a consistent manner (in the vein of Williams' extensive etch rate tables [41, 42]), does not exist. Therefore, the creation of such a reference has been undertaken, in order gain insight into the effects of our own processes of interest, and to provide a useful tool for future MEMS designers hoping to incorporate CNTs. This work is detailed in chapter 3.

In addition to building an example CNT rotor, it also became clear that there is a great deal of work still needed to understand the physics of the CNT bearing system. Few of the experimental demonstrations of CNT bearings have captured data on the friction, so the bulk of available data comes from simulations, typically employing molecular dynamics techniques. Unfortunately, the values for friction reported in this literature vary by as many as eight orders of magnitude, which make it difficult to use the data with confidence. Furthermore, a description of the mechanisms causing the friction, as well as knowledge of the dependence of friction on parameters of an individual CNT system, remains wanting. This work has therefore attempted to address these questions, by performing a suite of molecular dynamics simulations of diverse configurations and parameter sets, in a consistent and controlled manner. The goals are to establish the relative importance of and quantitative dependence on the system parameters, to identify the causes of the discrepancies in the literature, and to identify the underlying mechanisms causing the friction from a fundamental perspective. This work presents for the first time a comparison of the existing CNT bearing simulation literature, a consistently implemented array of simulations spanning the parameter space of that literature, and analysis of how the phonons (system natural modes) contribute to the interaction of MWNTs, providing new insight about the mechanisms driving friction. The simulation work is described in chapter 5.

1.3.1 Summary of Objectives

In summary, the scope of the thesis is bipartite: A prototype CNT bearing device is constructed, demonstrating a baseline fabrication process for CNT bearing devices, and simulations are conducted to study the friction in CNT bearings, focusing specifically on resolving the disagreement between reports in the literature on the quantitative value of friction, by spanning the parameter space and range of techniques employed in the by prior works with a consistently implemented suite of numerical experiments. The objectives of the work are to:

1. Construct a prototype CNT bearing device based on a vertically oriented isolated CNT
    a. Identify which MEMS fabrication processes are compatible with CNTs (chapter 3)
    b. Design a CNT bearing device for optimal performance (section 4.1)

c. Develop a fabrication process, address the issues arising during fabrication, and complete fabrication of the prototype device (section 4.2)
d. Develop a testing system to measure the prototype performance (section 4.4)

2. Simulate friction in CNT bearings
    a. Review the existing literature on CNT bearing friction simulation (sections 5.1 and 2.2.2)
    b. Develop a simulation protocol to re-implement the techniques reported in the literature using consistent parameters (section 5.2)
    c. Demonstrate agreement between independent simulation techniques (section 5.3.1)
    d. Determine the dependence of friction on the system parameters (section 5.3.3)
    e. Identify the mechanisms that cause friction, by exploring the natural modes that make up the system behavior (sections 5.3.2 and 5.2.7).

1.4 Impact

This thesis provides theoretical insight from the broad and consistent assessment of simulation techniques for estimating CNT friction, and practical fabrication development work on the prototype device (including testing of CNT compatibility with MEMS processes) for applications enabled by the proposed bearing technology.

1.4.1 Practice

The first major impact of this work is the development of a CNT bearing prototype fabrication process that builds on previous demonstrations. The new idea is to orient the CNT vertically, instead of horizontally. Figure 1-1 illustrates the general differences resulting from this orientation change. Because MEMS Fabrication relies so heavily on lithography for defining the geometry, fabrication capability is highly anisotropic; in the dimension normal to the substrate, only limited shapes can be constructed. By orienting the CNT in this dimension, both of the other two dimensions (which make up the plane of the rotor) become accessible to the geometry.

This seemingly simple change has wide-ranging implications. First, axisymmetry in the rotor and stator becomes possible. This is of immediate utility, because it allows improved control over the rotor balance, and hence, higher rotational speeds are attainable. Additionally, axisymmetry allows much finer control over the interfacing between the rotor and the stator. For example, electrodes for electrostatic actuation can be spaced arbitrarily around the circumference, in both the rotor and the stator. Additionally, the capacitive gap between rotor and stator can be tightly controlled, and consistent for all rotor angles. With this capability, rotors can be designed with high torque, uniform torque coverage, and bi-directional actuation capability, leveraging the extensive knowledge of electrostatic motors already developed [43]. Besides electrodes, other devices can also benefit from axisymmetric distribution around the rotor periphery, such as blades or vanes for interaction with fluids (e.g. turbines, compressors, or pumps), or optical redirection (e.g. mirrors or shutters).

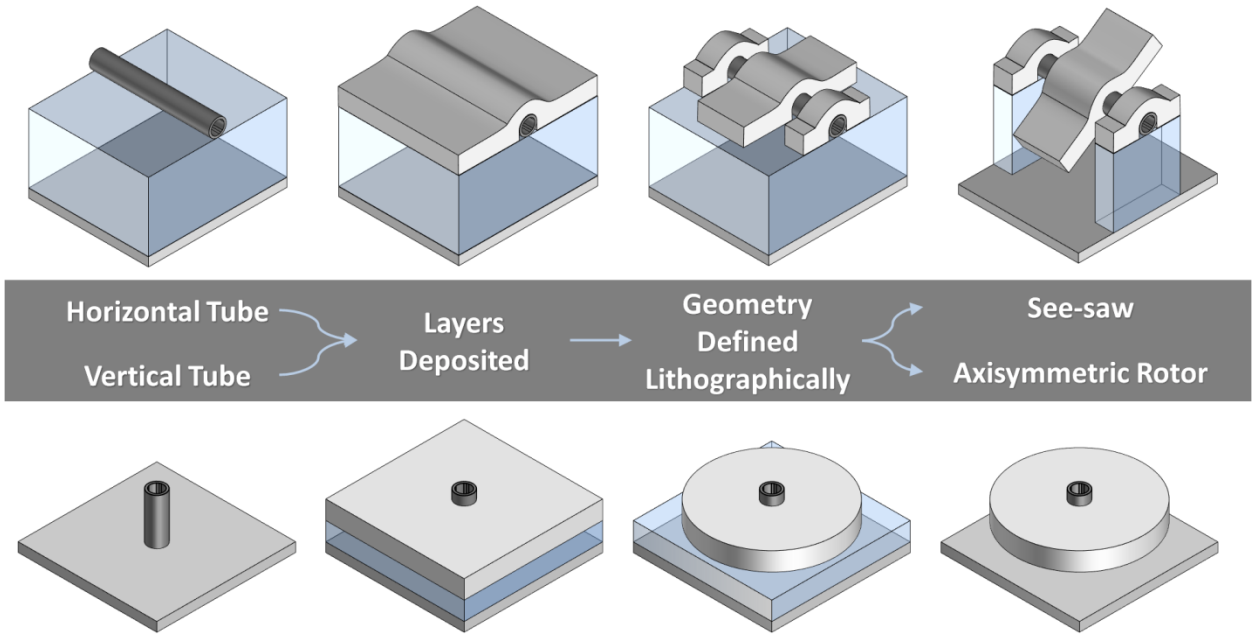

Figure 1-1: The advantage of a vertically oriented CNT, namely, the capability to fabricate axisymmetric or other flexible rotor geometries, is shown.

The prototype fabrication process developed for this work is the first CNT based rotor to use such a configuration, demonstrating an axisymmetric rotor with vanes. In essence, the device is a micro- or nano-turbine. In addition to proving that the concept can be fabricated, the prototype also serves as a platform, which can be used as a starting point for designing other devices that make use of the bearing. Insights gained on what fabrication steps pose the most challenges, and how they can be resolved, will be useful for future work in CNT bearing application design.

There are additional contributions that arise from the use of a vertical CNT as well. First, the prototype provides a model for how CNT bearings might be constructed in a more manufacturable fashion; instead of painstakingly hand-selecting CNTs and patterning features by e-beam lithography around each one, CNTs can be grown in place, with the vertical orientation, by Chemical Vapor Deposition (CVD). While current state-of-the-art CNT growth does not provide sufficient CNT quality to enable rotation, this will likely be a key enabler for wafer-scale mass-production of CNT bearing devices if that challenge can be resolved.

In the mean time, this work has also demonstrated manipulation and attachment of individual nanotubes to desired locations (see section 4.2.1.2). Vertical orientations have been obtained, with some error in the angle of alignment. This alternative strategy, while not cost-effectively manufacturable in high volumes, provides another route for incorporating CNTs into MEMS devices. In cases where CVD growth is not possible, manipulation can be a useful way to test proof of concept devices before investing in other CNT placement strategies. For example, the development time for any device requiring vertically oriented or isolated CNTs, such as field emitters using carbon nanotube tips [44-46] or Atomic Force Microscope (AFM) tips using CNTs for high resolution [36, 47] might be shortened by having such a rapid capability to attach individual CNTs to the desired locations.

Another major impact, derived from the efforts to develop a fabrication process for the prototype, is the creation of a knowledge base describing the compatibility of CNTs with common MEMS processes.

Data have been available on CNT compatibility on a piecemeal basis, as researchers try a few processes in fabrication of a particular device; however, a single catalogue of CNT compatibility does not exist. A wide variety of processes have been applied to CNTs in a consistent manner, and the morphological changes at a bulk and atomic scale have been assessed, by Scanning Electron Microscopy (SEM) and Transmission Electron Microscopy (TEM), respectively, in each case. While it may be of interest to have other quantitative data concerning the effects of the processes (such as Raman spectra, conductivity measurements, etc.), breadth (i.e. number and diversity of processes documented) has been emphasized over such depth. It is proposed that device designers interested in incorporating CNTs into their devices will want a quick check to see whether to even consider certain processes, and that having selected a process, they will characterize its effects in a manner that most closely evaluates the performance characteristics of interest for their application. This contribution is therefore important as an initial reference resource.

The test device paves the way for a host of micromechanical devices. Any rotating mechanical device would be a candidate for miniaturization with MWNT bearings, but a few applications in particular stand to benefit significantly.

MEMS chemical and biological sensors have been in development for decades [48-53]. However, these systems typically rely on a pump to push analyte through them, or a vacuum pump to evacuate them. To date, the best MEMS vacuum pump constructed (to the author's knowledge) can attain a pressure of 164 Torr [54] when backed by atmosphere; further vacuum performance might be possible with a rotary pump, such as those enabled by a suitable high-speed MEMS bearing. Other MEMS pumps have not proved capable of meeting the requirements of the sensors [50]. So far, in order to deploy these systems, bulky macro-scale pumping equipment has been needed. If a suitable MEMS pump could be developed, the entire system could be miniaturized to a convenient, portable size, while at the same time reducing power consumption. The MWNT bearing seems to be well suited to pumping applications, as its high stiffness can lead to high operating speeds. It is also capable of operating in a vacuum. Furthermore, it would not require an external electrical or compressed air supply, like some competing bearing technologies.

An additional application for which the MWNT bearing has promise is a microscale rotating gyroscope. Microscale gyroscopes exist based on the tuning fork design, but a true rotating disk could provide improved performance [55]. The ability of the bearing to provide very low "wobble" (angular displacement of the axis of rotation) could reduce the dominant cause of errors in dynamically tuned gyroscopes. The high stiffness could enable high-speed operation, leading to improved bandwidth and high sensitivity. In addition, the low friction suggests that the drive power to operate the gyroscope could be very low.

Another potential application is on-chip flywheel energy storage. The energy storage density capacity of a flywheel is limited primarily by the strength of the flywheel material. Any given flywheel can store energy per unit thickness scaling as the fourth power of the radius and the square of angular speed. However, to keep the stress below the material limit, the angular speed must vary inversely proportional to the radius. As a result, the energy storage per unit thickness scales with disk area, or in other words the energy storage density (energy per unit mass) is completely independent of the disk size. Scaling flywheels down to the microscale does not hurt performance, and in fact could improve it since micro-sized materials can be made with fewer flaws, and hence higher material strength. Energy stored in silicon flywheels has comparable energy density to batteries, but could potentially be discharged much faster – in other words the power density of the flywheels could be high, providing short bursts of power on demand. The MWNT bearing could potentially make such flywheels feasible by

enabling high-speed rotation, and by providing a low-friction support that reduces unwanted energy dissipation over time.

The prototype device is a simple microturbine, extracting work from the airflow to overcome the friction. Further development of more advanced (and more useful) turbomachinery based on CNT bearings would be another interesting application. Turbomachines have been proposed [56, 57] for providing electrical power at a small scale, as an alternative to batteries. The fact that the power produced scales as the area (which controls the airflow rate) while device weight scales with the volume indicates that microturbomachinery could have a substantial advantage in power density. If successful, the MWNT bearing technology developed here might serve as a unique alternative to the gas bearings so far employed in microscale turbomachinery, by potentially allowing further size reduction and higher speed operation.

1.4.2 Theory

On the simulation side, the thesis has addressed the ongoing issue of large discrepancies between reported values for friction in the CNT. It has been shown that by carefully controlling all the parameters of the simulation, friction numbers that agree well can be obtained even for several distinct types of simulation, and various methods of extracting the friction measurement from the simulation. By implementing these multiple, independent methods in a consistent manner, and obtaining good agreement among the results, confidence in the simulation's ability to predict device performance is improved. This confidence is critical to acceptance of these simulations as a useful tool in evaluating design concepts.

Furthermore, the dependence of the friction value on the different parameters that are expected to influence it is determined, by ensuring control over all parameters and systematically varying one at a time. The parameters include properties of the system (e.g. geometry, temperature, rotation speed) as well as simulation control parameters (e.g. simulation initial and boundary conditions, thermostat type, averaging windows, and strategies for measuring the friction). This information is important for all CNT simulators, so that a consistent approach to modeling CNT friction can be used.

Finally, phonon power spectra have been computed for CNTs undergoing simulation. Phonons are the natural modes of the system, and the goal is to identify which modes are responsible for friction. It is demonstrated that there is not a particular phonon or few phonons that contribute especially strongly to the interactions between rotating tubes; instead, the interaction appears to be broadband. There are two bands which are particularly emphasized, between about 10-14 THz and 18-25 THz, but these become broader and less well defined for higher rotational speeds.

1.4.3 Summary of Contributions and Main Outcomes

In summary, this thesis has advanced the state of knowledge about CNT bearings by both developing a prototype CNT bearing test device, and by examining CNT friction through simulation. The prototype, consisting of a rotor with vanes for air-driven actuation supported on a vertically aligned, isolated MWNT, proves the feasibility of constructing CNT bearing devices having such a configuration. Additionally, the fabrication process provides a guideline for how such devices can be constructed, based on a surface micromachining approach with a sacrificial release layer, polysilicon rotor layer, e-beam lithography and a combination of wet and dry etching. This fabrication process will be a useful starting point in designing fabrication plans for subsequent CNT bearing devices. The thesis also includes a consistent and broad assessment of the effects of MEMS processing techniques on CNTs, including those processes used for the prototype fabrication, as well as others of general interest to

MEMS fabricators. This reference will be a helpful tool for future researchers in selecting processing techniques for use in CNT device fabrication. The fabrication also includes a demonstration of manipulation and attachment of individual CNTs to a desired location, which is a useful technique for rapid evaluation of CNT-based micro-devices.

The simulation work in the thesis demonstrates that different simulation methods can be employed to estimate CNT friction, and still will yield agreeing quantitative results if they are implemented in a consistent fashion, carefully controlling all the relevant parameters. This important demonstration implies that the large (several order of magnitude) variation among different simulations in the literature to date must be due to numerical implementation issues, and not differences in the fundamental physics of the CNT bearing system when operated in the different modes. This work also determines the effect on friction of many important parameters, including sliding speed, temperature, and tube geometry. This information will be important for those wanting to design CNT bearing applications, by providing guidelines about what performance can be expected and how to achieve specific performance levels. Finally, analysis of the phonon spectra of rotating CNTs has been used to identify the modes that contribute most strongly to the phenomenon of friction, concluding that friction is due to broadband effects, not confined to particular individual modes.

1.5 Organization of the Thesis

This thesis is organized into five chapters in addition to this overview chapter. Chapter 2 presents a review of the relevant background information, which provides the motivation for the work of this thesis. The main motivation for development of a CNT bearing is the absence of a dominant bearing technology for MEMS; section 2.1 describes the most popular existing bearing technologies, and discusses their strengths and limitations, leading to the conclusion that the CNT bearing can provide improved performance in many situations. Prior work on CNT bearings in particular is discussed in section 2.2. The experimental demonstrations described in section 2.2.1 prove that the technology is feasible, and suggest further improvements, including the use of a vertically oriented CNT as in the device presented here. Section 2.2.2 examines the abundant literature on simulation of CNT friction, which shows that despite the quantity of research, a consensus on the quantitative value of CNT friction is far from being reached, and sources disagree about that value by as much as eight orders of magnitude. For this reason, the thesis attempts to identify the reasons for that discrepancy.

Before fabricating the prototype device, it is necessary to understand the effects of MEMS processes on the CNT. This information was not readily available in the literature, so a systematic effort to evaluate a suite of MEMS processes was undertaken, and is reported in chapter 3. The methods used to characterize the compatibility are discussed in section 3.2. These are organized by type of process: Deposition processes, wet etches, and dry etches are discussed in sections 3.3.1, 3.3.2, and 3.3.3, respectively.

Chapter 4 covers the fabrication of the prototype CNT bearing device. The device was designed using a classical dynamics model to choose optimal geometry, as described in section 4.1. The fabrication procedure, including a detailed description of each step, is laid out in section 4.2. This includes descriptions of the CNTs used in the fabrication (section 4.2.1), release and rotor layer depositions (sections 4.2.3 and 4.2.4), lithographic techniques (sections 4.2.2 and 4.2.5) and release (section 4.2.6). A plan and apparatus to test the completed device were developed, and are reported in section 4.4. Section 4.3 includes a summary of all the lessons learned.

It was clear from exploring the literature and discovering the orders of magnitude variation in reported friction that more work is needed to understand friction in CNT bearings; this idea is expounded in section 5.1. To answer that the outstanding question of what the friction is, a suite of simulations were developed, using the tools described in section 5.2.2 and validated in section 5.2.3. The simulation styles can be broken into steady and unsteady techniques, and are described in sections 5.2.5 and 5.2.6, respectively. Additionally, in order to better understand the underlying mechanisms contributing to friction, the phonon energy distribution was computed, illustrating which modes contribute most strongly to the inter-tube interactions that give rise to friction; the implementation of these phonon computations is described in section 5.2.7. The results of all the simulations are compiled in section 5.3. Particular attention is given in section 5.3.1 to the comparison of these simulations with the literature whence they were motivated. The results of the phonon computations are presented in section 5.3.2. To explain the variation in the literature, and to provide guidelines for future simulation and for device designs that rely on simulated results, the dependence of the friction on the important system parameters was determined, and is detailed in section 5.3.3. Finally, since CNTs are similar to graphene in structure, the friction in graphene was also simulated, providing an interesting comparison in section 5.3.4.

Chapter 6 provides a conclusion for the thesis, including both a summary of the accomplishments in section 6.1, and recommendations for further work on this topic in section 6.2.

[This page intentionally left blank.]

[This page intentionally left blank.]

2 BACKGROUND

2.1 Bearing Technologies for MEMS

As discussed in section 1.1, the field of MEMS faces a significant challenge in the area of bearings. While many Class IV devices have been demonstrated in the laboratory, none has yet been a commercial success, mainly due to limitations in the bearing, specifically, high friction and wear. It is critical to the success of this entire class of devices that a robust bearing technology be developed. An apt comparison is to the comb drive, which enabled a host of Class II devices, notably the ubiquitous MEMS gyroscope and accelerometer. As a similarly enabling technology, a good MEMS bearing (*i.e.*, a straightforward-to-fabricate bearing, exhibiting low enough friction to be drivable with available power and low enough wear to last for years) might be considered something of a "holy grail" in the industry.

Indeed the knowledge that MEMS bearings are ripe for development is widespread, and several complementary approaches to solving the problem are being actively investigated by a number of researchers. Here the current state of the art for several popular and promising bearings is summarized. In order to enable quantitative comparisons of the bearing friction performance, two metrics have been employed. The classical kinetic friction coefficient μ_k, defined as the ratio of the friction force to the applied normal load, is useful for comparing rotors of different sizes, where small rotors exhibit smaller friction torque regardless of bearing quality. However, for fluid-based bearings (gas or liquid,) this parameter is not well defined. However, the dependence of friction on rotational speed is more easily determined in these cases, and therefore, the friction torque constant, defined by McCarthy [58] as τ_f/ω, where τ_f is the friction torque and ω is the operating speed, has been used.

2.1.1 Silicon-Silicon Bearings

The simplest method of achieving sliding motion between two parts is to allow the parts to rub directly on each other. Initially, this meant surface micromachined polysilicon rubbing against itself. Many successfully rotating motors and other rotating devices were crafted using this approach [43, 59-62]. Typically, these devices have used a flange of polysilicon extending from a central pillar over a portion of the rotor, and with the rotor sliding against the flange, the pin, or a portion of the substrate.

It was immediately apparent that the friction was so high (Dhuler *et al.* [63] reported kinetic friction coefficients between 0.36 and 0.40) as to dominate the device dynamics, and systematic efforts were undertaken [62, 64] to characterize the behavior of the friction. They also reported friction torques between 1.2×10^{-12} and 1.3×10^{-12} N-m, corresponding to friction torque constants of 8.9×10^{-15} and 9.6×10^{-15} N-m/rpm for their operating speed of 135 rpm (tip speed of 707 µm/s for their 100 µm diameter rotor). An even more significant problem was wear. Device performance was observed [65] to quickly decrease with time, as damage accumulated in the bearing, including both geometry changes and accumulation of debris. Mehregany *et al.* [65] measured the wear rates and found that the clearance gap between rotor and stator increased in width by 28% (corresponding to a wear depth of about 65 nm) on average after about a million revolutions. Various coatings were also developed [66-68] in an effort to reduce friction and wear rates (yielding kinetic friction coefficients as low as 0.02 [68] and wear rates as low as 10^{-10} mm^3/N-m, reflecting a volume of material (mm^3) removed per meter that the contacts slide, with a given normal force), but these issues continue to be severe enough to preclude use of these bearings in devices that need to operate reliably over long periods of time.

2.1.2 Ball Bearings

Ball bearings are the perennial favorite at the macro-scale, and recent work [58, 69, 70] has shown promise in scaling them down to a point where they can be included in MEMS devices. Stainless steel balls, fabricated by conventional means, are available at sizes as small as a few hundred micrometers. These have been incorporated into raceways etched in the silicon by standard microfabrication processes. Demonstrations [58] have been performed at speeds up to 10^4 rpm (corresponding to a tip speed of 5.24 m/s for their 10 mm diameter rotor), and the friction and wear characteristics have been thoroughly investigated.

These bearings provide dramatically decreased friction (classical dynamic friction coefficients between 0.0005 and 0.025 of have been reported [58]) compared to rubbing bearings (although still not quite as low as the air bearings discussed in section 2.1.3.) Using a test device rigged with a pneumatic loading system, in order to provide a controllable thrust load on the bearing, McCarthy *et al.* [58] found the friction to vary proportionally with the angular velocity, and with the normal load to the power 0.444. For their applied normal loads between 10 and 50 mN, they measured friction torque constants τ_f/ω between 9×10^{-10} and 4.5×10^{-9} N-m/rpm.

Additionally, these bearings greatly reduce wear and contamination due to wear debris compared to rubbing bearings. Detailed morphological analysis of the bearing after operation [58] has showed that the balls do not exhibit any structural changes detectable via SEM. The raceways have experienced an erosion of material on the line where they contact the balls, but the depth of material eroded was measured to be less than 100 nm after 1 million revolutions. Nevertheless, performance degradation was noted over the course of operation. The main source of degradation was presumed to be the accumulation of debris particles in the bearing mechanism, based on the observation that a worn but cleaned and reassembled bearing exhibited similar performance to a new bearing. Thus, wear remains a substantial issue for ball-bearing technology.

2.1.3 Air Bearings

A great deal of effort has gone into the development of gas bearings for MEMS. In particular, the MIT micro-engine project and related research [56, 71-77] have invested in understanding the dynamics of air bearings, as well as practical implementation in MEMS turbine systems. Rotational speeds as high as 1.7 million rpm (corresponding to a tip speed of 370 m/s for the 250 µm diameter rotor) have been reported [77], along with a friction torque constant τ_f/ω of 5.9×10^{-12} N-m/rpm [78].

Air bearings exist in two basic types, using different techniques to maintain a film of air between the two moving surfaces. Hydrostatic bearings [74] require a pressurized gas source or pump to continually force air into a plenum, maintaining its pressure as fluid leaks out the sides of the bearing. This approach has had success in turbine applications, and is able to meet the stiffness and natural frequency requirements for both thrust and journal bearings. Gas bearings also practically eliminate wear issues and provide vastly decreased friction by eliminating the contact between solid moving parts. The main drawback of this approach is that they tend to exhibit very low length to diameter ratios, particularly compared with macro-scale rotating systems. This requirement is driven by the layout and fabrication of the device; since they are fabricated in silicon wafers, the length must be very short (a few hundred or thousand micrometers, or the thickness of several wafers) while the diameter must be large (of order many millimeters) to accommodate the turbomachinery blading. The bearings must be located near the edge of the rotor, because of the constraints of Deep Reactive Ion Etching (DRIE). Therefore, the bearings must work at high bearing sliding speeds (as high as 370 m/s [77])

Another significant issue is the requirement for a pressure gradient to be maintained. In turbine applications, pressurized air is expected to be readily available, as it must also drive the turbine itself. In other applications, there may not be such a source, and adding one to the design would often dramatically increase complexity.

The other possible air bearing type is the hydrodynamic bearing [79]. These work by using the viscous shear exerted by the moving walls to maintain the film. This presents a challenge because the pumping action of the moving rotor exhibits cross-coupled forces in the rotor plane; in other words, compressing the fluid in one side of the journal affects the stiffness of the journal bearing in the orthogonal direction. This can lead to whirl instability.

Furthermore, while journal bearings do away with the need for external pressurization, they are also relatively soft at low speeds, since the acting mechanism is strongly speed-dependent. This leads to instability at lower speeds, requiring a supplemental hydrostatic bearing for use at start-up and stop [74]. Thus, these bearings again have limitations when moving to applications without a compressed air supply.

The fabrication complexity for the air bearing itself is not greatly increased over rubbing bearings, although tight tolerances at high aspect ratios are required for the journal bearing, and no exotic materials are required. Thus, both types of air bearings, while effective in their intended applications involving turbomachinery, are limited by their high length to diameter ratios for these applications. For any other application, the main limitation is the requirement for pressurized air. For some applications, pressurized air could conceivably be supplied, but frequently at power costs too high to be practical in a MEMS system, and always at the cost of introducing complexity. For other systems, such as vacuum pumps (of great interest for micro chemical and biological sensors, see section 1.4), air bearings are not possible.

2.1.4 Liquid Bearings

Other MEMS researchers have also developed fluid bearings utilizing liquid [80]. The bearing consists of a thin film of liquid, confined between the stator and the rotor by hydrophobic boundaries around its location. This bearing provides axial stiffness in the same manner as the gas bearings (with an additional contribution due to surface tension), but also provides a lateral bearing through the surface tension forces. If the rotor moves off-axis, the surface tension between the hydrophilic section of the surface and the fluid provides a restoring force. Demonstration of this bearing, up to rotational speeds of 1800 rpm (tip speed of almost 1 mm/s for their 10 mm diameter rotor) has just been achieved [80], and characterization and modeling of its dynamics is ongoing, including measurement of a friction torque constant τ_f/ω of 1.2×10^{-9} N-m/rpm.

While the liquid bearing eliminates the need for a pressurized fluid source, it raises new issues. Introducing liquid into a MEMS system is a risky proposition; because of the relative strength of surface tension at this scale, stiction is a serious concern. Great effort is often expended in eliminating moisture from devices to prevent permanent adhesion due to stiction, and including liquid would directly counteract these efforts. Furthermore, the stage of the fabrication process at which liquid is added is of critical importance. Wet or dry chemical etches, as well as vacuum and high-temperature processes, all hallmarks of MEMS fabrication, obviously cannot be performed with liquid present, severely limiting the design freedom. Even after construction, the liquid may gradually evaporate or flow out of the bearing, absent a sealing mechanism. Furthermore, the bearing does not provide substantial stiffness against rotation of the rotor about axes normal to the primary rotation axis (known as “cocking.”)

2.2 Existing CNT Bearing Work

In light of all the advantages and disadvantages of the existing MEMS bearing technologies, the CNT bearing has been proposed as an additional contender in the arena of MEMS bearings. The atomic structure of CNTs, consisting of concentric nested tubes with no covalent bonding between them, was proposed [6] as a promising bearing building block almost immediately after the discovery of CNTs [81]. More details on the structure of CNTs are available in other works [3, 82]. Since that point, CNTs have been a favorite problem of atomistic simulations, and many have attempted to quantify the friction in the system (section 2.2.2). Finally, a few experimental demonstration prototypes of these bearings (section 2.2.1) have been constructed.

2.2.1 Experimental Demonstrations

Experiments involving CNT bearings have been challenging, primarily because of the difficulty of fabricating devices at such a small scale. MEMS has become a well-established field, and constructing devices with sizes measured in micrometers has become commonplace; however, at the nanometer scale, the processing toolbox available to MEMS designers is stretched to the limit. Even placing CNTs in a desired location is a substantial challenge, and fabricating additional device features that interact with them increases the difficulty. Nevertheless, a few intrepid groups have crafted devices that are able to demonstrate relative motion between CNT walls, and some have been able to make friction measurements. Still, measurement of friction remains difficult because the friction is very low compared to other forces in the system, such as the van der Waals restoring force caused by the increased surface energy when an inner tube is extracted from an outer tube. Additionally, friction in a rotating CNT bearing system has only been measured statically (at zero speed). This thesis attempts to address these issues, by developing a friction test stand that will enable measurement of friction in the rotating system (where the van der Waals force is absent) at a range of operating speeds.

2.2.1.1 Translational Bearings

One obvious mode of motion between adjacent walls is the translational sliding mode. In this mode, shells slide parallel to the axis of the tube, relative to each other. This mode can include short outer tubes sliding along a longer inner "rail," or inner tubes extending ("telescoping") and retracting from an outer casing. The latter case has so far been the only MWNT bearing system explored experimentally.

The first study on friction in translational CNT sliding, by Yu *et al.* [9], was performed in an SEM with manipulators capable of measuring force and displacement [83]. Yu's group was originally conducting tensile strength tests on CNTs [84] and discovered that the specimens tended to fail in the outer shells ("sword-in-sheath" mechanism), occasionally leaving some portion of the inner and outer tubes overlapping. In these cases, force and extraction length vs. time data were collected as the remainder of the inner tube was extracted, allowing examination of the forces involved in relative motion between shells.

Several types of forces were considered in this study. First, the "capillary" force was computed from the tube geometry. This force is caused by the van der Waals interaction between the adjacent sliding shells. As the tube is extracted, the surface energy is increased because the contact area between the inner and outer tubes decreases. The van der Waals attractive force, which tends to restore the contact area, is the derivative of the energy with respect to extraction distance [7]. Because the energy is directly proportional to the contact area (and hence inversely proportional to extraction distance), the result is a constant force acting to retract the inner tube into the outer tube. This restoring or spring force is not of interest for rotational bearings, since rotation does not change the contact area, and

hence the surface energy, but in these translational bearings it must be accounted for. In addition to this force, both static and dynamic friction forces, proportional to contact area, were assumed to be acting. Finally, it was noted that they could not distinguish between these surface friction forces and any additional forces arising from the interaction of the edges of the nanotubes.

One of the tubes Yu *et al.* [9] tested displayed a "stick-slip" behavior, stopping at several discrete locations until the force was increased back up (it was relaxed when motion began). They found that the force required to continue motion decreased proportionately with the length of overlapping contact area, to some constant at zero overlapping area. This is consistent with the assumption of area-dependent friction forces plus a constant van der Waals restoring force. A linear fit allowed estimation of the value of this constant force. Subtracting off this known force, they assumed the remainder of the force would be the frictional interface force, noting that they could not distinguish between surface-to-surface contact effects and any additional forces due to the interactions of the tube edge. This provided an estimate of static friction. The behavior of intermittent sticking may not seem promising for MWNT bearings, but it is important to recognize that the same static friction was detected at several different points. If the force to overcome the static friction had been continuously applied, sticking might not have occurred.

On the second tube, a more smooth motion was observed. By correcting again for the capillary force, the remaining friction could be found in the same way. However, this time, the friction represented a continuous resistance to the continuous motion, rather than a barrier to initiating motion at discrete locations. It was therefore considered to be an estimate for the dynamic friction. Interestingly, the force required to initiate motion in this tube was the same, indicating that the static and dynamic friction for the second tube are the same. However, the static friction was much less for the first tube. Yu *et al.* attributed the difference to commensurability differences, or possibly geometrical variations between the tubes.

While this experiment was able to establish some estimates for friction, Akita *et al.* took the research a step further [10, 11]. They performed a similar experiment in a similar apparatus, except for additional care taken with preparing the specimens. The mechanical breaking used previously to create specimens might have left extra dangling bonds and defects on the tube, resulting in unexpected additional friction from the interactions of the edge. In order to eliminate these effects, Akita *et al.* carefully burned off some portions of the outer tube using electrically induced local joule heating [85].

The force-displacement curve obtained by Akita *et al.* differed markedly from the work of Yu *et al*. The constant van der Waals attraction is readily apparent, but no variation with contact area is detectable. Since the contact-area-dependent portion of the force is assumed to be the friction, the friction was assumed to be so small that it could not be detected by the apparatus. This encouraging result indicates that if careful means are used to engineer the CNT to the desired configuration, superior friction performance can be obtained, compared with the more damaging specimen preparation methods used previously.

A different kind of experiment [7, 86, 87] was also conducted by Zettl's research group inside a transmission electron microscope (TEM) equipped with a nano-manipulator. This rare apparatus allows the nanotube to be probed mechanically and electrically while observing the atomic structure *in situ*. In order to extract inner nanotubes from the outer shells, the tip of the tube was burned off using similar local electrically-induced joule heating [88]. Then the manipulator was attached to the inner tubes by using a short, controlled electrical current pulse to induce deposition of organic materials present in the TEM, forming a "spot weld." This allowed the inner tubes to be mechanically extracted and reinserted.

Two types of forces involved in the system were investigated: the van der Waals attraction force discussed previously, and friction. By detaching the tubes from the manipulator, and allowing them to retract, two friction estimates were made. First, the van der Waals force (which was calculated from the measured tube geometry) must have been greater than the static friction to cause retraction, allowing an upper bound estimate on that static friction. With knowledge of the time taken for the tube to retract (it was less than one 33 ms video frame), an upper bound on the dynamic friction could also estimated from the computed van der Waals-induced acceleration.

Although a precise measure of friction was not possible, Zettl *et al.* established some important concepts. Since this was the first experiment capable of repeatably extracting and reinserting a single nanotube, it revealed the astounding reliability of the MWNT bearing system. Multiple different tubes were cycled approximately 20 times, with no behavioral change observed. Furthermore, no atomic damage was detected even at the highest TEM resolutions, indicating that such a system could actually be immune to wear over long periods of time. This result is believable when considering that nanotubes can have truly perfect, atomically stable, and smooth surfaces for the majority of their extent, and such a small inter-layer spacing that debris cannot accumulate and accelerate wear. Zettl *et al.* also noted that only one pair of tubes experienced relative motion in each system, which tends to confirm the idea that the optimal sliding interface is self-selected in a many-walled system. Both of these qualities are encouraging for the present work. Long-term reliability can be expected, and interface self-selection should allow tubes with even significant numbers of defects to rotate, provided they have at least one defect-free interface between tubes within their structure.

Yet probably the most important point raised by Zettl *et al.* is the distinction between the conservative van der Waals spring force and the dissipative friction force. It is easy to confuse the two, since both resist motion for the telescoping case. In fact, some of the other studies have not made the distinction, or are not clear about what is friction and what is a conservative force. However, the spring force is ***only*** present for the telescoping configuration – rotating systems and sliding systems with a short tube on or in a large tube do not experience a change in contact area over their movement range, and hence are immune to this spring force.

Zettl *et al.* went on to examine this exact problem more rigorously in a new experiment [12]. The same basic setup was used, except the addition of a manipulator with a known spring constant allowed force measurement by observing its deflections in the TEM. This time the tube was cyclically actuated, and the force-displacement curve used to extract data. In this manner, friction can be distinguished from conservative spring forces, as friction will cause a non-zero integral of force vs. displacement over one cycle, indicating net work input was required. This net work input is a direct demonstration that dissipation has occurred during the cycle, since the work contributes only to maintaining the motion, and the resulting energy input must therefore be dissipated as heat.

The results showed a generally constant force over the displacement cycle, corresponding to the spring force as expected. Superimposed on that average was a highly irregular, non-periodic fluctuation with a much smaller amplitude. The irregularity probably indicates the presence of defects in the tube, which is expected for a real-world situation. Remarkably, however, the irregularity was highly repeatable – over many cycles, in both extraction and retraction, the force-displacement curve was essentially unchanged, including the irregular variation. Two important conclusions were drawn from that fact: first, stable defects are present, creating a unique force-displacement profile for each tube. Second, since the curve retraces itself without hysteresis, there is no detectable dissipation (the net integral of Fdx over a cycle is zero), or friction. In a few cases, temporary hysteresis was observed, however, generally within a few cycles it disappeared, restoring the original force profile. The sudden appearance of dissipation was attributed to the introduction of defects, which can be caused by the

electron irradiation inherent in TEM. That means the restoration of the original force trace indicates that the defect was eliminated as suddenly as it was introduced. While it may seem remarkable that the MWNT is able to rapidly repair damage it sustains in the form of introduced defects, it makes sense in the context of the nanotube structure. A perfectly bonded graphene sheet is stable, while defects are not, particularly severe defects such as vacancies and inter-shell bonding, which resist inter-shell sliding. The mechanical energy provided by the continual motion could be enough to break these defects, allowing them to re-form in the more stable, defect-free configuration.

These studies are promising for the idea of a carbon nanotube bearing. They show that motion between shells in a MWNT is possible, and friction is low, as expected. Furthermore, the evidence that stable defects do not necessarily lead to dissipation, and unstable defects can be self-repaired, indicates that even an imperfect tube (such as those produced by CVD as required for this project) may be able to serve as a bearing.

In summary, translational CNT bearings have been studied experimentally, mainly by forced telescoping of the inner portion of the CNT with respect to the outer portion. It has been challenging to distinguish the dissipative friction force from the conservative van der Waals force, since the friction is several orders of magnitude weaker. Some groups have not been able to make a measurement of the friction because it was below their measurement threshold, while others have used indirect techniques to determine the friction by observing its impacts on the energy dissipation in the system. Full characterization of the friction, including dependence on sliding speed and other factors remains to be done; this can eventually be achieved using the test device of this thesis.

2.2.1.2 Rotational Bearings

Unlike translational sliding friction, experimental data on rotating friction in CNTs remains scarce. Two experiments [1, 2] have demonstrated that the general concept of a rotating CNT bearing is feasible. In both cases, a MWNT was placed horizontally on a substrate, and anchored in place with metal electrodes patterned by electron beam (e-beam) lift-off. In the first study, by Zettl *et al.* [1], a seesaw-like paddle was build onto the outside of the nanotube in the same step as the electrodes. Two additional electrodes were also patterned near the ends of the paddle, and a third electrode was buried under the device. At the end of the process, the paddle was released by undercutting the electrodes with a wet etch.

The paddle was then actuated by applying appropriate voltages to the electrodes, causing electrostatic attractions and repulsions. Initially, the actuator was torqued and released, returning to its initial position. This gave some interesting data on the torsional properties of the nanotube, but the device was not a true rotor at that point. However, Zettl *et al.* proceeded to remove or sever the outer shells of the nanotube to allow free rotation of the paddle around an intact inner axle. Several methods were attempted, but the one finally used was simply the application of sufficient torque to shear the outer tubes mechanically. Once the tube was free, complete revolutions at consistent speeds, as well as positioning to specific angles, were demonstrated with appropriate voltage signals. Additionally, continuous operation for thousands of cycles revealed no apparent wear, as the group had shown for translational bearings [7]. The experiment proved beyond doubt that it is possible to make a rotational bearing from an MWNT, and such a bearing may serve as a reliable component for rotary NEMS.

While the experiment was a remarkable proof of concept, Bourlon *et al.* went on to improve on the design [2]. Instead of simply torquing the nanotube until failure, they used the electrical breakdown technique (as used for some of the translational bearing experiments [85]) to selectively vaporize some of the outer walls of the tube before the paddle was constructed. The rationale was that in this way a

cleaner interface between the rotor (consisting of the long inner tube and attached paddle) and the stator (the outer shells remaining embedded in the electrodes on the ends) could be obtained than from mechanical fatigue-induced failure.

When actuating the device, Bourlon *et al.* first noted that the paddle did not return to the original position when released, indicating that the electrical breakdown technique was successful in defining a clear slipping interface, preventing the tube from torquing. However, they did observe a "stick-slip" behavior similar to what one of the translational experiments found [89]. They attributed the behavior to the same cause, namely the presence of defects at specific locations. While it is troubling that smooth behavior was not obtained, the friction at these sticking points was low enough that the electrostatic actuation system could overcome it.

In fact, Bourlon *et al.* were able to estimate the friction quantitatively. To the author's knowledge, this is the only data point on rotational friction in MWNTs in the literature to date. To determine the static friction, the group estimated the electrostatic torque required to initiate rotation of the device (which would be equal to the static frictional torque) based on a finite-element electrical capacitance model for the system. The result is the highest experimental estimate for friction yet reported. However, the friction was still well within the capabilities of the actuation system to overcome. In addition, the previous rotational experiment might be expected to have higher friction (though it was not measured) due to the rough edges left by the mechanical fatigue-induced failure, and even so, the friction was sufficiently low to allow actuation and continuous rotation. Together the two demonstrations provide confidence that rotational bearings are feasible and realizable.

These two demonstrations are just the starting point; the specific area of experimental measurement of rotating friction in CNTs is ripe for work. A great deal more data on both static and dynamic friction remains to be gathered, across a wide variety of tube types, speeds, defect densities, and other parameters.

The new approach investigated in the present work could provide advantages in furthering rotational friction research. Most importantly, the vertically oriented tube used here could enable substantial geometric improvements. Rather than the two or three actuator electrodes available in the previous studies, which resulted in asymmetric driving forces [8] and lack of coverage around the entire revolution [2], the new design suggests the possibility of arbitrarily many evenly spaced symmetric electrodes, with multiple phases and complete, fine-grained coverage for the entire 360 degrees. Furthermore, the vertical alignment might improve the rotor placement accuracy, improving balance and enabling high-speed rotation. Finally, the opportunity for a manufacturable, patterning-based process, instead of the single-shot hand-selection approach previously required, suggests that rapid production of many test devices could be used to examine the friction data across a wide space of nanotube geometry and quality. Eventually experimental rotating MWNT bearings may become a critical instrument for furthering the state of knowledge about CNT inter-shell friction; establishing such a test stand is the primary experimental goal of this thesis. Chapter 4 describes the design and fabrication of the prototype device, which could fill this need for a rotary friction testing apparatus.

2.2.2 Simulation Work

The theoretical investigation and simulation of friction in MWNTs has been a popular topic for several reasons. First, the theory is what originally inspired the notion of using MWNTs as bearings. Long before direct experiments were possible at this scale, it was noted by Charlier and Michenaud [6] that the intrinsic lack of bonds between concentric layers in carbon nanotubes could present a unique

opportunity for extremely low friction. Theory was the only available way to address the problem at first.

In addition, an MWNT is a particularly interesting system to study using the available atomic and molecular scale models. In some sense, models capable of addressing the dynamics of the system were created without a specific problem in mind, and the MWNT bearing was a good fit. Most of these models have been developed *ab initio,* building up from knowledge of atomic physics and dynamics rather than working from existing data. One popular approach is the numerical solution of the equations governing inter-atomic forces, called molecular dynamics (MD). While that approach is fitting, especially since the behavior of nano-scale systems often differs substantially from macro analogues, the lack of validation for the models from experimental evidence is apparent from the wide range of results. In fact, the theoretical friction predictions are spread over almost eight orders of magnitude, while the experiments all lie within three. It is important to realize that some models may not capture all the important concepts, and to not be lulled into false security by the preponderance of data they can generate.

Nevertheless, theory is critically important in understanding the true nature of friction in MWNTs. Only with knowledge of the underlying principles behind friction can intelligent designs for practical systems be pursued. To that end, this thesis includes work (chapter 5) on identifying the causes of the discrepancies between reported results in the literature, as well as development of a consistent approach to simulating CNT friction via MD.

2.2.2.1 Translational Simulations

The simulation of friction in translating MWNT systems has covered a range of different motions, including infinitely long tubes in relative motion, and small tube sections moving inside and outside of longer tubes. Because of the high computational cost, MD simulations are typically limited to a double-walled nanotube (DWNT), the smallest MWNT capable of relative sliding. The simplest simulation involves tubes moving relative to each other at a prescribed speed or extraction force, similar to the tension-testing experiments.

In fact, one of the groups that was able to perform an experiment on translational friction, Akita *et al.* [10, 11], also conducted a molecular mechanics simulation. They computed the potential energy of a tube as it was extracted from another tube based on an empirical model [90]. The resistance force was then taken to be the derivative of that potential with respect to the spatial coordinate (*i.e.* the van der Waals force). Like the experiment, the tensile force resisting tube extraction was constant at all overlapping areas, with only a variation of about 0.05%, periodic in the period of the carbon lattice. While the experiments have displayed a non-periodic variation [12], these non-periodic variations were attributed to the likely presence of defects in the real case. In the theoretical case, there is no disorder, so any variation would have to be from the regular carbon lattice. The quantitative estimate for the van der Waals force from the model was 4 nN, in agreement with the measured force of 4 nN (no uncertainties were reported [10].) Since the model, being quasi-static in design, considers only potential (conservative) forces, and not dissipative forces, the fact that the experiment agrees serves to reinforce the notion that only the spring forces due the van der Waals interaction are being measured in the experiment. The friction (which would make up the difference between the theoretical and experimental results, if such difference was apparent) should therefore be less than the uncertainties in the friction measurement and prediction.

Rivera *et al.* [14, 15] also examined the telescoping mode using molecular dynamics. A single infinite DWNT was simulated using MD with an established numerical potential model [91]. Different

constant relative velocities were imposed on the tubes, and the force resisting the motion was recorded. This force should represent the friction, since in an infinite tube there is no contact area change and hence no van der Waals restoring force. They found the friction to depend strongly on the sliding velocity, but not in a regular way. A monotonic increase in friction with velocity was observed between 100 and 250 m/s (12.7% and 31.8% of the average thermal velocity), and between 750 and 1000 m/s (95.3% and 126% of the average thermal velocity), but friction appeared independent of velocity between 250 and 750 m/s. No mechanism explaining the trend was proposed. Further study of exactly how friction depends on velocity is needed; the simulation work described in chapter 5, as well as experimental data eventually generated by the prototype in the present work, could be useful in that regard.

Another sliding mode has been popular in these simulations: If a tube is extracted from its outer shell, and released, as in one of the experiments by Zettl *et al.* [7], the van der Waals restoring force will pull it back in. If both ends of the tube are uncapped, the inner tube will continue going through and out the opposite end, until the spring force reverses its direction. The result is a simple translational oscillator. It is not a true harmonic oscillator, because the force is constant, not proportional to the "spring extension," or the separation of the inner and outer tubes' centers of mass. Friction is an important factor in these oscillators, as it controls the damping and the rate at which the oscillations decay. This system has been the subject of several theoretical studies and simulations.

Rivera *et al.* [14, 15] examined DWNT oscillators in addition to the telescoping simulations described earlier. First, several systems of different sizes and commensurabilities were simulated using MD with an established numerical potential model [91]. The inner tube was extracted and released, and the simulations showed decaying oscillations as expected. The velocity (computed as a numerical derivative of the position vs. time) showed a saw-tooth profile with constant positive and negative slopes, indicating the axial accelerations and forces were roughly constant in magnitude, only changing in sign as the tube crossed the midpoint. This is consistent with a constant van der Waals restoring force.

While over one or two cycles, the axial force appeared constant, over many oscillations the amplitude of motion clearly decayed, indicating the presence of friction. In order to determine the friction, a simple model was fit to the simulated result. Assuming that the restoring force is constant and always acts towards the center, while friction is constant but always acts against the velocity, each period can be divided into four sections based on the combination of the two force signs. The motion is a simple quadratic, and fitting each quarter-period to that quadratic gave the value of the two forces. Examining the resulting forces over time as the oscillations decayed yielded two interesting notes. First, Rivera *et al.* noted that the van der Waals force is constant for most of the duration, as expected. It only changes when the oscillations damp down to approximately the same magnitude as random thermal fluctuations, where the simple model breaks down. That is not of interest for the present work, as the restoring force is absent in rotating systems. Second, the friction force is at least two orders of magnitude smaller than the restoring (van der Waals) force. That is encouraging for bearing designs.

Rivera *et al.* examined a few parameters briefly to determine their effects on friction. Temperature is always a consideration for MD simulations, so it was an obvious choice for variation. They found that elevated temperatures cause the oscillations to damp out more quickly. They hypothesize that the higher temperatures lead to greater fluctuations in the geometry due to random motion, leading to more interaction between adjacent walls. They also reported that the oscillations damped out quickly for a perfectly commensurate system, in agreement with expectations that the aligned ridges would interlock easily.

However, Rivera *et al*. also recorded the normal force between tubes over the length of the oscillations, and the report mentioned that the friction force could be considered some fraction of it. This is not in agreement with the prevailing view that micro-scale friction is not dependent on the normal force. Furthermore, the friction force was assumed constant for the model, while the recorded normal force fluctuated wildly, with amplitude more than 5 times the friction force. In addition, the time scale of the normal force fluctuations is significantly shorter than the oscillation period, and hence if the friction really does depend on it, could not be treated as constant for each quarter-period. It is not clear what effect, if any, the normal force has, which warrants further investigation.

Guo *et al.* [16] attempted to quantify friction in DWNT oscillator simulations by a different method. Rather than working with position vs. time data directly, they observed the energy dissipation rate as the oscillations damped out. Specifically, they monitored the decay in the amplitude of the potential energy present due to the axial displacement of the inner tube. Friction was taken to be the time derivative of the energy divided by the average sliding velocity. This procedure yielded friction measurements for several systems.

Guo *et al.* also checked for the influence of additional parameters on the friction. For temperature, they found the same trend of increased dissipation at high temperature. However, they reported a more severe impact of this trend than the previous group. Their simulations were performed at 8K and 150K, and they reported oscillations dying off as fast as 3 ns for the higher temperature. Extrapolating to 300K, they expect that even a few cycles may be difficult, while the previous group's simulations persisted oscillating for hundreds of cycles. Some experimental data on friction vs. temperature may help clarify the exact dependence. Guo *et al.* also reported much stronger damping in commensurate systems, as expected.

Guo *et al.* also calculated forces in a different way. Rather than simulating the entire motion, they evaluated the potential energy from the model at many different possible displacements, independent of time. The force was then computed as the derivative of the potential with respect to position. They observed a constant mean force (the restoring van der Waals force) with a smaller periodic variation superimposed on it. They noted that for different systems, when the friction increased, so did the amplitude of this variation. It is not clear why the two should correlate, because the friction is a dissipative force, while the amplitude variations in the restoring force are conservative (they were computed as the gradient of a potential). A quantitative relationship between the two, established by more data points, might help elucidate the mechanism responsible for this perceived trend.

In addition to these oscillator studies, Guo *et al.*, also performed additional static simulations of combined sliding and rotation [13], focusing on the effects of commensurability in nanotube friction. They considered linear sliding and rotating in two configurations: a short outer nanotube sliding along an infinite inner tube, and a long inner tube telescoping out of the outer tube. In each case they examined the variation of potential energy (computed by two different methods, [92] and [93]) with distance as the nanotubes are displaced relative to each other. They then compute the forces simply as the spatial gradient of the potential energy. The tubes are assumed completely rigid, and the effects of deformation of the tubes is demonstrated to be negligible by comparison of a few cases with full MD simulations.

Guo *et al.* found that the rotational force was significantly lower than the linear sliding force (which both of which forces are computed as a derivative of a potential, and hence may not capture the important phenomena of dissipation and friction). This is expected, as there is no overall displacement during a complete rotation of the tube. However, in contrast with the prevailing view, they found that certain commensurate systems (in which both tubes are either zigzag or armchair) experience a very low

resistance compared with incommensurate systems. This might be explained by the fact that for these special cases, the ridges align with a circumference of the tube, so that their interlocking would prevent linear sliding motion rather than rotary motion. Indeed, these systems experienced the maximum linear sliding resistance, with any other tubes (commensurate or incommensurate) having about two to five orders of magnitude lower friction.

Guo *et al.* Also assert that the dependence of resistive force on tube size is opposite for different systems. For some systems, the force increases with either length or radius, while for others it remains constant. The former is indicative of a contact area dependence, while the latter would suggest there is no such dependence. It is not clear ***why*** the difference is observed, and it would be important to establish what is responsible for the perceived qualitative difference.

However, as discussed previously, it may not be warranted to equate resistance forces with friction. The paper states that fluctuations in the forces are directly linked to energy dissipation, so that a tube which experiences a large amplitude in resistance force over a given motion will dissipate energy quickly. This is based on their own prior MD calculations [16]. However, it is not clear why this correlation should hold, especially since the forces are computed as the gradient of a potential, and are therefore conservative by definition. A complete rotation of a bearing would result in zero net frictional work if the resistance forces were in fact truly potential. However, the MD simulations they use for comparison show a clear decrease in the amplitude of the fluctuation over time, indicating that the time-independent potential model is not capturing some important dynamics. It could be true that the amplitude with which the resistance force varies correlates in some way to the conversion of rotational motion into phonons, leading to the eventual loss of energy as heat, but the precise manner of such a relationship was not given, and in any case such a mechanism cannot be detected by a method which begins with the use of explicitly conservative forces. Furthermore, combined sliding and rotation is not expected to occur in the initial device, but it could be a topic of interest for future CNT bearing devices. More work is needed to clarify the true nature of the underlying phenomena.

In summary, translational CNT bearing simulations have attempted to compute the friction in the CNT system, by comparing forces computed as derivatives of the atomic potential, by fitting modeled dynamic behavior to the trajectory data, and by monitoring the energy dissipation in CNT oscillators. Some of the dependence of the friction on parameters including sliding speed and temperature has been investigated, but studies do not agree with each other in general, particularly on the quantitative value of friction. A unified and consistent treatment the various simulation modes is needed to explain the discrepancies reported; while this thesis includes such a broad study for rotational CNT bearings, translational CNT bearings are left for future work.

2.2.2.2 Rotational Simulations

While rotation has not been simulated as extensively as linear sliding, a few studies have been conducted. Zhang *et al.* [20] examined two DWNT systems of the same size but different commensurabilities. They first computed the potential energy from an established model [93] at several angular positions. They noted that for armchair or zigzag tubes, which have high rotational symmetry, the potential varies much less than for chiral tubes, which indicates that no particular relative angular displacement is preferred strongly. For the chiral case, certain discrete locations, with a period determined by the chirality of the tubes, would be more energetically favorable. These systems might therefore tend to "lock" in place in the absence of actuation. This is not truly friction, however, because the forces involved are conservative – tracing a complete revolution (or a period of symmetry) returns the potential to its original value, and the net work done is zero. The group also noted that these

potential energy barriers are about an order of magnitude smaller than those reported for linear sliding, indicating that rotational bearings should exhibit even less loss than linear bearings.

Since these time-independent computations do not capture the dynamic effects leading to friction, MD simulations were also performed. The edge of one tube was held still while the edge of the other was forced to rotate. The rest of the tubes were dragged along by the bonding dynamics with their neighbors, until the whole tube was rotating. The whole assembly was allowed to dissipate heat to a constant temperature reservoir. The potential energy was observed to fluctuate with a magnitude approximately an order of magnitude higher than for the steady case, indicating that it did not in fact capture the main causes of friction. Like some of the linear sliding simulations, Zhang *et al.* determined the friction by observing the energy dissipation rate, in the form of heat leaving the system. Friction is the energy dissipation rate divided by the frictional sliding speed. Once the simulations reached a steady state, the energy dissipation rate (and friction) was constant.

Zhang *et al.* also examined the effect of speed by adjusting the applied rotational speed at the edge. It was found that the friction increased more than linearly with rotational speed. The speeds simulated were limited by the mechanical strength of the tube – above 500 rotations per nanosecond (corresponding to an interfacial speed of 2450 m/s or 3 times the average thermal velocity, which is well beyond the expectations of any practically attainable speed), the bonds between the atoms were not strong enough to accelerate the free atoms in the tube to the enforced edge speed before the tube disintegrated. Such a problem could be corrected by simulating a slow enough acceleration to the desired speed that the forces due to inertia do not exceed the bond breaking strengths, but even without that a few good data points on rotational friction vs. speed were found. Experimental data on dynamic friction at different speeds could be provided by the project, which would help to validate the trend.

Zhang *et al.* also made use of a friction coefficient, a proportionality constant between friction and the normal force. As noted previously, the notion that friction scales with normal force is not necessarily true for atomic scale systems. While it was possible to compute the coefficient by averaging the friction force and the normal force extracted from the simulation, it is not clear whether this is a relevant parameter. There was no direct evidence given that the normal force causes the friction force, and the two tubes simulated had similar normal forces and friction forces, so it is difficult to make a comparison. Further study would be needed to truly understand the effect of normal forces.

Omata *et al.* [21] tried a simpler MD simulation, in which the inner tube was given an initial angular velocity, and as time progressed the inner tube slowed down while the outer tube sped up, presumably under the influence of friction. Observing the angular momentum of the inner tube revealed a gradual decrease, as momentum was transferred to the outer tube. There were also two oscillations superimposed on the trace. A short period, small amplitude variation matched the frequency of the radial breathing mode, a mechanical mode in which the nanotube expands and contracts. This variation was not significant compared to the overall trend, and was ignored. However, there was a much larger and slower variation, which was reported to stem from a flaw in the simulation. Unlike other similar simulations, this one was conducted adiabatically, with no way for the frictionally generated heat to escape. As a result, the researchers supposed that the heat energy was injected back into the tube as kinetic or potential energy, leading to the variations in angular velocity. While that might not be the actual cause of the variation, it would be an important flaw to correct for future simulations. Despite the large, unexpected, and probably erroneous fluctuations, an average frictional torque estimate was made by dividing the total angular momentum transferred by the total time. While the alternate method of a coast-down simulation (compared with enforced constant velocity) could provide friction predictions, it must be refined before the results can be considered accurate.

Servantie and Gaspard [24] made several refinements to the coast-down method. Their MD simulations, employing Tersoff-Brenner potential [94] for intra-wall interactions and the Lennard-Jones model [92] for inter-wall interactions, included a pair of CNTs coasting to equilibrium when given an initial relative velocity of about 1 rad/ps. Servantie and Gaspard found that the friction appears to vary linearly with the rotational speed, leading to an exponential time-evolution of the angular velocity and angular momentum, as the relative angular velocity decays to zero (this exponential decay is also discussed in section 5.2.6.1). Fitting an exponential function to the angular velocity trace (which was averaged over about a thousand trajectories to reduce noise) yielded an exponential time constant of 476 ps, which can be converted into a friction constant (which when multiplied by the angular velocity gives the friction) using the inertia of the tube. They also went on to examine the effect of temperature, and found that the friction constant depended on temperature to the power 1.53. By addressing both the variability from run to run (by ensemble averaging over many runs) and by precisely capturing the dependence of friction on speed via the exponential fitting function, this work provides what appears to be the best estimate available to date. It will also be shown later (figure 5-15) that the quantitative estimates from Servantie and Gaspards' work agree most closely with the simulations conducted for this thesis.

One other set of simulations on rotational friction in CNTs has been reported by Zhu *et al.* [27]. These studies again relied on a constant-speed approach, like Zhang *et al.* [20], but without a thermostat to maintain the outer tube at a prescribed temperature. This adiabatic boundary condition causes energy to build up in the system as the kinetic energy supplied by the constant-velocity boundary condition is continually converted to thermal energy. Thus, while Zhang *et al.* tracked the rate of energy exiting the system via the thermostat, Zhu *et al.* tracked the rate of energy accumulation. The result is essentially the same, except for the effect of the temperature increasing because of the lack of a thermostat. Zhu *et al.* reported a more-than-linear dependence of friction on speed (which may be caused by the larger temperature increase at higher speeds, compounding the friction increase; see section 5.2.5.2). They also found that the total friction increased linearly with contact area, or the friction per unit area is independent of geometry. Finally, they investigated the effect of varying inter-wall spacings, finding that friction increased when the spacing was either larger or smaller than the equilibrium spacing (0.34 nm).

These simulations do give a starting point for estimating the friction in rotating MWNT bearings, but more work is needed to establish the relationship between friction and the possible governing parameters. An effort to investigate these relationships, and to identify the causes of discrepancies amongst the literature results, is presented in chapter 5 of this thesis. Experimental data could also help validate or invalidate the models, and provide more points on curves matching friction to these parameters. The friction test stand described in chapter 4 is developed with the goal of providing that data.

2.2.2.3 Discrepancies in Reported Friction Values

CNT friction has been a popular topic for research. However, while it is universally recognized that friction in CNT systems should be "low" (some have even gone so far as to use the term "super-lubricating," [9, 12, 15] evoking comparison with such phenomena as superconductivity), exactly how low the friction is remains a point of contention. In other words, the quantitative value of friction is still unknown. Comparing all the friction data reported in the literature is quite instructive. Figure 2-1 shows all of the literature mentioned so far plotted together, as a function of sliding speed. This plot includes both experimental and theoretical works, for translational and rotational bearings. It is immediately obvious that there is a very wide (many orders of magnitude) range of what the friction is

reported to be. If nanotube bearings are to be used in practical applications, it will be critical that reliable, accurate, and consistent methods for predicting the friction be available.

One of the main goals of this work is therefore to identify the reasons behind this large variability, and to gain an understanding of what parameters control the friction. One issue that arises when trying to compile all the friction data scattered throughout the literature is the use of different units and conventions among the different reports. Conversion of units is typically not a challenge, but in some cases, the units used are not directly compatible, and some ambiguity exists with regard to what exactly is being reported.

One example is that the friction is commonly quoted in two different ways. Some authors report friction as a shear force, that is, in units of force per area. Other authors report it as a force per atom. In order to convert between the two, it is necessary to know the number of atoms in a unit area. Unfortunately, this is not a universal constant of nature, but a property of the geometry of a particular nanotube that can change as bonds stretch and bend (although it should remain within a narrow range). This "number of atoms in a unit area," hereafter called the surface atomic density, could be computed as

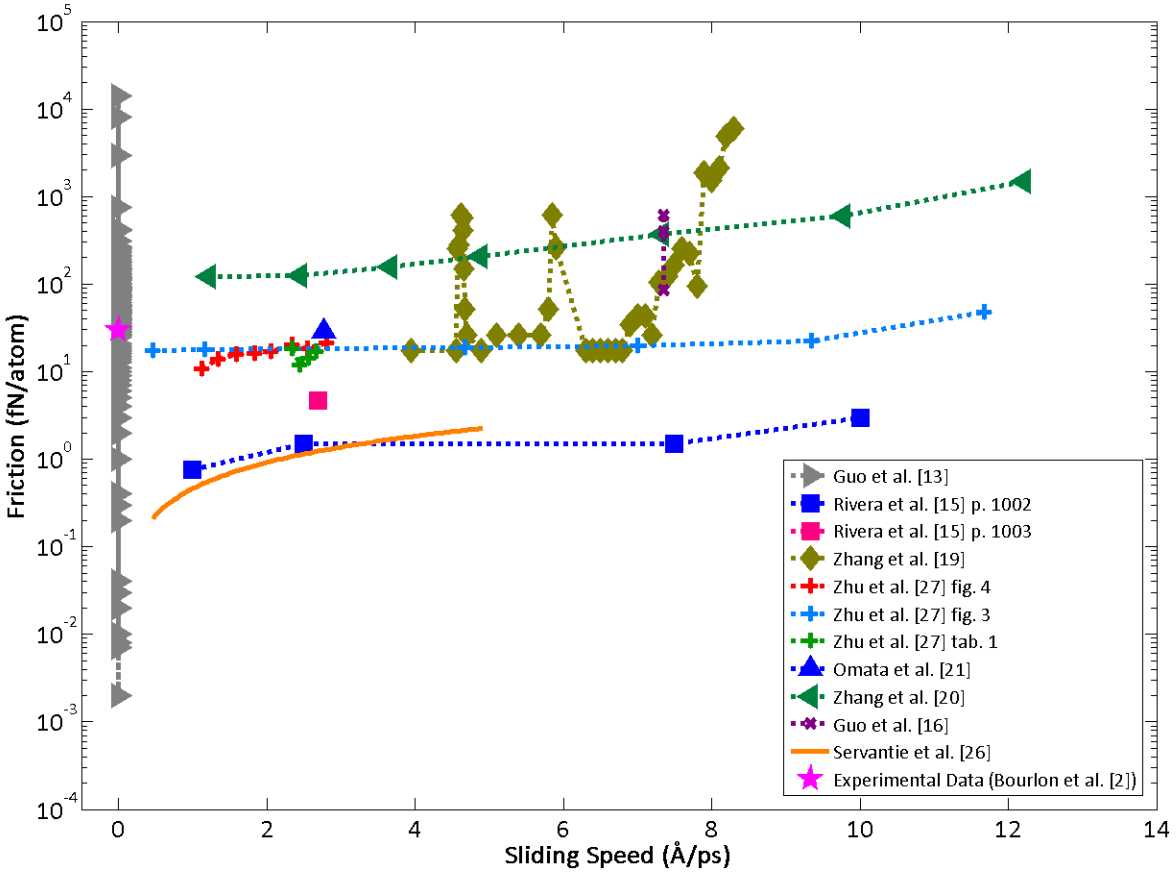

Figure 2-1: Friction in CNTs as reported in the literature; the quantitatibe value of the friction estimates varies by eight orders of magnitude.

$$\rho_S = \frac{N}{2\pi r L}$$

where ρ_S denotes the surface atomic density and has units [atoms/length^2], N is the number of atoms in a given CNT, and r and L are the radius and length of that CNT.

However, there is the additional complicating factor of how to count the atoms. The interpretation of the surface atomic density just described is one possible description, yet it strictly applies only to one CNT. To be more consistent with the data reported as friction per area, where the interfacial area between two CNTs is typically meant, the radius and length in the formula could also be taken as interfacial properties (*e.g.* mean radius and overlapping length). In that case, the number of atoms should also be the total atoms in both participating tubes, in order to appropriately reflect that it is an interface property. This gives a similar formula:

$$\rho_I = \frac{(N_1 + N_2)}{2\pi \bar{r} L}$$

where ρ_I will be called the interface atomic density, $\bar{r} = (r_1 + r_2)/2$ is the interface radius, and L is the length of the overlapping interface. Note that if the number of atoms in a CNT is directly proportional to the radius (as it should approximately be), the interface atomic density gives a number that is a factor of two greater than the surface atomic density.

The results reported in the literature do not generally specify which interpretation is used (i.e. does "per atom" mean "per surface atom" or "per interface atom") so it is necessary to make a guess. In this work, friction force per atom is taken to mean the total force in the system (computed as the total torque divided by the interface radius) divided by the total number of atoms in the system; this definition is therefore consistent with the interface atomic density. This convention has also been used to convert the data in the literature as needed, when the convention used therein was not specified.

Having chosen a convention, it is necessary to compute the numerical value of the surface atomic density. Geometric data collected from the MD simulations of chapter 5 were used to compute the interface atomic density. After relaxing under the conditions of the simulation (described in section 5.2.2), the radii of a (9,9) and a (14,14) CNT were measured to be 6.034 Å and 9.397 Å, respectively, while the lengths were 47.238 Å. This gives ρ_I = 0.801 atoms per Å^2. This value was used when papers did not report a value and one was needed to convert the units. Table 2-1 compares this value with interface and surface atomic densities reported in the literature.

The other data from the literature used when assembling this comparison (namely sliding speed and temperature) were also interpreted from the papers where not explicitly specified. Temperature was frequently specified, since its importance in MD is well known and it is relatively straightforward to measure, and is even commonly controlled to a desired setpoint (see section 5.3.3.2). Sliding speed was less frequently reported. The sliding speed was determined based on known times, distances, and accelerations when given, and in some cases was inferred based on provided trajectories of specific CNT bearings.

Table 2-1: Reported and computed values for the atomic density in CNTs, showing differences between sources.

Reference	Convention	Surface Atomic Density[1] ρ_S [atoms per Å^2]	Interface Atomic Density[1] ρ_I [atoms per Å^2]
This work (9,9)	Surface	0.3988	0.7975
This work (14,14)	Surface	0.4016	0.8031
This work (9,9) and (14,14)	Interface	0.4005	0.8009
Servantie and Gaspard [24]	Surface	0.379	0.758
Cumings and Zettl [7]	Surface[2]	0.287	0.574

[1]Either Surface Atomic Density or Interface Atomic Density was given, indicated by the "Convention" column; the other value was computed using the factor of two difference as discussed.

[2]The convention was not explicitly specified, but was assumed based on the low value given.

Yet these issues of interpretation are not enough to explain the nearly eight order of magnitude range of values reported for the friction. While the speed used in this comparison is frequently a rough estimate, the friction should not vary by more than a factor of two due to the ambiguity of convention discussed previously, but a several order of magnitude variation is observed.

There are many parameters which could cause the variation. One obvious possibility is geometry. Most studies selected CNTs of different chiralities, and hence different diameters. Such variations could lead to differing friction values because of both the changes in average diameter, and therefore curvature of the tube wall, as well as the spacing between adjacent walls. These effects are explored in section 5.3.3.5. Still, these variations are not expected to explain all of the variation among literature reports. For example, Zhu *et al.* [27] investigated the effects of varying inter-wall spacing, and reported a change in friction of 36% for spacings between 2.7 Å and 4.8 Å; This may seem like a large variation, but it is still less than a single order of magnitude.

Other factors causing the variations are more subtle and difficult to assess. One important example is the use of different empirical force fields to describe the forces in the system. Many models exist, including those by Lennard-Jones [92], Tersoff [95], Komogorov and Crespi [93], and Brenner [94], as well as its derivatives such as the Adaptive Intermolecular Reactive Empirical Bond Order (AIREBO) potential used here [96, 97]. While these potentials have all undergone extensive validation, it is still possible that not all the assumptions inherent in them were strictly valid in each case where they were employed, which could lead to variations in reporting.

Even more difficult to assess is the use of different simulation modes and boundary conditions reported in the literature. Researchers have employed various forms of adiabatic and temperature-controlled simulations, under both steady state and transient conditions. Even among simulations of the same basic type, the precise means of specifying the boundary conditions differ. Overly restrictive boundary conditions can impose non-physical behaviors on the system. For example, Omata et al. [21] explain some large amplitude oscillations as a result of an adiabatic boundary condition reflecting energy back into the system.

In order to reconcile all the friction data to date, all of these factors must be taken into account. The strategy pursued in this work is to conduct a fresh suite of MD simulations, which span the space of possible variations in the literature, but which are carefully and rigorously controlled so as to maintain consistency in all the other parameters while one parameter is explored. Thus, simulations of different types (adiabatic/constant temperature and steady/transient) were performed, with variations in geometry as well as initial conditions, boundary conditions, and operating parameters explored one at a time. The resulting improvements in narrowing down the range of friction estimates are described in detail in chapter 5.

[This page intentionally left blank.]

[This page intentionally left blank.]

3 Compatibility of Carbon Nanotubes with MEMS Processes

In order to construct a MEMS device utilizing a CNT as the bearing, it was necessary to develop a fabrication plan for the device. One important concern regarding this fabrication plan was the dearth of knowledge of how CNTs react to the available MEMS processes. It was therefore determined to generate a consistent and broad assessment of a suite of MEMS processes (listed in table 3-1,) which could be used as a reference for the development of the present and future fabrication plans. The parameters used for the wet and dry processes are listed in table 3-2 and table 3-3, respectively, and the results of the study are summarized in table 3-4.

Table 3-1: MEMS processes tested for compatibility with CNTs

Depositions	Wet Etches	Dry Etches
PECVD SiO_2	Piranha	SF_6+O_2 RIE
PECVD SiN_x	RCA SC1	SF_6+O_2 cryogenic RIE
PECVD a-Si	KOH	SF_6 RIE
LPCVD p-Si	Aqua regia	CF_4+O_2 RIE
	Isopropanol	CF_4 RIE
	Acetone	CHF_3+CF_4 RIE
	Nitric acid	DRIE
	Buffered HF	O_2 RIE
		O_2 ash
		Ar ion mill
		Vapor HF
		Vapor XeF_2

3.1 Motivation

While CNTs have recently been successfully incorporated into MEMS devices using some standard MEMS processes [1, 2, 28-37, 39, 40, 98], the literature has in general explored only those processes that are directly relevant to the fabrication of a particular device. A comprehensive reference describing the compatibility and behavior of many different typical MEMS processes, such as those produced by Williams et al. [41, 42] for silicon and other common MEMS materials, does not exist for CNTs. This chapter attempts to present a consistent and broad assessment of the effect of a suite of common MEMS processes on CNTs based on new experiments and a survey of the existing literature.

The breadth of processes studied here has been emphasized over the depth of characterization for each process, based on the expected utility of such results. Williams' papers [41, 42] are invaluable aids in selecting fabrication processes for a device fabrication plan. It is hoped that this report will aid MEMS fabricators in selecting processes for CNT-based devices, by demonstrating which processes are benign, and which cause substantial damage to CNTs. It is assumed that incompatible or damaging processes will not be of interest to the fabricator. Therefore, in-depth characterization of the precise damage

mechanisms of the process, as well as mechanical, electrical, and surface contamination properties of the remaining CNTs has been left to future work.

The approach has been to use scanning-electron microscopy (SEM) and transmission-electron microscopy (TEM) to examine specific individual nanotubes before and after application of each MEMS process under evaluation. SEM allows a quick determination of whether the process caused massive bulk damage (i.e., etching or removal of tubes, gross geometric changes to the tubes, etc.). However, SEM is not capable of detecting mild damage, thin coatings and adsorbed material, or other subtle changes to the CNTs; it can only assess obvious morphological changes. Therefore, in cases where the SEM did not show significant damage, TEM was used to investigate further. TEM allows inspection at the atomic level, which is a powerful tool for detecting even minute changes to the nanotube structure.

Chemical vapor deposition (CVD) and plasma-enhanced CVD (PECVD) of four common MEMS materials were tested for compatibility with the CNTs. Eight commonly used wet processes and thirteen dry etches were also evaluated. Parameters used for the wet processes (etches and solvent soaks) and the dry processes (depositions and etches) are listed in table 3-2 and table 3-3, respectively. The process methods are explained in more detail in the text, along with characterization results, sample electron micrographs, and comparison to existing literature for each process. Table 3-4 summarizes the compatibility of all processes with CNTs.

3.2 Methods

3.2.1 Carbon Nanotube Growth

Two different types of multiwall nanotubes, shown in figure 3-1, were tested in this study. First, tubes produced by CVD techniques (figure 3-1a) were evaluated. These tubes can be produced in highly controllable geometries by varying the size and location of the catalyst, as well as growth parameters such as temperature and applied electric field. These tubes are attractive for device manufacturing because they can be grown in place and integrated into a standard MEMS process. However, because the growth temperatures are typically much lower than other growth methods, the tubes tend to have defects and structural deficiencies. For this study, CVD tubes with diameters on the order of 100 nm and lengths of 5 to 10 µm were used; this size of tube is comparable to the tubes used in fabrication of the prototype bearing device (chapter 4) and were therefore both readily available, and directly relevant to the fabrication work of this thesis. These tubes were left attached to the original substrate (which was either silicon or glass with a chromium conduction layer of a few hundred angstroms), vertically oriented in a “forest” configuration. CNT forests were obtained from NanoLab, Inc. [99] and from Z.F. Ren of Boston College. They were produced using PECVD reactors, with Ni catalyst and C_2H_2 source gas, between 550°C and 750°C.

Arc-discharge tubes (figure 3-1b) were also tested, because these are the types of tubes that have been used in all successful CNT bearing demonstrations to date. These tubes tend to be much smaller, and much closer in structure to an ideal nanotube, which makes them more likely to rotate with low friction and wear. While their structure is superior, they are more difficult to work with because of their small size and the requirement that they must be manipulated into place. For this study, arc-discharge multiwall nanotubes with 5 to 10 walls, and diameters on the order of a few tens of micrometers, from Materials and Electrochemical Research Corporation [100], were used.

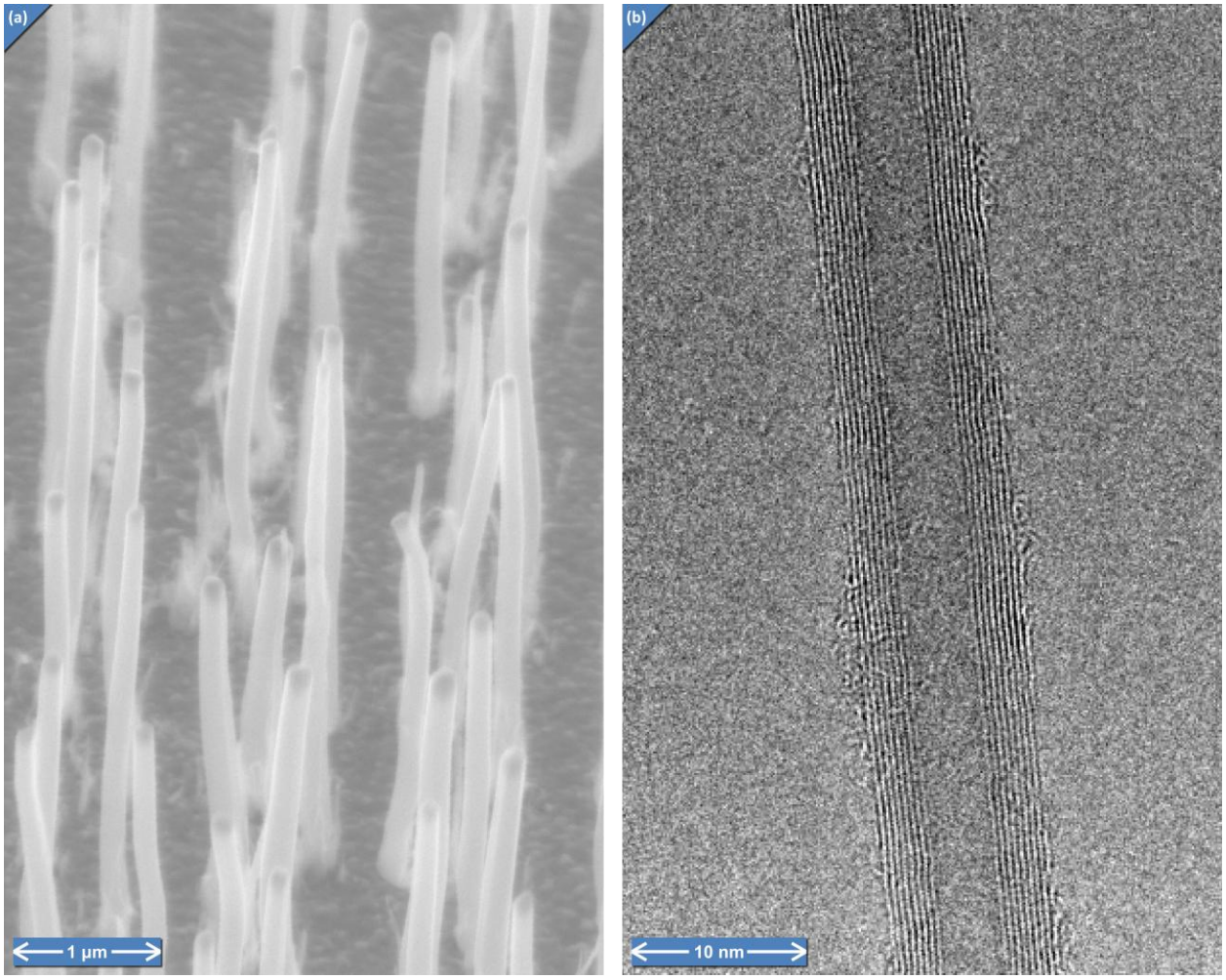

Figure 3-1: Unprocessed nanotubes, (a) produced by CVD and inspected by SEM, and (b) produced by arc-discharge and inspected by TEM.

3.2.2 Scanning Electron Microscopy

SEM was used primarily to assess large-scale damage or destruction of CNTs. In this way, processes that cause large-scale, obvious damage can be identified without the need for the more time-consuming TEM analysis. A forest of vertically aligned catalytic CVD tubes was examined before and after each etching process. Tubes were evaluated for obvious damage (e.g., sharpening, thinning, bending, or complete removal). A Zeiss Gemini Supra 35VP SEM at 5 kV, at Draper Laboratory, was used for this analysis.

3.2.3 Transmission Electron Microscopy

TEM was used to determine the level of damage caused by a given process in most cases where the SEM analysis did not show obvious incompatibility with that process. Arc-discharge tubes were examined and compared before and after each process, in the same 20- to 30-nm region on the tube whenever possible, to look for changes at the atomic level. Each sample was prepared by suspending the tubes in isopropyl alcohol and mixing ultrasonically for 30 minutes. The solution was then dropped onto TEM grids and allowed to evaporate, leaving isolated tubes. The entire grids were then run through each process under evaluation. To survive certain high-temperature processes, such as low-

pressure CVD (LPCVD) polysilicon deposition, special silicon TEM grids from TEMwindows.com [101] were needed. All other processes were conducted on standard carbon-coated copper grids. By using a high-resolution TEM (a JEOL 2010F field emission apparatus, at BC), at 200 kV and 10 µPa, individual atomic-scale features could be identified. For each process, we report the nature of the changes induced in the nanotube structure by the process (e.g., removal of outer walls) if any.

3.3 Results

3.3.1 Deposition Processes

3.3.1.1 PECVD Silicon Dioxide (SiO_2)

Silicon dioxide is a well-known material in microelectronics (as an insulator) and MEMS fabrication (as a release layer). SiO_2 has previously been used in conjunction with nanotubes. SiO_2 applied using a spin-on-glass technique [45] was found to form uneven coatings, based on TEM analysis. A liquid-phase deposition technique [102] produced conformal, uniform coatings. Both studies produced coatings without damaging the nanotubes, based on Fourier Transform Infrared (FTIR) [45] and Raman [102] spectral analysis.

SiO_2 is a particularly relevant material for this thesis; this is the material that forms the sacrificial layer, and which must coat the outer walls of the CNT (as described in section 4.2.3). While the studies just discussed provide some information about SiO_2 on CNTs, they do not address the specific technique (PECVD) used in our fabrication process. Thus, the examination of the effects of PECVD SiO_2 was one of the primary motivations for undertaking this study.

Here, PECVD deposition was used to apply layers between 5 and 300 nm thick to CNTs. PECVD might be expected to cause more damage than the liquid phase techniques reported in the literature, but it was found to be mild enough not to cause damage. Figure 3-2b,d shows the resulting coatings on CVD tubes, while figure 3-3c shows thinner coatings on arc-discharge tubes. An increase in diameter is evident, showing a uniform, conformal coating. TEM (figure 3-3c) shows no change to the walls of the tube, indicating that damage was minimal or negligible despite the energetic ion bombardment inherent in the PECVD process. PECVD appears to be capable of applying conformal SiO_2 coatings without damaging the CNT, and is therefore a suitable process for the fabrication of the prototype bearing device.

3.3.1.2 PECVD Silicon Nitride (SiN_x)

Silicon nitride was also applied to the nanotubes in a similar PECVD process. Prior studies have reported using SiN_x with CNTs, applied by thermal CVD processes [34, 40, 103, 104] with success. While Kojima et al. [103] reported damage to the nanotube when using a PECVD process (process parameters were not given), here, the PECVD process was found not to cause significant damage, as shown for both large-scale (hundreds of nanometers, figure 3-2c,e) coatings on CVD tubes and thinner (tens of nanometers, figure 3-3b) coatings on arc-discharge tubes. The difference in result between the current study and [103] could be attributed to variations in the PECVD processing parameters, as well as variations in the nanotube properties. In general, PECVD is capable of coating with SiN_x without damaging the underlying nanotubes. Although SiN_x specifically is not used in the fabrication process for the present device, the knowledge that it is safe to use on CNTs is useful for future applications, which may require additional materials for their specific properties or to have more selective etching options.

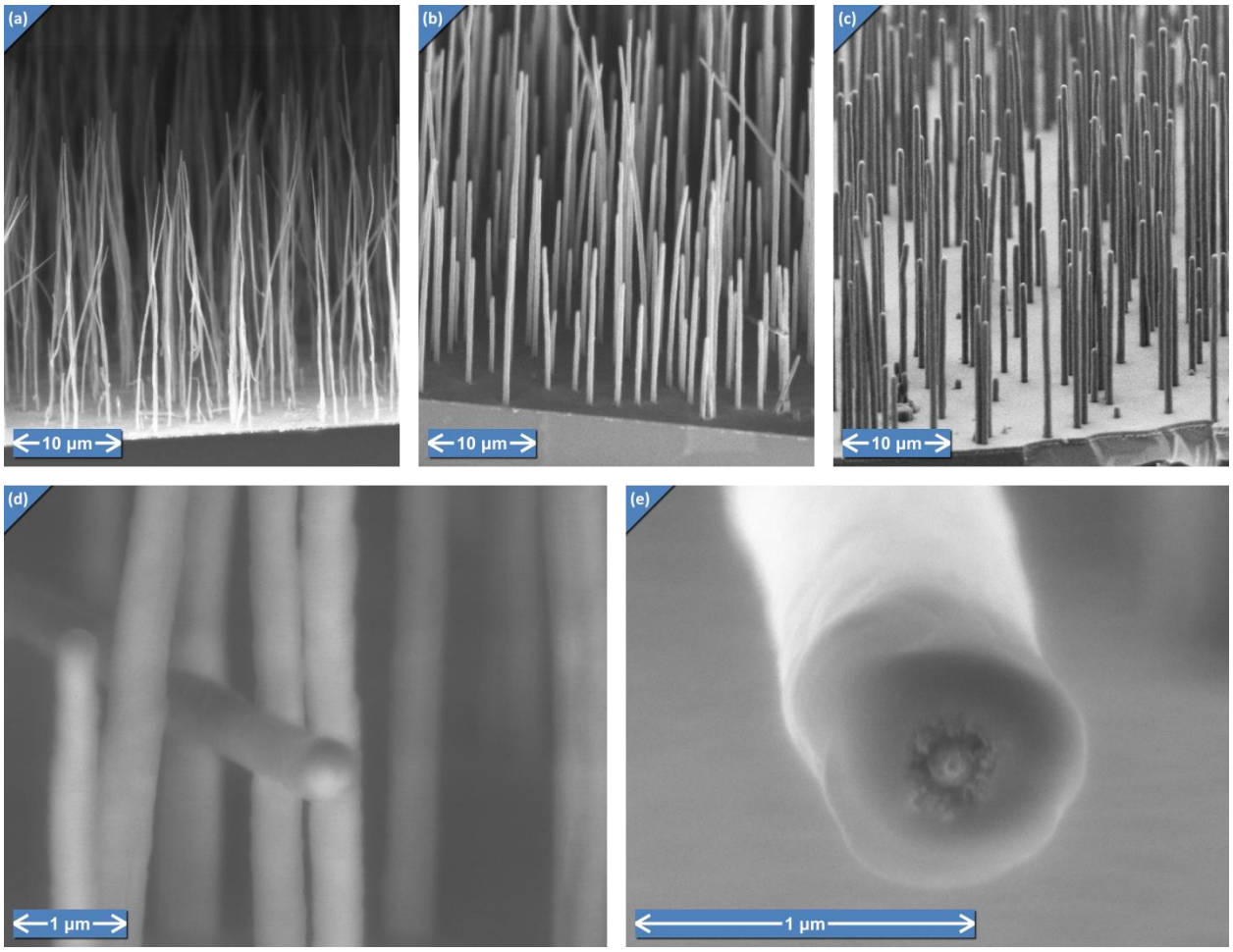

Figure 3-2: MEMS deposition processes with CNTs. Unprocessed CVD CNTs are shown in (a). CVD CNT forests coated with PECVD SiO_2 (b) and (d) and PECVD SiN_x (c) and (e) show uniform, conformal coatings. The nanotube is visible in the center of the structure in (e).

3.3.1.3 PECVD Amorphous Silicon (a-Si)

The same PECVD apparatus was used to deposit amorphous silicon layers on CNTs. The coating is uniform, even in very thin layers, and all the CNT walls remain intact, as visible in the TEM imagery in figure 3-4, indicating that few or no defects were introduced by the PECVD process. Amorphous silicon is not used in the prototype fabrication process, but again is included to give future device designers more material selection options.

3.3.1.4 LPCVD Polycrystalline Silicon (p-Si)

Silicon was also deposited using a thermal LPCVD process. This process is critical to the fabrication of the prototype device. After the oxide has been cleared from the top of the CNT, the polysilicon layer applied by LPCVD must bond to the outer walls of the CNT, and form the rotor. It is very important that the coating be conformal (so that the rotor wraps around the axle) and that the process does not introduce substantial defects (which would hinder rotation).

The effects of the LPCVD polysilicon process were observed in both SEM and TEM. While the tube structure was again essentially undamaged, the coating is shown (figure 3-3d) to be highly non-uniform

at thicknesses comparable to the tube diameter. This is a product of the polycrystalline nature of the silicon; the isolated portions of material are the nucleated silicon crystals prior to agglomeration into a polycrystalline layer. However, once the coating time becomes long enough that the individual grains coalesce, the coating thickness becomes more uniform, much as LPCVD polysilicon is commonly used to apply uniform thin films to flat substrates. LPCVD appears to be a viable technique for applying conformal polysilicon at thicknesses larger than the tube diameter. For the prototype device, the film thickness (2 µm) is more than an order of magnitude larger than the tube diameter (100 nm) so the polycrystalline nature of the film is not a problem.

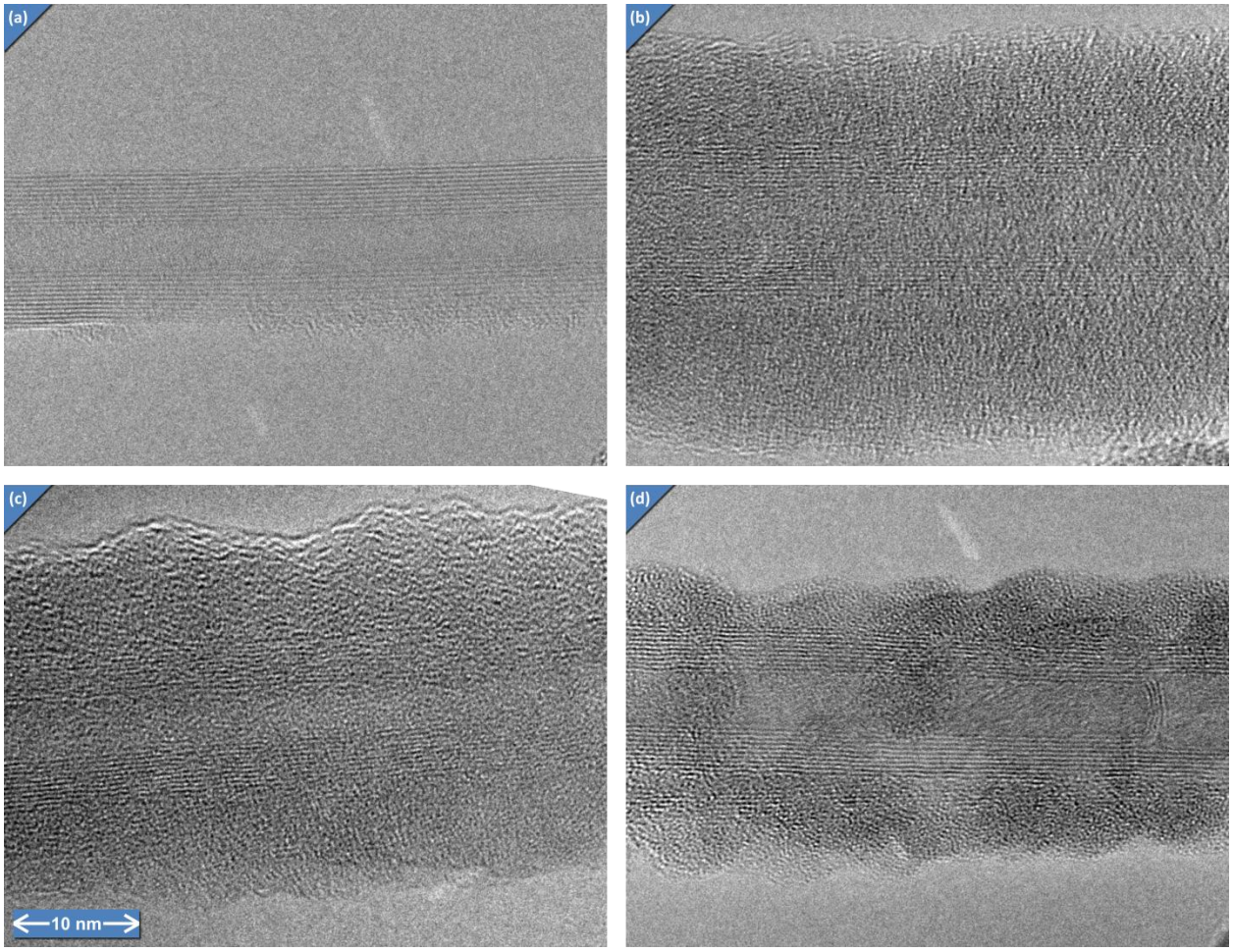

Figure 3-3: A 12-wall arc-discharge CNT before any processing is shown in (a). The same tube after a thin SiN_x layer has been deposited is shown in (b). The walls remain intact, although somewhat obscured by the amorphous SiN_x coating. Similar results were found for PECVD SiO_2 (c) and LPCVD polysilicon (d). To summarize, all deposition processes tested appear not to damage the underlying CNTs.

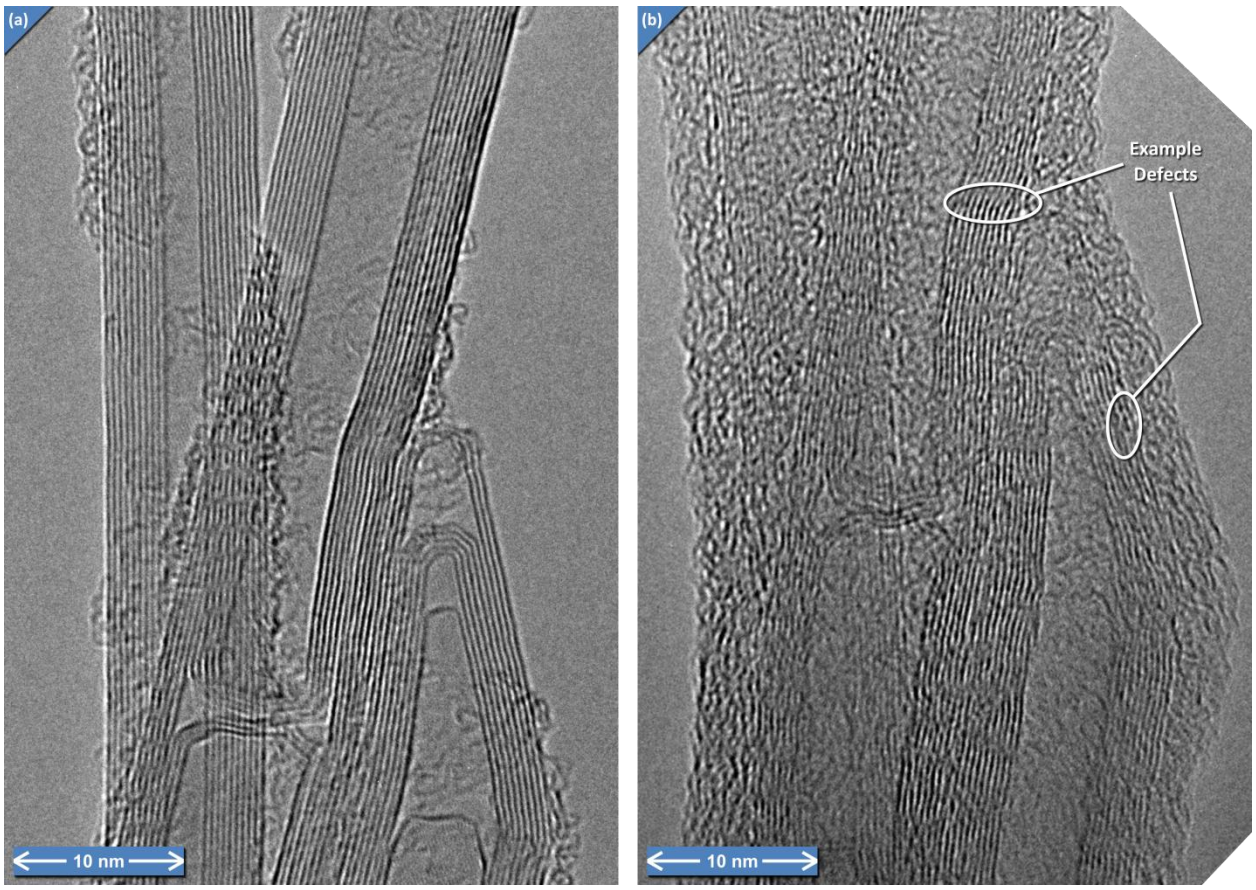

Figure 3-4: Amorphous silicon deposited on CNTs by PECVD. (a) Unprocessed arc-discharge CNTs showing some defects and amorphous carbon material. (b) The same tubes, with amorphous silicon coating. Only slight defects are introduced to the tube structure.

3.3.2 Wet Etches

Wet etches were performed on both vertically oriented CVD CNT forests and on TEM grids populated with arc-discharge CNTs. In all cases, a critical point dryer was used to eliminate clumping via stiction. Samples were rinsed in de-ionized (DI) water (except where the wet chemical under evaluation was a solvent) and isopropyl alcohol, and then dried in supercritical carbon dioxide (CO_2). All wet etches were performed for 30 minutes, except where otherwise noted; the purpose of the conservative (long) etch time was to ensure that any adverse effects from the wet etches would be captured even if they are subtle. Table 3-2 summarizes the parameters used in wet etching.

3.3.2.1 Piranha

Piranha is a mixture of sulfuric acid and hydrogen peroxide, commonly used to clean organic material from MEMS samples. The precise mixture used is described in table 3-2. For this work, tubes were subjected to a freshly mixed piranha bath for 30 minutes. No damage to the nanotubes was observed by SEM imaging, as shown in figure 3-5b. The results of the TEM also showed no damage, even down to the atomic scale, indicating that although nanotubes are organic, the nanotube structure is strong enough to be compatible with piranha. This information could be helpful when cleaning future CNT devices.

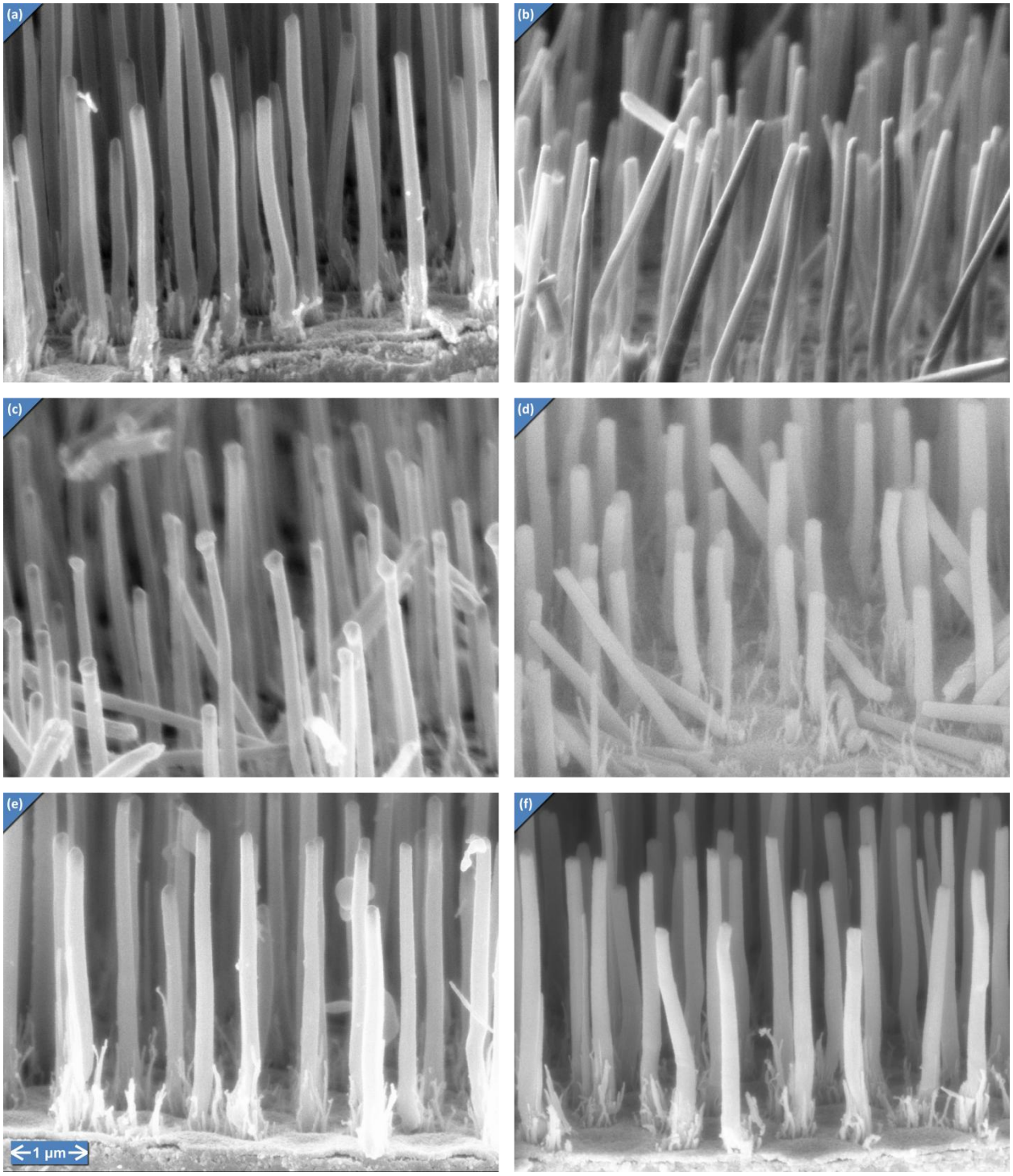

Figure 3-5: These SEMs show CVD nanotube forests subjected to wet etches. (a) Unprocessed CNTs. (b) Piranha does not cause noticeable damage to the CNTs. (c) KOH did attack outer layers of the CVD CNTs, thinning the CNTs over the 30-minute process. (d) Aqua regia attacked and removed the catalyst particles (dark spots at the CNT tips). (e) Acetone did no damage even after overnight exposures. (f) Nitric acid also attacked the catalyst.

Table 3-2: MEMS wet processes - parameters used

Name	Composition	Temperature (°C)
Piranha	3 H_2SO_4 : 1 H_2O_2 (30%)	(self-heating)
RCA SC1	1 NH_4OH : 1 H_2O_2 (30%) : 5 H_2O	25
KOH	KOH (45%)	80
Aqua regia	1 HNO_3 (60%) : 3 HCl (35%) : 2 H_2O	25
Isopropanol	C_3H_7OH	25
Acetone	C_3H_6O	25
Nitric acid	HNO_3 (10%)	25
Buffered HF	6 NH_4F (40%) : 1 HF(49%)	25

3.3.2.2 RCA SC1

Standard Clean 1 (SC1), developed by Radio Corporation of America (RCA) is another organic cleaning solution composed of ammonium hydroxide and hydrogen peroxide in water. The precise mixture used is described in table 3-2. Like the piranha, this etch caused little or no damage to the CNTs after 30 minutes of exposure. Thus, multiple chemical solutions that target organics are available for use on CNTs, without causing damage to the CNTs. However, not all organic-target processes are safe for use with CNTs (in particular, oxygen plasma strongly attacks CNTs; see section 3.3.3.12).

3.3.2.3 Potassium Hydroxide (KOH)

Potassium hydroxide is a common wet etchant that targets silicon in an anisotropic, crystallographically oriented fashion. The compatibility of KOH with carbon nanotubes has been examined in the literature, in the context of activation of carbon for hydrogen storage. Several groups [105-107] found that powdered KOH, mixed with CNTs at temperatures between 550°C and 800°C introduced defects and pores on the outer few walls of multiwall nanotubes without compromising their overall structure, based on TEM observation [105, 106] and Raman spectroscopy [106]. Clearly, KOH etching of CNTs is of interest to many MEMS designers, even though it is not directly relevant to the prototype device fabrication process.

In this study, we found a similar result. CNTs were exposed to liquid premixed KOH from a commercial supplier. The KOH bath was maintained at 80°C, and the CNTs were submerged for 30 minutes. KOH was found to remove substantial material from the exterior of CVD tubes, as shown in figure 3-5c. For arc-discharge tubes, KOH caused significant damage to the exterior layers, converting them from highly crystalline to near amorphous, while introducing some deeper defects as well. However, the superior crystallinity of the arc-discharge tubes prevented substantial material removal, as in the CVD case. These structural changes can be observed in the TEM imagery in figure 3-6. The increasing damage caused by KOH when applied to increasingly defective CNTs is consistent with literature studies. Raymundo-Piñero *et al.* [105] found that CVD tubes grown at a higher temperature, which are expected to exhibit more complete graphitization, resisted the KOH better; Chen and Huang [106] found a similar result with CVD tubes annealed at different temperatures. In general, KOH is not recommended for nanotubes if the structure must be preserved, particularly in the case of low-quality tubes or long etch times.

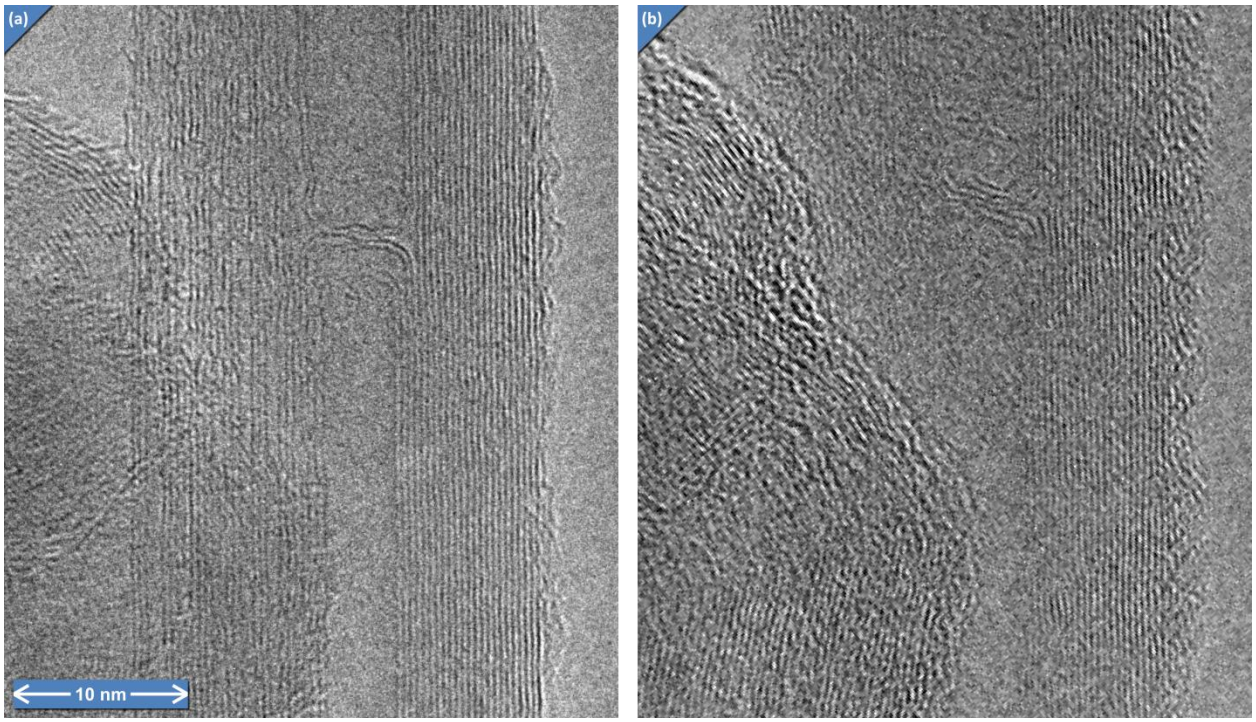

Figure 3-6: KOH caused some damage to the outer walls of the MWNTs, introducing defects and rendering the carbon more amorphous (less crystalline). The tube is shown before etching (a), with straight, ordered walls, and after etching (b), where some outer walls are no longer crystalline.

3.3.2.4 Aqua Regia

Aqua regia is an ancient solution intended for etching gold and platinum. The precise mixture used is described in table 3-2. A slightly more dilute formulation of Aqua regia has been used to remove catalyst material from single-wall nanotubes [108] without apparent damage to the structure, aside from the introduction of a few functional groups. The same result was observed in these tests. Figure 3-5d shows the removal of catalyst particles at the tip of CVD grown tubes. This chemical etch may therefore be of interest when removal of catalyst or other metals without damaging the CNT structure is desired.

3.3.2.5 Isopropyl Alcohol (C_3H_7OH)

Isopropyl alcohol is a common solvent in MEMS fabrication. It was found to be completely compatible with CNTs. Even tubes left in solution for days exhibited no damage or etching. The benignity of isopropyl alcohol to CNTs is particularly important for critical point drying. Critical point drying can avoid adverse mechanical effects such as stiction that result from the surface tension forces during ordinary liquid drying by passing through the supercritical region where there is no clearly defined boundary between liquid and vapor. Carbon dioxide (CO_2) is the most common medium for this process, and in order to transfer the workpiece into the liquid CO_2, it must be immersed first in another medium that is miscible with the liquid CO_2; the alcohols ethanol, methanol, and isopropanol (isopropyl alcohol) fit this bill. The compatibility of CNTs with isopropyl alcohol therefore enables critical point drying of CNT structures, which may be important for many devices given the high flexibility of the CNTs and the resulting propensity for sticking to each other and the substrate.

3.3.2.6 Acetone (C_3H_6O)

Acetone is used frequently to remove photoresists and other organic compounds. Some studies [109, 110] on acetone adsorption on single-walled nanotubes have concluded that acetone chemisorbs to the nanotube wall without inducing defects, in agreement with molecular dynamics [110] and quantum-mechanical computer simulations [109]. In this study, acetone was found to be completely compatible with both types of highly crystalline arc-discharge CNTs, and defect-ridden CVD CNTs, even when the CNTs were continuously submerged in acetone for several days. The still pristine CNTs are shown in figure 3-5e. Like piranha (section 3.3.2.1) and RCA SC1 (section 3.3.2.2), acetone is a useful option for removing certain organic materials without damaging the CNTs.

3.3.2.7 Nitric Acid (HNO_3)

Dilute nitric acid has been proposed as a purification agent for CNTs [111, 112]. These studies found, using X-ray diffraction, that nitric acid attacks the catalyst metals, removing them from CNT samples. At higher concentrations, they also reported based on TEM that the carbon material itself was attacked, especially amorphous or poorly graphitized regions. For this study, CNTs were immersed in a concentration of 10% HNO_3 in H_2O. It was found that catalyst particles were removed without substantial bulk etching to the tubes after 30 minutes. The effect of the nitric acid is illustrated in figure 3-5f. In general, nitric acid should be safe to use on CNTs, so long as the concentration is low and removal of catalyst is acceptable.

3.3.2.8 Buffered Oxide Etch (BOE)

BOE (whose primary ingredient is HF) is a common MEMS wet etchant used to selectively remove SiO_2 without attacking other materials. BOE is also the material used to release the prototype bearing devices, as discussed in section 4.2.6; it is therefore of paramount importance that BOE not cause any damage to the CNTs, which would inhibit rotation of the device. The literature is encouraging on the compatibility of BOE with CNTs: BOE has been used on several MEMS devices that incorporate CNTs [113-115] as a device release process without apparent damage to the CNTs. In this study, a similar etch was performed with the specific intent of assessing any damage caused to the tubes by the etch. After 30 minutes of exposure, the nanotubes showed no signs of etching or atomic-scale defects.

3.3.3 Dry Etches

Several common dry etches (including chemical and plasma etches) were examined; the process parameters are summarized in table 3-3.

3.3.3.1 Hydrofluoric Acid (HF) Vapor

Vapor HF etching is an alternative to liquid HF etching, which also selectively targets SiO_2. The main advantage provided by etching with HF vapor is that it obviates the need for critical point drying. The sample is never submerged in liquid, and thus surface tension at the drying stage is not present to cause stiction. In this study, vapor HF etching was conducted using a commercially available system from Idonus that works by suspending a sample upside-down above a pool of liquid HF in a sealed container. HF vapor was applied for 30 minutes, resulting in no apparent damage to the CNTs at either the bulk or the atomic scale. This is important, as it provides a useful alternative for future CNT device fabrication plans when needing to selectively remove SiO_2 without damaging the CNTs.

Table 3-3: MEMS dry processes - parameters used

Process	Equipment	Gas Flows (sccm)	Temp. (°C)	Pres. (mTorr)	Power[a] (W)	Power Density (W/cm^2)	Time (min)
PECVD SiO_2	Oxford PlasmaLab 100	SiH_4: 22 N_2O: 750 N_2: 430	380	1800	20	0.0452	0.5
PECVD SiN_x	Oxford PlasmaLab 100	SiH_4: 20 NH_3: 20 N_2: 1000	380	650	20	0.0452	2
PECVD a-Si	Oxford PlasmaLab 100	SiH_4: 50	380	1950	9	0.0199	2
LPCVD p-Si	MRL LPCVD furnace	SiH_4: 80	585	150	-	-	5
SF_6+O_2 RIE	Oxford PlasmaLab 100	SF_6: 60 O_2: 10	25	60	100	2.21	30
SF_6+O_2 cryo	Oxford PlasmaLab 100	SF_6: 60 O_2: 10	-25	60	100	2.21	30
SF_6 RIE	Oxford PlasmaLab 100	SF_6: 60	25	60	100	2.21	30
CF_4+O_2 RIE	STS RIE	CF_4: 25 O_2: 5	20	60	100	1.23	30
CF_4 RIE	STS RIE	CF_4: 25	20	60	100	1.23	30
CHF_3+CF_4 RIE	STS RIE	CHF_3: 14.6 CF_4: 1.4	20	20	200	2.47	30
DRIE (etch)[b]	STS Multiplex ICP	SF_6: 130 O_2: 13	20	20	600 (ICP) 22 (platen)	7.67	30
DRIE (passivate)[b]	STS Multiplex ICP	C_4F_8: 100	20	20	600 (ICP) 22 (platen)	7.67	30
O_2 ash	March Asher PX-250	O_2: 40	(NC)[c]	200	55	-	30
Ar ion mill	STS RIE	Ar: 30	20	60	100	1.23	30
Vapor HF	Idonus vapor phase etcher	HF: n/a	40	(NC)[c]	-	-	30
Vapor XeF_2	Xactix Xetch X3	XeF_2: n/a	(NC)[c]	3000	-	-	25

[a]Power was supplied at 13.56 MHz in all cases except PECVD SiN_x, for which a cycle of 7 seconds at 50 kHz and 14 seconds at 13.56 MHz was used.

[b]DRIE works by cycling between etching and passivation (polymer deposition). The two steps are listed separately for clarity, but represent only one process. The etch step was 8 seconds, followed by a 5-second passivation step.

[c](NC) indicates "not controlled," *i.e.* that parameter was not actively regulated or measured.

3.3.3.2 Xenon Difluoride (XeF_2) Vapor

Xenon difluoride is used to selectively etch Si without damaging other materials, in particular, SiO_2. The XeF_2 etching was performed using a commercially available system from Xactix. SEM analysis of the CVD nanotubes revealed that no substantial bulk damage was done to the nanotubes (while the silicon substrate was substantially etched). The results of the TEM analysis (figure 3-7) confirm that no significant defects were introduced at the atomic level, at least for the wall portion of the CNT (the less-stable end cap suffered some small deterioration). While not directly relevant to the prototype bearing device fabrication, this result is included for its importance to future CNT device fabrication efforts.

3.3.3.3 Argon (Ar) Ion Milling

Ion milling removes material by physically sputtering with high-energy argon ions. In general, it is not selective, but etches most materials. Ion milling has been used on CNTs [116] to improve field emission properties. Chen et al. [116] reported significant damage and even removal of thinner or "weaker" tubes, while thicker tubes were sharpened at the tip. Similar results were found here, as shown in figure 3-8a. The sharpening of the tip can likely be attributed to the concentration of the electric field in the plasma at the CNT tip. Use of argon ion milling on exposed CNTs is not recommended unless such sharpening is desired. However, sharpening may be desired for certain applications such as field emission or AFM cantilever tips; in those cases, this process could be useful.

3.3.3.4 Sulfur Hexafluoride (SF_6) Reactive Ion Etch (RIE)

Reactive ion etching (RIE) with SF_6 is a common method for anisotropically etching silicon for MEMS fabrication. CVD nanotubes were exposed to the plasma for 30 minutes, after which they exhibited extreme damage, as shown in figure 3-8b. The tips of the nanotubes were sharpened, likely because of

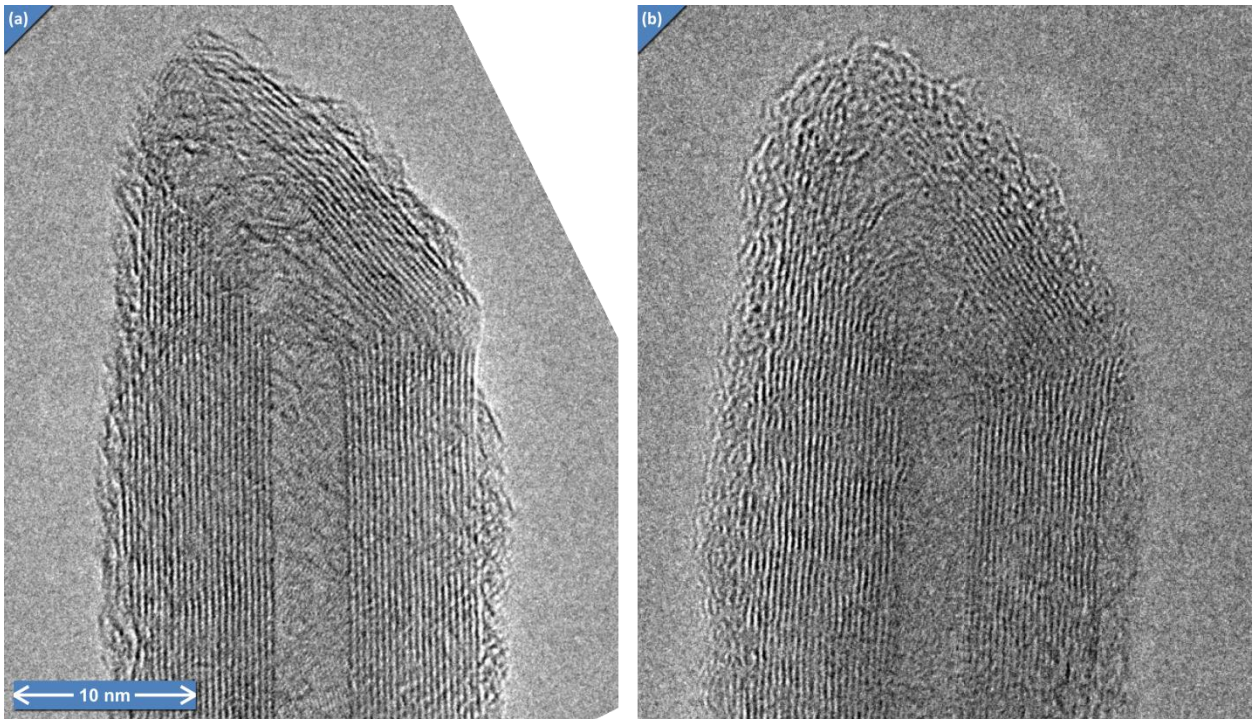

Figure 3-7: Xenon difluoride did not cause any significant damage to the CNT walls, although in this case the less-stable end cap was slightly attacked after 30 minutes of etching. The tube shows good crystallinity after the etch (b) compared with before the etch (a).

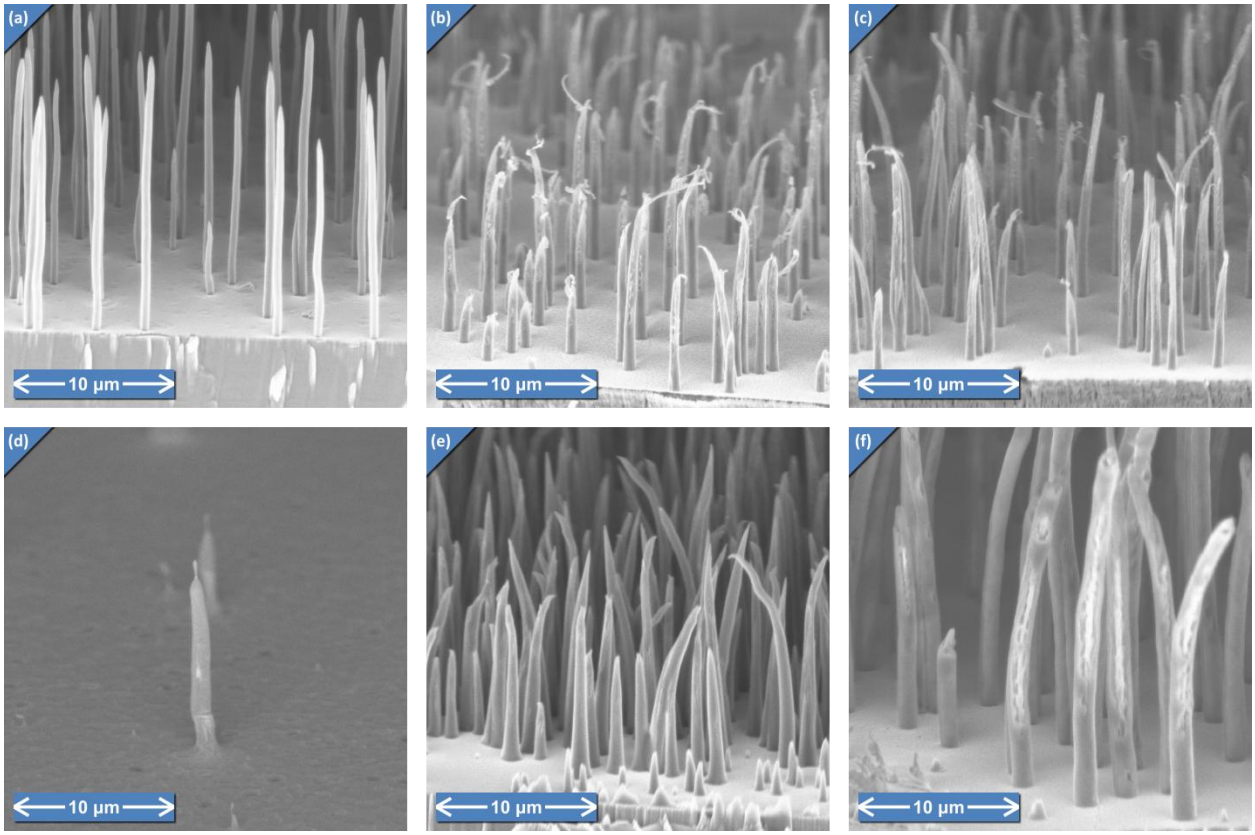

Figure 3-8: These SEMs show that ion etch process inflict substantial damage on the tubes, for the following chemistries: Argon (a), SF_6 (b), SF_6/O_2 (c), CF_4/O_2 (d), CHF_3/CF_4 (e), and CF_4 (f). Common damage modes include tip sharpening due to the field concentration in the tip region (all), and bending due to tube weakening and defect introduction (b,c,e,f).

the increased etching due to the electric field concentration at the nanotube tips. The nanotubes also showed extensive obvious damage throughout their lengths, as well as substantial curvature. While "plain" SF_6 etching was not used for the prototype fabrication process, there are many possible variations that see widespread use in MEMS, and one variant in particular (section 3.3.3.6) was used. Several of the more common variations, including this baseline process, were included here for completeness.

3.3.3.5 Sulfur Hexafluoride and Oxygen (SF_6/O_2) RIE

The addition of oxygen to an SF_6 plasma increases the etch rate of Si at the expense of selectivity over photoresist. The effect of this etch on CNTs was much the same as the pure SF_6 plasma, and is shown in figure 3-8c.

3.3.3.6 Cryogenic SF_6/O_2 RIE

Cryogenic cooling of the SF_6/O_2 RIE process can be used to obtain a highly anisotropic silicon etch, with vertical sidewalls, to substantial depths. This is achieved because the low temperature inhibits the chemical reaction on the walls, which receive no energy from the incoming ions in the plasma. A cryogenic SF_6/O_2 RIE process was used to define the rotor in the prototype bearing fabrication process (see section 4.2.5), although the CNT was encased in a polysilicon layer and protected from the etch by a metal mask. Still, in future device versions it may be desirable to leave the CNT exposed during a silicon etch; therefore the compatibility of the CNT with the etch process was investigated.

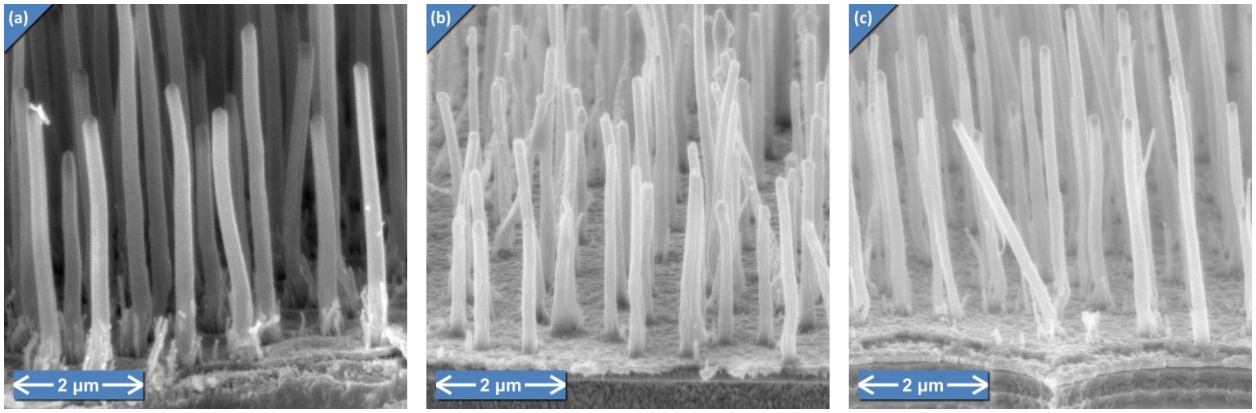

Figure 3-9: Unprocessed CNTs are shown in (a). Little or no damage was observed for SF_6/O_2 cryogenic etching (b), and Bosch Process DRIE (c). Common damage modes include tip sharpening due to the field concentration in the tip region (b—g), and bending due to tube weakening and defect introduction (c,d,f,g).

The cryogenic cooling significantly reduced damage to the CNTs during the plasma etch process. Some slight thinning of the CNTs was observed (shown in figure 3-9b), but the marked sharpening and bulk damage evident in the other plasma etches is absent. Cryogenic SF_6/O_2 etching is may be usable on CNTs where this modest removal of material is acceptable; however, if the atomic structure must be preserved it is likely a process that should be avoided.

3.3.3.7 Bosch Process Deep RIE (DRIE)

The Bosch Process is another method for anisotropically etching silicon. The process works by alternating between an SF_6/O_2 RIE process and a C_4F_8 polymerization process. The deposited polymer inhibits etching on the sidewalls, maintaining an anisotropic etch.

For etching of CNT forests, the polymerization also protected the CNTs from all directions. The DRIE caused no visible damage to the CNTs, as is evident in figure 3-9c. Note also the scalloping of the underlying silicon edge due to the cyclic nature of the Bosch Process. Arc-discharge CNTs were not examined under TEM for this process. Furthermore, the recipe used (parameters are described in table 3-3) was relatively mild; a more aggressive recipe might be used for deep (hundreds of micrometers) features, and should be investigated for CNT compatibility. Future work is therefore recommended to fully establish the compatibility of DRIE with CNTs.

3.3.3.8 Tetrafluoromethane (CF_4) RIE

CF_4 is another common etching chemistry in MEMS, used for etching various materials, including Si, SiO_2, and SiN_x. This process was found to cause significant damage to the nanotubes at a bulk level, including tip sharpening, bending, and defects introduced along the length of the tubes. The results are shown in figure 3-8f. The CF_4 family of etch chemistries was not used in the prototype bearing device fabrication, primarily because an anisotropic etch of materials other than silicon was not required. However, this common etch is likely to be used in future CNT devices where such etches are required, and therefore the baseline and variations are included here for reference.

3.3.3.9 Tetrafluoromethane and Oxygen (CF_4/O_2) RIE

The addition of O_2 to the CF_4 etch increases the etch rate at the expense of selectivity over photoresist. This particular etch has been used on CNTs [104], however, the compatibility of the process or the damage done to the nanotubes was not explicitly considered. In this study, it was found that this

etch was also incompatible with CNTs, resulting in severely shortened and sharpened tubes. The bulk etching results are shown in figure 3-8d.

3.3.3.10 Trifluoromethane and Tetrafluoromethane (CHF_3/CF_4) RIE

CHF_3 with CF_4 is another common chemistry used in RIE, which targets SiO_2 and SiN_x. Nanotubes that underwent this process showed similar bulk damage to the other RIE chemistries, as shown in figure 3-8e.

3.3.3.11 Oxygen (O_2) RIE

Oxygen plasmas are commonly used to etch photoresists and other organic materials. O_2 RIE is done in a similar apparatus to the other plasma processes, in contrast to an asher. Oxygen plasma treatments have been used on CNTs; Lee et al. [117] reported etching of the outer walls of the CNTs, resulting in reduced diameter, after a short etch. O_2 RIE was not performed during this study, but a similar O_2 plasma process, called ashing, was evaluated and is discussed in the following section.

3.3.3.12 Oxygen Ash

Ashing is also an O_2 plasma process using a different configuration. Instead of placing the sample flat on the powered electrode, the sample is in a basket above the unpowered electrode. This configuration protects the sample from direct exposure to the highest energy ions, resulting in lower etch rates but less ion bombardment damage.

Oxygen ashing has been used on CNTs [115], and in that case, was found to quickly and completely etch away single-wall nanotubes. For this study, multiwall nanotubes were subjected to 30 minutes of O_2 plasma in an asher. The resulting damage was significant. CVD-grown CNTs (shown in figure 3-10a) were observed to thin substantially, leaving a “matchstick” appearance with the catalyst particle for a head. They also bent substantially. Higher quality arc-discharge tubes (figure 3-10b) were able to withstand some ashing. Defects were introduced in the outer walls of the tube, and amorphous material removed, but the general internal tube structure remained intact.

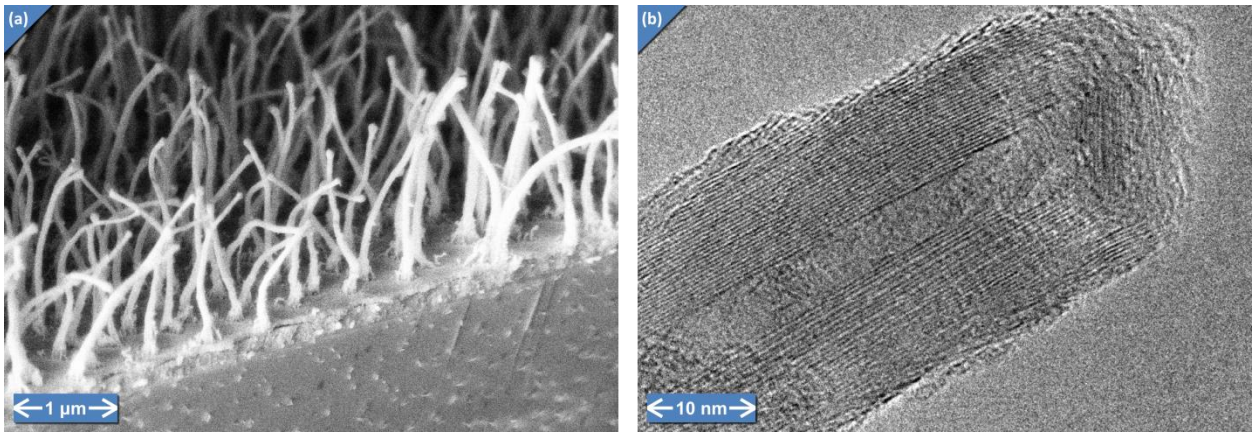

Figure 3-10: Oxygen ashing causes substantial damage to poor quality CVD nanotubes (a) and only some damage to the outer walls of a high-quality arc-discharge CNT (b).

3.4 Summary

For the first time, carbon nanotube compatibility with a suite of many typical MEMS processes has been assessed consistently and coherently. While previous literature addressed individual MEMS processes on a piecemeal basis, focusing only on those processes relevant to their particular application, here both processes relevant to the prototype bearing device fabrication and many other processes of general interest have been studied. The resulting information about which processes are compatible with CNTs (collected in table 3-4) will be a valuable resource for those wishing to design CNT devices in the future, and needing to quickly select processes without evaluating each one individually. The more detailed information of section 3.3, which compares the present results with the results from the existing literature, and discusses specifically what effects are caused by each process, will also be useful in deciding which processes are good candidates for a particular application.

In general, CVD deposition of material onto the CNTs works well. Amorphous materials were deposited in conformal, uniform coatings, as were polycrystalline materials above a critical thickness. Wet etches and dry chemical etches without ion bombardment or atomic oxygen, which typically exhibit good selectivity compared to plasma etches, also tended to leave the nanotubes mostly undamaged or only slightly damaged.

On the other hand, plasma-etching processes with direct ion bombardment or atomic oxygen present were shown to cause significant damage to nanotubes at a bulk scale. While short periods of exposure to these etches may be acceptable for some chemistries, longer periods should likely be avoided.

It is worth noting that the damage caused by the plasma processes appeared consistent across many plasma chemistries. This suggests that the damage may result primarily from ion bombardment, and not from chemical reactions. Therefore, fabrication processes that have the nanotubes completely encapsulated or shielded from direct ion bombardment during plasma etching processes may not experience significant nanotube damage.

Table 3-4: Carbon nanotube compatibility with MEMS processes

Name	Compatible	SEM	TEM	Related Literature
Piranha	Yes	X	X	
RCA SC1	Partially	X	X	
KOH	Partially	X	X	[105-107]
Aqua regia	Partially	X		[108]
Isopropanol	Yes	X	X	
Acetone	Yes	X		[109, 110]
Nitric acid	Partially	X		[111, 112]
Buffered F	yes	X	X	[113-115]
PECVD SiO_2	Yes	X	X	[45, 102]
PECVD SiN_x	Yes	X	X	[103, 104]
PECVD a-Si	Partially		X	
LPCVD p-Si	Yes		X	
SF_6+O_2 RIE	No	X		
SF_6+O_2 cryo	Partially	X		
SF_6 RIE	No	X		
CF_4+O_2 RIE	No	X		[104]
CF_4 RIE	No	X		
CHF_3+CF_4 RIE	No	X		
DRIE	Yes	X		
O_2 RIE	No			[117]
O_2 ash	No	X	X	[115]
Ar ion mill	No	X		[117]
Vapor HF	Yes	X		
Vapor XeF_2	Yes	X	X	

SEM and TEM columns indicate whether a process was examined by those methods in this study. Processes with neither column checked were not performed for this study; they are included based on the literature listed.

[This page intentionally left blank.]

[This page intentionally left blank.]

4 Carbon Nanotube Bearing Prototype

The prototype CNT bearing device fabricated as a part of this thesis comprises a silicon rotor disk supported on a vertically aligned CNT, which serves as the axle and bearing. Figure 4-1 shows a schematic representation of the device. The goals are to demonstrate the feasibility of this configuration for CNT bearings, and to gather data on the friction performance of the bearings.

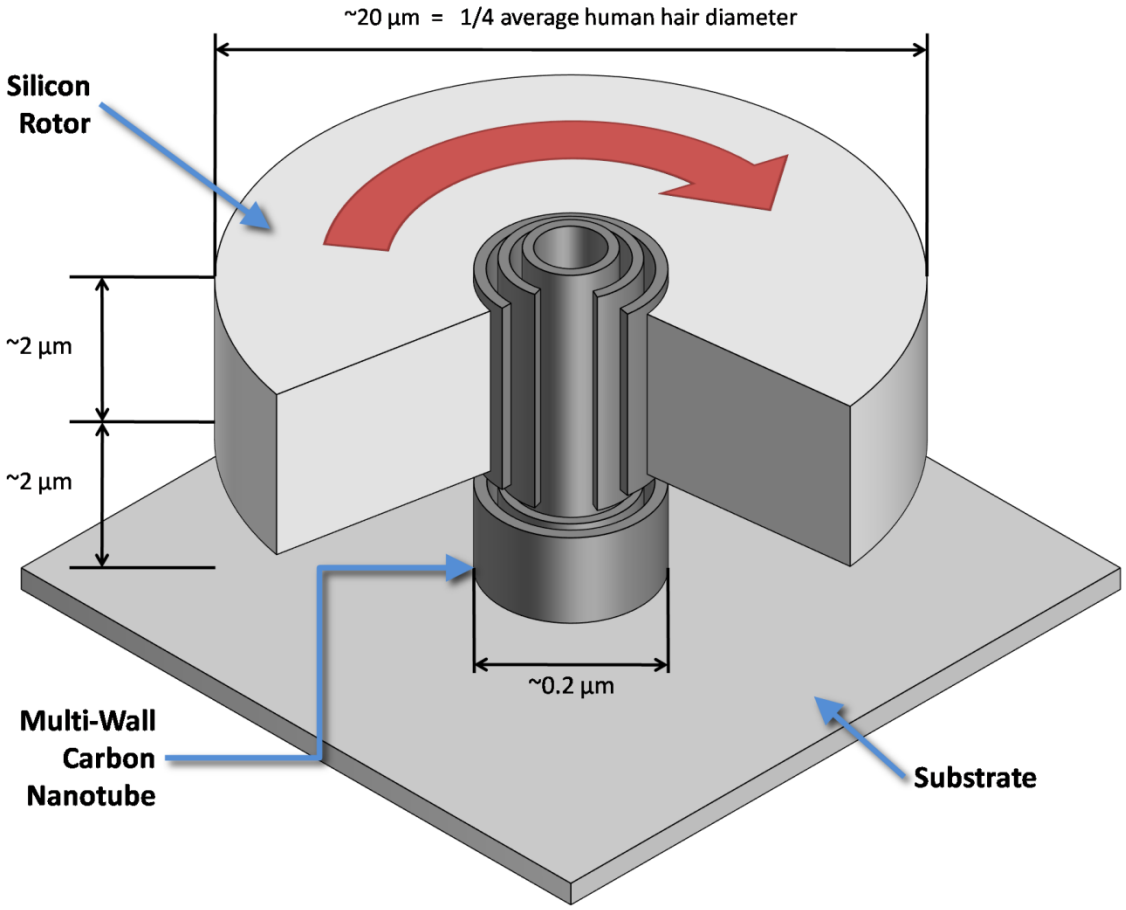

Figure 4-1: A schematic representation of the CNT bearing prototype, with a cut-away showing the structure of the CNT in the center.

4.1 Prototype Design

The purpose of the prototype device is to demonstrate rotation in a CNT bearing featuring a vertically aligned CNT. Therefore, it could be quite simple, having only a rotor and some actuation mechanism to cause rotation. When initially considering what configuration the prototype should take, both doubly supported (with both ends of the shaft supported) and singly supported (cantilevered shaft) layouts were considered. These configurations are sometimes known as the "Jeffcott" [118] and "Stodola" [119] rotors, respectively, after those who initially modeled their dynamics. Based on the exceptional stiffness and strength of the CNT, it was decided that while the Jeffcott configuration would provide substantially improved stiffness, and hence higher possible operating speeds and lower deflections, the Stodola configuration would be sufficient to initially demonstrate rotation. This

conclusion was borne out by the classical model described in section 4.1.1. The Stodola configuration also enables a greatly simplified fabrication process by reducing the number of lithography, deposition, and etching steps required.

To actuate the device, a mechanism for applying torque needed to be included in the device design. Several mechanisms were examined, and have been thoroughly discussed previously [3]. One obvious choice for rotational actuation would be to build an electrostatic motor around the rotor. This actuator would work by attracting electrodes on the rotor to corresponding stator electrodes around the periphery by applying appropriate voltages across the gap. This technology has been demonstrated in MEMS rotational motors [43, 59-64] (although these motors suffered from the limitations of their bearings). Additionally, their behavior has been well modeled [43, 63], and design [60, 62], fabrication [61, 62], and characterization [59, 64] of these motors have been studied in depth. However, implementation of these motors requires complex external control electronics, as well as additional fabrication steps to add the rotor and stator electrodes and traces to contact pads that can interface with the outside world. It was desired to avoid this extra complexity, since initially the main goal is only to demonstrate any rotation at all. However, it should be noted that electrostatic motors are an excellent candidate for actuation of future devices and applications based on the bearing, since it can provide bi-directional actuation, uniform torque coverage, 360° actuation at high angular resolution, and precise electronic control.

For the initial prototype, it was decided to actuate the device using jets of air directed at blades defined on the rotor. This can be accomplished without any extra lithography steps, since the blades can be defined in the same step as the rotor itself. The most challenging part of this actuation scheme is to direct jets of air with size comparable to the rotor at the vanes in a balanced, but offset, manner, in order to cause a torque. This was accomplished by blowing the air through micropipettes, which have a tip diameter of only 5 µm. These pipettes were affixed to micro-positioners designed for electronic probing and testing of microdevices, allowing them to be aimed with sub-micrometer precision, directly at the rotor vanes. The air was supplied by a syringe pump, through tubing to the micropipettes, at flow rates necessary to provide the necessary force on the vanes. A schematic of this testing setup is shown in figure 4-24. Laser radiation pressure was also considered as a means of applying force to the vanes on the rotor, but it was computed that the rate of heat delivered to the device by this method, given the wattage needed to provide the necessary force, would be much too great to be dissipated through conduction, convection, or radiation before melting the device.

4.1.1 Stodola Model

In order to choose the geometry of the prototype, a model of the device performance was developed; details on the development of this model are available in [3]. The model predicted several failure modes in the system and computed the main performance metrics (maximum speed and coast-down time) as a function of geometry, allowing the geometry of the prototype to be optimized. The geometry selected in [3] was used here, and the model was not further developed in this work. The methods and results from [3] are summarized in this section.

The basis of the model is the well-known Stodola rotordynamic model, of which Childs [120] provides a thorough treatment. This model considers the rotor to be a rigid disk, supported on a shaft, which is treated as a classical beam element. There are several assumptions which underpin this model. First, the assumption of a rigid disk relies on the flexural rigidity of the disk being large compared to that of the supporting beam. In the present case, that assumption is warranted, because even though the modulus of the silicon is less than that of the CNT by an order of magnitude, the disk thickness (on which

the rigidity depends as the cube) will turn out to be more than two orders greater than the CNT diameter.

A more critical assumption is that the CNT can be treated in a continuum fashion, using a classical beam model. Some researchers, including Yakobson and Avouris [121], have not been satisfied with continuum mechanics as an adequate description for the mechanical behavior of CNTs. They point out that molecular scale structures possess substantial anisotropy and local variation in properties corresponding to the actual atoms and bonds, and that material properties across the nanotube are therefore not truly uniform. Furthermore, it is difficult to define geometric features such as cross-sectional area for atoms and molecules, leading to a variation in quantities such as density and Young's modulus depending on the somewhat arbitrary choice of dimension on which the measurements are based. However, the CNTs used in this device are relatively large (50 or more walls,) thus closer to a true classical continuum than the single- or few-walled tubes favored for study by the theoreticians. The ambiguities associated with defining the geometry are less important, since the variation in any given dimension is smaller relative to the dimension itself. Furthermore, experimental investigations [122] have indicated that for large tubes, mechanical properties that do not vary from tube to tube can be established with some degree of accuracy and repeatability. Since the only mechanical property used in the analytical model (the Young's modulus) is used to describe beam bending, which was exactly the phenomenon used to determine the Young's modulus in the study [122], it is expected that the continuum model will be a good starting point for describing the mechanical behavior of the nanotube in this device. That Young's modulus value of 1.28 TPa was used for the model.

Using these assumptions, the model describes the physics of a 5 degree of freedom system (three angles of rotation and two translations, in the plane of the rotor). The model predicts deflections, as well as stresses in the structures, as a function of operating speed, rotor geometry, and rotor imbalance, determined by the translational misalignment (a function of the lithographic alignment precision, assumed to be 1 μm) and angular misalignment (a function of CNT orientation, which was measured to be on within 10° of vertical based on TEM analysis of several tubes) of the rotor. The stresses were checked against the known material strengths, and the deflections against prescribed limits (for example, the rotor angular deflection cannot be so large that the rotor "crashes" against the substrate) for a range of geometry and operating conditions. This procedure resulted in an envelope of candidate designs.

Within the envelope, an optimal design was selected by assessing performance parameters. The main performance parameter is the coast-down time, or the time the rotor would take to come to rest if given an initial spin rate. This parameter should be maximized, in order to have the best possible precision in measuring the friction in the rotor via a coast-down experiment. Assuming a constant friction of 0.85 MPa, based on the most similar experimental measurement available [2], the coast-down time is proportional to both the maximum possible speed and the disk inertia. The diameter of the disk should therefore be maximized. The maximum possible diameter was 20 μm, taking into account the deflection and stress constraints, as well as fabrication limits for the CNT and the rotor disk itself. This corresponds to a disk thickness of 2 μm, a CNT length of 4 μm, and an expected coast-down time of about 1 ms, from a maximum speed of 3.2 Mrpm. This resulting design (with selection criteria and performance detailed in [3]) provides optimal coast-down time for friction measurement, while avoiding failure by remaining within the deflection and stress constraints, and remaining within the limits of available fabrication capability.

4.2 Prototype Fabrication Process

The initial efforts to develop a fabrication process for the prototype CNT rotor are described in detail in previous work [3]. At that stage, the fabrication process development was still incomplete. The general approach was established, using an SiO_2 release layer and polysilicon rotor layer to construct a cantilevered device. However, most of the processing steps were not refined, and there were problems that have since been resolved. The most important issue was that the release layer intervened at both the substrate-CNT interface and the rotor-CNT interface, resulting in devices that came completely detached in the release step. This issue was solved by introducing an extra step to remove the unwanted oxide, described in section 4.2.3. Additionally, the rotor layer etch had numerous problems including a failure to cover the central portion of the rotor due to resist coverage. The solutions to that problem were developed here, using a double-masking technique described in section 4.2.5. The current, improved fabrication process is the version that is described in this chapter.

The general approach to fabricating the device (illustrated schematically in figure 4-2, and with images of an example device in figure 4-3) was to use surface micromachining. After first obtaining an isolated, vertically oriented CNT, a release layer was deposited to separate the rotor from the substrate. Then the rotor layer was deposited and etched into the rotor shape. Finally the release layer was removed with a selective chemical etch, leaving the rotor supported solely on the CNT. A detailed description of each process step follows, with discussions of the challenges encountered and their resolutions. The parameters used in each process can be found in table 4-1.

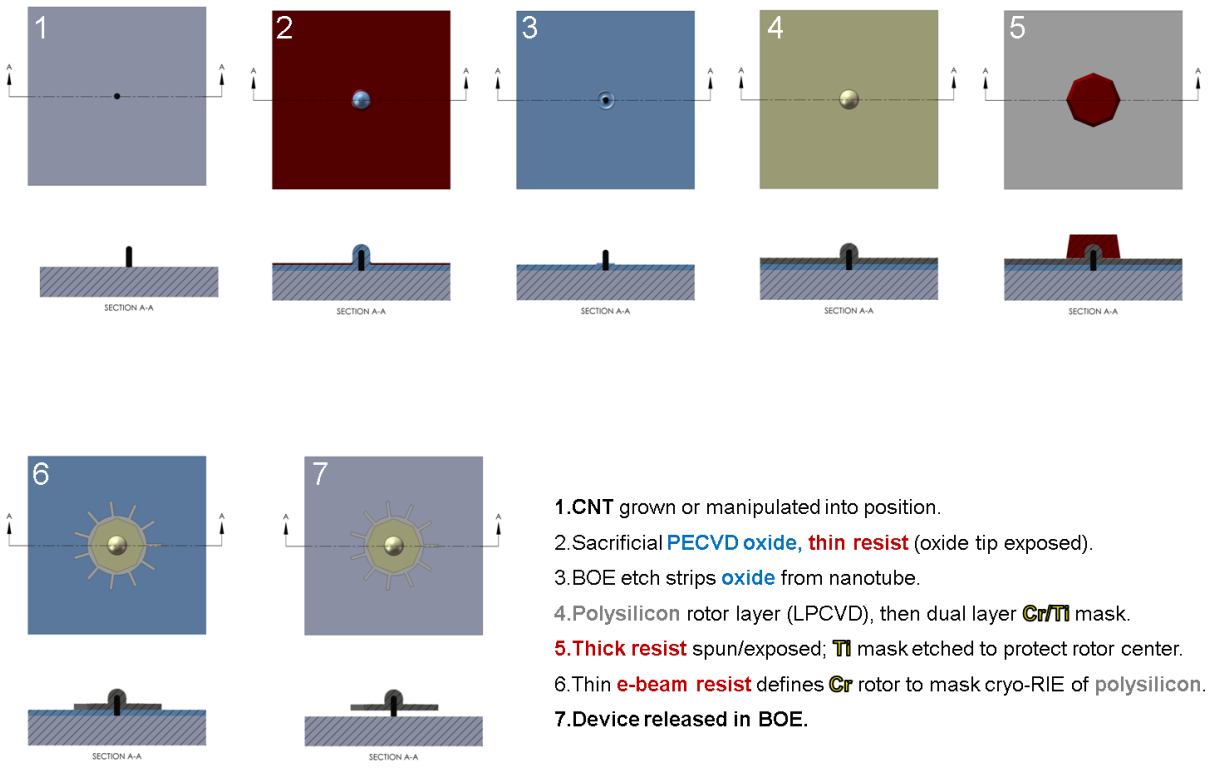

Figure 4-2: The overall fabrication process.

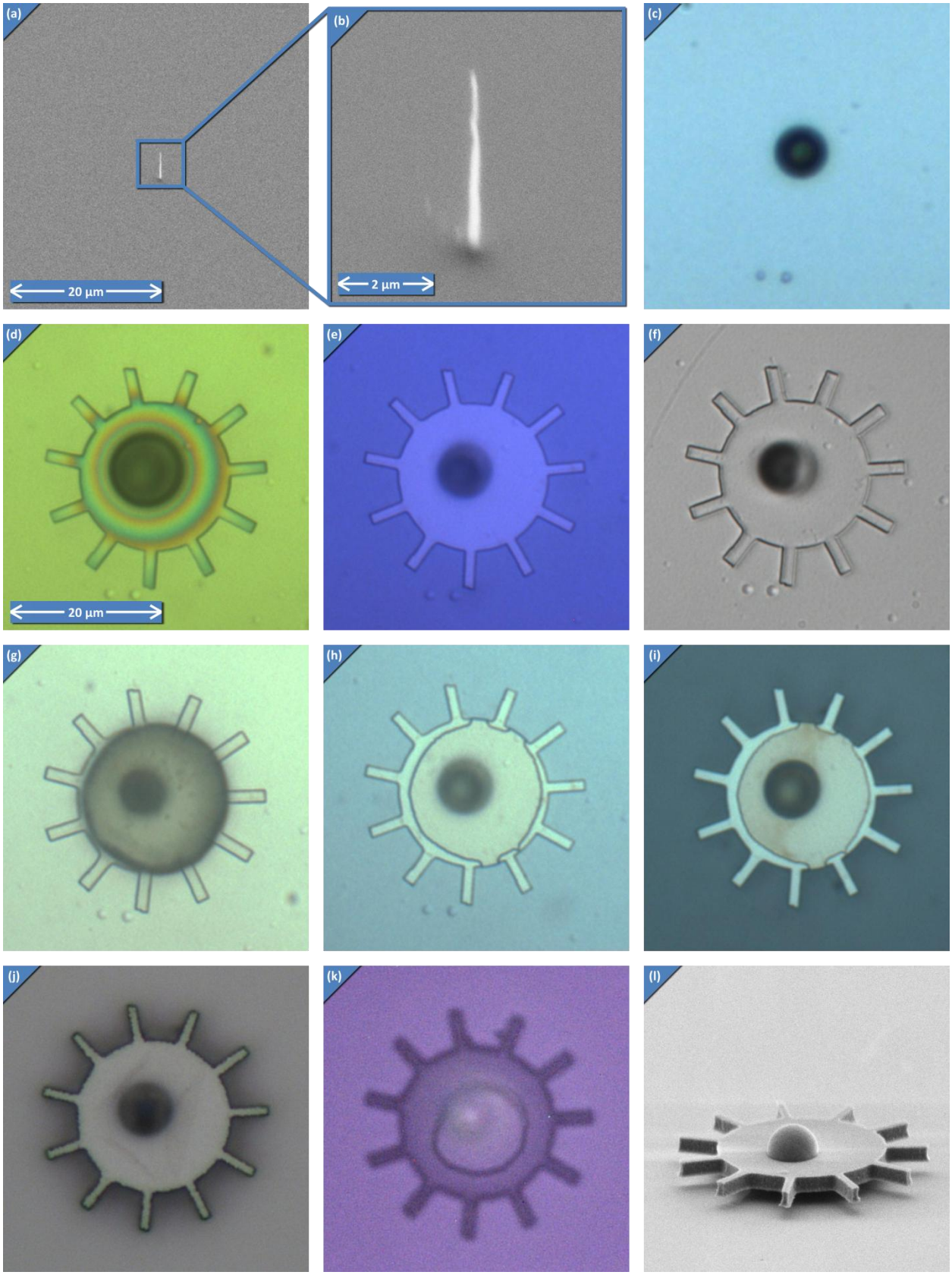

Figure 4-3: Complete fabrication of a single device: CNT growth (a,b), SiO_2 deposition (c), Polysilicon and Cr layer deposition and rotor e-beam patterning (d), Cr etch and resist strip (e), Ti deposition (f), thick resist lithography (g), Ti etch and resist strip (h), Si etch (i), Ti/Cr strip (j), and BOE release via IR transmission (k) and SEM (l).

Table 4-1: Process parameters for prototype fabrication process

Process	Equipment	Chemistry	Temp. (°C)	Pres. (mTorr)	Power (W)	Target thickness (nm)	See section
Nickel Pattern[1]	Nabity SEBL	PMMA resist					4.2.1.1
Nickel Liftoff[1]	e-beam evaporator						4.2.1.1
CNT growth[2]	Custom PECVD chamber	C_2H_2 : 80 sccm NH_3 : 160 sccm	625	6000	100 (DC)	4000	4.2.1.1
Pattern mapping	Raith 150 SEBL						4.2.2
SiO_2 layer	Oxford PlasmaLab 100 PECVD	SiH_4 : 22 sccm N_2O : 750 sccm N_2 : 430 sccm	380	1000	20 (13.56 MHz)	2000	4.2.3
Resist barrier		maN-2403 resist					4.2.3
Top SiO_2 strip		BOE					4.2.3
p-Si layer	MRL LPCVD furnace	SiH_4 : 80 sccm	585	150		2000	4.2.4
Metal mask	Mill Lane sputterer	Cr Ti				100 100	4.2.5
Top metal etch	Optical microscope	Futurrex NR9-3000P resist, 100:1 H2O:HF				5 µm	4.2.5
Bottom metal etch	Raith 150 SEBL	maN-2403 resist, Transene 1020				0.5 µm	4.2.5
Poly etch	Oxford PlasmaLab 100 ICP	SF_6 : 50 sccm O_2 : 10 sccm	-25			2000	4.2.5
Metal strip		100:1 H_2O:HF, Transene 1020					4.2.6
Release		BOE					4.2.6

[1]Prior to transitioning the initial nickel pattern e-beam writing and nickel liftoff to Boston College, a Raith 150 system at MIT and an e-beam evaporator at Draper Laboratory were used.

[2]CNT growth was performed by Z. Ren and T. Paudel of Boston College [123].

4.2.1 Carbon Nanotube Production

The first step in fabricating the device is to obtain an isolated, vertically oriented CNT. Two methods to achieve this configuration were considered. The first was to grow a single CNT in the correct location, using catalytic CVD. It has been shown that CNTs can be made to grow in specific locations during a CVD process by defining small regions of catalyst material on the substrate prior to the CVD process

[123].These catalyst dots can be shaped using standard high-resolution lithographic techniques available in microfabrication facilities. At first glance this method appears to be advantageous because it avoids the tedious problem of having to layout device structures by hand around CNTs which have been scattered randomly, as was necessary for previous CNT bearing demonstrations [1, 2]. Indeed, in the long term this seems to be the only viable method for mass-producing CNT bearing devices in a batch fashion. However, as described in 4.2.1.1, this method presents its own unique problems; most importantly, the crystalline quality of CNTs grown by CVD to date is so inferior to that of the arc-discharge CNTs used in prior demonstrations that rotation is likely impossible, because of the abundance of bonds between each adjacent pair of walls within the tube.

In the short term, the other option is to place CNTs grown by other methods into the proper location manually, using manipulators with very fine motion control. This approach is quite time-consuming, because an operator must manually pick up, attach in place, and release each CNT one at a time. Furthermore, the limitations on the degrees of freedom, travel, and precision available in the manipulators, as well as the vision limitations of a real-time SEM system, make the procedure difficult. Nevertheless, placement of CNTs is possible, as shown in 4.2.1.2, and placement of tubes of sufficient quality should enable the prototype device to function.

4.2.1.1 CVD Growth of Carbon Nanotubes

In order to obtain isolated, vertically aligned CNTs grown by CVD, it was decided not to invest in developing the CVD process in-house, as that would substantially increase the scope of the project. Instead, the aid Prof. Z. Ren, of Boston College (BC), was enlisted. Ren has done substantial work on growing CNTs by CVD [124, 125] and in particular on isolated CNTs by patterning the catalyst [123].

Ren's existing process for CNT growth consisted of e-beam patterning and lift-off of nickel catalyst dots on top of a glass substrate coated with a chromium layer to provide conductivity. The substrate with catalysts was placed in a direct-current PECVD system, which uses acetylene (C_2H_2) as the carbon source and ammonia (NH_3) as the diluent and plasma medium. For the prototype device, glass is not an acceptable substrate, because it is similar to the PECVD SiO_2 used as a release layer, and highly susceptible to etching in HF, which is the release agent. Therefore, silicon was used as the substrate. The conductivity of doped silicon is high enough to obviate the need for the chromium conduction layer,

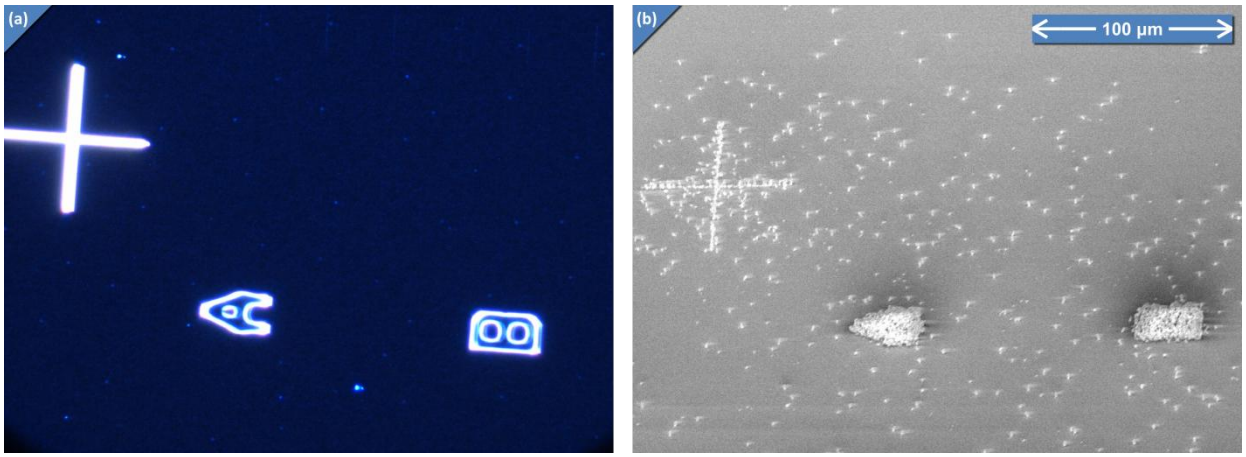

Figure 4-4: CNT growth on silicon substrates. (a) A dark-field optical microscope image shows the nickel catalyst before CNT growth. At this magnification, only the alignment cross and labels are visible; the nickel dots intended to generate CNTs are too small to see. (b) An SEM shows that after CNT growth, the catalyst appears to have diffused around the substrate, leading to extraneous CNTs growing in unintended areas.

so this layer was initially omitted from the fabrication. In addition, we performed the e-beam patterning of the catalyst particles ourselves, since BC did not have that capability at the time. Early results from this process are shown in figure 4-4. Even though nickel was successfully patterned into shapes by the lithography (figure 4-4a), CNTs did not grow only in the catalyzed areas as expected (figure 4-4b). Instead, CNTs were found to grow all over the substrate, especially in areas near (but not within) the nickel-covered regions. The interface between the bare silicon and the nickel is likely responsible; whereas the glass-chromium-nickel stack appears to have held the catalyst in place during CNT growth, the nickel placed directly on silicon diffused or was sputtered and re-deposited during the high temperature, plasma-enhanced CNT CVD process.

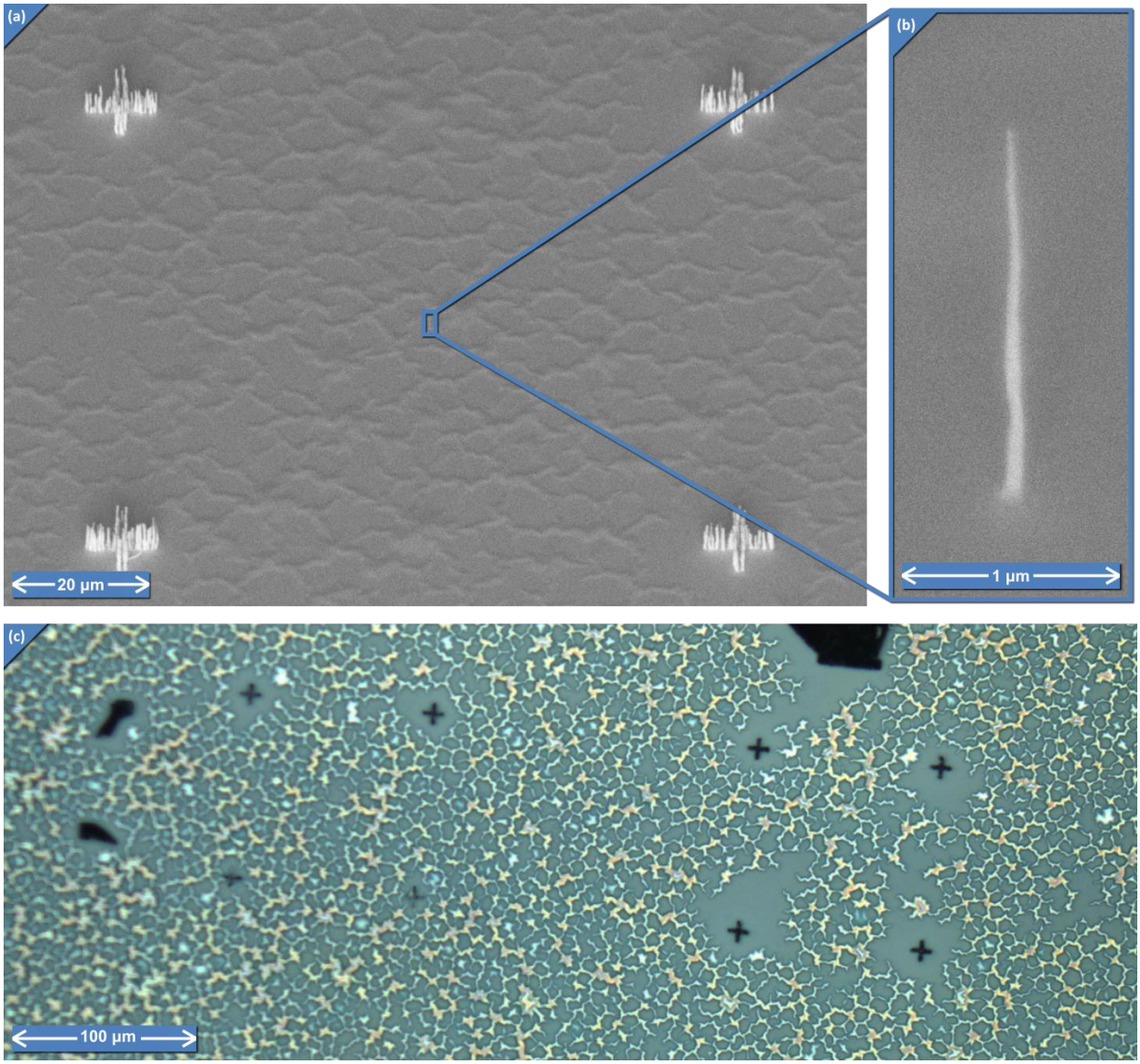

Figure 4-5: Chromium layers used in some CNT growth runs experienced significant peeling. Two device areas are shown in the optical micrograph (c), and a closer view of a single device is shown in SEM (a), along with the central isolated CNT in (b).

In order to remedy the diffusion issue, the chromium layer was reintroduced to the fabrication process. The layer was applied by Boston College, using sputtering with identical parameters to those used previously on their own glass substrates. While the result did appear to be free from diffusion, a new problem surfaced. The chromium layer experienced large scale buckling and peeling from the silicon surface, as shown in figure 4-5. This was not evident until after the CNT CVD process, and occurred despite adhesion testing showing that the chromium was thoroughly adhered. We initially suspected a thermal expansion coefficient mismatch as the cause of the delamination, but even with sputtering the film at a temperature comparable to the CNT reactor temperature, the result was the same (buckling appeared only after CNT growth.) Since the chromium process was just as problematic as the bare silicon process, at this point it was decided not to pursue the chromium process any further, and rather to concentrate on the improving the bare silicon process, since it was the original plan and involves fewer steps to troubleshoot.

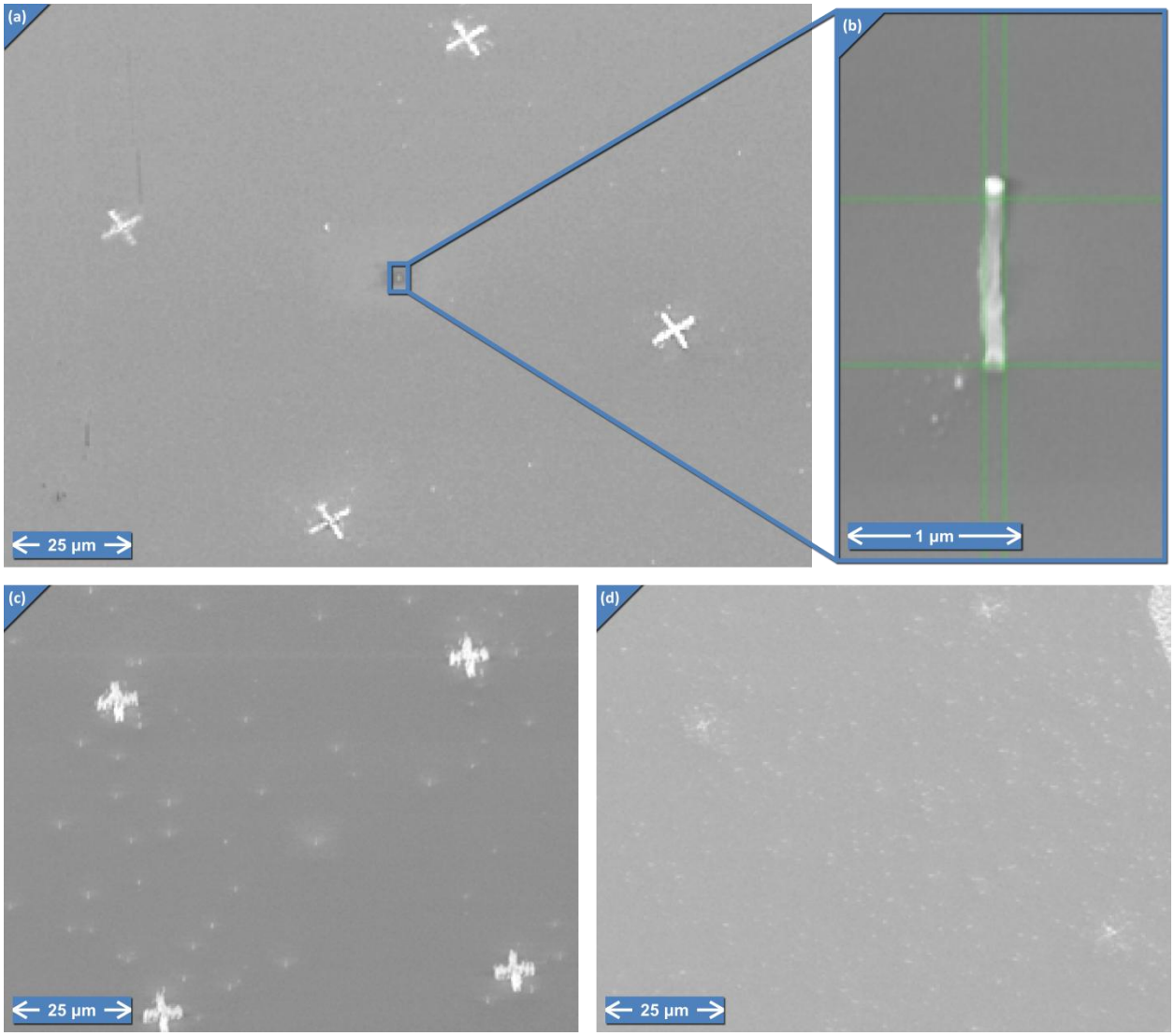

Figure 4-6: Lack of repeatability is shown in three CNT growth runs. Run (a) shows a near ideal result, with a single vertical tube in the center of the field (b). Runs (c) and (d) show increasing amounts of unwanted CNTs.

In order to determine the cause of the nickel catalyst diffusion and subsequent growth of extraneous CNTs, the collection of samples generated thus far was carefully examined for inconsistencies. It was discovered that the nickel catalyst diffuses only on some samples, and that which samples experience diffusion did not seem to be correlated with variations in process parameters. Figure 4-6 demonstrates several runs in which the amount of extraneous CNTs varies, despite running with the same process conditions. The only possible cause for the variation was the length of time that passed between processing steps for each run. Because of the difficulty in scheduling time on the MIT e-beam tool, as well as difficulty in arranging a time to transfer samples from Draper to BC, samples sometimes sat in storage for as long as a month between e-beam catalyst patterning and CNT growth. In order to address this issue, it was decided to have BC perform the fabrication steps up to CNT growth, including e-beam catalyst patterning, without allowing long periods to elapse in between steps.

BC's e-beam tool does not have the resolution capability of the MIT e-beam tool, but more importantly, it does not have the capability to align adjacent write fields with high precision. As a consequence, subsequent lithographic features can be misaligned by as much as a micron relative to the initial pattern. To combat this problem, we developed a process in which the as-grown CNT's were taken to the MIT e-beam tool, and the exact locations recorded relative to the outer alignment marks. While this process is tedious, it circumvents the lesser functionality of the BC e-beam tool while still enabling it to be used, shortening the time interval between e-beam writing and CNT growth. Additionally, this technique allows for small errors in CNT location (due primarily to remaining diffusion of the catalyst) to be corrected. Furthermore, when we later decided to switch to manipulated tubes (see section 4.2.1.2) this process was already in place, allowing tubes to be located almost arbitrarily on the substrate, and still to align subsequent features to them.

Switching e-beam tools did improve process repeatability substantially, as shown in figure 4-7, although there was still variation in tube length and location, as well as the occasional extra tube. However, the crystalline quality of the tubes was still quite poor. TEM imagery in figure 4-8 shows the lack of graphitization, as well as larger scale defects present in many of these CNTs. There have been reports in the literature of achieving improved graphitization in CNTs, by annealing them after production [126-130], and particularly with localized Joule heating caused by passing current through the CNTs. This method was attempted by the BC team to achieve the highly graphitized tubes necessary for a fully functioning CNT Bearing. They reported that with successive passes of current through these CNTs, the resistivity decreased, which would tend to indicate a more crystalline and less amorphous structure. They further showed with TEM images (selection shown in figure 4-9) that the structure was indeed transformed from mostly amorphous to more highly graphitized. However, there was no long-range order to the graphitization; instead of forming long, straight cylinders, the graphitic planes meandered, split, and joined in a random fashion. The hypothesized reason for this behavior is that the current chooses the initial path of least resistance, which may be a tortuous path in the initially amorphous and unstructured tube. As the current flows preferentially in these regions, it anneals the graphitic planes into that same tortuous shape. If the tubes did not have so much larger a diameter than those used in prior electric-current-annealing demonstrations, the initial current would not have meandered as much, and results more similar to those demonstrations might be obtainable; however, the large diameter is necessary in this work for the structural capability of the CNT to support the rotor.

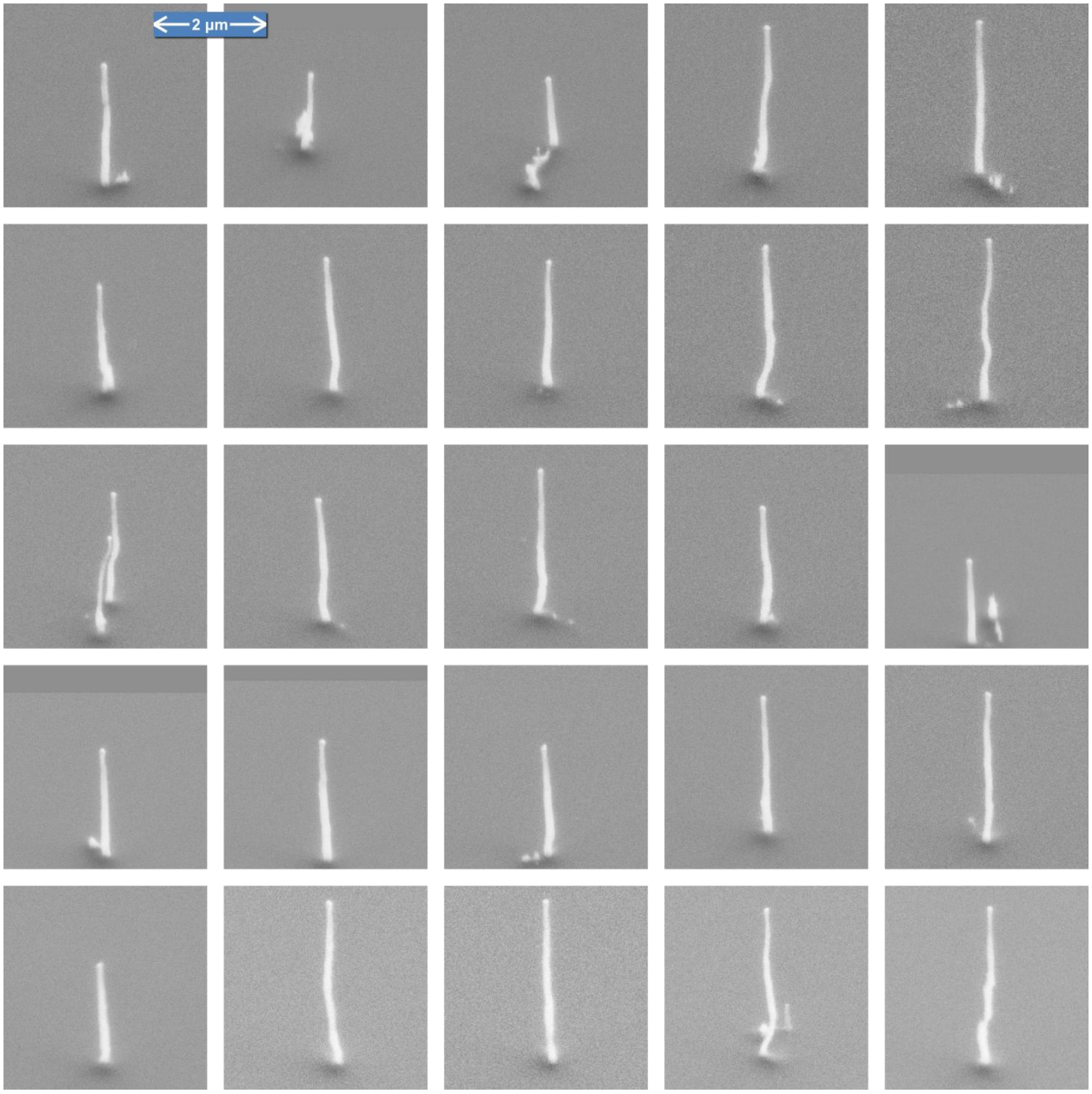

Figure 4-7: This image shows the 25 central isolated CNTs from a single sample containing a 5x5 array of devices. After switching to the BC e-beam tool for catalyst patterning, repeatability improved substantially, although some diffusion of the catalyst (manifesting here as extra tubes or stumps) as well as non-uniformity of tube geometry is still present.

Additionally, the growth process proved to have problematic consequences for the later release step (section 4.2.6). Because nothing was done to remove the native oxide prior to nanotube growth, the nanotube bases were found to be releasing from the substrate, resulting in completely detached devices. To address this problem, HF dips were introduced immediately prior to catalyst patterning. However, while the process did prevent CNTs from releasing during HF etching, as a side effect it also reintroduced the catalyst diffusion and repeatability issues that had been dealt with previously. Because of the poor tube quality, and the continuing problems with repeatability of the process, it was decided instead to pursue manual manipulation of CNTs in to the correct locations.

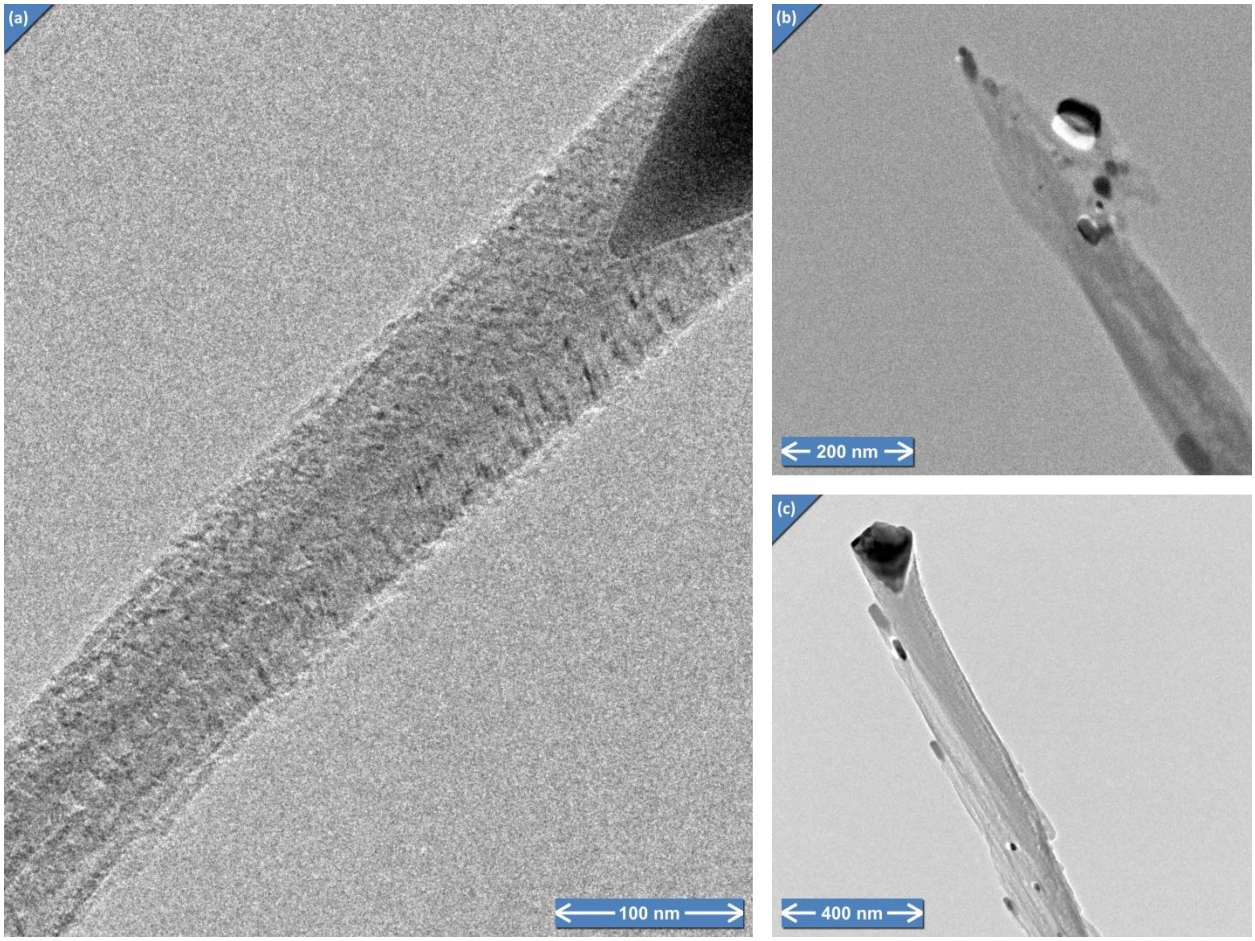

Figure 4-8: TEM images showing the poor crystalline quality of the CVD CNTs. A high magnification image (a) shows that there is almost no graphitization in the tube, while (b) and (c) show much larger scale defects present in many tubes.

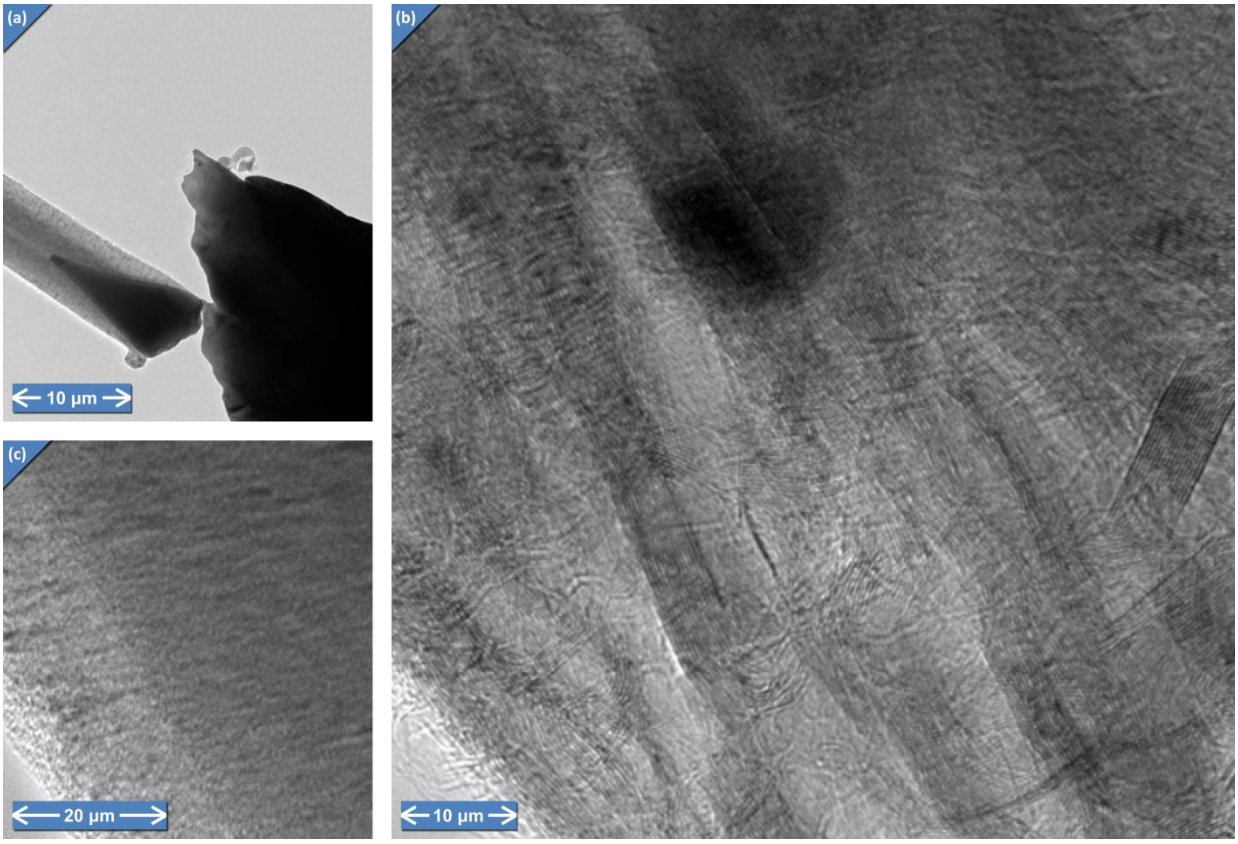

Figure 4-9: TEM Images taken by the Boston College team show the results of current annealing. A CNT is contacted by a probe (a) and current passed through out. The amorphous structure before annealing (b) is transformed in to a much more graphitized structure (c), but the graphitic planes are poorly aligned and not straight.

4.2.1.2 Manipulation of Carbon Nanotubes

Manipulation was performed using a JEOL dual bean system at the BC cleanroom facility, equipped with both SEM & Focused Ion Beam (FIB) capabilities, and outfitted with nanomanipulation probes from Kleindiek Nanotechnik [131]. The goal of the manipulation process is to place high-quality arc-discharge CNTs in the isolated, vertically oriented configuration on a substrate. Initially, highly crystalline loose CNTs were selected. However, these CNTs were difficult to work with, for two reasons. First, the as-produced CNTs obtained from the vendors are highly impure. The powder containing the CNTs also contains large amounts of amorphous carbon, graphite flakes, and other fullerenes. Additionally, the CNTs within the powder tend to clump up due to the van der Waals interactions, resulting in tight balls of CNT. These two factors together make it difficult to access a single CNT with the manipulators. Also, the manipulators do not have a rotational degree of freedom, so it is necessary to find a tube that is already in the proper orientation to be transplanted to the new substrate. To assist with this task, we initially spread loose, highly graphitic CNTs on a substrate with pre-etched ridges, in the hopes that some tubes would stick to the sidewall in a vertical orientation. The result, shown in figure 4-10a,b, still suffered from the purity and clumping issues. In order to speed up the development of the manipulation process, it was decided instead to use vertically aligned forests of CVD-grown CNTs as the tube source. Two types were used: CNTs grown using BC's nanosphere lithography technique (figure 4-10c, described in [132]) and CVD-CNT forests from NanoLab [99] (figure 4-10d).

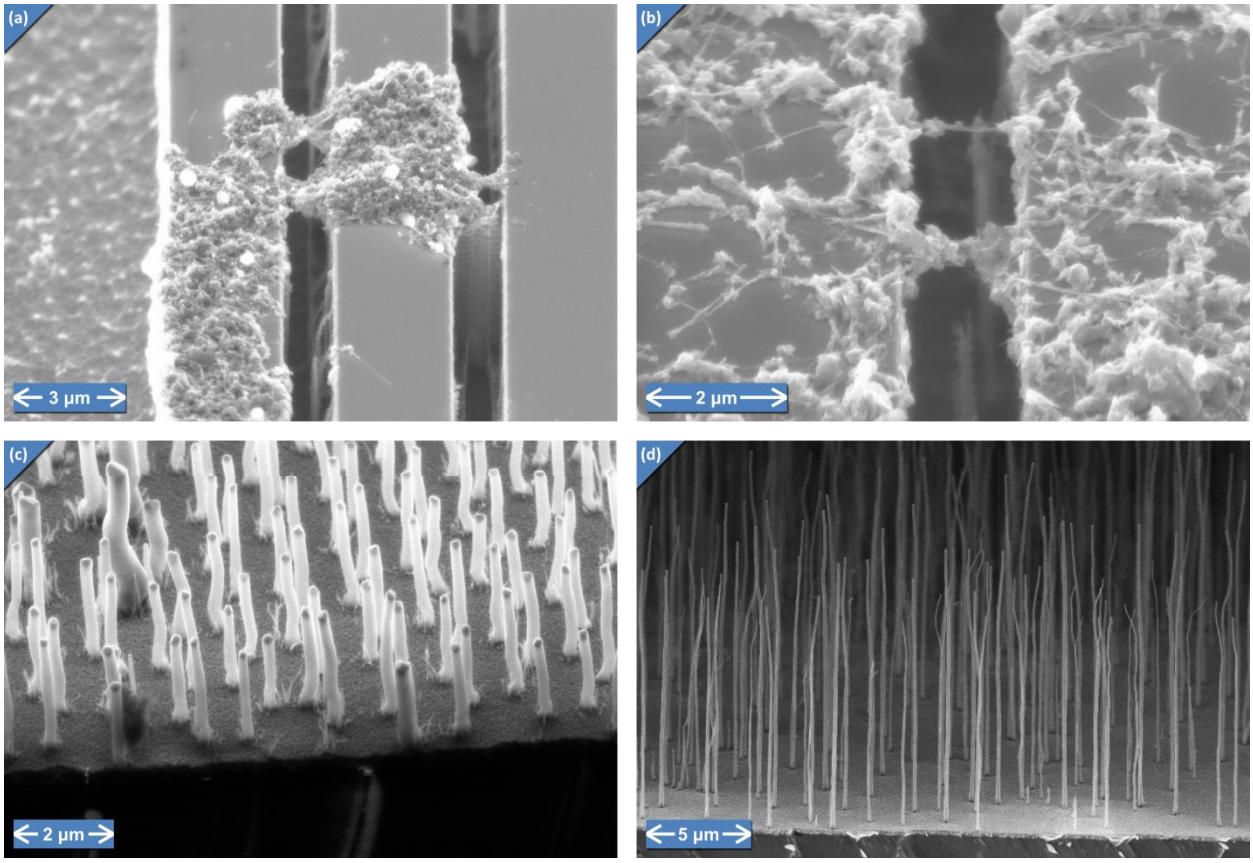

Figure 4-10: Loose arc-discharge CNTs, shown in (a) and (b), contain many impurities, and tend to clump together under the influence of van der Waals forces. CVD-CNT forests, like those produced by BC (c) and NanoLab (d) are easier to manipulate, although they do not have the necessary crystalline quality.

To maneuver the CNTs into position, a manipulator was first attached to an individual CNT tip using a product called SemGlu, available from Kleindiek Nanotechnik [133]. This glue works under the high vacuum environment of the SEM/FIB instrument, and is hardened by a polymerization process that occurs when it is irradiated with a highly focused electron beam (low level radiation during imaging does not cause the reaction). Although the glue bond was sufficiently strong that CNTs could be removed from their initial substrate by simply tearing them off, it was found that using the FIB milling function to cut the bottom of the tube near the base resulted in better control over the picked tube length. The procedure of selecting a CNT, attaching to it, cutting the base, and lifting the CNT, is shown in figure 4-11.

After moving the CNT into position on the new substrate, it needs to be secured in place. Initially this was attempted with the same SEM glue. However, after consulting with the manufacturer and testing the glue, it was discovered that the glue dissolves in HF. This is problematic, because the tube needs to stay attached during the final release step in HF. Fortunately, the FIB system has the capability of depositing amorphous carbon or tungsten in a prescribed area, by injecting a gaseous precursor near the target area and scanning the ion beam over the that area. This works essentially like a very small PECVD reactor, using the energy of the accelerated ions to activate the chemical reactions involved. Carbon was used because of its known capability to withstand HF. Additionally, the ion beam was used to mill away the native oxide on the target before the CNT was attached, to make sure that oxide would not release under the HF treatment. Both shallow, broad areas and deeper, narrower pits were milled;

the former are easier to contact with the CNT tip, but the latter offers a more secure attachment. Both are illustrated in figure 4-12. Figure 4-12c also shows a final, attached tube (using the amorphous carbon deposition.

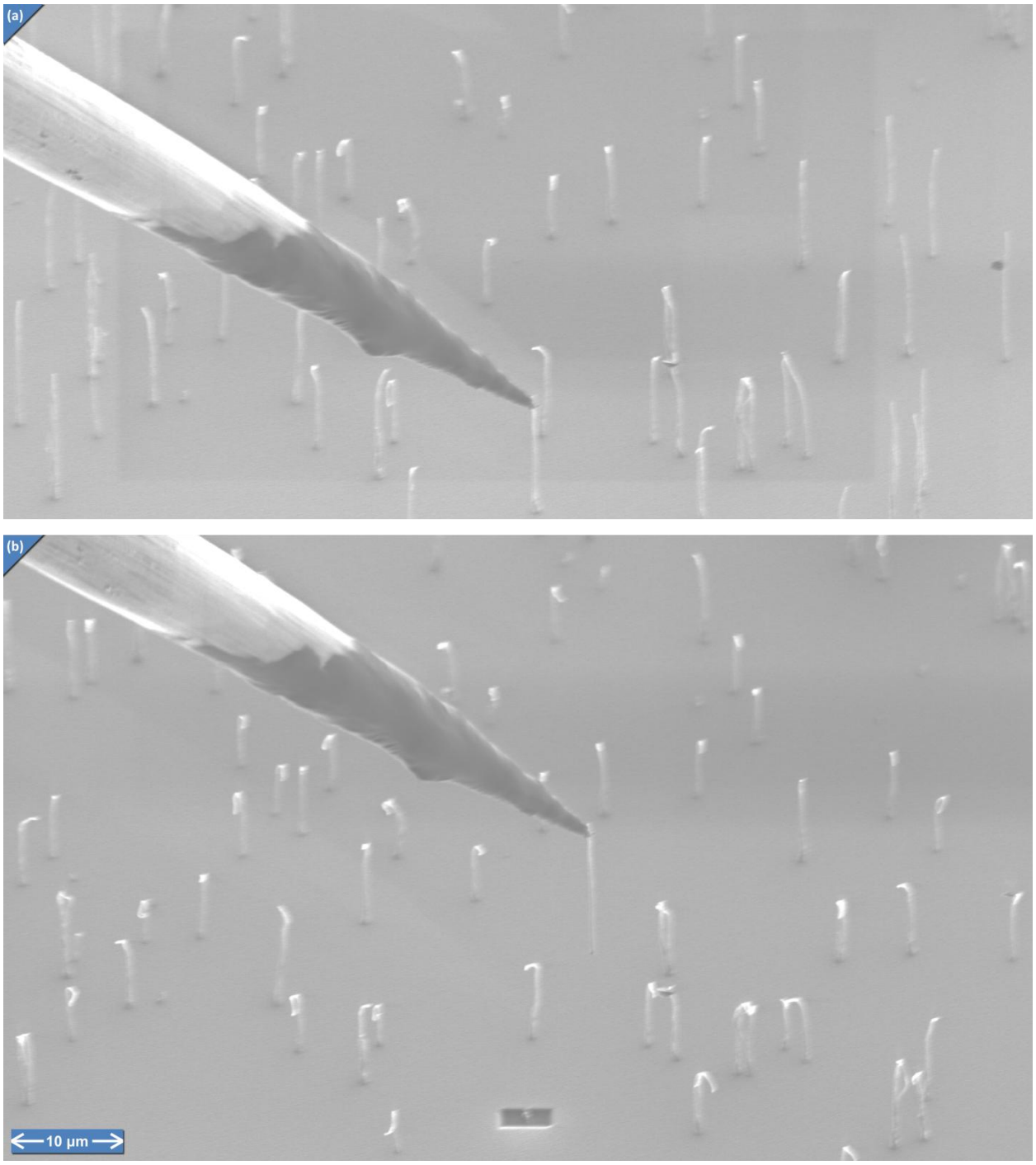

Figure 4-11: Fetching or "picking" a CNT from a forest of tubes from NanoLab. (a) The tube is contacted with the manipulation probe, whose tip is coated in glue (dark region). (b) The bottom of the tube is cut using ion milling, leaving a cavity where the substrate behind the tube was milled (small dark rectangle). The tube is lifted with the manipulator tip.

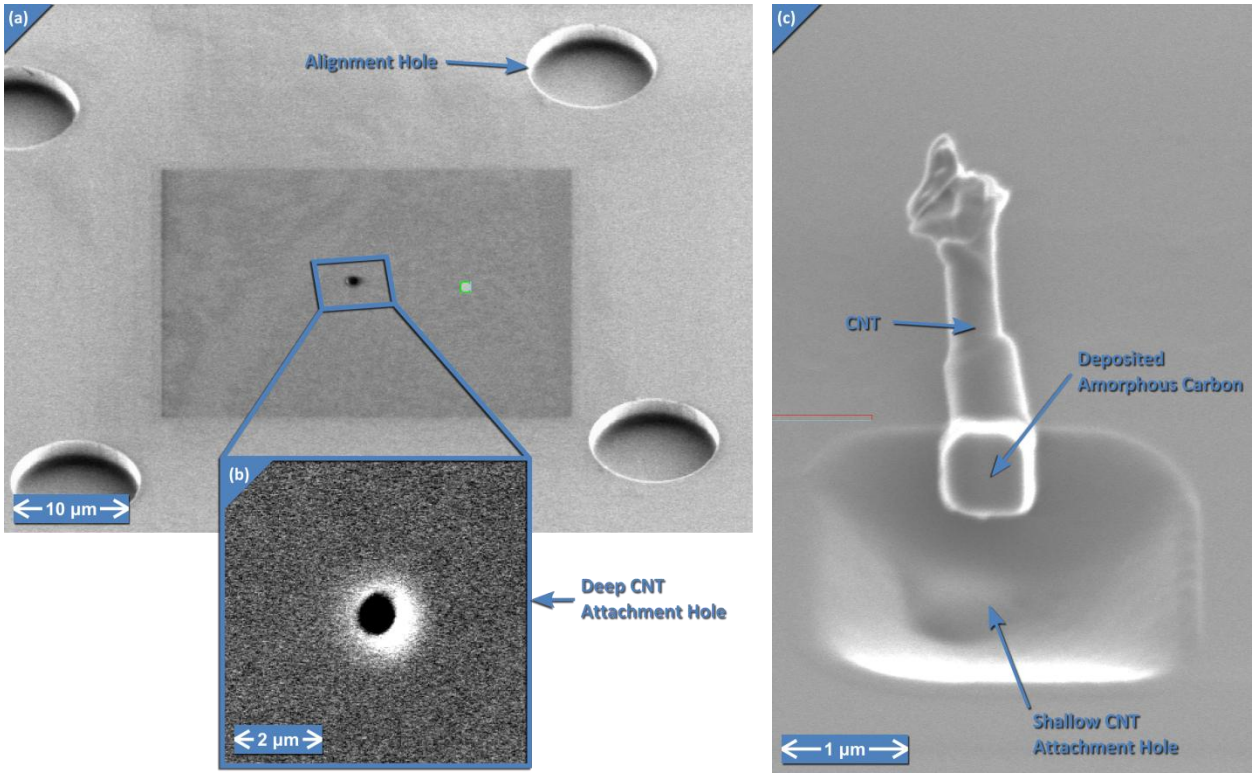

Figure 4-12: Three types of holes were etched in the target prior to tube placement. The large holes in (a) are for alignment of later process steps. These were etched in the silicon using the same etch as that used to define the rotor, described in 4.2.5. The small hole in (a) and (b) was made using the FIB milling function, to clear the native oxide. This hole is difficult to insert a CNT into, but provides for a strong attachment. (c) shows a shallower, wider basin, with a CNT already attached to it. The square at the base of the CNT is the deposited carbon.

Some significant issues still remain with the manipulation process, however. One issue is the limited vision capability afforded by the SEM during real-time observation. This limitation is well illustrated by figure 4-13 and figure 4-14. During the manipulation process (figure 4-13), the tube appeared straight and well aligned. However, once the viewing angle was changed after the fact, it became clear that the geometry was quite different than expected (figure 4-14). This is an area for further development of CNT manipulation. Nevertheless, while this CNT will not lead to a functional device, it has been useful in practicing the fabrication procedure, since it provides a portion that is roughly vertical, and well attached to the substrate.

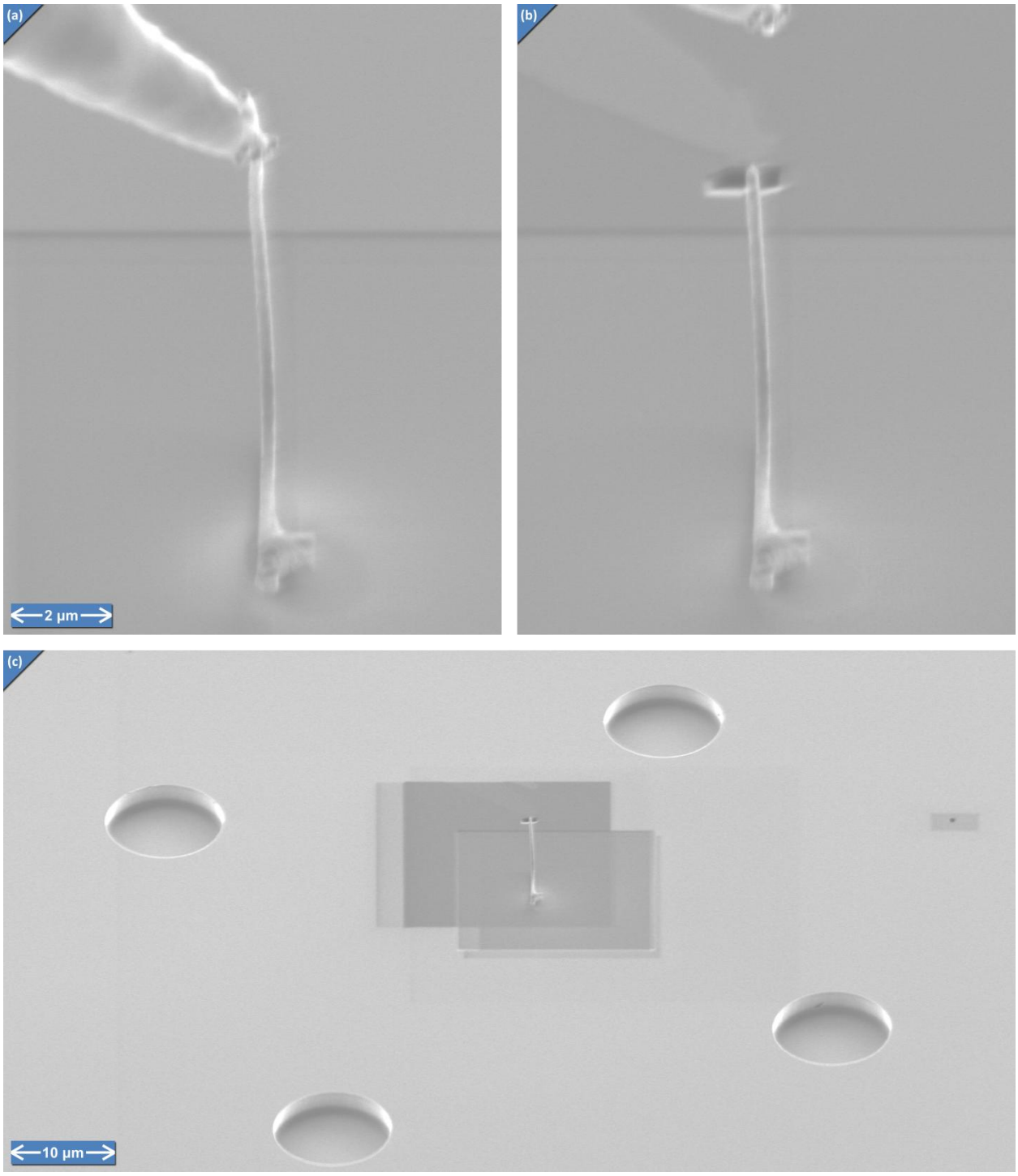

Figure 4-13: The final stages of manipulating a CNT into place. After the base is attached with carbon deposition (a), the top of the tube is cut from the manipulator by FIB milling. The lone CNT is shown among its alignment marks in (c).

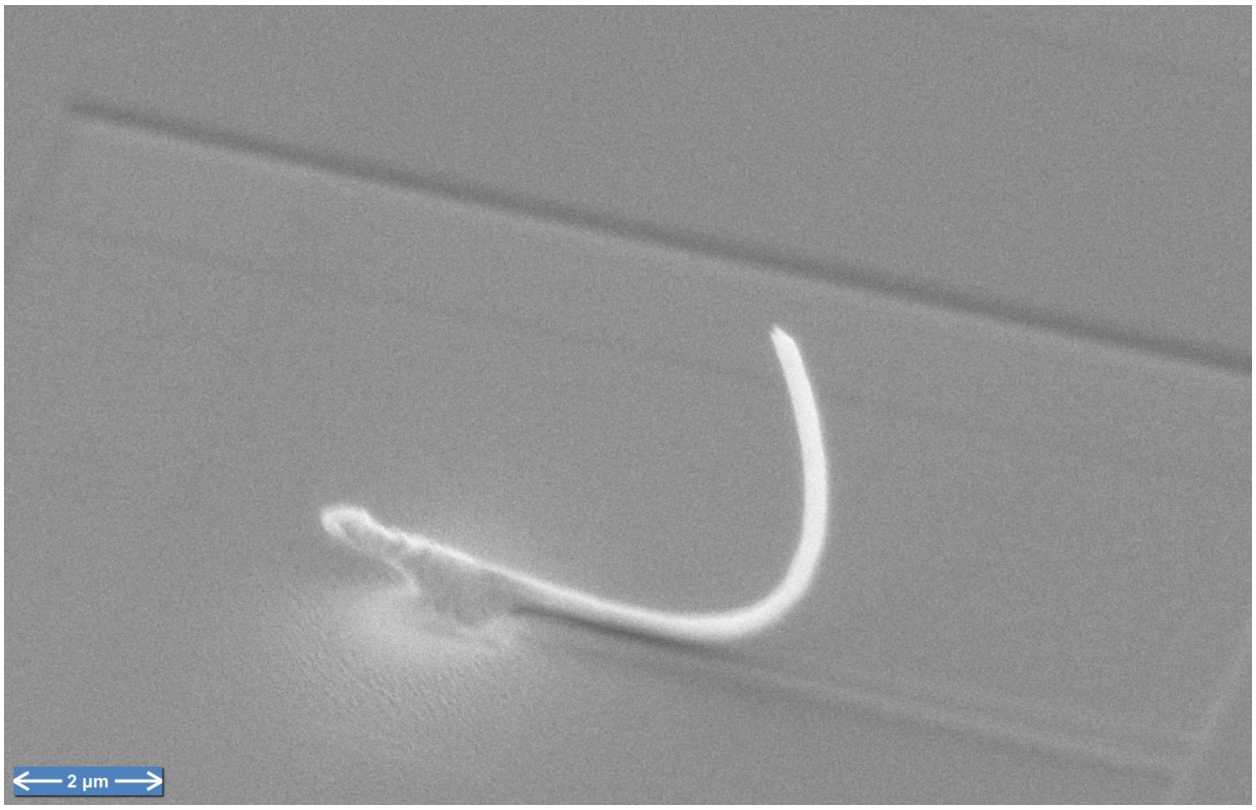

Figure 4-14: When viewed from the side, the CNT in figure 4-13 turned out to be heavily curved. While this type of tube will not lead to a functional device, it is useful for practicing the fabrication process.

4.2.2 Mapping of Nanotube Locations

The original fabrication plan called for the use of the same e-beam lithography tool for creating the initial catalyst pattern and the later rotor lithography. This tool, a Raith 150 at MIT, has the capability to align write fields (subsections of the device which are written as a unit) with high precision, using a laser interferometer to measure the stage position. Because of the relatively large area needed for a set of CNT patterns (about a square millimeter), multiple write fields are required. If these fields are not properly aligned, to each other on each use of the tool, the rotor lithography geometry will be misaligned to the CNTs (whose locations are controlled by the catalyst lithography). This requirement became an issue when it was decided to use the BC e-beam tool instead (see section 4.2.1.1). Because that tool lacks the same write field alignment capability, another alignment strategy was required. After each CNT growth, the sample was taken to the MIT tool, and the locations of the CNTs according to the e-beam coordinate system were recorded. In this way, the subsequent rotor lithography can be precisely aligned by specifying the rotor centers as equal to these measured coordinates.

In addition to solving the problem of the two different e-beam tools, the mapping strategy also alleviated the problems due to catalyst diffusion. It no longer mattered where the catalyst originally had been patterned, so long as the final location of the CNT could be determined. Another benefit of the mapping process was that it enabled CNT manipulation as a viable vertical CNT production technique. It is difficult to place the CNT in a precise absolute location using the manipulators, but again the location can be known precisely after the fact by mapping.

4.2.3 Release Layer

The first fabrication process step after obtaining isolated, vertically oriented CNTs in known locations is to deposit the release layer. SiO_2 was selected as the release layer, because it is well understood in the context of microfabrication. It has a readily available chemical release agent (HF) which is known not to attack the CNT, or the polysilicon rotor layer. Additionally, SiO_2 can be deposited at relatively low temperature, and in a conformal manner.

The SiO_2 was applied by a PECVD process, using an Oxford PlasmaLab System 100. This system achieves a conformal layer of uniform thickness, with residual stress under 50 MPa as measured using a wafer curvature system. The target thickness of the release layer, which would later become the gap under the rotor, was 2 µm, according to the design chosen using the classical model (see section 4.1.1), although thinner layers were also used in testing, when the CNT height was shorter than anticipated. The parameters used for the deposition process are shown in table 4-1. The resulting conformal layer is shown in figure 4-15.

Originally, it was planned that the release etch would be timed, so that the portion of the oxide between the CNT and the rotor (i.e. around the top of the CNT) would not be etched. In practice, this proved difficult for several reasons. First, the alignment of the rotor to the CNT was not always as good as anticipated, particularly before the CNT mapping procedure was instituted. If the alignment is poor enough, the portion of SiO_2 surrounding the CNT will be etched before the SiO_2 is completely cleared from the gap between rotor and substrate, a situation shown in figure 4-16. (Note that the CNT is missing; it has been completely released from the rotor due to the etching of this intervening oxide.) Additionally, it can be difficult to determine the progress of the release etch, since it cannot be directly observed in a standard microscope because the view of the gap is obstructed by the rotor itself. Finally, although the etch rate of the etchant is well known, it can still vary with oxide density, gap, and geometry, and relying on the etch rate as the only mechanism to control the geometry is not an ideal solution.

Instead, a method was devised whereby the portion of the SiO_2 surrounding the top of the CNT could be cleared before deposition of the rotor layer. This ensures that the rotor makes contact directly with the CNT, and there is no intervening oxide that can later result in the complete release of the rotor. The unwanted oxide is cleared using the same etchant as the release step (BOE), while the portions of the oxide that are desired are protected by photoresist. This can be accomplished relatively easily by taking advantage of the existing topography. Because photoresist is spun on, it does not in general form a conformal coating. Areas that stick up above the base planar surface tend to receive little or no resist coverage, leaving them exposed to the subsequent etch. An e-beam resist (maN-2403) was used for this purpose because it was conveniently available, and capable of good performance at low thickness (a thickness of 0.5 µm was used, allowing plenty of access to the protruding CNT, which is several micrometers long). Any thin resist would be suitable for this purpose, and a less exotic and expensive one would likely be used in any large-quantity fabrication run. Immediately after the BOE etch, the resist was stripped using acetone, followed by a commercial wet resist strip agent (SVC-14), in order to ensure that organic residue from the resist would not interfere with subsequent process steps.

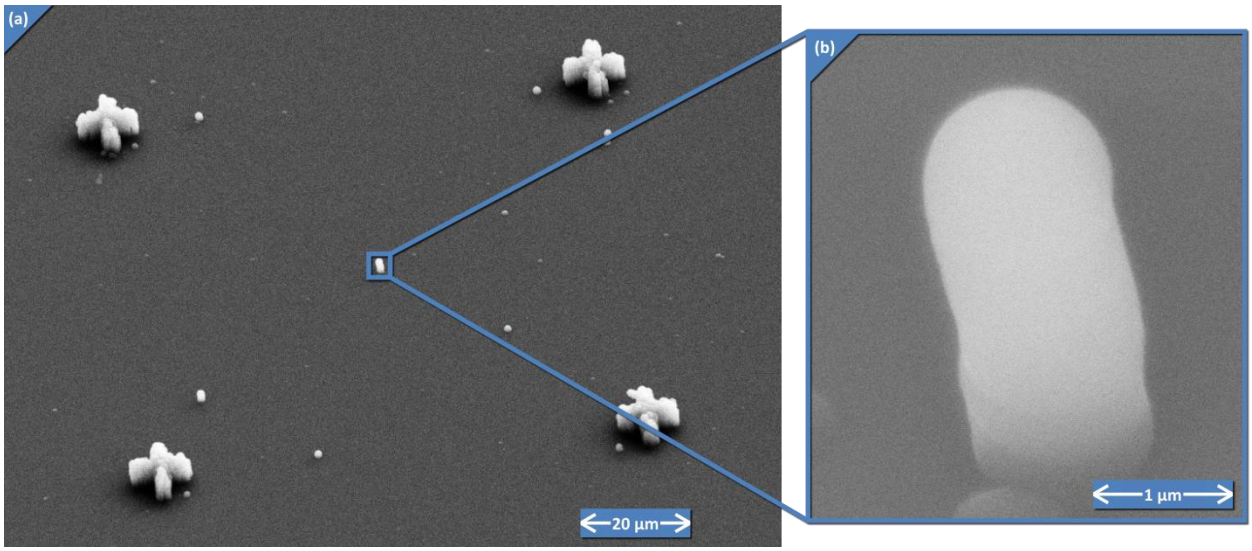

Figure 4-15: PECVD SiO_2 was applied to provide a space between the substrate and the rotor layer .The oxide also conformally coated the CNT, shown in the center of (a) and enlarged in (b).

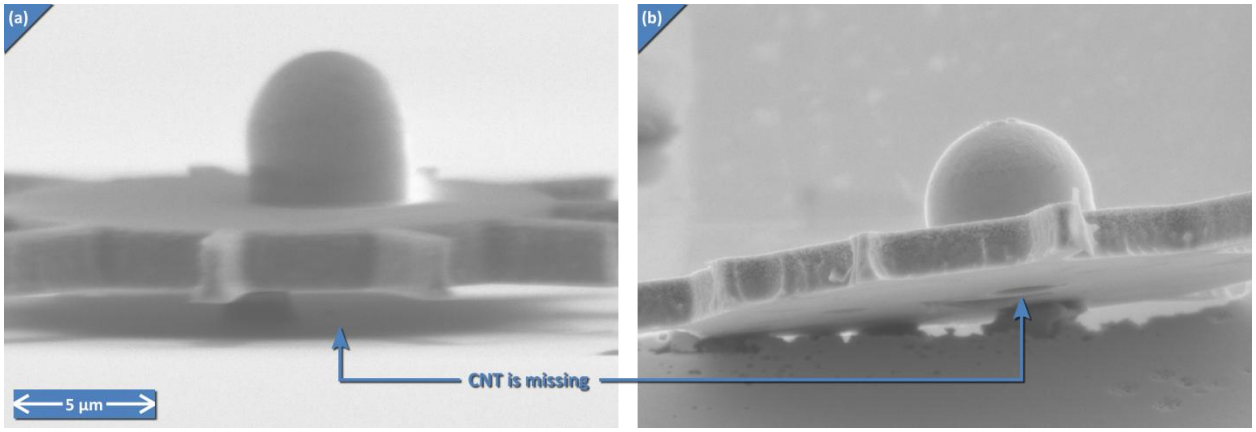

Figure 4-16: The conformal oxide layer caused problems when releasing the rotors. As shown in (a), if the rotor was not properly aligned, the oxide could be cleared from the CNT-rotor interface before it is complete cleared from the rotor-substrate interface; although the CNT has been completely released from the rotor and the substrate (it is missing altogether) a pillar of SiO_2 remains under the rotor. After further etching (b), the pillar is removed, and it is clear from the bottom of the rotor that the SiO_2 "hump" surrounding the CNT is gone, leaving a pit in the rotor underside.

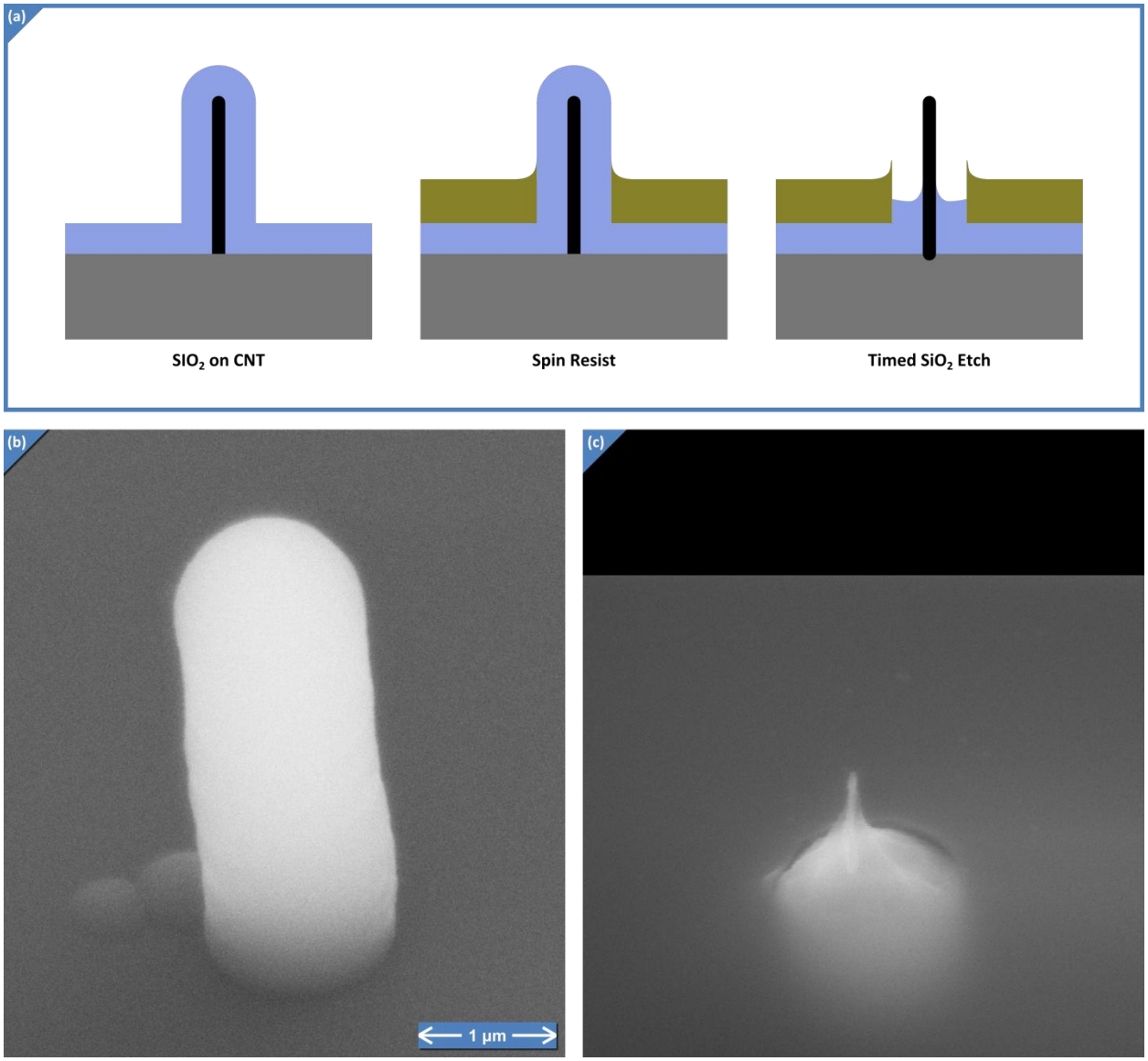

Figure 4-17: Turning the non-conformality of the resist coating process to advantage, the SiO_2 encasing the top of the CNT can be removed with HF whilst protecting the underlying release layer with photoresist. The process is shown schematically in (a), with SEMs from before (b) and after (c).

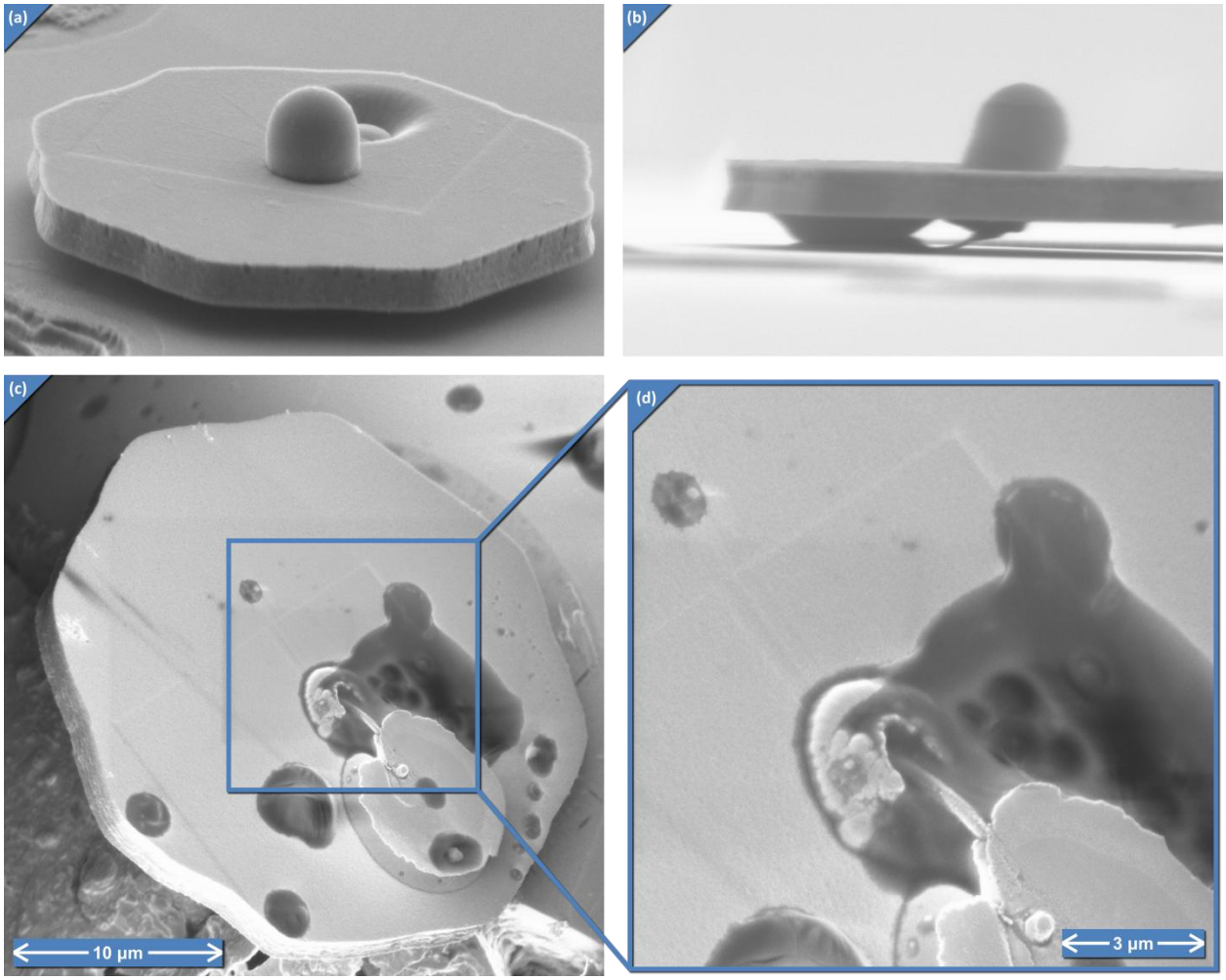

Figure 4-18: This released rotor was constructed from the curved, manipulated CNT pictured in figure 4-14. The rotor was still attached to the substrate (a and b) by the CNT and a pillar of polysilicon (which resulted from the topology caused by the horizontal portion of the bent CNT). The CNT is visible under the rotor, showing that the improved rotor-to-CNT bond was successful. When removed from the substrate and flipped over (using manipulators), the CNT is very clear (c and d).

4.2.4 Rotor Layer

The rotor layer was fabricated out of Polysilicon, a common material for surface micromachining. Polysilicon has excellent mechanical properties (similar to bulk single crystal silicon), and is highly compatible with the standard suite of MEMS processes, and in particular stands up well to the BOE used to release the device in the last step. For this process, a typical LPCVD process was used to apply the polysilicon layer, and the parameters for the deposition can be found in table 4-1.

4.2.5 Lithography and Etch

The features of the rotor require that high-resolution lithography be used to define its geometry. Although the design based on the classical model (section 4.1.1) calls for a rotor diameter of 20 µm, which is well within the capability of ordinary lithography equipment, the vanes required for fluidic actuation of the rotor must be much thinner, of the order 1 µm. To achieve this resolution, e-beam lithography was selected. E-beam lithography offers the additional benefit that the topography of the CNT will not interfere with the exposure (as it would in contact lithography.) Furthermore, the design parameters of the rotor can be changed relatively easily within the template file, rather than investing in

new masks, which is also a key enabler of the CNT location mapping technique (section 4.2.2). Since the number of devices being produced for demonstration purposes is small, and the area of the rotor, which needs to be written on each device, is small, the time costs associated with e-beam lithography are mitigated. For eventual large-scale production, assuming the issue of CNT placement accuracy were resolved (eliminating the need for location mapping), a stepper or other non-contact lithographic technique could be used to increase throughput.

The initial fabrication plan called for a single lithographic step to define the rotor. The rotor was written in a layer of maN-2403 negative photoresist (spun to a thickness of 0.5 µm), aligned to the location of the isolated vertical CNT using the alignment marks generated either during CNT growth or before manipulating the CNT into place, and using the previously recorded mapping data.

Several etch processes were considered to cut the rotor out in the polysilicon layer. DRIE is a common technique for etching silicon in MEMS, capable of generating straight sidewalls, with high selectivity over oxide and photoresist, which alternates between etching and depositing a polymer layer to protect the sidewalls from further etching. However, DRIE is designed with very deep etches in mind, up to hundreds of micrometers. For this application only a 2 µm etch was desired, so a non-aggressive

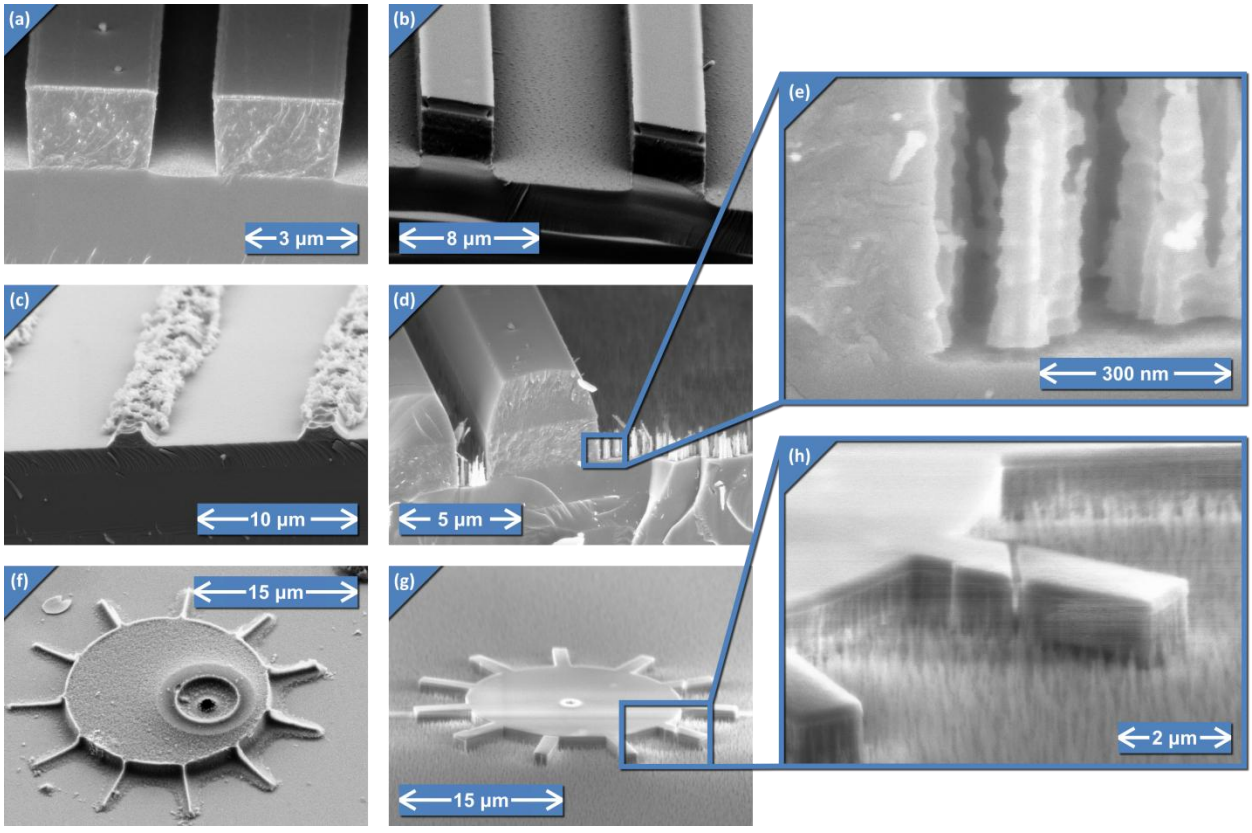

Figure 4-19: Cryogenic (a,c,f) and DRIE (b,d,e,g,h) silicon etches are shown. The cryogenic recipe produces good anisotropic etch profiles (a), but only when used with a metal mask; Otherwise, the resist cannot withstand the etch (c) and the rotor vanes are mostly etched away (f). The DRIE recipe can also produce good results, with only a resist mask (b). However, because the etch depth is so shallow, a non-aggressive recipe is used, which is highly sensitive to chamber temperature. Small, uncontrolled temperature fluctuations can lead to the formation of "grass," or unwanted residual silicon pillars, illustrated in (d) and (g). The characteristic scalloping markings on the sidewalls, due to the alternating nature of the DRIE process, are visible in the close-ups (e) and (h).

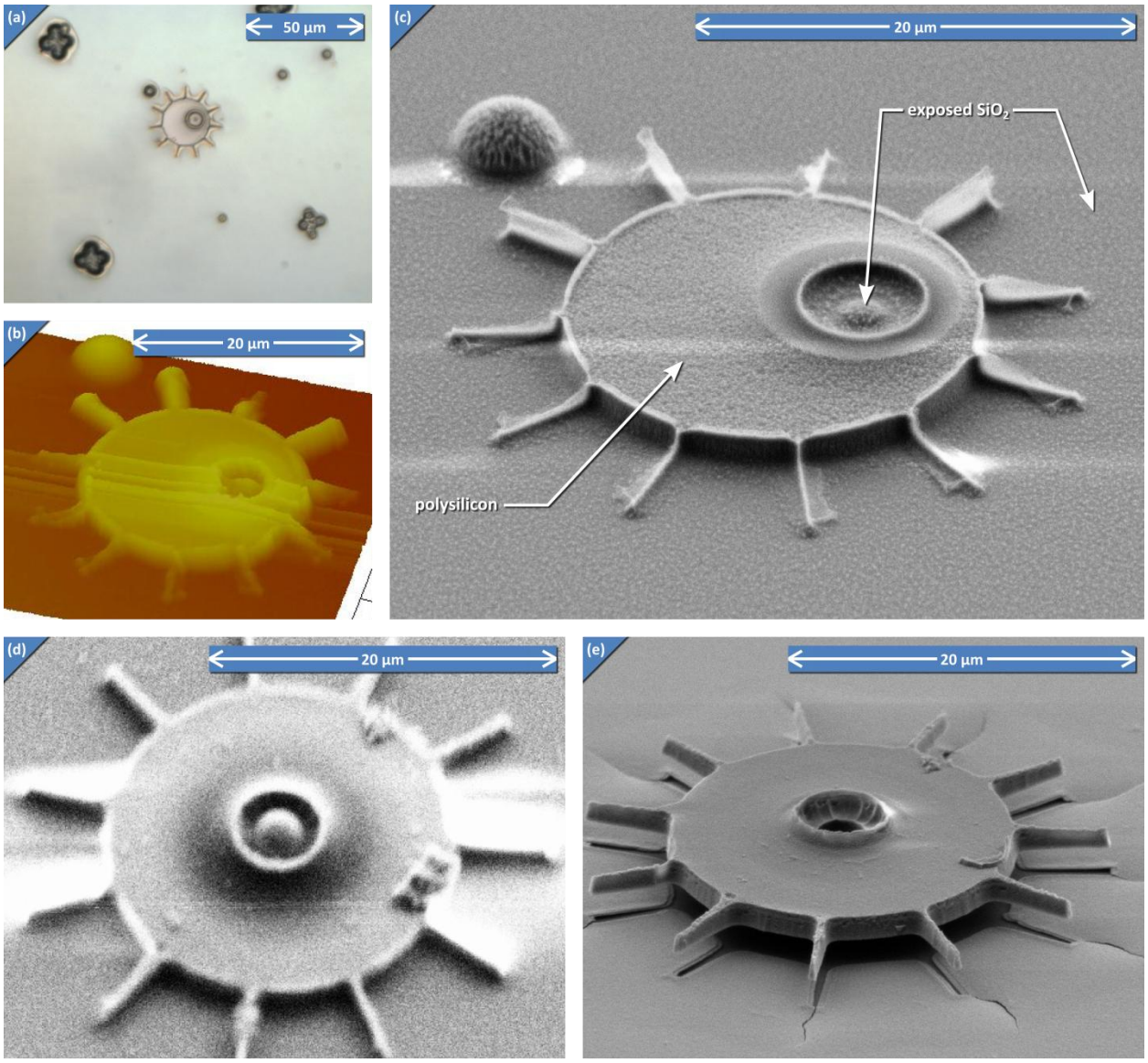

Figure 4-20: The resist did not coat the top of the CNT pillar at the rotor center. This allowed the polysilicon to be removed during the rotor etch, exposing the CNT shaft and the SiO_2 surrounding it. This defect is shown optically (a), by AFM profile (b) and by SEM (c). Another device is shown before (d) and after (e) partial release.

DRIE recipe was selected (parameters listed in table 4-1), so that the etch rate is slow enough to allow for the etch time to be well controlled. The results of this etching recipe are shown in figure 4-19b,d,e,g,h. Although good results can be obtained (figure 4-19b), the recipe is sensitive to chamber temperature, and frequently results in "grass," or unwanted residual silicon pillars (figure 4-19e,h).

Since the DRIE process was not repeatable, an alternative cryogenic etch process was used. This process uses identical chemistry to the etch step of the DRIE process. However, instead of alternately passivating with a polymer to protect the sidewalls, the sample is cooled via a liquid nitrogen system, which decreases the chemical reaction rate on the sidewalls. The horizontal surfaces still experience substantial etching, since the thermal energy deficit is overcome by the impacts of high-energy ions bombarding the horizontal surfaces. Initially, this process experienced issues with resist robustness; the etch was attacking the resist before completion, resulting in some of the protected features also being

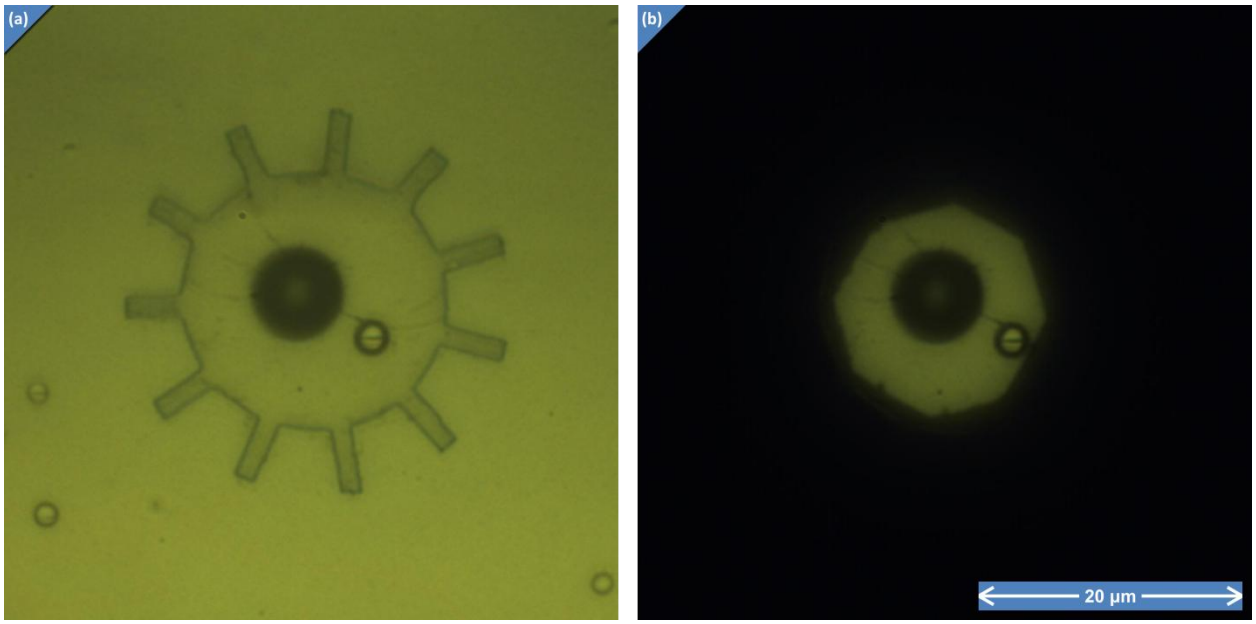

Figure 4-21: An optical microscope was used to expose the thick resist. At 150x magnification, the aperture (b) can be reduced such that the light covers an octagon of approximately 15 micrometer diameter, sufficient for protecting the center portion of the rotor (a).

etched away (figure 4-19c,f). A chrome mask, applied by sputtering and etched with a commercial wet etchant, provided sufficient additional resistance to protect the desired features.

Another issue with the etching process was identified later. In order to obtain the required resolution on the vanes of the rotor, a thin photo resist (maN-2403, spun to 0.5 µm) was used. However, since resist is spun on, it does not generally form a conformal coating. For this device, since the CNT can stick up several microns above the planar level of the rotor itself, the top of the CNT does not receive any resist coating. During the subsequent etching of the rotor, the polysilicon is then cleared from this region, exposing the oxide-coated CNT (figure 4-20). The release step then attacks the oxide, leaving the CNT completely detached from the rotor.

A two-step lithography procedure was introduced to protect the CNT in the center, while still affording the required resolution. Two metal layers (Chrome and Titanium) were first sputtered on the sample. A thick negative resist (Futurrex NR9-3000P) was applied, providing ample coverage of the protruding topology caused by the CNT. A relatively simple procedure for the exposure of this resist was developed. Since a roughly circular pattern is desired, the aperture of an optical microscope can be used to do the exposure. At sufficient magnification, the aperture restricts the light exposure to an octagon of approximately 15 micrometer diameter, and the microscope illumination, when turned to maximum brightness, is sufficient to expose the resist in 3 minutes. Figure 4-21 shows an optical micrograph with the aperture adjusted to the proper size, and aligned manually to a rotor. After etching the first metal layer with this thick resist mask, the rotor itself is then patterned using e-beam lithography and the other metal layer is etched using that mask. The order of the deposition, lithography, and etching of the two metal layers is largely irrelevant, since only the underlying polysilicon layer is of interest. Furthermore, the alignment of the rotor to the CNT depends only on the rotor lithography step, so precision is not needed for the thick resist lithography, so long as the target area can be kept within the rotor area. Results of the two-step lithography process can be seen in figure 4-3d-i.

4.2.6 Release

Release of the rotor consists of etching away the sacrificial oxide layer, leaving the rotor fully supported on the CNT. BOE was used for this purpose, as it provides a controllable, slow etch rate. In order to monitor the progress of the etch in clearing the oxide under the rotor, an infrared microscope was used (figure 4-22). Silicon is partially transparent to infrared, so this microscope allows the oxide layer to be viewed through the rotor (after the chromium and titanium masks are removed with a commercial etch from Transene, and 50:1 HF in DI water, respectively.)

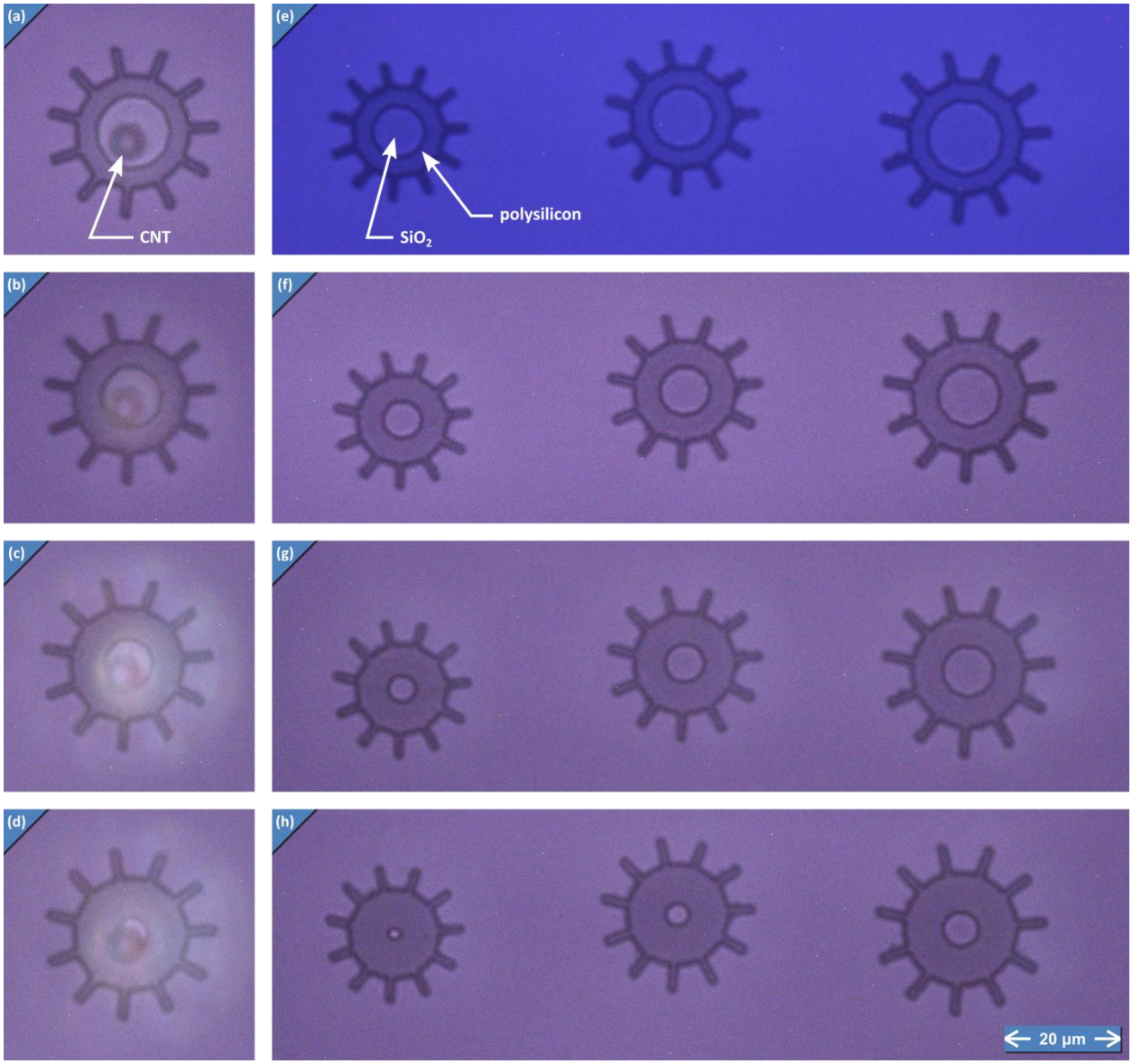

Figure 4-22: BOE is used to remove the sacrificial oxide layer from underneath the rotor, as illustrated by infrared transmission microscopy. The oxide is the light colored circle in the center of the rotors. On the left (a-d), rotors with CNTs (the small dark circle in the center) are shown, while the rotors on the right (e-h) have no CNTs, and vary in size to assist in monitoring etch progression. These images were taken after 45 minutes (a,e), 60 minutes (b,f), 75 minutes (c,g), and 90 minutes (d,h) of etching.

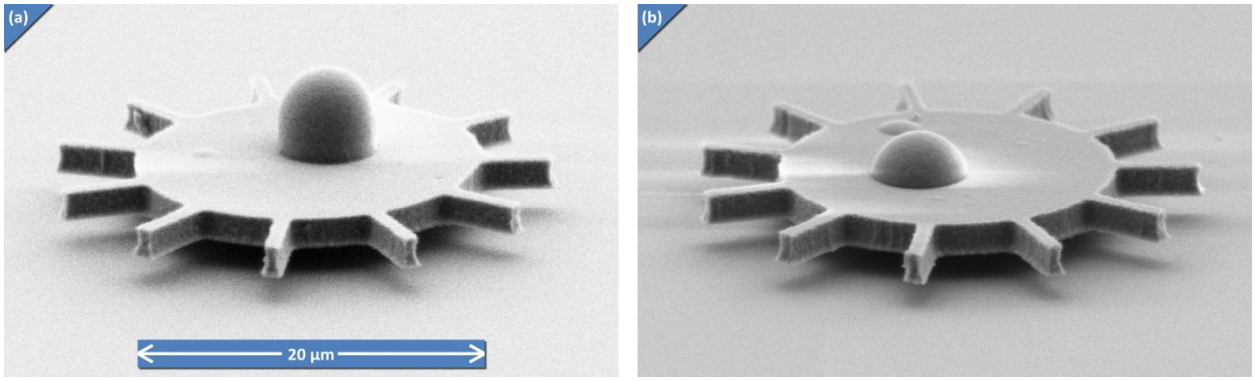

Figure 4-23: These rotors are almost completely released, supported by a thin oxide pillar underneath the rotor.

A pair of almost completely released rotors is shown in figure 4-23. Two issues were experienced during the release process. For the rotors pictured in figure 4-23, the tube was released from the rotor underside, as shown when the rotors were flipped over after complete release, in figure 4-16. This problem, due to the oxide layer intervening between the CNT and the rotor poly layer around the tube, was corrected using the additional photoresist step described in 4.2.3. Problems were also experienced with the chrome rotor etch mask not covering the central pillar, due to the interactions between the resist and this topography, as shown in figure 4-20. The solution was a dual-lithography process, described in 4.2.5. Having resolved these issues, the almost-released devices shown in figure 4-23, as well as the released devices constructed around a manipulated CNT (figure 4-18), demonstrate that the fabrication process is sound, even though CNTs of sufficient quality are not available to produce a working device.

4.3 Summary of Challenges and Solution Guidelines

This chapter has presented the fabrication process for the prototype CNT bearing device in detail, describing each step in order. It may be useful to bring all of the problems encountered and their solutions together, as a summary of the lessons learned during the development of the fabrication process. This section therefore concisely presents the “best practices” for each of these issues.

For CNT growth, it was discovered that there are competing interests for a process attempting to grow high quality, isolated, vertically oriented CNTs. For CNT quality, it is important to have a high temperature, to enable annealing of defects before they set; however, high temperature also can lead to diffusion of the catalyst particle from its desired location, as well as break-up of the catalyst to form multiple, unwanted catalysis sites. Several ways to limit the catalyst diffusion (and enable higher temperatures) are possible, including potential surface treatment to hold the catalyst in place via chemical interactions, or placing catalyst in the bottom of etched wells, physically preventing them from wandering. The specifics of these methods were not determined or tested during this work, but should be of interest for future work involving isolated CNT growth. This topic was covered in section 4.2.1.1.

The release of microstructures attached to the CNT also encountered issues. Specifically, CNTs were released from both the substrate and the rotor during the final BOE etch. Detachment of the CNT from the substrate was shown to be caused by the native oxide on the silicon (section 4.2.1.1). This detachment can be prevented by removing the native oxide before CNT growth using HF. The release of the CNT from the rotor was more complex, and was a result of the conflict between a thin resist (required for resolution purposes) and the underlying topography (caused by the vertically oriented CNT). The solution for this issue was to do the lithography in two steps, as described in section 4.2.5. By

using two metal masks, the high-resolution thin pattern, and the thick pattern that covers the central bump caused by the CNT, can be done independently; the metal masks then transfer the sum of both patterns into the silicon during the silicon etch. A similar two-step procedure could be useful in a wide variety of devices, where thin resist and coverage of topography are required simultaneously.

Finally, the prospect of manipulating CNTs into a vertically oriented configuration at a desired location on a substrate was investigated. The main issues here are separating an individual tube from the rest of the tubes, and creating a secure attachment at a desired angle. Separating the tube can be addressed two ways. First, CNT forests can be used, and allow the manipulator to easily contact only one tube at a time. However, this method suffers the disadvantage that the CNT forest tubes are of inferior crystalline quality, which is important for the present application. Alternatively, loose tubes must be dispersed on a substrate, and oriented to have an end accessible to the manipulator. This might be accomplished by pre-patterning topography on the substrate. These issues were discussed in section 4.2.1.2.

To attach the tubes, it is important to clear the native oxide on the sample first, which can be done easily in an FIB system. However, deeper holes, intended to help maintain the desired orientation, were difficult to place the CNT into, because of the limited vision capability (in terms of viewing angles simultaneously available) in the SEM/FIB manipulation system, in addition to the limits on the degrees of freedom of the manipulators. We have also investigated various attachment technologies, and found that in-situ carbon deposition resists the BOE used to release the device. All of these discoveries were reported in section 4.2.1.2.

4.4 Testing Apparatus

As mentioned in section 4.1, it was decided to actuate the rotors by air jet. Figure 4-24 shows a schematic representation of the testing set-up. A microelectronics probe station was converted to interface with glass micropipettes (available from a medical equipment supplier) instead of electronic probes. These micropipettes, having a tip orifice diameter of 5 µm, can direct air at the vanes of the prototype device from opposite sides, providing a balanced torque. Given the small size of the pipettes, and the sub-micrometer precision of the probe station manipulators, the tips of the pipettes can be brought within one blade length of the blades, providing a jet of air to impinge on the blades (as seen in figure 4-25). The air to the micropipettes is supplied by a syringe pump, which provides air at flow rates from under a microliter per minute to milliliters per minute.

The initial objective of testing is simply to demonstrate rotation of the prototype device. In order to achieve this milestone, simple microscope video recording capability was employed to monitor the rotor as it is subjected to torque via the air jets. Image data from an example test is shown in figure 4-25. To date, a successful test has not been performed. Although air has been confirmed to be flowing from pipettes (by a water submersion test), and hence a torque is applied, no motion of the rotor has been observed. The suspected reason is that the CNTs used in construction of prototype devices thus far have exhibited poor crystalline quality, as discussed in section 4.2.1.1. These CNTs (of which TEM imagery is available in figure 4-8) are of mostly amorphous structure, and do not exhibit the concentric wall structure that is required for rotation. Substantial further work in improving the available CNT quality, either by manipulation of high-quality tubes into place or improving the quality of CVD-grown tubes, is required in order to achieve a functional prototype.

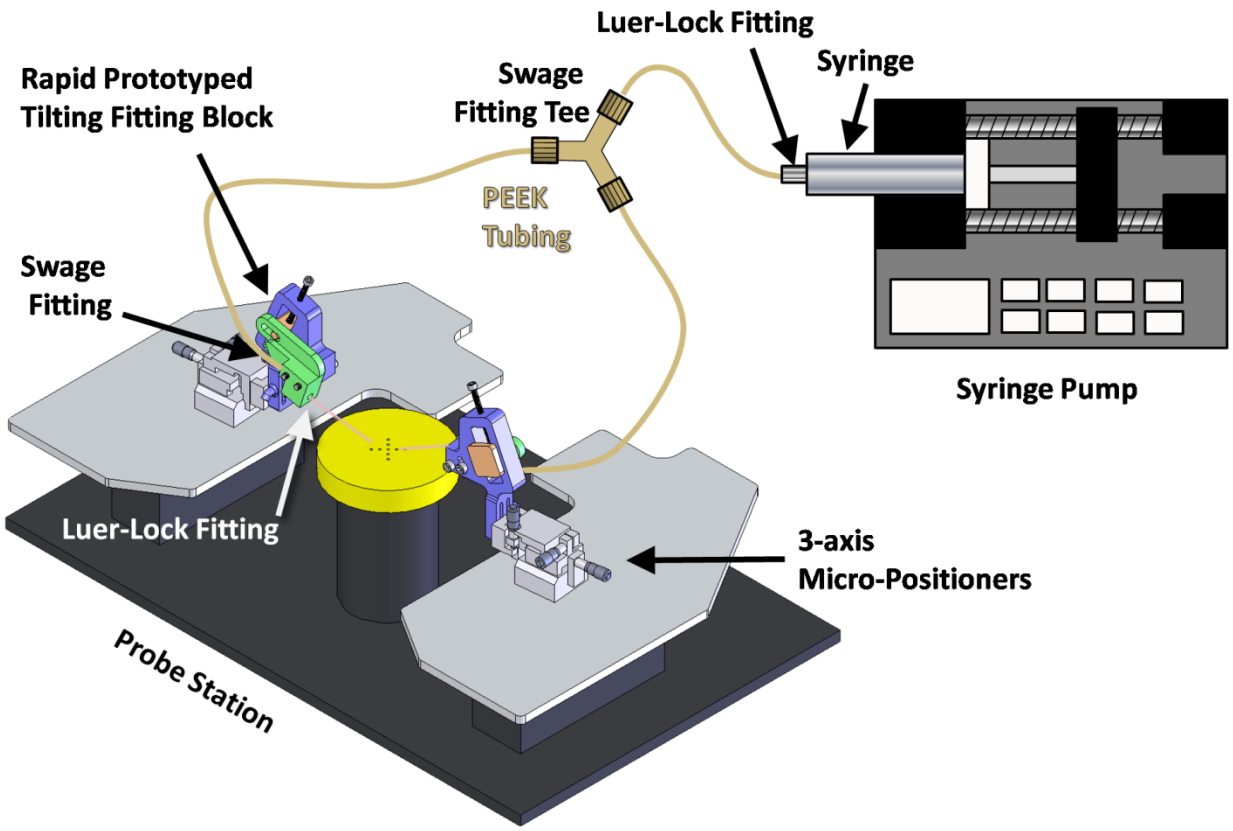

Figure 4-24: A schematic diagram showing the testing apparatus, consisting of micro-pipettes directed at the vanes of the rotor by a microelectronic probe station, and supplied with air by a syringe pump.

The video capture system is able to detect simple rotation, and quantify the speed at sufficiently low speeds (below about a hundred revolutions per minute). It could also detect some degree of torsion of the CNT, by observing the deflections of the rotor disk. Failures would also be captured on video, and could provide information on how to avoid them in subsequent tests. Video of a rotating device would be a compelling demonstration of the prototype.

However, in the longer term, a more accurate measurement system will be desired in order to make quantitative estimates of the friction performance of the bearing. Such a system could utilize fiber optic probe systems, such as those available from Philtec, Inc. [134] These sensors, which have had some success at monitoring rotating MEMS devices in operation [76, 78], are capable of measuring rotation rates as high as millions of revolutions per minute, by bouncing light of a structure on the rotor, and measuring the frequency of oscillations in intensity. Additionally, such sensors can provide information about deflections of the rotor as it rotates, by analyzing the amplitude of these variations. This information would be useful in measuring the deflections of the rotor under operation, providing feedback on the applicability of the classical dynamics model (section 4.1.1).

Even though a successful test has not yet been performed, substantial progress in developing the prototype device has been accomplished. The test apparatus and protocol are usable on future devices, and as the quality of available CNTs improves, will hopefully provide valuable data on the performance of the first successful device.

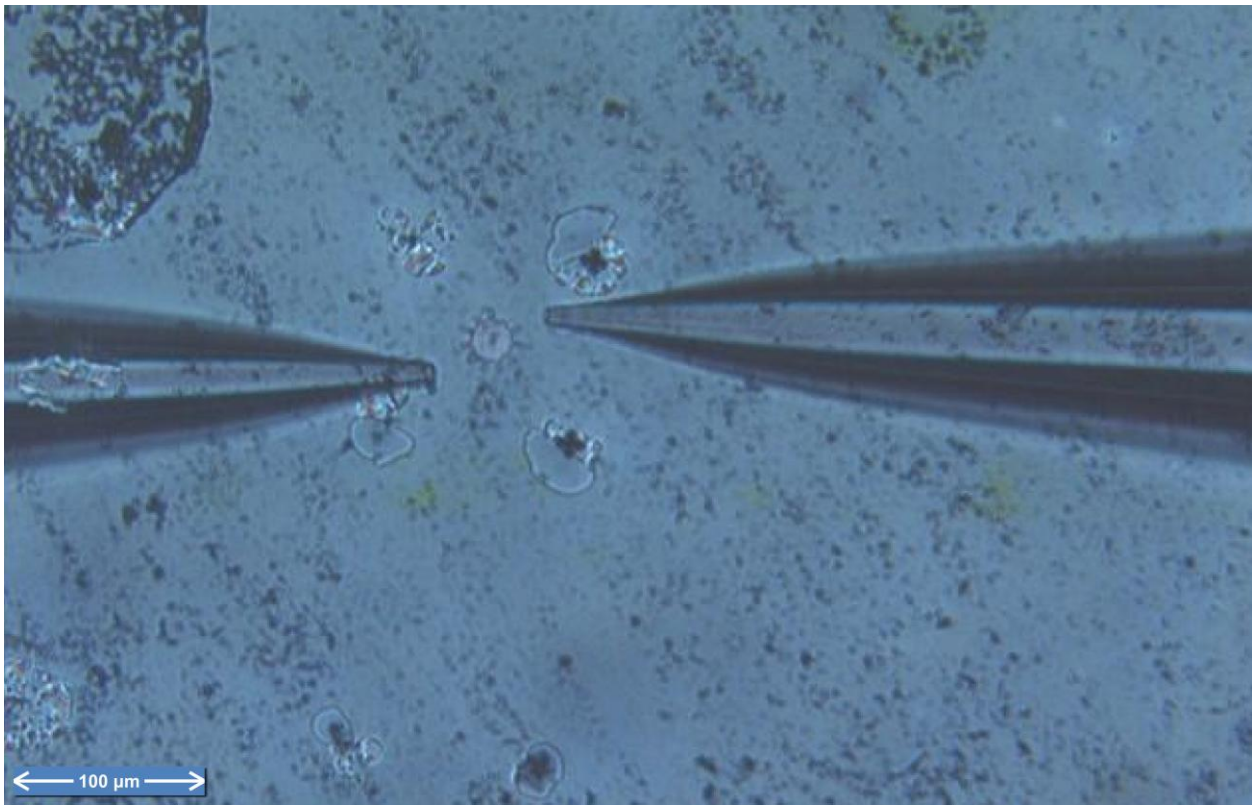

Figure 4-25: A still image captured from a test in progress, showing the rotor, alignment marks, and glass micropipettes. No tests have succeeded in spinning a rotor, due primarily to the low quality of available CNTs.

[This page intentionally left blank.]

[This page intentionally left blank.]

5 Atomistic Simulations of Carbon Nanotube Friction

5.1 Motivation

The unique structure of carbon nanotubes (CNT) has made them interesting as a candidate bearing system, since a short time after their discovery [6]. Multiwall carbon nanotubes (MWNT) have remarkable strength, owing to the strong covalent bonds joining carbon atoms within each individual tube wall. At the same time, the interactions between adjacent walls are very weak in comparison, due only to the van der Waals interaction. Because of this weak interaction, it is universally agreed that CNTs should exhibit "low" resistance to relative motion between these walls. Excited by such a prospect, many research groups have endeavored to determine what the resistance force, or friction, is, and on what parameters it depends. Many of these earlier studies have used atomistic simulations to address the problem [10, 11, 13-17, 19-21, 24, 27], while a few experimental investigations have also been performed [2, 7, 9-12]. A summary of the techniques used in these prior works can be found in section 2.2.

However, the exact magnitude of this friction remains a point of contention, as discussed in section 2.2.2.3. In fact, the values of friction reported in the literature vary by almost eight orders of magnitude (see figure 2-1). A large part of this variation can be attributed to the different definitions of friction, and to the different approaches used to measure it. In some atomistic simulation studies, molecular statics have been used to study the friction [10, 11, 13, 15-17, 20]. In these approaches, individual walls of MWNTs are displaced relative to each other either along the tube axis (translational motion) or around the tube circumference (rotation). For each displacement step, the energy of the system is measured, in some studies after relaxation of the system. Then, using this energy versus displacement data, the force or torque is computed as the numerical derivative of the energy with respect to displacement. There are two limitations with this approach. First, the calculations are time independent, and do not capture any dynamic effects. Since a substantial portion of the interaction between walls of a MWNT may be due to phonons in one tube exciting phonons in the other, the treatment of this interaction as a static phenomenon may not be warranted. Further, because the energy in the system is computed based on a potential, and the force is the derivative of this potential, the force must be conservative, by construction. For example, integrating this torque about a complete revolution in a rotating system yields identically zero:

$$\int_{\theta_0}^{\theta_0+2\pi} \frac{dE}{d\theta} \equiv 0.$$

This tautology indicates there can be no energy dissipation when considering only these potential resistance forces in a static manner. Friction is not conservative, but rather dissipative. Thus, this resistance force cannot be equated to the friction.

Recognizing the limitations of the static analyses, some of the aforementioned studies [15, 16, 20], as well as others [13, 14, 17, 19, 21, 24, 27], have used molecular dynamics to simulate such systems. In these simulations, the equations of motion based on the empirical potential are integrated in time, resulting in a trajectory for each atom. For some works [19, 20, 27], a steady-state approach has been used, wherein a constant relative velocity [20, 27] or force [19] is applied to the tube walls. Other works [13-17, 21, 24] have elected to study unsteady situations, with no constraints on the relative motion of

the tube. In these cases, the speed or amplitude of the motion decays with time as friction transfers energy from the orderly overall motion into random thermal motions.

While both translational and rotational motions have been addressed in the existing literature, for this work it was decided to concentrate on rotational motion in carbon nanotubes. Translational motions must contend with a restoring force due to van der Waals interactions: the van der Waals energy in the system decreases as the contact area between adjacent walls of the MWNT increases. Thus, when walls are displaced axially, there is a force that tends to increase the contact area by aligning the walls in the axial direction. Rotational motions do not exhibit this force, because the contact area does not change as one tube rotates within another. Rotational motion was therefore selected in order to eliminate this force, which could be difficult to distinguish from a true friction force (as well as the fact that rotational motion is more directly applicable to the experimental work.) Considering only the literature which addresses rotation in a dynamic way [20, 21, 24, 27], the range of predicted friction forces is dramatically decreased, from eight orders to only three, as shown in figure 5-1; however, the reason for the remaining discrepancy has not yet been explained. It is the goal of the present work to identify the source of this discrepancy, by comparing results from several different simulation techniques.

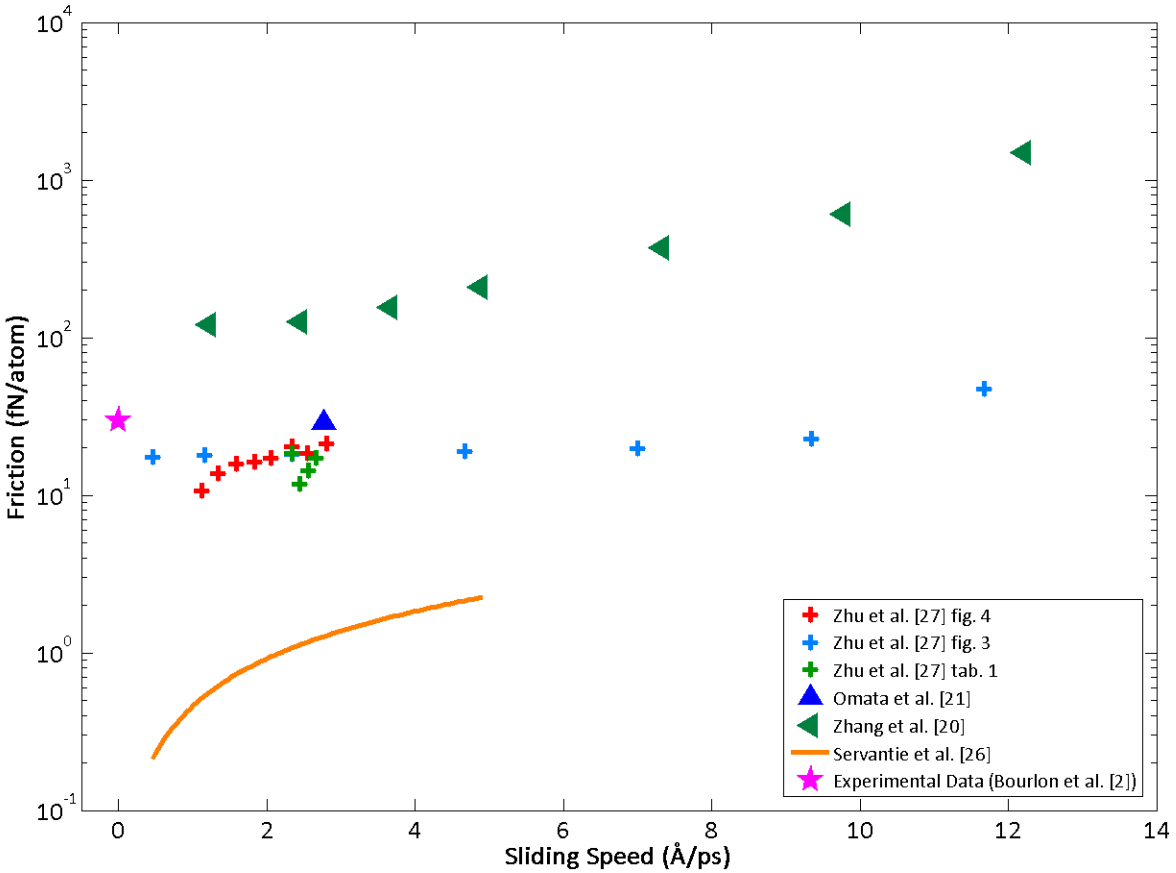

Figure 5-1: Friction reported by the four selected literature studies (the selection criteria were dynamic simulations that studied the rotational case) is plotted versus sliding speed. Selecting the most relevant papers has reduced the variation between reports to 2-3 orders of magnitude.

The potential reasons for the discrepancy must be among the differing details of the implementations of all the reported friction simulations. These simulations employ a range of CNT geometries, initial conditions, boundary conditions, as well as parameters of the simulation itself. The lack of consistency in implementation across the broad variety of reported simulations leads to an "apples-to-oranges" comparison, where the causes of the differences are obscured by the large number of candidate reasons, stemming from the large number of differing parameters. A consistent and rigorous approach, carefully controlling all but one parameter at a time, is necessary to be able to identify the true dependence of CNT friction on each of these parameters. If agreement can be demonstrated between disparate simulation methods for a single CNT system and operating condition, it will build confidence in the ability of the simulations to provide reliable and therefore useful data for performance estimation.

5.2 Simulation Methods

5.2.1 General Strategy

The main goal of the work is to demonstrate that even with different simulation methodologies, as used in the various studies in the literature to date, one can still expect to get the same value of friction in the CNT system. In other words, we expect the friction in the CNT to be an intrinsic property of the material, the geometry, and the operating conditions; the value obtained should not depend on the measurement method. To that end, multiple friction measurement methods have been employed to extract friction data from multiple types of simulations, with the aim of reducing or eliminating the variability in friction measurement across methods. Additionally, insight into why the different reported measurements are so different is desired, and therefore the effect of a broad range of parameters has been studied. This will provide information on which parameters have strong effects on the friction, and need therefore to be carefully controlled when simulating the system.

Note should be made that simulation of CNT friction has differences with other possible MD friction simulations in terms of chemistry. Bond breakage and formation are not expected, as the tubes are not actuated in the plane of their graphene walls. These effects could be substantial if other materials were simulated in rotating mode with such intimate contact. Indeed these phenomena would govern the wear exhibited by other non-atomically-smooth materials in such a simple sliding bearing, such as silicon.

5.2.2 Tools

For the present work, simulations were carried out using the Large-scale Atomic/Molecular Massively Parallel Simulator (LAMMPS) code [97, 135]. This is a well-known and thoroughly validated classical molecular dynamics code, which determines the trajectories of atoms within the simulation by directly integrating the forces on the atoms, using an efficient numerical integration scheme. The geometry, integration parameters, initial and boundary conditions, as well as the model for the inter-atomic forces (known as the potential or force field, since it is a scalar potential function of the degrees of freedom of the atoms, whose derivatives with respect to those degrees of freedom give the forces) can all be specified in detail. The tool also allows for the extraction of a wide variety of data during a simulation run, including position, velocity, and force data, temperature and heat transfer measurements, angular velocity, momentum, and kinetic energy, as well as user-defined derived quantities computed in-simulation.

For a force field, the Adaptive Intermolecular Reactive Empirical Bond Order (AIREBO) potential [96] was used. This potential, which was designed for molecules comprised of carbon and hydrogen, is based on an earlier empirical potential by Brenner [94], which describes the interactions between covalently bonded carbon and hydrogen atoms. It also includes four-body terms, which account for energy changes due to torsion of the bonds between atoms, about their equilibrium positions. In addition, the LAMMPS implementation of this potential includes a Lennard-Jones [92] style potential term, used to describe long range van der Waals type interactions between atoms not within the same molecule.

Except where otherwise noted, an integration time step of 1 fs has been used; this timestep is about one order of magnitude smaller than the timescale of the fastest phonons [95], and so should adequately capture all the relevant dynamics. The baseline starting point geometry (about which other variations in geometry were later explored) is shown in figure 5-4 and consisted of a (9,9) CNT inside a (14,14) CNT, with lengths of 60 nm and 50 nm and radii of 0.619 nm and 0.963 nm, respectively; these comprise 886 and 1120 atoms, respectively. The spacing between walls is 0.3438 nm, which agrees well with the known equilibrium distance between CNT walls, an important consideration to ensure that the simulation accurately approximates nature. This geometry was selected because it is representative of the geometries used in the literature.

At the beginning of each simulation, following an energy minimization, the tubes were allowed to equilibrate under a Langevin-style thermostat to 300K before any rotation was introduced. All simulations then proceeded with no axial or radial loads applied to the bearings; introduction of such effects has not been reported in the literature, and while it will certainly be of interest in applications of the bearing, it is left to future work in the interest of consistency with the existing work to date.

Rotation was simulated at rates between 25 and 250 GHz. On the low speed end, the limitations are computational cost (the length of real time required to run the simulation is proportional to the simulated time), as well as noise; at low speeds, the energy in thermal motion is of the same order as for the faster speeds, but the energy in rotation and the energy transfer rate due to friction are lower, and it is thus more difficult to distinguish the friction signal from the noise. The problem can be addressed by increasing the simulation length (to increase the total friction work done) or simulating multiple systems and averaging to reduce noise, both of which also compound the computational cost. On the fast end, the limitation is the structural integrity of the tube; as the rotation becomes faster, centrifugal forces as well as torque applied by the boundary conditions to enforce rotation become strong enough to break bonds within the tube. The threshold for this type of failure has been reported to be around 500-750 GHz [20].

Furthermore, the high-speed regime is not of interest to device designers. For example, existing MEMS bearing technologies and applications that use them (such as those discussed in section 2.1) have thus far not exceeded a few million rpm, while simulations access speeds as high as hundreds of billions of rpm. The same is true for the present prototype device; even though the simple classical model of section 4.1.1 predicts that the maximum speed of the test rotor should be on the order of MHz, it will likely not achieve that maximum when first tested, since the model optimistically does not take into consideration the defective structure of available CNTs. In the rotational experiments on CNT systems to date [1, 2], frequencies of a few Hz have been achieved. There is therefore a chasm between the speeds accessible by experimental and simulation methods for probing the CNT friction. Although there is no obvious reason that the friction should behave in a qualitatively different fashion at lower speeds when compared to higher speeds (and hence extrapolation from the simulation results into the regime

of the experiments might be useful), this assumption needs to be verified. As fabrication capability improves, increasing the speeds attainable by experiment, and computational power increases, allowing the simulations to access slower speeds, this gap may be bridged, allowing direct validation of the simulations with experimental data.

5.2.3 Simulation Tool Validation

Before using the simulation tool to extract data from for CNT friction, it is important to ensure that the simulation is functioning correctly, and that the results are correct and adequately capture the physics of the real system. To that end, validation studies were conducted using the simulation tool, before engaging it for the intended purpose.

First, a set of simulations were conducted to test that the mechanical properties of the CNT were adequately captured. One example problem that relies on the bending properties of the tube is the computation of the stable configuration for a "squished" CNT. For a given CNT, there are two competing energy mechanisms governing the shape of the cross section. On the one hand, there is elastic energy present in the bending of the graphitic plane that comprises the CNT wall. There is always a local energy minimum for tubes at a circular cross-section, where the bending energy is evenly distributed in the sheet. For small tubes, this is also the global energy minimum. However, if the tube is forcibly flattened, there is some energy reduction due to the interaction of the two sides of the tube in close proximity; that is, the increased bending energy is partially counteracted by the decreased van der Waals energy. It is well known [136] that for a certain tube diameter ($d > 24.2$ Å), the surface energy contribution is enough to create a local energy minimum (stable configuration) in the collapsed configuration. For even larger tubes ($d > 62.4$ Å), surface energy component overwhelms the bending energy contribution, and the flattened state becomes the *global* energy minimum, or most stable state.

We expect the present simulation tools to properly capture this phenomenon, as validation of their proper implementation. To that end, a series of simulations were performed whereby tubes were placed in the flattened state, and allowed to move under the influence of the inter-molecular forces of the potential. The tubes in table 5-1 were each initially placed in a collapsed configuration, comprising two parallel portions separated by the equilibrium inter-wall distance for graphite (3.4 Å), and half-cylindrical portions joining the edges of the sheet. This initial configuration is illustrated in figure 5-2a. The tubes were allowed to move under the influence of the force field, with an artificial viscous dampening force applied (to prevent oscillations and cause the tubes to settle into minimum energy configurations more quickly). At the end of the simulation, the CNTs were motionless, and in stable, minimum-energy configurations, shown in figure 5-2b.

Table 5-1: CNT geometries used to validate simulation by testing for stable collapsed configurations.

Chiral Indices	Diameter (Å)	Stable Collapsed Configuration Exists	Stable Collapsed Configuration Achieved
(5,5)	6.86	No	No
(10,10)	13.73	No	No
(15,15)	20.59	No	No
(20,20)	27.46	Yes	No
(25,25)	34.32	Yes	Yes
(30,30)	41.18	Yes	Yes

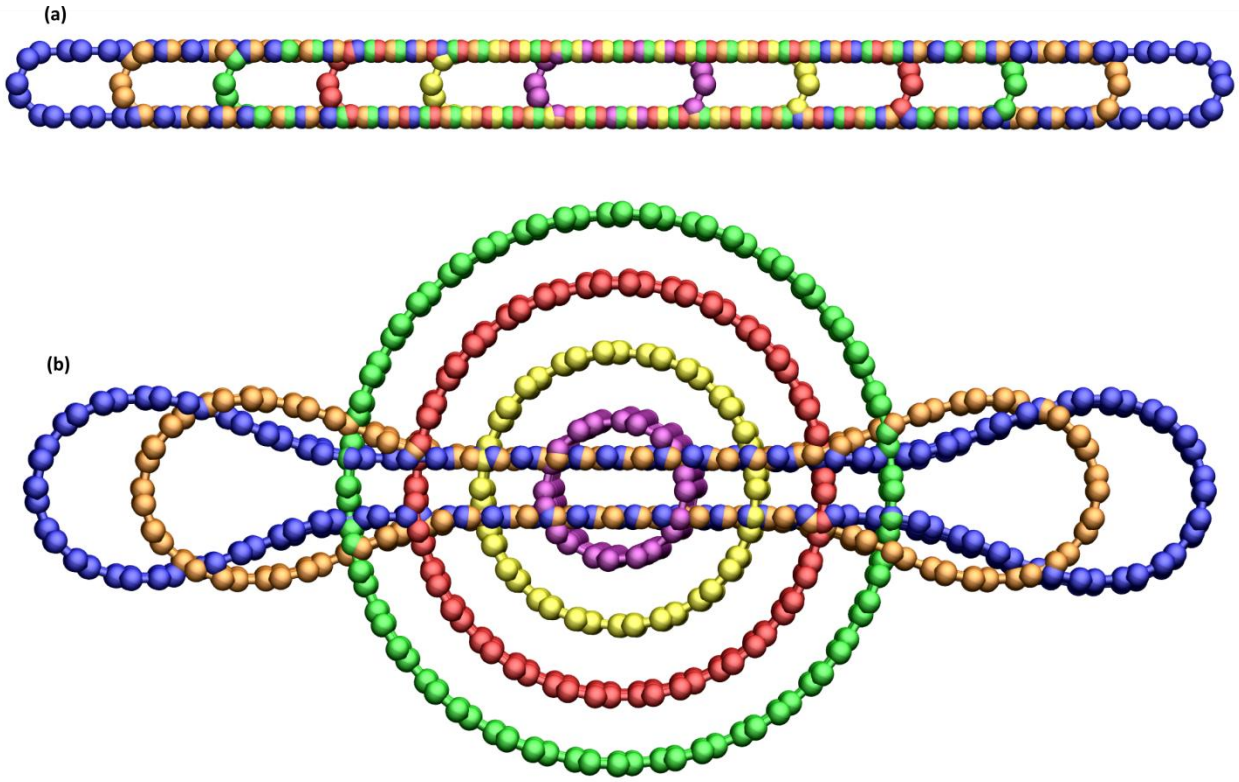

Figure 5-2: The initial (top) and final (bottom) configurations of CNTs used in validating the simulation. These CNT cross-sections are superimposed on each other; in each simulation, a single tube was simulated independently, without interactions with any other CNT. The (5,5), (10,10), (15,15), and (20,20) CNTs migrated to the cylindrical stable configuration, while the (25,25) and (30,30) CNTs remained stable in the collapsed configuration.

As expected, small diameter tubes were not stable in the collapsed configuration, while larger ones were. The exact crossover point, at a diameter of 24.2 Å (as documented by Zhang et al. [136] and extensively verified, see references of [136]), was not captured, however; a (20,20) tube, with a diameter of 27.46 Å, transitioned to the cylindrical state even though the collapsed configuration should be stable. This fact however is not necessarily an indictment of the simulation. As illustrated in figure 5-2, the initial, flattened configuration was not precisely the minimum-energy configuration that should be stable for larger tubes. Because of the geometrical complexity in specifying the atom locations, the "barbell" shaped knobs on the edges of the tubes were not implemented in the initial configuration. Therefore, the initial configuration involves some excess strain energy in the bending of the CNT wall; this energy was likely sufficient to propel the (20,20) tube through the collapsed configuration energy minimum via inertia, until it came to rest at the next minimum (the cylindrical configuration). For larger tubes, the depth of the collapsed configuration energy minimum is increased sufficiently that the tubes do come to rest in that minimum.

The fact that the simulation captures the expected mechanical behavior of individual CNT walls is encouraging, and supports the methodology as being accurately implemented. The cross-sectional motion of the CNTs is expected to play a role in the CNT friction, as the spacing between walls varies with this motion. While it is impossible to completely validate the simulation for its intended purpose (i.e. friction measurement) without real experimental data on CNT friction, validation against data on

similar phenomena, or phenomena that rely on the same fundamental CNT properties, such as the energy dynamics in CNT collapse, is helpful in building confidence that the simulation is implemented correctly.

In addition to validating the mechanical behavior of individual CNTs, it was important to establish some confidence in the simulations' capabilities to predict the inter-tube interactions. These interactions are what drive the friction, so it is very important that they be properly captured by the simulation. Several studies have been conducted on these forces, using molecular statics techniques, that is, by examining the energy potential as a function of displacements between adjacent tubes. One study in particular [23] included detailed maps of the energy landscape for DWNTs, as a function of rotational angle and translational distance. That work was reproduced using the simulation techniques of this work. Rigid CNTs, of chiralities (14,1) and (14,12), and lengths 125 Å and 60 Å, respectively, were placed concentrically in the simulation domain. Then, the inner tube was rotated and translated, by increments of 0.25 Å of translation and 1/120 rotation, generating a matrix of energy in the system vs. translational and rotational displacements. The resulting energy map is shown in figure 5-3, and agrees well with the results reported previously [23]. Three important effects are captured in the plot. First, there is a periodic variation in the energy with respect to the rotational displacement. This variation is caused by the small changes in the average distance between atoms in the two tubes as atoms align and un-align in the circumferential direction. Second, the overall energy tends to increase with increasing axial displacement; that is because axial displacement of the tubes reduces the amount of overlapping area in contact, increasing the surface energy due to the van der Waals interaction. Finally, the angle of minimum energy varies linearly with the axial displacement. This phenomenon is attributable to the fact that the "grooves" of minimum energy wrap around the tube in a helix, corresponding to the helical wrapping of the lines of carbon atoms, or the chiral angle.

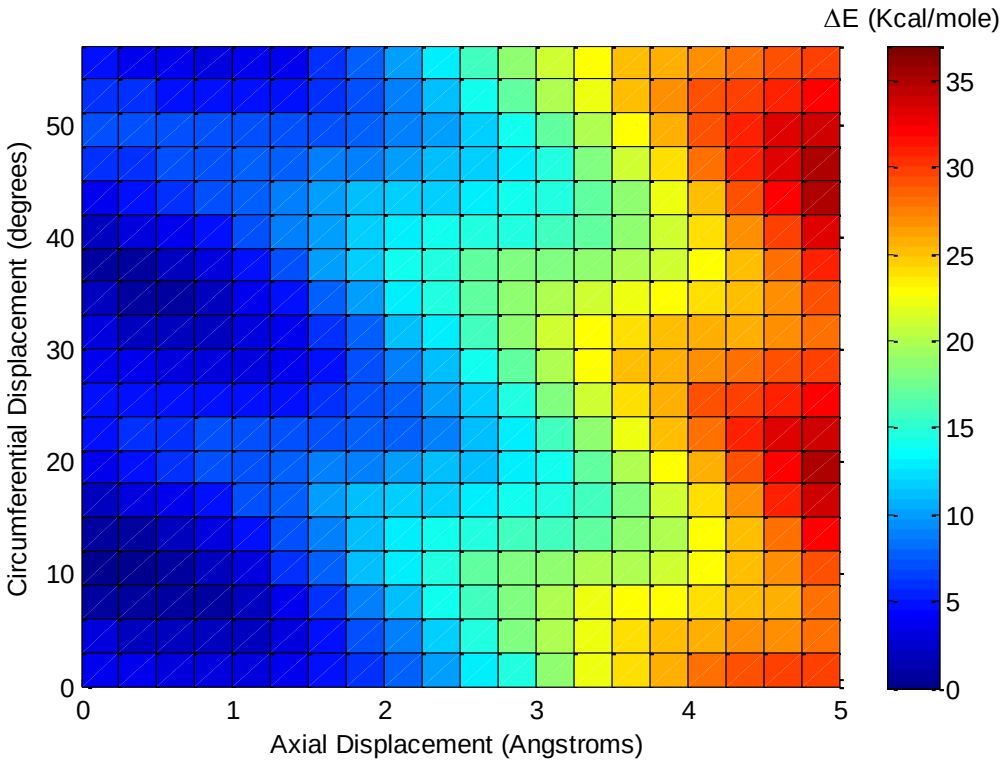

Figure 5-3: Map of energy landscape for a (5,5)/(10,10) DWNT, as a function of translational and rotational displacements.

In summary, both the intra- and inter-molecular forces in the simulation behave as expected, when compared to literature, as demonstrated from the collapsing CNT and energy landscape simulations. The intra-wall interactions are important in determining how the spacing between tubes behaves, and the inter-tube interaction is critical in determining their interactions, including energy transfer and dissipation via friction. Together, this agreement indicates that the simulations are capturing the known physics of the CNT system, and should properly predict the friction in the system.

5.2.4 Overview of Simulation Types

As mentioned in section 5.2.1, one main goal of the simulations is to demonstrate that friction estimates that agree quantitatively can be obtained even from different simulation techniques. Four different techniques have been employed here, which span the possible techniques reported in the selected literature [20, 21, 24, 27] as well as one new technique (Spin-Up). Table 5-2 summarizes the key differences between these simulation types, including the boundary and initial conditions (shown geometrically in figure 5-4) and the parameters and equations used to compute the friction. The details of these simulation types are described in sections 5.2.5 and 5.2.6.

5.2.5 Steady State Simulations

5.2.5.1 Isothermal Case

One method of determining the friction in a CNT system is to set it rotating in a steady state, and to extract the friction at this steady state condition. For this method, the inner tube rotated at a constant angular velocity, while the outer tube was held fixed. These constraints were accomplished by enforcing zero velocity or the prescribed angular velocity on a few rings of atoms at one end of each tube. A Nosé-Hoover-style thermostat [137, 138], described in section 5.3.3.2, was applied to the outer tube, to simulate contact with a large heat reservoir, also at 300K. The simulation can therefore be referred to as isothermal. After an initial transient, during which the stationary atoms in the center tube accelerate to catch up with the constrained atoms at the tube end, the system reaches a steady state. The atoms in the inner tube rotate with approximately uniform speed. Figure 5-5a clearly shows the transient in the angular velocity, and the eventual steady rotation which results, for an example simulation at 200 GHz. This transient consists mostly of the torsional mode in the rotating CNT, excited by suddenly torquing the end atoms to enforce the rotation rate.

The friction forces tend to slow down the rotating tube by transferring that orderly kinetic energy into random thermal motion. However, the enforced velocity constraint causes the kinetic energy of the inner tube to be maintained, resulting in an accumulation of thermal energy. The thermostat on the outer tube continually extracts thermal energy to maintain the temperature (figure 5-5c). Temperature is computed during the simulation using kinetic theory:

$$T = \frac{m_C \bar{v}_T^2}{3k_B}$$

where $\bar{v}_T$ is the average thermal velocity of each atom, m_C is the atom's mass, and k_B is the Boltzmann constant. The term "thermal velocity" is used to indicate that these velocities are corrected for the bulk motion of the tube, that is, the angular velocity $\vec{\omega}_i \times \vec{r}_i$ is subtracted from each atom's velocity before calculating the average. Atoms that are constrained by boundary conditions are also neglected in the temperature calculation.

Table 5-2: Comparison of simulation types

Simulation Type		Steady Isothermal	Steady Adiabatic	Coast-Down	Spin-Up
		Steady State		Transient	
Boundary conditions	1	Fixed	Fixed	Free	Free
	2	Thermostated	Free	Free	Free
	3	Spinning	Spinning	Free	Spinning
	4	Free	Free	Free	free
Initial conditions	1	Motionless	Motionless	Temperature	Temperature
	2	Temperature	Temperature	Temperature	Temperature
	3	Spinning	Spinning	Spinning	Spinning
	4	Temperature	Temperature	Spinning	Spinning
Friction extracted from		Energy exchange at thermostat	Energy accumulation	Angular momentum change	Angular momentum change *or* Energy accumulation
Friction measurement equation		$P = F_f \bar{r} \omega$		$\frac{dL}{dt} = \pm F_f \bar{r}$	
Discussed in section		5.2.5.1	5.2.5.2	5.2.6.1	5.2.6.2

"Temperature" indicates that the atoms have random thermal motion, but no orderly bulk motion (i.e. rotation).

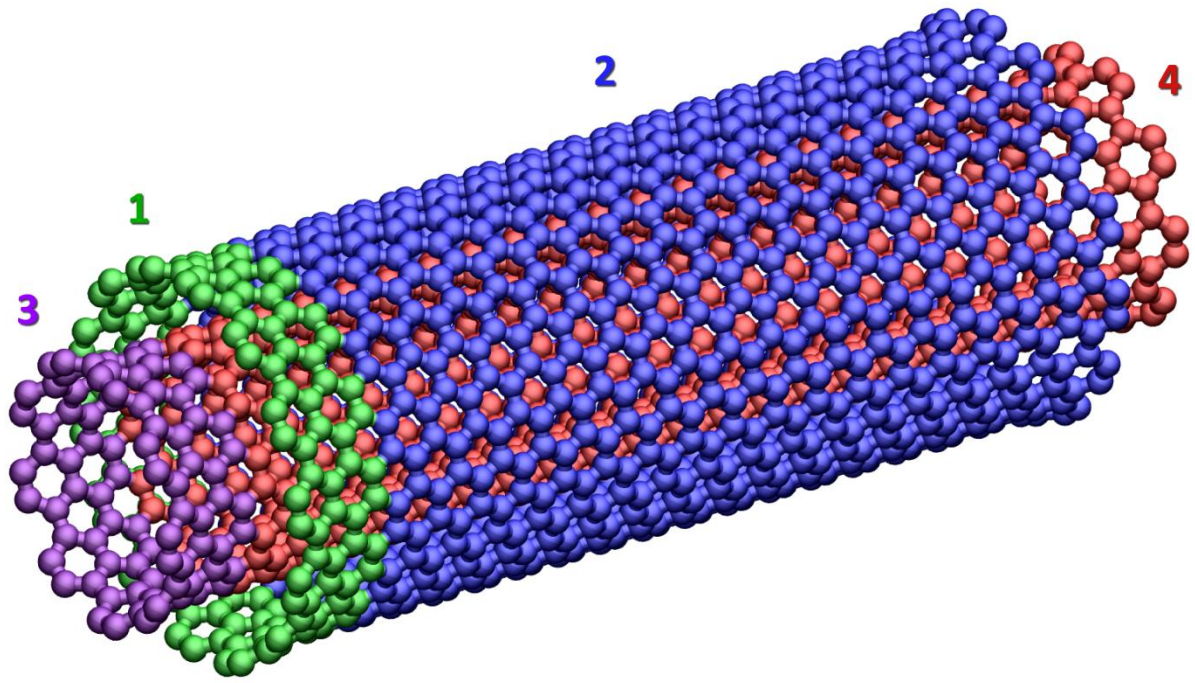

Figure 5-4: Boundary condition regions in the baseline geometry (a 60 nm (9,9) CNT centered in a 50 nm (14,14) CNT).

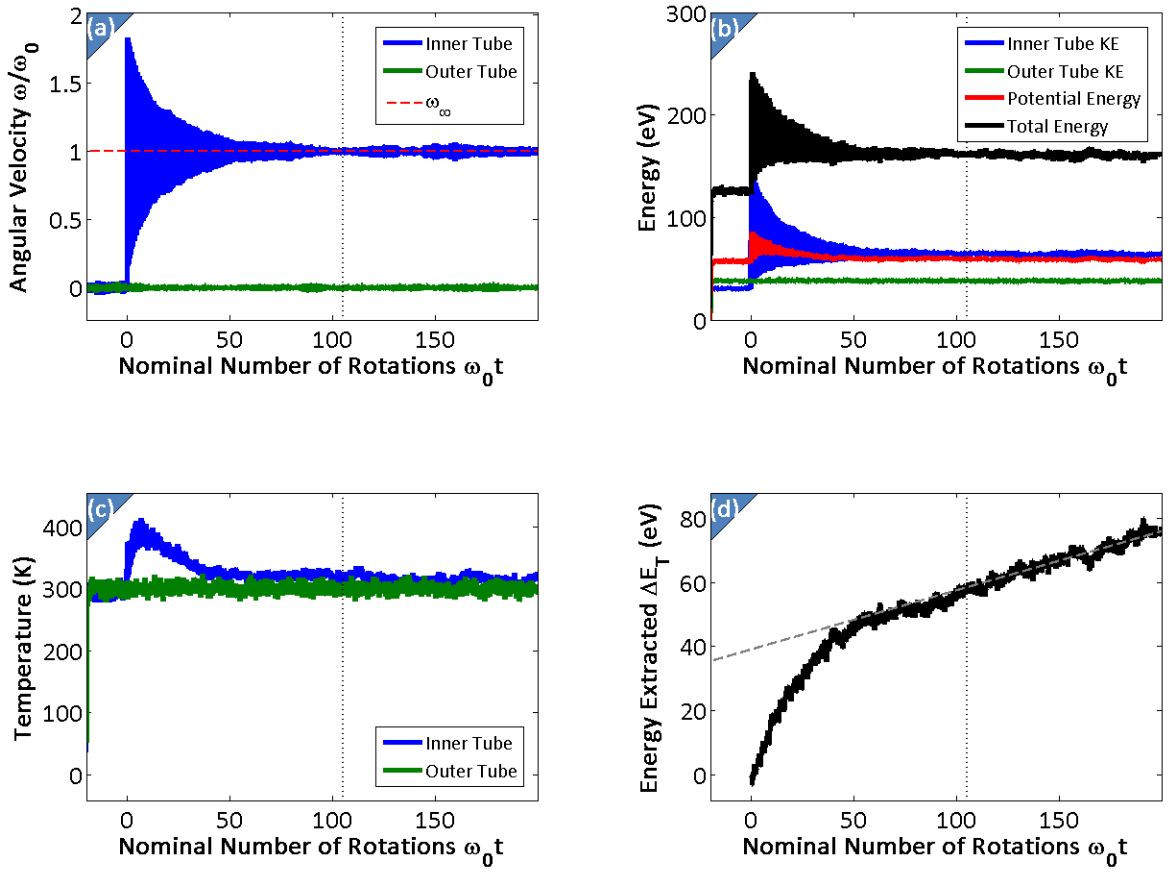

Figure 5-5: Example data collected from an isothermal constant velocity simulation at 200 GHz, showing angular velocity (a), temperature (c), and kinetic energy (b) of each tube, along with other energies (b) and the running total of energy extracted via the thermostat (d). The dashed vertical lines represent the end of the startup transient and the beginning of the region used for fitting.

At steady state, the total energy E is not changing with time (see figure 5-5b), so the rate of kinetic energy addition equals the rate of thermal energy extraction $\dot{Q}$, which is also equal to the rate P at which the frictional work converts the kinetic energy into thermal energy. Thus, by measuring the rate of heat extraction at the thermostat (example shown in figure 5-5d), the friction power and hence the friction is known. This is the same approach used by Zhang *et al.* [20].

To compute the friction from the thermostat energy extraction data, it is necessary to compute the rate $\dot{Q}$ at which energy is extracted via the thermostat. For the steady state simulation, this rate is constant, so the total energy extracted

$$\Delta E_{\mathrm{Q}}(t) = \int_0^t \dot{Q}\,dt$$

is a linear function of the simulation time. The rate was taken to be the slope of a least squares fit to the portion of the energy extracted data after the transient has damped out. The vertical dotted lines in figure 5-5 mark the time at which the transient was deemed extinguished, and the dashed, sloped line in figure 5-5d is the linear fit. The friction power is then equated to the energy extraction rate

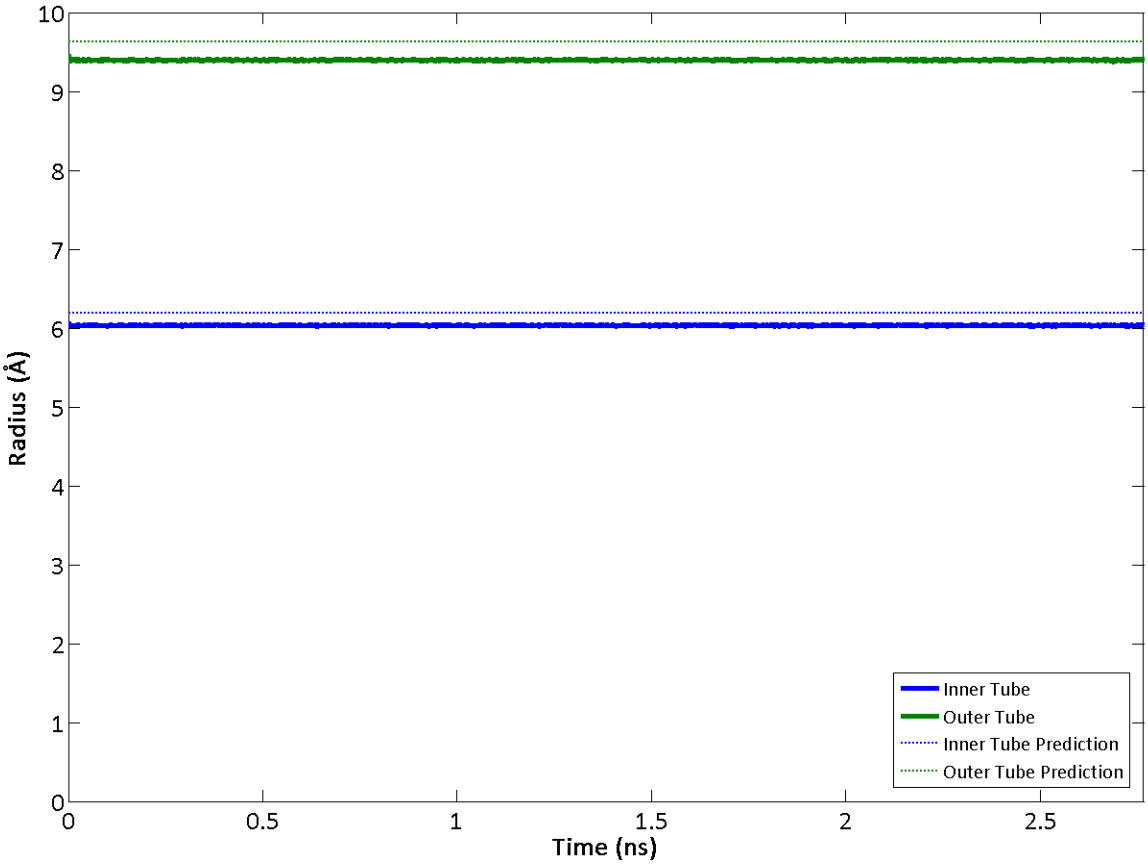

Figure 5-6: Radius data is shown over the course of an example simulation; the true radius differs slightly from the prediction.

$$\dot{Q} = P = \tau_{\mathrm{f}}\omega = F_{\mathrm{f}}\bar{r}\omega$$

allowing the friction toque τ_{f} and the friction force F_{f} to be extracted (recall that $\bar{r}$ is the interface radius, or average of the two tube radii). These are the total torque and force, respectively, exerted in the whole system.

The radius of a CNT can be estimated based on the known carbon-carbon bond length, and knowledge of the geometrical configuration, *i.e.* the chiral indices. Dresselhaus *et al.* [139] give the following formula for determining the CNT diameter:

$$r = \frac{\sqrt{3}a_{\text{C-C}}}{2\pi}\sqrt{m^2 + mn + n^2}$$

where $a_{\text{C-C}} = 1.44$ Å is the carbon-carbon bond length, and (m, n) are the chiral indices. However, the actual diameter of the CNT can deviate slightly, based on the interactions with other tubes in the vicinity. Another way to determine the diameter is to measure it directly from the simulation, by taking the average distance from the centerline of all the atoms in the tube. This can then also be averaged over time to give the diameter of the tube. Figure 5-6 shows that while the radius is quite stable, it

differs from the prediction. This measured radius was used in all calculations for the greatest possible accuracy.

5.2.5.2 Adiabatic Case

A variant of the constant-velocity method is to eliminate the thermostat on the outer tube, resulting in an adiabatic or constant energy simulation. The result is that as kinetic energy is continually added, and converted into thermal energy by the friction, the total energy of the system builds up over time (shown in an example simulation in figure 5-7d). The friction power is then equal to the energy accumulation rate. Because energy is accumulating, the system is not strictly in a steady state, as the temperature is increasing with time (figure 5-7c). However, if the change in temperature is small compared to the absolute temperature, and this effect is neglected, the resulting friction is close to the isothermal result. This is the approach used by Zhu *et al.* [27].

Like the isothermal case, the rate of energy change P (here built up in the system instead of extracted via thermostat) is constant in the steady state, leading to a linear evolution of the system total energy E, and again the friction is found from

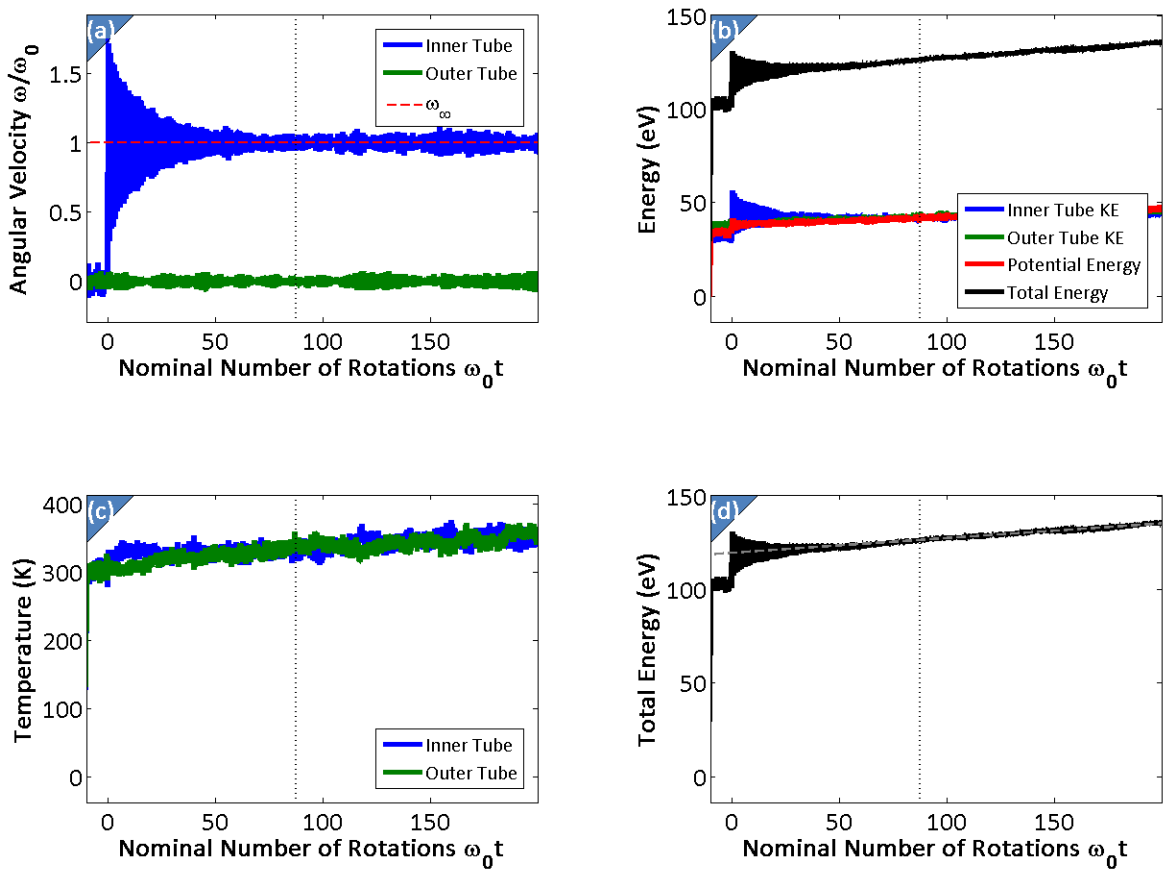

Figure 5-7: Example data collected from an adiabatic constant velocity simulation at 100 GHz, showing angular velocity (a), temperature (c), and kinetic energy (b) of each tube, along with other energies (b) and the total energy in the system (d). The dashed vertical lines represent the end of the startup transient and the beginning of the region used for fitting.

$$\frac{dE}{dt} = P = \tau_{\mathrm{f}}\omega = F_{\mathrm{f}}\bar{r}\omega$$

Neglecting the temperature change, allowing the simulation to be treated as steady, is reasonable for low speeds. For example, the 100 GHz case shown in figure 5-7 experiences a temperature rise of $55\ \mathrm{K}$, or 18% of the original temperature over the course of the simulation. For higher speeds, with higher energy conversion rates, the change is much more. For example, at 250 GHz, the temperature rise is $280\ \mathrm{K}$; the temperature nearly doubles. Therefore, the adiabatic simulation does not effectively isolate the effect of temperature on the friction.

Another way to quantify the importance of the unsteadiness due to temperature increases is using the reduced frequency, defined as

$$\beta = \frac{t_{\mathrm{system}}}{t_{\mathrm{unsteady}}}$$

where t_{unsteady} is the timescale of the unsteady behavior, and t_{system} is the timescale of the processes that drive the system. Therefore β is large when the unsteady effects happen quickly, and therefore have a large influence. For this case, we can take

$$t_{\mathrm{unsteady}} = \frac{E_{\mathrm{T}}}{P} = \frac{N\frac{3}{2}k_{\mathrm{B}}T_0}{P}$$

meaning that the timescale of this thermal effect is the initial thermal energy divided by the rate at which thermal energy is accumulated. The time scale of the system t_{system} is simply the simulation length. The reduced frequencies for the two runs discussed above are shown in table 5-3.

Table 5-3: Reduced frequency for evaluating quasi-steady assumption in adiabatic simulations

Rotation Rate $\omega/2\pi$ (GHz)	Energy Rate P (eV/ns)	Simulation length t_{system} (ns)	Reduced Frequency β
100	9.38	2	0.241
250	116	0.8	1.19

The reduced frequency is almost one order lower than 1 for the 100 GHz case, indicating that the quasi-steady approximation is reasonable here; indeed, at these low speeds the adiabatic simulations agree with the isothermal results to within the error bars for low speeds. On the other hand, at 250 GHz, the reduced frequency is greater than one, and the friction value reported by this adiabatic method is likely to be too high (if taken as the friction at the starting temperature) since friction increases with temperature (see section 5.3.3.3). The differences between the adiabatic simulation and the thermostated simulations due to this effect, particularly at high speeds, are evident in figure 5-22.

5.2.6 Transient Simulations

An alternative method to determine the friction is to allow a rotating CNT to move freely, and to observe how the friction affects the evolution of this motion. This method has the advantage that motion need not be imposed on any atoms in the simulation in order to maintain a consistent speed in the presence of friction. Therefore, all the atoms in the simulation are free, and thus experience the

proper physics (and not an artificial boundary condition.) However, the drawback is that as a result of the frictional torque, the CNT accelerates or decelerates, and the conditions under which friction is being measured change throughout the simulation. These unsteady simulations have been used as a compliment to the steady simulations, with the goal of demonstrating that the same friction value can be computed independent of simulation method.

5.2.6.1 Coast-Down Simulations

For the unsteady coast-down simulations, there are no constraints on the walls of the MWNT. Instead, the inner tube is given an initial angular velocity, and the two tubes are allowed to move freely. The friction causes the rotating tube to transfer its angular momentum to the stationary tube, so that the rotating tube slows down and the stationary tube gradually accelerates. The friction is the only torque on either tube, so the friction torque can be found directly as the time rate of change of the angular momentum of either tube:

$$\tau_{\mathrm{f}} = \pm \frac{dL}{dt}$$

where the friction torque τ_{f} is taken to be positive, and the sign in the equation is therefore positive for the outer tube (initially at rest) and negative for the inner tube (initially rotating). An example angular momentum trace is shown in figure 5-8d. This is the approach used by Omata *et al.* [21] and Servantie and Gaspard [24].

Because the tubes are accelerating, the angular velocity is not constant in time. There are two possible ways to deal with this issue. If the total change in velocity over the course of the simulation is small with respect to the absolute velocity at the beginning of the simulation, it can be assumed that the friction does not change as a result of velocity changes. Therefore, the friction is constant over the simulation, and the angular momenta of the tubes should vary linearly, with slope equal to that friction:

$$L_1 = L_0 - \tau_{\mathrm{f}} t$$

$$L_2 = \tau_{\mathrm{f}} t$$

where L_1 and L_2 are the angular momenta of the inner and outer tubes, respectively; $L_0 = \omega_0 I_1$ is the initial angular momentum of the inner tube (the outer tube starts at rest and does not contribute to the initial angular momentum.) This linear relationship between angular momentum and time (or angular velocity and time, since $\omega = L/I$) is a reasonable approximation for short simulation periods and low friction. The torque is extracted by fitting a least-squares line to the angular momentum data for each tube, starting just after the rotation; these fits are the dashed, sloped lines in figure 5-8a,d. Throughout the text, we will refer to this as a "linear unsteady fit." The sign of the error introduced by the constant friction assumption is known: This method will under-predict the friction, because the average speed during the simulation is in fact lower than the nominal speed, and hence the friction reported actually corresponds to a slightly lower speed.

However, the assumption breaks down for longer simulations or for higher relative speeds between the tubes. To treat the situation more accurately, we can assume that the friction varies proportionally with the relative angular velocity between the two tubes (as is done by Servantie and Gaspard [24]), i.e.

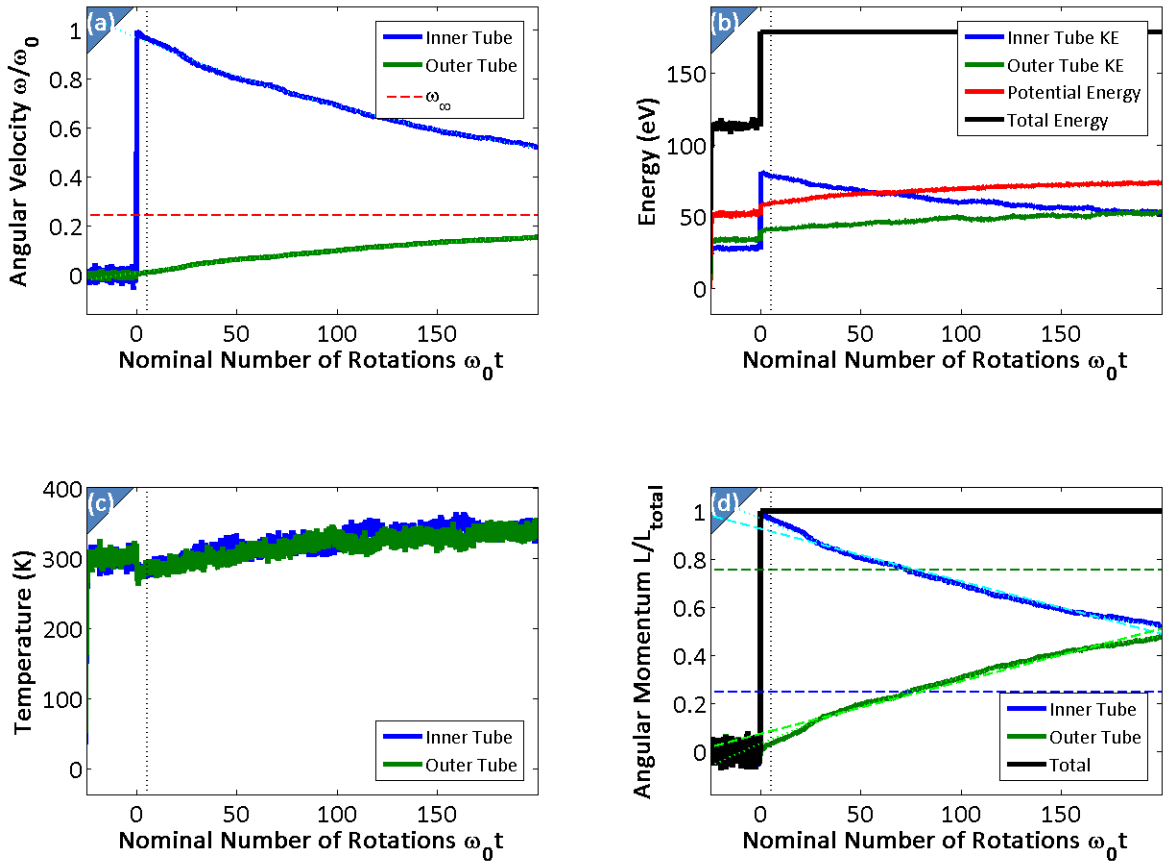

Figure 5-8: Angular velocity evolution (a) during an example coast down simulation at 250 GHz. The small initial transient motion is due to the release of the constraints on the end atoms used during thermal equilibration. The rate of change of the angular momentum (d) can be approximated as linear for this short time simulation, or it can be fit with an exponential for longer times; these are shown as dashed and dotted lines, respectively. Temperature (c) and energy (b) are also recorded during the simulation.

$$\pm\frac{dL}{dt} = \tau_f = \frac{I_1 I_2}{I_1 + I_2} B(\omega_1 - \omega_2)$$

where B is the proportionality constant, and the moments of inertia I_1 and I_2 have been introduced to simplify the algebra later on. We can then use the knowledge that there are no external torques, so angular momentum is conserved in the simulation, or the total angular momentum is always equal to the initial angular momentum:

$$I_1\omega_1 + I_2\omega_2 = L_0$$

to eliminate one of the angular velocities from the differential equation:

$$\omega_2 = \frac{L_0 - I_1\omega_1}{I_2}$$

$$-\frac{dL_1}{dt} = \tau_f = \frac{I_1 I_2}{I_1 + I_2} B(\omega_1 - \omega_2) = \frac{B}{I_1 + I_2}[I_1 I_2 \omega_1 + I_1^2 \omega_1 - I_1 L_0] = B\left[I_1 \Omega_1 - \frac{I_1 L_0}{(I_1 + I_2)}\right]$$
$$= B\left[L_1 - \frac{I_1 L_0}{(I_1 + I_2)}\right]$$

The solution is an exponential:

$$L_1 = A_1 \exp(-Bt) + \frac{L_0 I_1}{I_1 + I_2}$$

We note that at the end of the rotation, friction will have eliminated the relative angular velocity, and both tubes will have the same velocity ω_∞ (marked with a red dashed line in figure 5-8a), which can again be found by conservation of angular momentum:

$$(I_1 + I_2)\omega_f = L_0 = I_1 \omega_0$$

$$\frac{L_0}{I_1 + I_2} = \omega_\infty$$

Substituting this into the equation gives:

$$L_1 = A_1 \exp(-Bt) + I_1 \omega_\infty$$

and it can be similarly shown that

$$L_2 = I_2 \omega_\infty - A_2 \exp(-Bt)$$

These exponential functions can also be fit to the experimental data, allowing the extraction of the parameter B, which will always be positive. The exponential fits for angular momentum and angular velocity are the dotted lines in figure 5-8a,d. Once B has been determined, the friction at a given rotation rate is computed from

$$\tau_f = B\left[L_1 - \frac{I_1 L_0}{(I_1 + I_2)}\right] = B I_1(\omega_1 - \omega_\infty) = B I_2(\omega_\infty - \omega_2)$$

This method will be referred to as an "exponential unsteady fit." Note that the exponential unsteady fitting technique can provide estimates for the friction at any speed from a single run; in later graphs, the speed chosen to demonstrate the results will be the initial speed ω_0 of each simulation.

Another important note is that because the velocity constraint is released at the beginning of the simulation, and there is no thermostat, the energy in the system is necessarily conserved during these simulations. This is illustrated in figure 5-8b. An important consequence of this is that unlike the steady adiabatic simulations (section 5.2.5.2), where the temperature increases dramatically during the simulation due to the kinetic energy added by the velocity constraint, for the coast down simulation the temperature rise is much more modest. Even for the highest speed (250 GHz,) the temperature increases by only about 43 K, or 14% of the initial temperature.

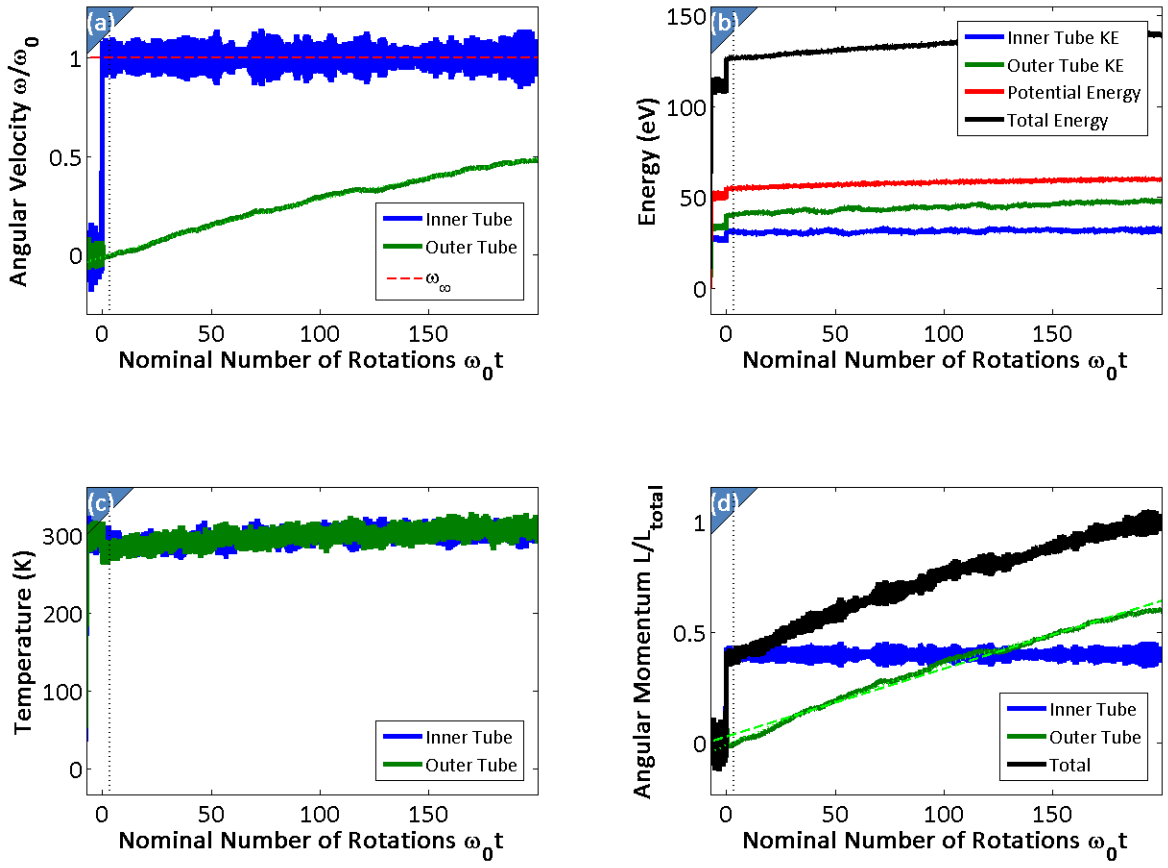

Figure 5-9 - Angular velocity (a), energy (b), temperature (c), and angular momentum (d) evolution during a spin-up simulation at 75 GHz. The inner tube's angular velocity and angular momentum are held constant, while the outer tube gradually catches up.

5.2.6.2 Spin-Up Simulations

An additional type of unsteady simulation was performed wherein the inner, rotating tube is constrained to keep rotating using the same enforced velocity at the tube end as in the constant velocity case. Figure 5-9 shows the angular velocity evolution for this case. The outer tube, however, remains free, and gradually accelerates due to the friction torque. The final, asymptotic angular velocity ω_∞ is thus equal to the initial angular velocity ω_0. The friction torque can be measured in the same manner as for the coast-down simulations, that is, by fitting either a linear function

$$L_2 = \tau_f t$$

or exponential function

$$L_2 = I_2\omega_\infty - A_2\exp(-Bt)$$

$$\tau_f = BI_2(\omega_\infty - \omega_2)$$

to the angular momentum of the accelerating tube, and extracting the constant or velocity-proportional friction value from the fit coefficients. Note that the spin-up simulations suffer from the same temperature increases as the adiabatic steady simulations, since energy is constantly being added by the enforced velocity boundary condition.

5.2.7 Phonon Computations

In addition to simulating the motion of CNTs, with the intent of measuring the friction and its dependence on various simulation parameters, it was desired to gain some deeper understanding of the mechanism whereby friction occurs in these systems. One way to better understand the phenomena going on in the system is to compute and observe the phonons in the system. Phonons are the quanta of vibration in crystalline systems, and are analogous to natural modes in classical physical systems. By determining which phonons are most active, or contribute strongly to the dynamics of a system, we can learn what modes dominate the system behavior, if any, and in particular at what frequencies the interactions between the two CNTs are most important in determining the friction.

It is helpful to consider a lumped-parameter classical dynamic system, consisting of springs and masses, with which to compare phonons. A crystal consists of infinitely many atoms, and "springs" (representing the interaction forces between atoms) arranged in a regular, periodic array. Because there are infinitely many elements, there are infinitely many phonons. However, as in the continuum mechanics case, the lower the frequency of the phonon, the lower its energy, and therefore the more likely it is to be populated; that is, in any given motion of the system, when decomposed into its phonons, the lower frequency phonons make up the majority of the contributions.

There are a number of ways to compute the phonons in a system. The most straightforward is to compute them for a zero-temperature (motionless) crystal. In this case, the masses of the atoms are known, as are the forces between them (by using the same sort of empirical potential model as those used in the molecular dynamics simulations). One can therefore directly construct the dynamical matrix, which relates the forces on each atom to the displacements of all the atoms. This matrix is exactly analogous to the stiffness matrix in a classical lumped-parameter model, or finite element simulation. The natural modes, or phonons, and their frequencies are the eigenvectors and eigenvalues, respectively, of the matrix.

There is a slight complication due to the periodic, infinite nature of the crystal. Instead of constructing the infinitely large stiffness matrix, a Fourier transform is used to represent the spatially periodic system as a finite set of wave number vectors, which capture the structure of the crystal. The matrix can then be determined in this reciprocal space, which yields the eigenvalues as a function of the wave number vector.

A number of codes exist for computing these zero temperature phonons. Since they are straightforward to use and relatively computationally inexpensive, one such program, the General Utility Lattice Program (GULP) [140, 141] has been used to compute zero temperature phonons for a few example CNTs. Two types of data are produced by GULP. The first is a phonon dispersion curve. This curve plots the first several phonon frequencies as a function of the wave number vector. An example zero temperature dispersion relation is shown in figure 5-10. Additionally, the code computes the phonon density of states, which is an integral of the dispersion relation over the wave number vector axis. It shows at what relative density natural modes exist for a given frequency. An example zero temperature density of states is shown in figure 5-11.

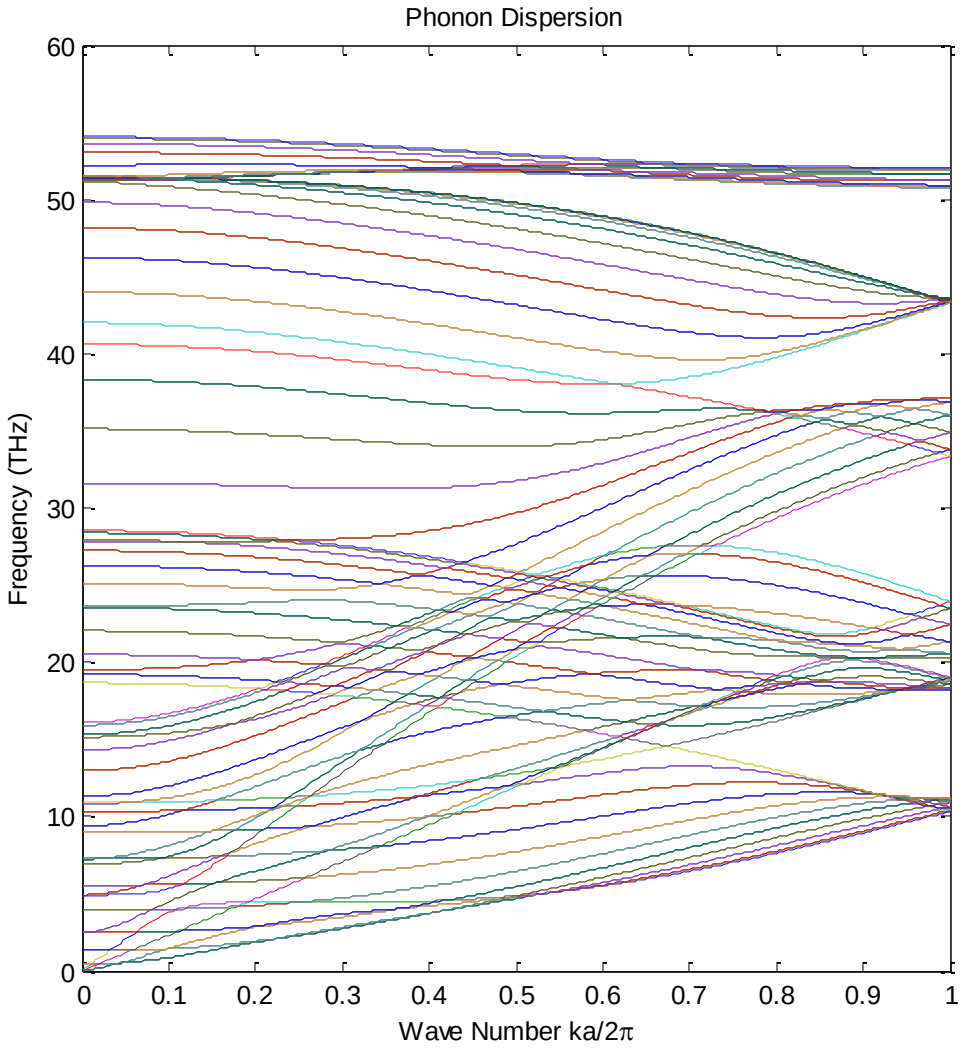

Figure 5-10: Example phonon dispersion relation at zero temperature, for a (10,10) CNT, computed by GULP.

While this zero temperature method does describe the natural modes of the CNT, it does not capture the effect of any forcing functions on the CNT's motion. Specifically, that means that the results do not include the effects of anharmonic random motions of the atoms due to thermal energy at a non-zero temperature. Additionally, the effect of any bulk motion of the tube (for example the rotation of the bearing) and the effects any other atomic motions excited by tube-to-tube interaction under this motion are not included. Yet it is precisely these motions that we are interested in studying; we want to know what modes are populated to a greater or lesser extent under motion, so that we can infer which modes contribute strongly to causing the friction. Therefore, a different method is necessary.

One possible method to include the effects of temperature, motion, and interaction has been proposed by Thomas *et al.* [142] This method begins with the output of a molecular dynamics simulation, the trajectory of each atom within the simulation. It then performs a Fourier transform in all the spatial directions to decompose those actual motions in to their component phonons, or modes. The result is the spectral energy density, which describes what portion of the overall kinetic energy is

present in each frequency. This is similar to the phonon density of states, except that the density of states (computed without any motion) describes how many modes exist at a given frequency, whereas the spectral density describes how much of the total energy is present in the modes having a given frequency. In other words, the spectral density shows how "active" the modes of each frequency are. Indeed, methods are presented [142] to derive the expected density of states and dispersion relation from the recorded spectral energy density.

Unfortunately, however, an implementation of the method described by Thomas *et al.* [142] is not readily available. Writing an implementation was considered, since the method is well documented and straightforward in theory. However, the implementation presented numerous numerical hurdles, mostly stemming from the vast quantity of data required (each atom, of which there are thousands, must store on the order of 10^7 positions in order to have the trajectory with the necessary resolution). Substantial effort would need to be invested in numerical optimization to produce a workable code, which is outside the scope of this thesis.

Another similar method [143, 144] does exist to compute the phonons, taking into account the actual motion of the system. This code has been made available as an add-in to LAMMPS [145]. This method makes use of the equipartition theorem, which states that at equilibrium, energy is equally stored in thermal, kinetic, and potential forms. The spring constants that make up the dynamical matrix can therefore be derived by comparing the computed thermal energy with the potential energy due to displacements of the atoms from their equilibrium positions in the crystal (the spring forces of the

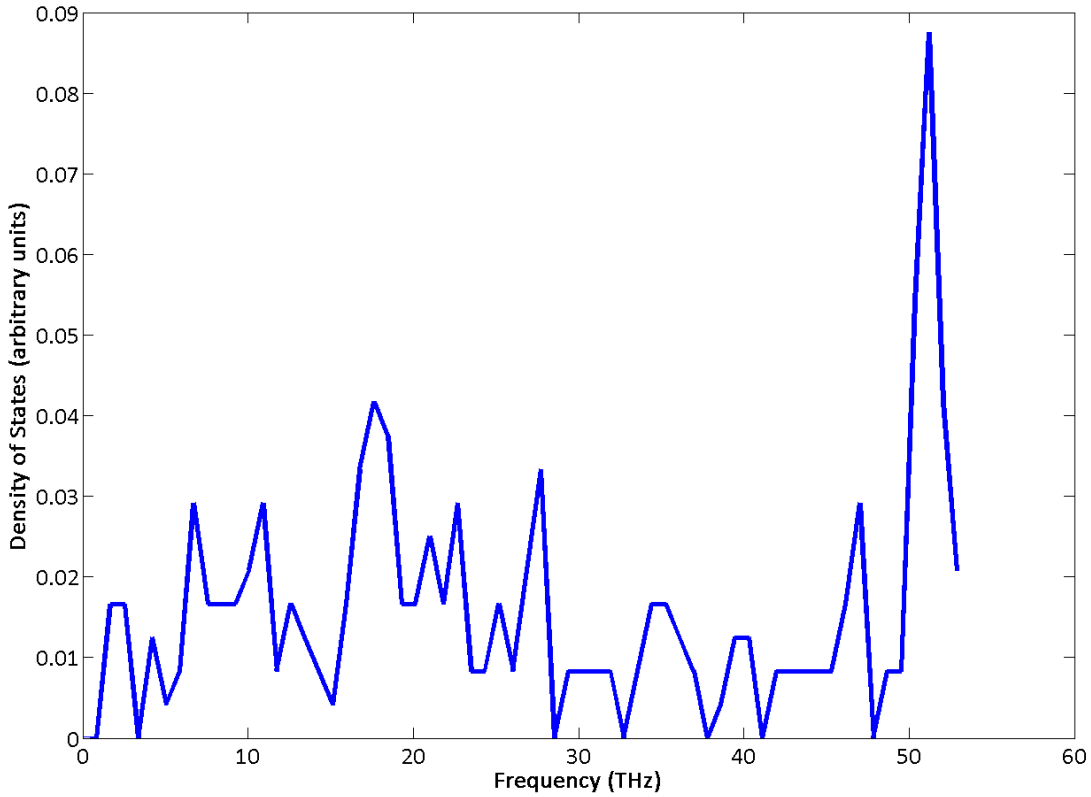

Figure 5-11: Example phonon density of states at zero temperature, for a (10,10) CNT, computed by GULP.

atomic interactions). The density of states (which in fact reflects the changes in occupation of these states due to the actual motion of the tube, since the matrix was inferred from the actual moving tube) is again computed by integrating the phonon dispersion relation across the wave number vectors making up the spatial decomposition. The method has also been well validated against known analytical solutions, other codes, and experimental data [143].

We hypothesize that the spectral density calculations will reveal which frequencies are most active in an individual tube, appearing as peaks in the power spectrum. Furthermore, we expect that these peaks might change as different effects are applied to the tube. For example, when two tubes are in contact, their interactions may damp some modes while reinforcing others. Once the tubes are rotating, the power spectrum may change again, exhibiting peak shifts due to the interactions that make up the friction between tubes. We further expect that these shifts might depend on operating conditions, such as the rotational speed or temperature, since the friction force depends on these parameters.

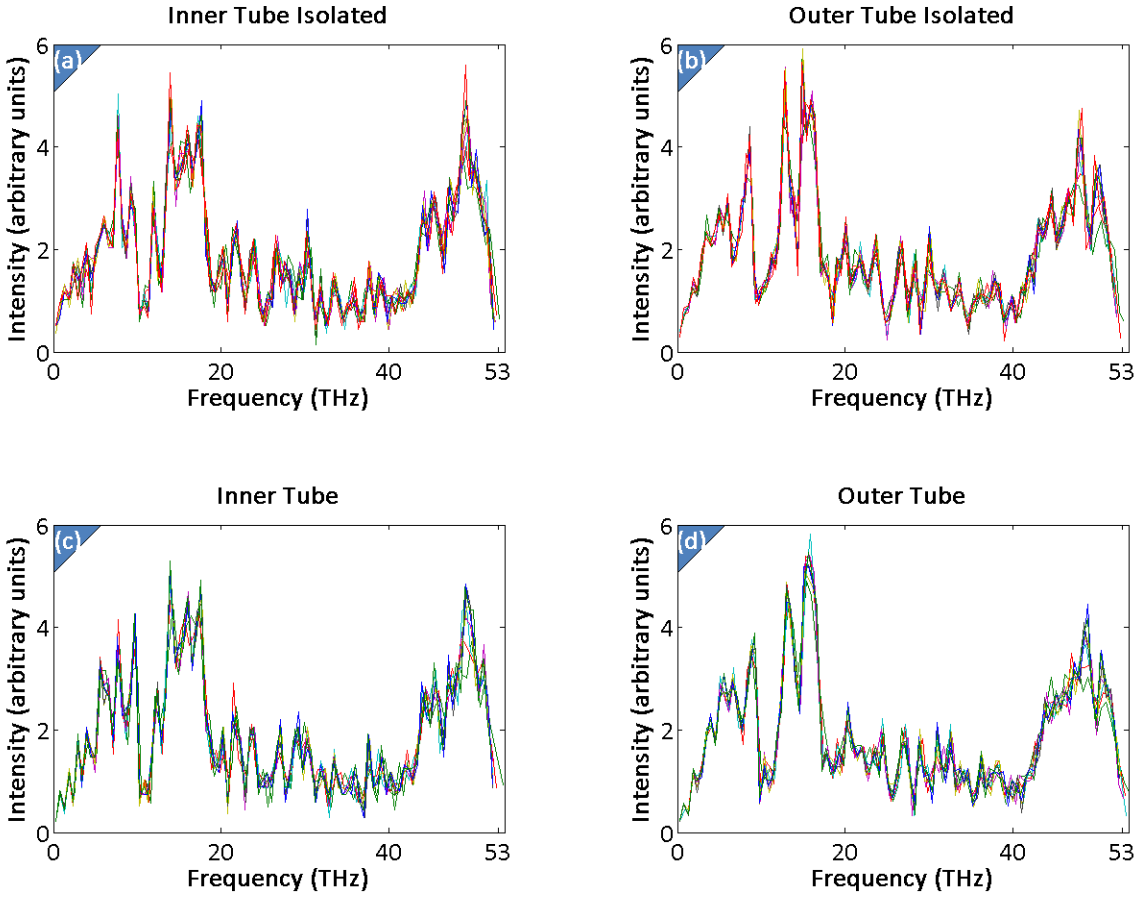

Figure 5-12: Example phonon power spectra for a (9,9) CNT within a (14,14) CNT. The top row shows the power spectrum for each tube including the interactions with the other tube, while the bottom row shows the spectrum for that tube in isolation. Each spectrum was measured 6 times, and the results are overlaid in different colors.

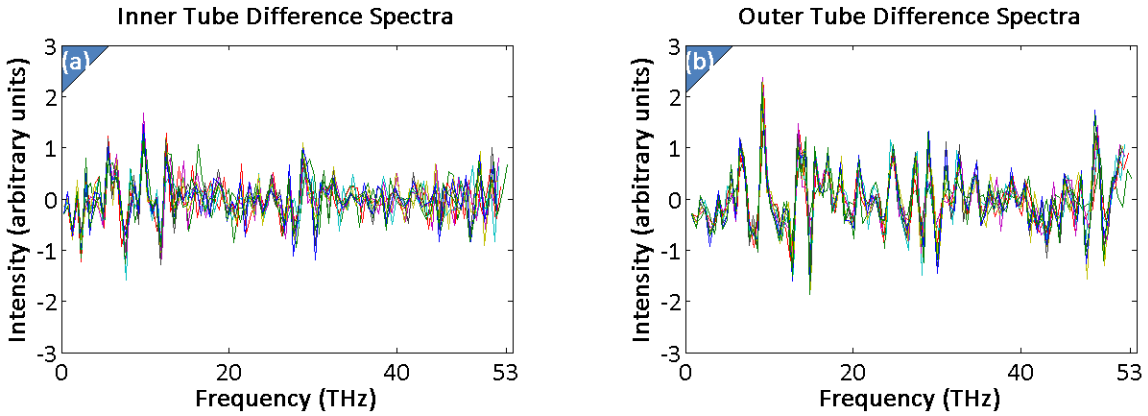

Figure 5-13: Difference spectra, showing the subtraction of the isolated tube spectra from their respective interacting spectra. Each colored line corresponds to a different integration window in the simulation, all of length 1 ns.

To establish an operating procedure for this phonon computation method, the power spectrum was computed for the baseline geometry, without rotation, at 300K. The power spectrum was also computed for each tube individually, in isolation, to determine how the interaction between the two tubes affects the phonon population. These spectra are shown in figure 5-12. At first glance, it appears that there is no significant difference between the tube spectra, when comparing the isolated tube to the tube with interactions. However, the changes in the spectrum might be highlighted by taking the difference of the two spectra. This difference is shown in figure 5-13. There are a few peaks that could potentially be identified, but still, in general, the differences are broadly spread across the spectrum. This would indicate that there are not particular phonon modes that are excited or damped more than others are, due to this simple tube-tube interaction.

While the example phonon computations for the two tubes without rotation did not highlight a particular frequency that seems to be strongly affected by the interactions, the phonon computation tool represents a new approach to examining the fundamental dynamics of the CNT system. Indeed the information that the interaction is prevalent across the broad frequency range is in itself useful for understanding the coupling of the dynamics for the two tubes; this means that the simple presence of another CNT in proximity does not substantially alter the governing dynamics of the single tube. When applied to more complex systems, including rotation, different temperatures and geometries, it is hypothesized that the spectral differences will highlight particular modes of interest; if not, then it may be the case that there is no one dominant mode, and that energy transfer in CNTs occurs by the interaction of many of the modes, i.e. at a broad range of frequencies.

To summarize, power spectra have been computed for stationary CNTs at 300 K, and compared to spectra for the same tube when interacting with an adjacent tube. The resulting difference spectra show no modes that are particularly damped or reinforced by this interaction, illustrating that interactions with adjacent CNTs alone do not qualitatively change the behavior of the CNT.

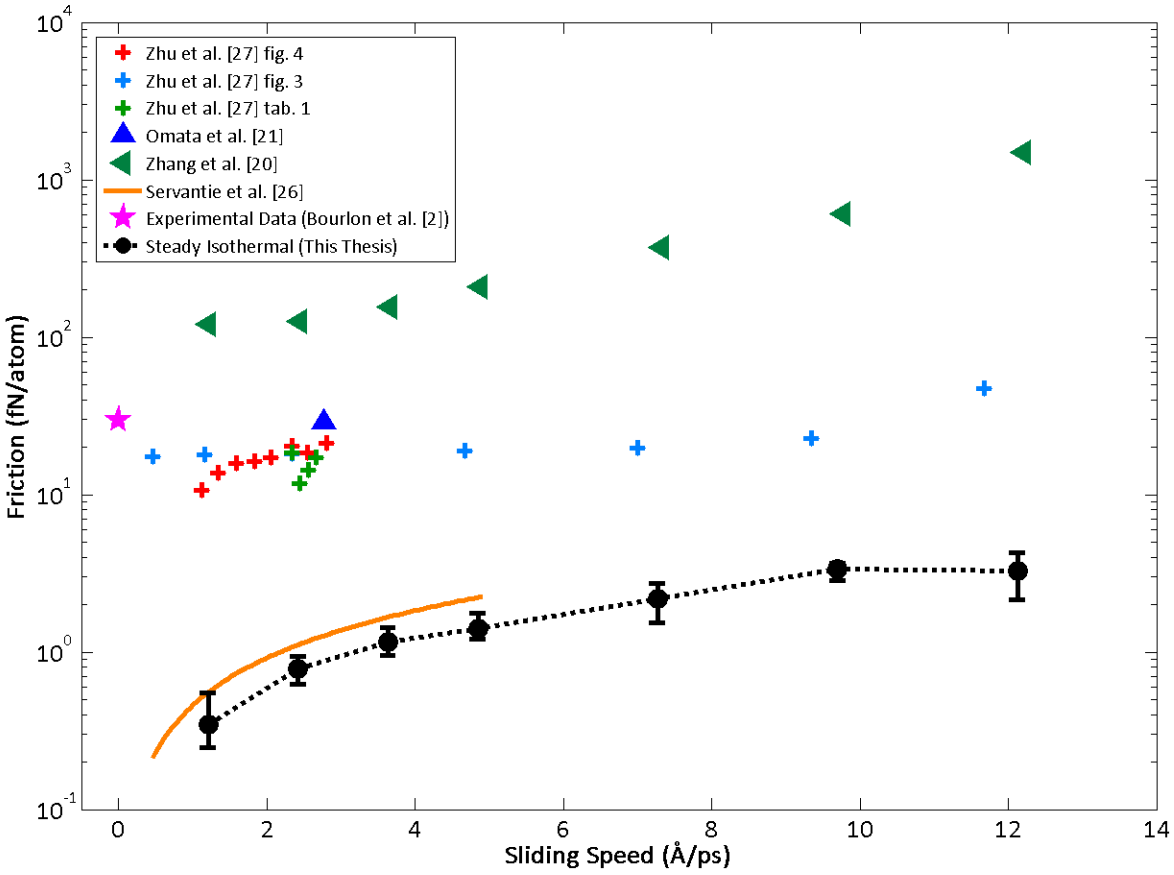

Figure 5-14: Baseline (steady isothermal) simulations compared with selected results from the literature; the baseline simulation agrees well with Servantie and Gaspard [24], which is the most recent rotational friction study.

5.3 Results

5.3.1 Comparison with Existing Literature

The first results of the baseline simulation are shown in figure 5-14, compared with the literature selected as most relevant, from section 5.1. The baseline simulation consists of isothermal constant speed simulations, set up as described in section 5.2.5.1. The dependence of friction on the speed of motion is shown.

The baseline simulation, plotted in figure 5-14, also includes error bars. These bars were derived by taking an ensemble average. Because molecular dynamics simulates the full dynamics of the system, including the random thermal velocities, it requires a random seed as an initialization parameter. Simulations run with different initial random seeds are expected to exhibit the same bulk, or average, quantities when measured. The error bars here correspond to the minimum and maximum friction measured over five runs; min-max error bars were used in order to be as conservative as possible.

The baseline simulation is in reasonable agreement with the results of Servantie and Gaspard [24], which is the lowest of the selected literature, and which also employs ensemble averaging. The baseline simulation also captures the same trend of the friction, namely a linear dependence on speed (note that

the friction in figure 5-14 is plotted on a logarithmic scale). This is remarkable, in particular because the baseline simulation is a steady state simulation, whereas the work by Servantie and Gaspard employs unsteady methods, similar to those described in 5.2.6.1.

Figure 5-15 (and a magnified version in figure 5-16) further illustrates the good agreement that can be obtained over a variety of simulation techniques. Here, the four possible simulation techniques are overlaid onto the literature result, and they all agree with each other within less than an order of magnitude, and for most of the range even within the ensemble error bars. This is much better than the three-order variation in the literature. This is an important result, because it illustrates that the variations amongst the literature results are not due to inherent differences in the physics of the CNT system depending on the simulation mode (*e.g.* steady state vs. transient, isothermal vs. adiabatic) but instead are artifacts introduced by inconsistencies in the implementations. If consistency of implementation is emphasized, as it has been in this thesis, even independent and complementary simulation methods yield the same quantitative results.

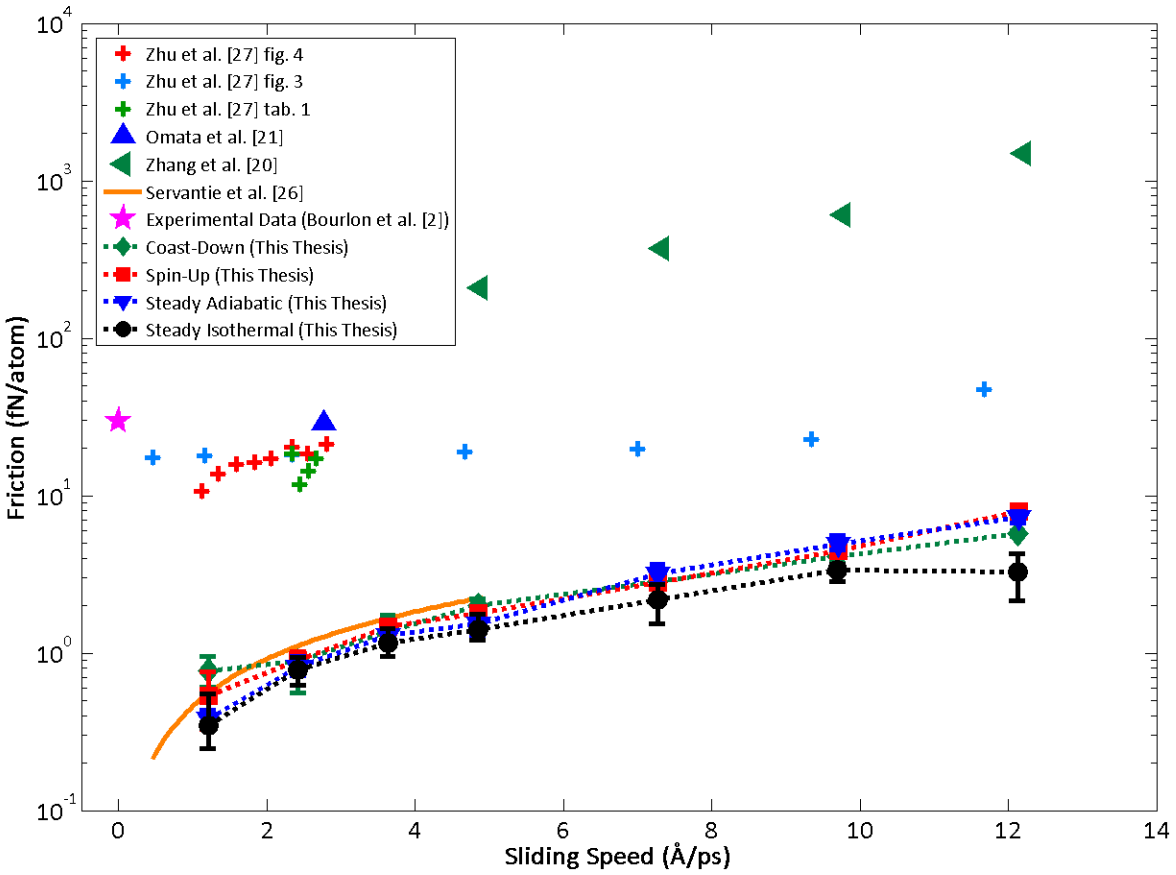

Figure 5-15: Results from all the independent simulation strategies are superimposed on the results from the literature. In the legend, "Coast-Down" (section 5.2.6.1), "Spin-Up" (section 5.2.6.2), "Steady Adiabatic" (section 5.2.5.2), and "Steady Isothermal" (section 5.2.5.1) refer to simulation type. The unsteady simulations included here employ the exponential fitting technique.

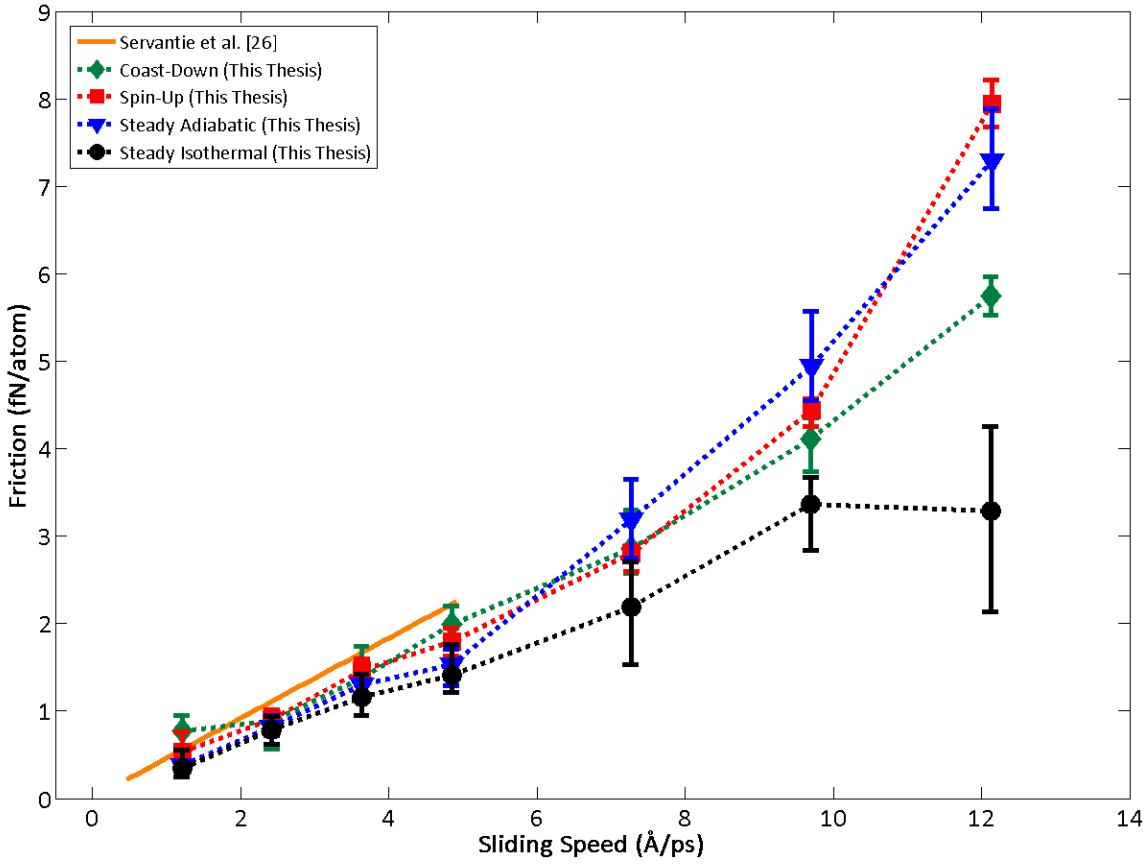

Figure 5-16: The same results are shown as figure 4-15, with a linear scale, and with some literature results removed, to better show the level of agreement between simulation types. Note that while the spin-up and steady adiabatic results appear higher at higher speeds, this can be explained by the temperature accumulation inherent in these simulations, as explained in section 5.2.5.2. The coast-down simulation experiences less temperature rise (since energy is conserved, see section 5.2.6.1), and the isothermal simulation experiences no temperature rise (since a thermostat actively regulates temperature).

However, the agreement is not perfect. The spin-up and steady adiabatic simulations result in distinctly higher friction estimates, particularly at higher speeds. This effect is caused by the temperature increase which takes place during these simulations. As discussed in section 5.2.5.2, the adiabatic boundary conditions coupled with the enforced velocity constraint on some atoms results in kinetic energy accumulating in the system, and manifesting as increased temperature. As will be shown in section 5.3.3.3, increased temperature increases the friction. Therefore, since these simulations are measuring friction at a higher average temperature than the nominal starting temperature, the friction reported is higher. The same effect applies to the coast-down simulations, but to a lesser extent; in the coast down simulation there is no velocity constraint, so kinetic energy is not being introduced to the system, and the only temperature rise is due to the existing kinetic energy due to the initial rotation being dissipated into disorderly thermal kinetic energy.

The agreement between different simulation types can be improved by taking these temperature effects into account. One straightforward method of correcting for these effects is to non-dimensionalize the friction in such a way that it scales with the temperature. This can be done on an

energy basis. Begin with the rate P at which energy is converted from orderly kinetic energy to disorderly thermal kinetic energy. The energy so converted during a single revolution of the CNT is:

$$\delta P = \frac{P}{\omega/2\pi}$$

Since the energy rate is equal to the friction power (see section 5.2.5.1), this can be written as:

$$\delta P = 2\pi \frac{P}{\omega} = 2\pi \frac{F_{\mathrm{f}} \bar{r} \omega}{\omega} = 2\pi F_{\mathrm{f}} \bar{r}$$

This energy can then be normalized by the thermal kinetic energy in the system:

$$E_{\mathrm{T}} = \frac{3}{2} N k_{\mathrm{B}} T$$

yielding

$$F^* \triangleq \frac{\delta P}{E_{\mathrm{T}}} = F_{\mathrm{f}} \frac{4\pi \bar{r}}{3 N k_{\mathrm{B}} T}$$

This non-dimensional force per atom describes how strong the friction is relative to the thermal energy present in the system; in other words, it is the fraction of the existing thermal energy that is produced by the work done by the friction force during each cycle. For the adiabatic simulations, the temperature increases during the simulation. As a rough approximation, the average temperature for the simulation has been used in the force non-dimensionalization.

The sliding speed can also be reported in non-dimensional terms. One possible normalizing factor can be derived from the inherent dynamics of the system. It is common in MD to use the Lennard-Jones unit system, which is based on the Lennard-Jones [92] potential force field. The Lennard-Jones force field, which is a simple but accurate description of the non-bonded van der Waals interactions among atoms, uses only two parameters: an energy ε characterizing the depth of the energy minimum, and a distance σ characterizing the equilibrium distance between atoms. For carbon, these parameters are [146]:

$$\varepsilon = 2.39 \text{ meV}$$

$$\sigma = 3.41 \text{ Å}$$

Based on these parameters, along with the mass of the carbon atom (2×10^{-23} g), it is possible to define units for all physical quantities. The Lennard-Jones velocity is

$$v_{\mathrm{LJ}} = \sqrt{\frac{\varepsilon}{m_{\mathrm{C}}}} = 139 \text{ m/s} = 1.39 \text{ Å/ps}$$

for carbon. As can be seen from figure 5-14, the speed ranges accessible via simulation are of comparable order, so this will make a suitable non-dimensionalization factor:

$$v^* \triangleq \frac{\bar{r}\omega}{v_{\mathrm{LJ}}}$$

For comparison, the average thermal velocity, defined via kinetic theory to be

$$\bar{v}_{\mathrm{T}} = \sqrt{\frac{3k_{\mathrm{B}}T}{m_{\mathrm{C}}}}$$

is 789 m/s = 7.89 Å/ps for carbon at 300 K.

A Lennard-Jones force can also be defined:

$$F_{\mathrm{LJ}} = \frac{\varepsilon}{\sigma}$$

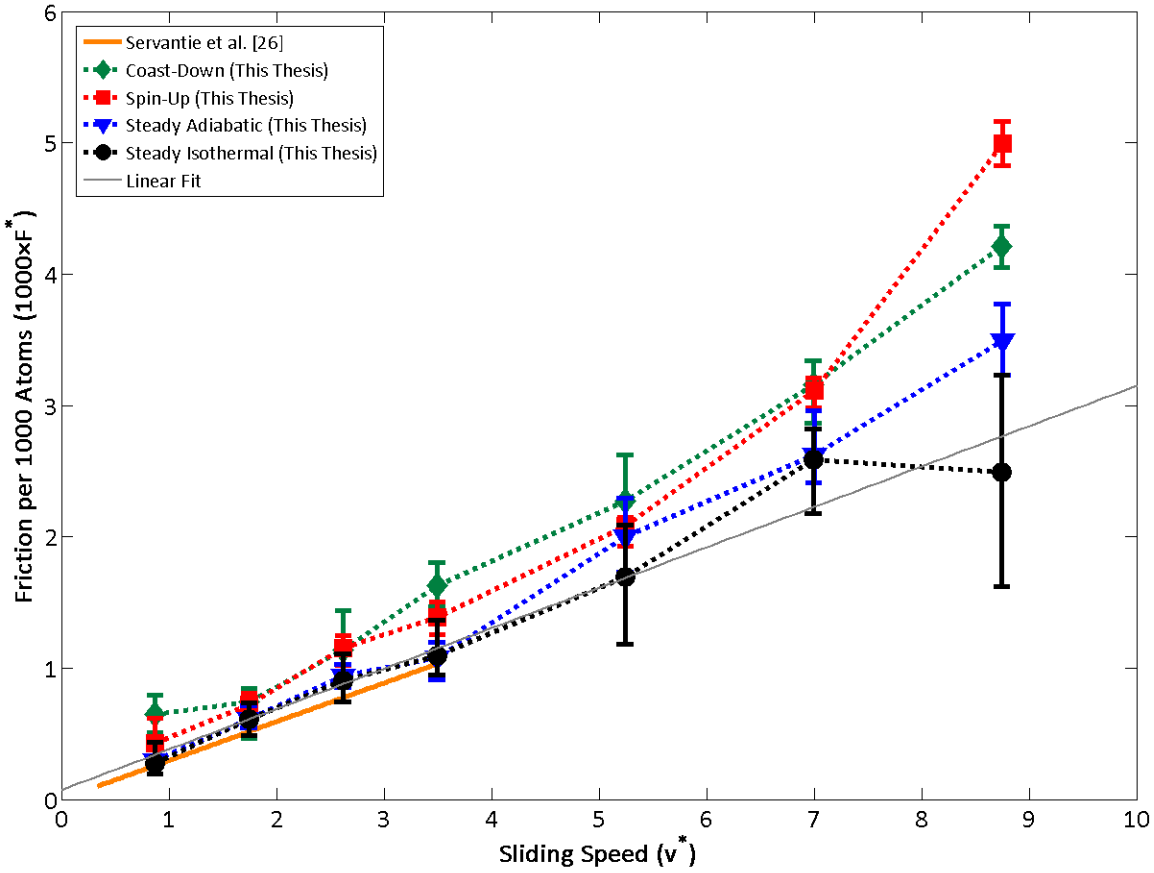

Figure 5-17: When non-dimensionalized by the thermal kinetic energy the dependence of friction on sliding speed is in excellent agreement across a range of simulation styles, particularly for low speeds. The grey line is a least squares linear fit of the isothermal steady simulations.

which is 1.12 pN for carbon. (For reference, 1 pN is approximately the weight of one typical cell [147].) Note that the friction forces (as seen in figure 5-14) are several orders lower than this force, which is a characteristic strength of non-bonded van der Waals interactions, and is itself much weaker than bonding forces. The friction is therefore very low compared to all other interactions in the system; this has been one of the main reasons that its measurement has been so difficult.

When applying the non-dimensionalization factors to the friction results, even better agreement is obtained, as shown in figure 5-17, since the average temperature used to non-dimensionalize the adiabatic simulation results is the measured average temperature, which is higher than the nominal or initial temperature. In this way, the non-dimensionalization corrects for the temperature effects inherent in these simulations; this is particularly evident when comparing the two (isothermal and adiabatic) steady simulations.

One of the primary goals of this thesis is to establish the governing principles for friction in the CNT system. Part of that is the ability to express analytical relationships between friction and the various parameters on which it depends. So far, friction has been plotted as a function of speed; we begin therefore with the dependence of friction on the speed of the contact. For the unsteady simulations, the dependence of friction on velocity needed to be implicitly specified *a priori* (see section 5.2.6) in order to fit the angular momentum evolution; friction independent of speed was assumed for a linear fit, and friction directly proportional to speed was assumed for the exponential fit. However, we would like to determine the relationship without making these assumptions *a priori.* To that end, we must use the steady-state simulations. These are the only simulations in which the speed is held constant for the entire simulation, and hence for which the friction is truly measured at a particular speed. Furthermore, we expect that friction will depend on temperature; since the steady state isothermal simulations are the only ones that control temperature for the simulation duration, the fit will be based on these results.

Examination of the steady isothermal simulation curve in figure 5-17 suggests a linear dependence, consistent with the assumptions made in the unsteady simulations reported here, as well as by Servantie and Gaspard [24]. A fit of the baseline simulations yields the relation

$$F^* = A(v^*) + B$$

with the dimensionless coefficients being:

$$A = 4.62 \times 10^{-2}, \;\; B = 1.08 \times 10^{-2}$$

This fit is plotted in figure 5-17, and always falls within the error bars, capturing the general trend.

Figure 5-18 compares the various fitting techniques for the transient simulations; the apparent differences in these results can be explained by known limitations of the simulation styles. As discussed in section 5.2.6.1, the angular momentum evolution of the CNT for transient simulations can be fit by either a line or an exponential; the linear fit is known to underpredict the friction for longer simulations, because the average speed at which friction is measured is lower than the nominal speed, yielding a lower friction value. Indeed these results are the lowest. Likewise the exponential fit should be the most accurate, and these values (the ones used in figure 5-15, figure 5-16, and figure 5-17) are also closer to the baseline – they even agree well with Servantie *et al.* [24] who used the same exponential fitting procedure. Even further agreement is possible among different friction measurement techniques applied to the same simulation; the momentum and energy methods yield identical results for the spin-

up simulation, and the friction measured from the inner and outer tubes also match for the coast-down simulation.

In summary, the initial simulation results demonstrate that the wide variation reported in the literature can be reduced by carefully controlling all the relevant parameters, from several orders of magnitude to less than one order. The remaining spread is explained by considering the known sign of the deviation for the three adiabatic simulations (due to the temperature rise), and can be partially corrected by non-dimensionalizing the force with the thermal energy. Finally, a simple relation between the speed of rotation and the friction force has been proposed, based on the constant-speed friction simulations. This new result, namely the ability to achieve agreement in quantitative estimates for the CNT friction from completely independent simulations employing different simulation strategies, is important for building confidence in the simulations. It demonstrates that it is critical to control all relevant parameters in the simulation and ensure a consistent implementation; if the implementations are consistent, the result is independent of the measurement technique, as it should be. If the implementations are inconsistent, as the various results from the literature are, the result depends more strongly on the implementation parameters than on the actual physical parameters, leading to several orders of magnitude variation in the predicted value of friction.

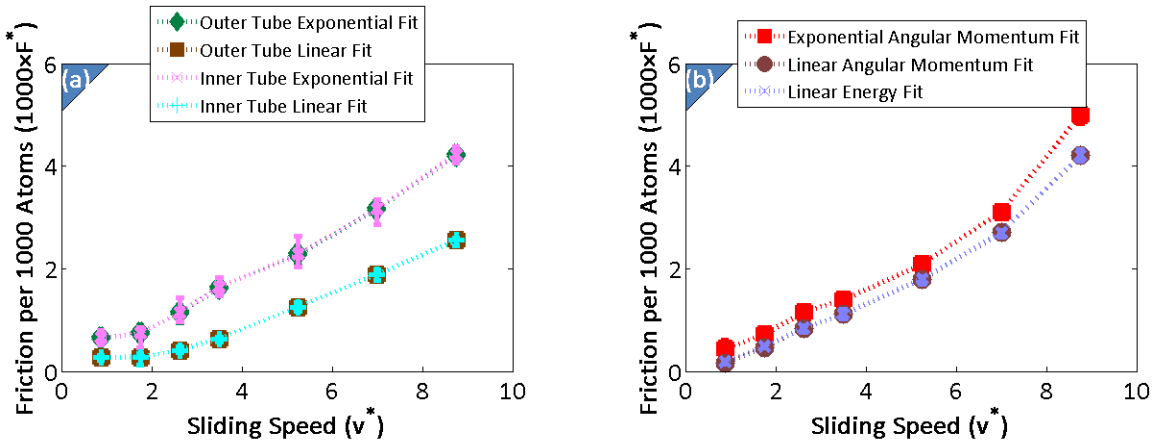

Figure 5-18: The linear and exponential fitting techniques for the coast-down (a) and spin-up (b) simulations are compared. For the coast down, only angular momentum can be fit; the results agree well for the inner and outer tube. For the spin-up, the total energy method can also be used, and agrees with the linear angular momentum fit. In both cases, the linear method underpredicts the friction, for reasons described in section 5.2.6.1.

5.3.2 Phonon Speed Dependence

We would also like some insight in to the reason that the friction depends on speed. For that purpose, phonons have also been computed for spinning tubes in the adiabatic constant velocity experiment. Figure 5-19 shows these computed spectra, and figure 5-20 shows the same spectra with the component from a still tube subtracted off. In order to confirm that the integration length for these spectra (chosen to be 1 ns, as is used prior literature [142]) is sufficiently long that it captures a representative sample, two techniques were employed. First, the spectra were computed many times in a simulation, with integration windows starting at different times (but always of length 1 ns). These are shown as the different colored traces in figure 5-19 and figure 5-20. They clearly agree, indicating that the result is stable and independent of the time at which it was measured (as it should be for a steady state simulation.) Additionally, a shorter integration window (0.1 ns) was attempted; figure 5-20 shows that the two integration windows give matching results, indicating that both window sizes are adequately long.

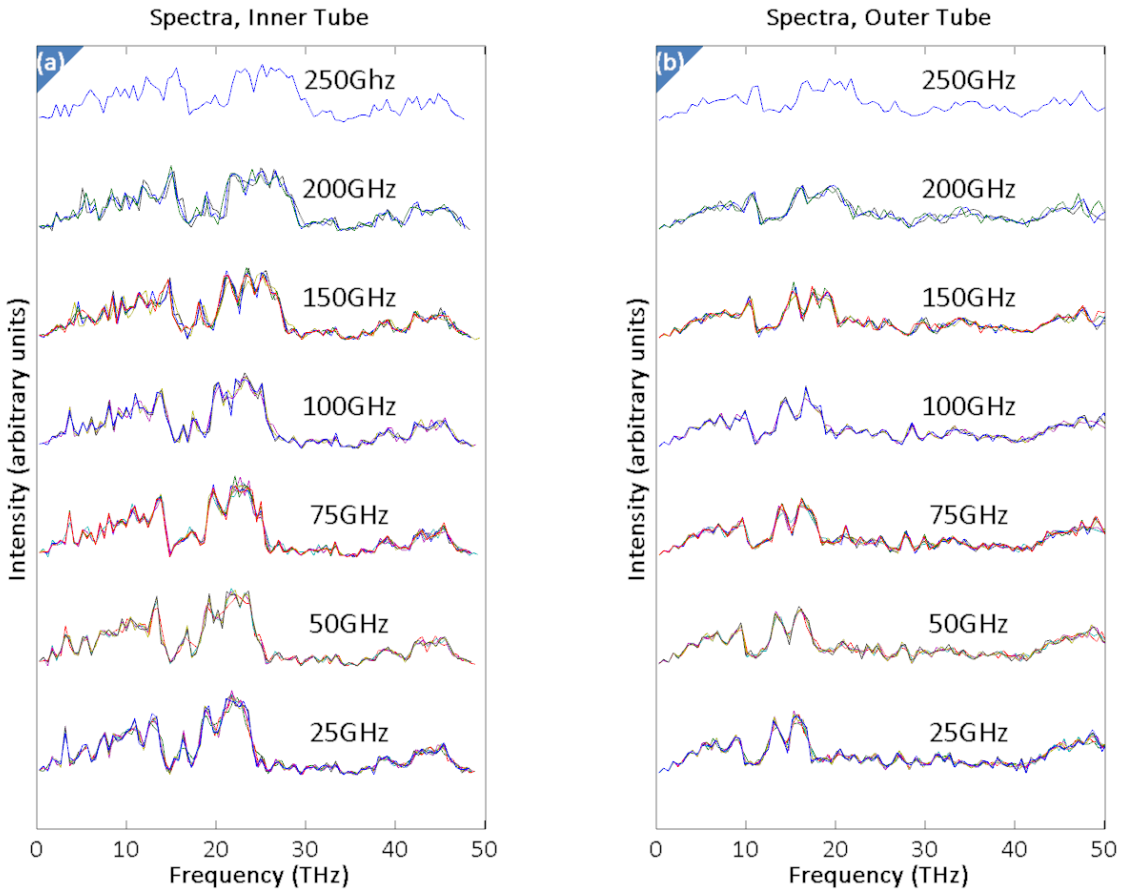

Figure 5-19: The dependence of the phonon spectrum on sliding speed is examined for the adiabatic constant velocity simulation. The labels indicate the rotational speed for which that spectrum was computed, and each colored line represents a different integration window, each of length 1 ns. Units have been omitted from the y-axis because the units are arbitrary (the spectra were normalized to unit area) and spectra have been shifted vertically for ease of comparison. The frequency ranges that are most active during rotation are visible as plateaus of elevated intensity, at about 10-14 THz and 20-25 THz (the intensity between about 25-40 THz is nearly zero.)

The spectra differences give insight into which modes are most excited during rotation. Most of the action occurs in the neighborhood of 10-25 THz for both the inner and the outer tube, with especially strong differences between 18 and 25 THz. While these "mesas," comprising frequency ranges, do not identify individual modes, they are helpful in showing what frequency ranges are most affected by rotation. Additionally, with increasing rotation speed, some of the energy within the 17-25 THz range shifts to slightly higher frequencies, while energy in the 10-13 THz range shifts to lower frequencies. We can also detect a broadening of the distribution of affected frequencies as rotation speed increases. At 25 GHz, the right group of frequencies is almost square (most evident in the inner tube spectra) while it becomes much smoother at higher speeds. This result would seem to indicate that the interaction between tubes is even less confined to a particular mode, and more broadly distributed for faster rotation. The change in shape of this group becomes more pronounced at about 100 GHz; this corresponds to the point where temperature increase due to energy accumulation in the adiabatic simulation becomes more apparent; the same effect is manifested as an increased slope for the adiabatic case in figure 5-16 (blue triangles) at about 100 GHz. The inner tube also exhibits a clear decay in the upper frequency range, indicating that these high-frequency phonons are suppressed by the rotation.

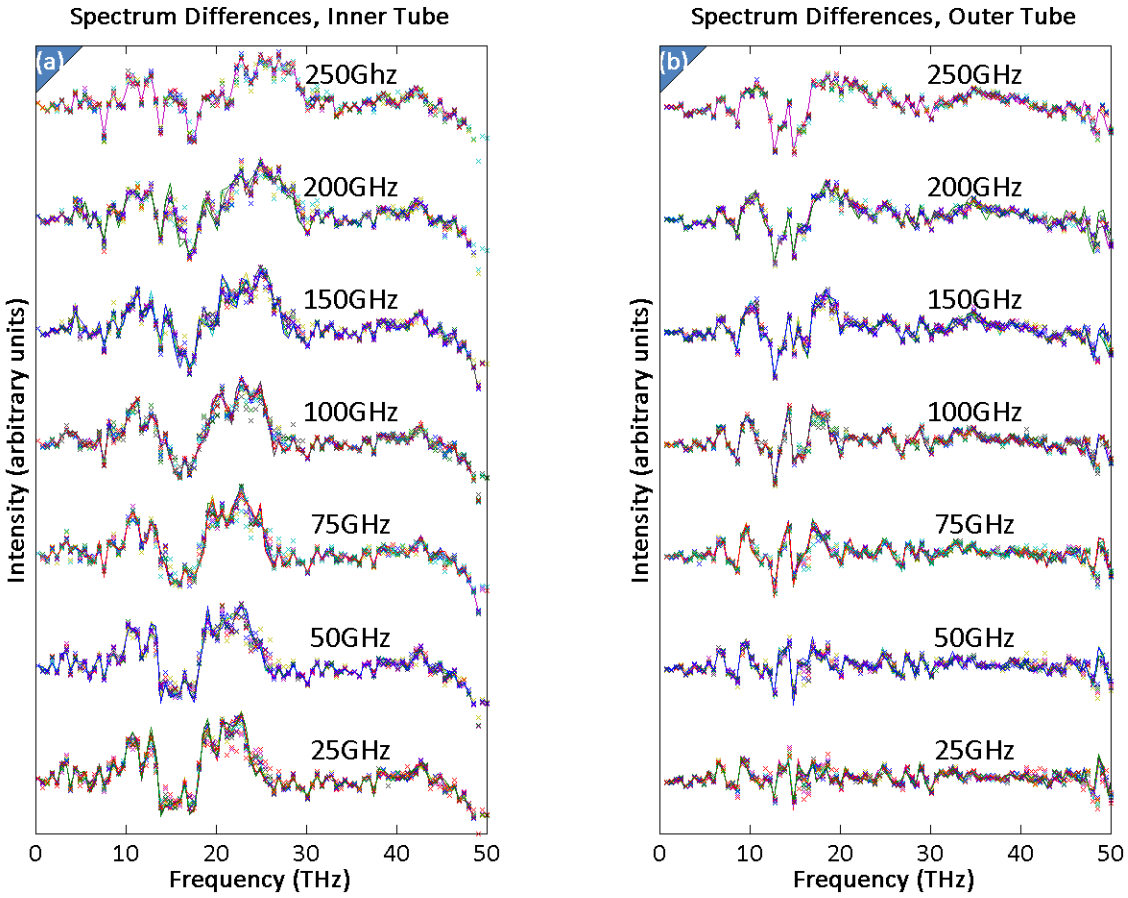

Figure 5-20: The spectra of the rotating CNTs, with the spectrum of a still tube subtracted off to highlight the differences. The labels correspond to the rotational speed at which the spectra were measured. Each different colored line corresponds to a different measurement interval, of length 1 ns (lines) or 0.1 ns (x's). The agreement between different lines as well as x's and lines indicates that the integration parameters are of adequate resolution. Two regions in which there is a lot of phonon activity (9-13 THz and 17-25 THz) are visible, especially in the inner tube.

5.3.3 Parametric Studies

As discussed in section 2.2.2.3, the significant differences in estimated friction values among the literature reports is partially due to differences in the underlying parameters of the simulations, and in some cases a lack of control over or measurement of these parameters. In order to be able to accurately predict the friction in the CNT bearing, it is necessary to control all the parameters that influence that friction. To that end, the simulations reported here employ techniques to ensure that each parameter is controlled as well as measured, so that the results are consistent and comparable.

It is important also to go further, to identify the dependency of the resulting friction measurement on the parameters of interest. Some parameters may not have a strong influence, implying that tight control over them is not as critical; others may be more important. Identifying the functional dependence is also useful where possible, in order to allow corrections to be made, or for eventual applications, to tailor the properties of the CNT bearing to optimize the performance. Therefore, an array of simulations (listed in table 5-4) have been performed, testing the dependence of the friction on the parameters that are expected to have an influence.

Table 5-4: Parameters investigated for their effects on CNT friction

Parameter	Range Investigated	Effect on Friction	Discussed in section
Speed	25 – 250 GHz (v^* between 1 and 9)	Friction varies proportionally with speed	5.3.1
Temperature	150 – 450 K	Friction varies proportionally with temperature	5.3.3.3
Tube Length	6 – 24 nm	Increased variability as length increases because of tube softening	5.3.3.4
Tube Interface Radius	0.439 – 0.772 nm	None in that range	5.3.3.5
Inter-Tube spacing	0.319 – 0.337	Friction increases with decreased spacing	5.3.3.5
Chirality	(4,4)/(9,9), (15,0)/(23,0) (9,9)/(14,14), (9,9)/(22,4)	None observed	5.3.3.5
Simulation Technique (Boundary / Initial Conditions)	Steady Isothermal Steady Adiabatic Coast-Down (Adiabatic) Spin-Up (Adiabatic)	None at speeds below 100 GHz; above 100 GHz friction increased for adiabatic simulations due to temperature increase	5.3.1
Averaging Implementation	Downsampling factor 50 – 500	None in that range	5.3.3.1
Thermostating Implementation	None (Adiabatic) Nosé-Hoover [137, 138] Berendsen [148] Langevin [149]	None for Nosé-Hoover or Berendsen, artificially inflated friction for Langevin, temperature effects increase friction for adiabatic case above 100 GHz	5.3.3.2

5.3.3.1 Averaging Effects

It is first of critical importance to ensure that the simulation is running properly, and that measurement artifacts from the numerical implementation do not have a substantial effect on the results. One possible mechanism for the numerical scheme to affect the results is the averaging system. Because the simulations can run over as many as 10^9 timesteps, it is impractical to record data at each timestep. Furthermore, the simulation can experience fluctuations in bulk properties, stemming from the random thermal motion of the atoms. It is therefore necessary to average the data over a suitable window, to report the data with a lower sample rate.

The default averaging technique for this work was to average every 50 timesteps worth of data; *i.e.* the downsampling factor was 50. Other averaging schemes were also used, and their results compared with the default, in order to ensure that the averaging scheme did not influence the friction value. As shown in figure 5-21, increasing the averaging by a factor of 10 did not affect the results significantly; the curves and error bars almost overlap, indicating that the averaging scheme used in the baseline is adequate.

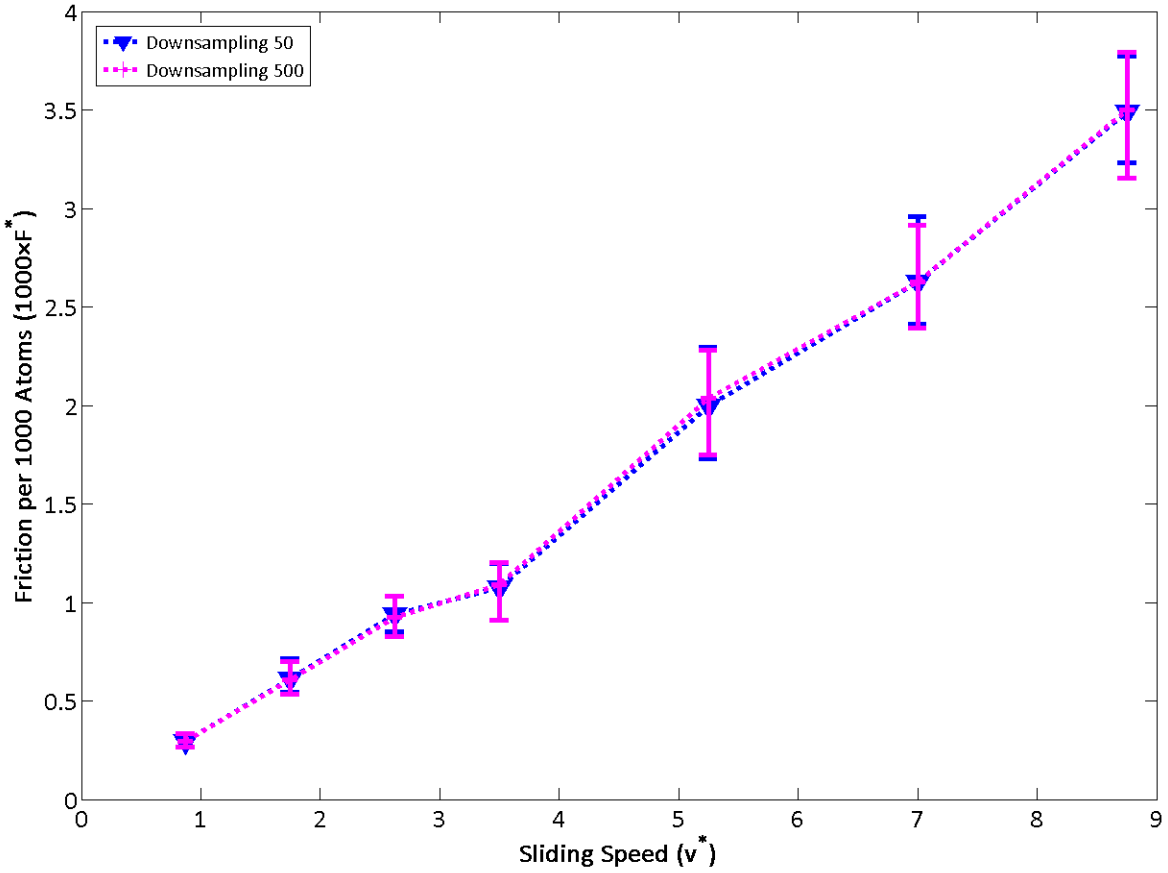

Figure 5-21: Changing the averaging scheme does not affect the friction measurement. Shown is the baseline adiabatic steady simulation, which averages 50 timesteps, and additional adiabatic steady runs averaging 500 timesteps.

5.3.3.2 Thermostat Effects

Another possible mechanism whereby the results could be modified in a non-physical way is in the thermostating. While the adiabatic simulations do not employ a thermostat, the other steady state simulations do (see section 5.2.5) in order to maintain a constant temperature and to allow energy to pass out of the system as heat. These thermostats achieve the required temperature changes by directly altering the velocities of atoms within the simulation. This is not something that actually happens in nature, but rather an artificial way if imposing a constant temperature boundary condition. Thermostats can therefore introduce unwanted effects if not used properly.

In order to ensure that the thermostats employed here are not unduly affecting the results, simulations have been conducted using several different thermostats. The first thermostat used is called a Langevin thermostat [149, 150]. It employs two fictitious forces to influence the velocities. One is a drag or damping term proportional to the particle's velocity, that is, a force on each atom opposing the atom's motion. This tends to smooth out the random velocities. The other term simulates a fluid at the desired temperature bumping into the atoms to be controlled. This force has a maximum magnitude

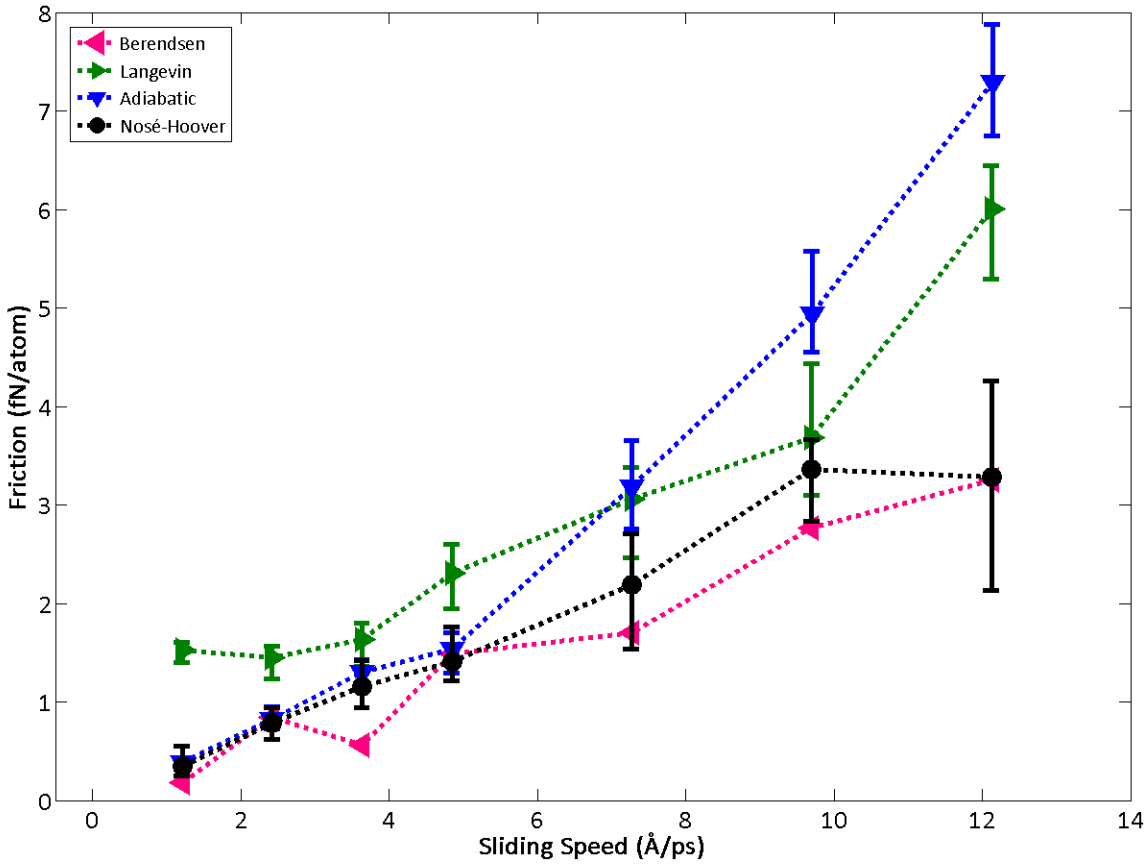

Figure 5-22: Comparison of various thermostating techniques with the baseline (unthermostated, adiabatic) simulations. The Langevin thermostat consistently over-estimates the friction, while the Berendsen and Nosé-Hoover thermostats agree well.

$$F_{\text{solvent}} = \sqrt{\frac{k_B T_0 m_C}{\alpha \delta t}}$$

where k_B is the Boltzmann constant, T_0 is the desired temperature, m_C is the atom's mass, α is a coefficient governing the strength of the thermostat, and δt is the simulation timestep. The magnitude of the forces is randomly distributed uniformly over the range from zero to this magnitude, and the direction is uniformly distributed in space. Thus, this thermostat gradually changes the velocity of each particle by reducing its magnitude and re-adding additional magnitude based on the desired temperature distribution.

A second type of thermostat is called a Berendsen thermostat [148]. This thermostat is relatively simple, and works by directly scaling each particle's velocity by the factor

$$\lambda = \sqrt{1 + \alpha \delta t \left(\frac{T}{T_0} - 1\right)}$$

after each integration step. Here T is the measured temperature of the particle; thus, no scaling is applied if the temperature is already correct.

The final type of thermostat employed is called a Nosé-Hoover thermostat [137, 138, 151]. This method works by modifying Newton's equations of motion, introducing an extra degree of freedom, denoted s and representing a reservoir of energy. The modified equations of motion are then:

$$m_i \frac{d^2 \vec{r}_i}{dt^2} = \vec{f}_i - s m_i \frac{d\vec{r}_i}{dt}$$

$$\frac{ds}{dt} = \frac{k_B g}{q}(T - T_0)$$

where m_i and $\vec{r}_i$ are the mass and position, respectively, of each atom, g is the number of degrees of freedom, and q is some "mass", which controls how aggressively the reservoir absorbs or releases energy (similarly to the timescale parameters for the other thermostats). The energy of the real system can thus change, by exchange with the reservoir. This method, while not physically accurate, has been shown [152] to produce trajectories which approximate the distribution that would be expected in a constant temperature situation, for equilibrium or quasi-equilibrium processes.

Figure 5-22 gives a comparison of the three different thermostat styles with the adiabatic simulations. Recall that the adiabatic simulations do not employ a thermostat, as discussed in section 5.2.5. The data show that the Berendsen and Nose-Hoover thermostats agree to within the error bars over the entire range, and further agree within the error bars with the adiabatic simulations for the lower speed range. This indicates that these two thermostats have a negligible influence on the dynamics of the system (at least compared to the measurement precision), and the measured friction can be independently confirmed. The deviation between the adiabatic simulations and the thermostated simulations at high speeds can be attributed to temperature effects. At higher speeds, the amount of thermal energy that builds up during the simulation is substantial due to the high friction, and the temperature actually increases significantly during the simulation, causing the friction to

increase. (This effect is discussed also in section 5.2.5.2.) In these cases, the thermostated simulations should be considered more accurate, as they control the temperature at a constant value.

It is however troubling that the Langevin thermostat does not give similar results to the other two thermostats. When used, the Langevin thermostat causes the friction to be consistently high. The apparent increase in friction is likely a result of the fictitious damping term introduced by the Langevin thermostat; this term causes additional energy to be removed from the simulation at each time step, beyond that dissipated by the friction. The other thermostat results should therefore be considered more accurate; that is the reason the Nosé-Hoover thermostat was used for the baseline and all other simulations.

5.3.3.3 Temperature Effects

Figure 5-23 illustrates the effect of temperature on the friction. Three cases, thermostated at 150K, 300K, and 450K are shown; these use the Nosé-Hoover thermostat to regulate the temperature. Temperature does significantly influence the magnitude of the friction. The effect is intuitive; for higher temperatures, the atoms are vibrating randomly with higher amplitudes, making it easier for atoms to

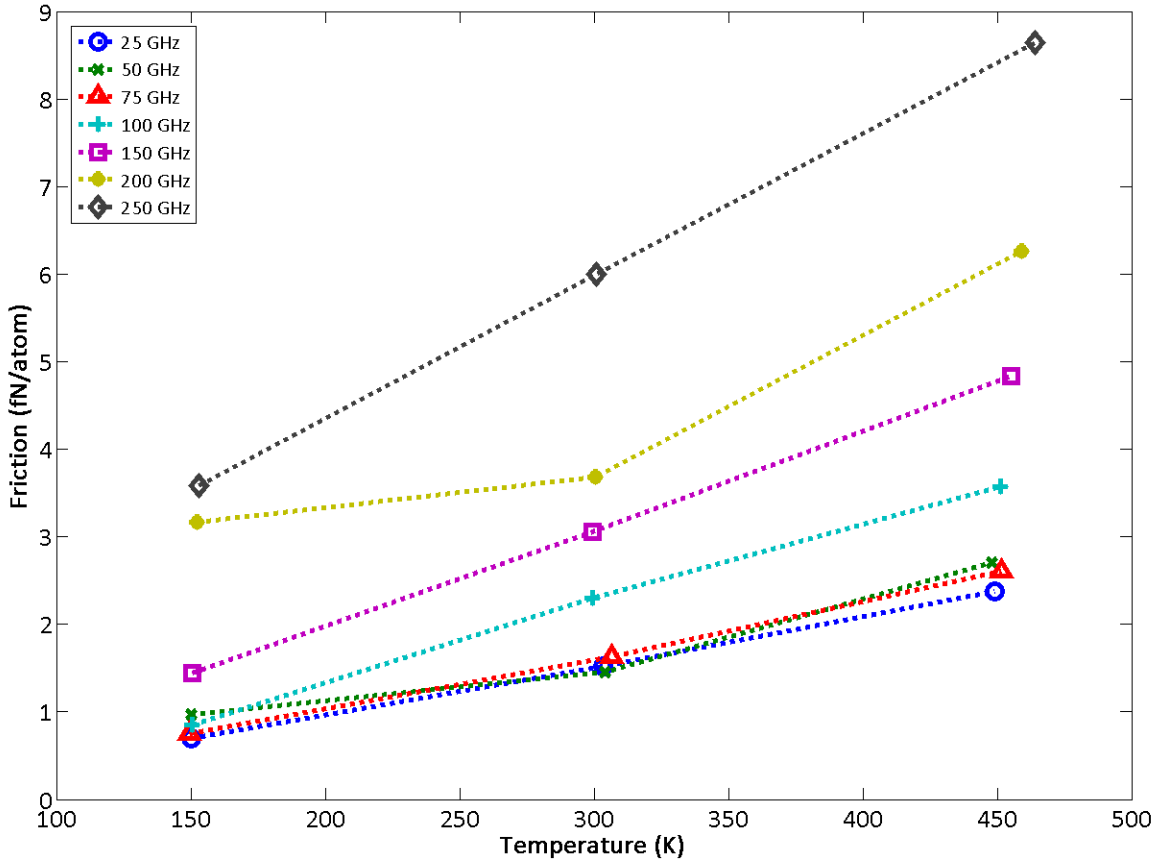

Figure 5-23: Dependence of friction on simulation temperature. These steady isothermal simulations use a Nosé-Hoover thermostat to regulate the temperature

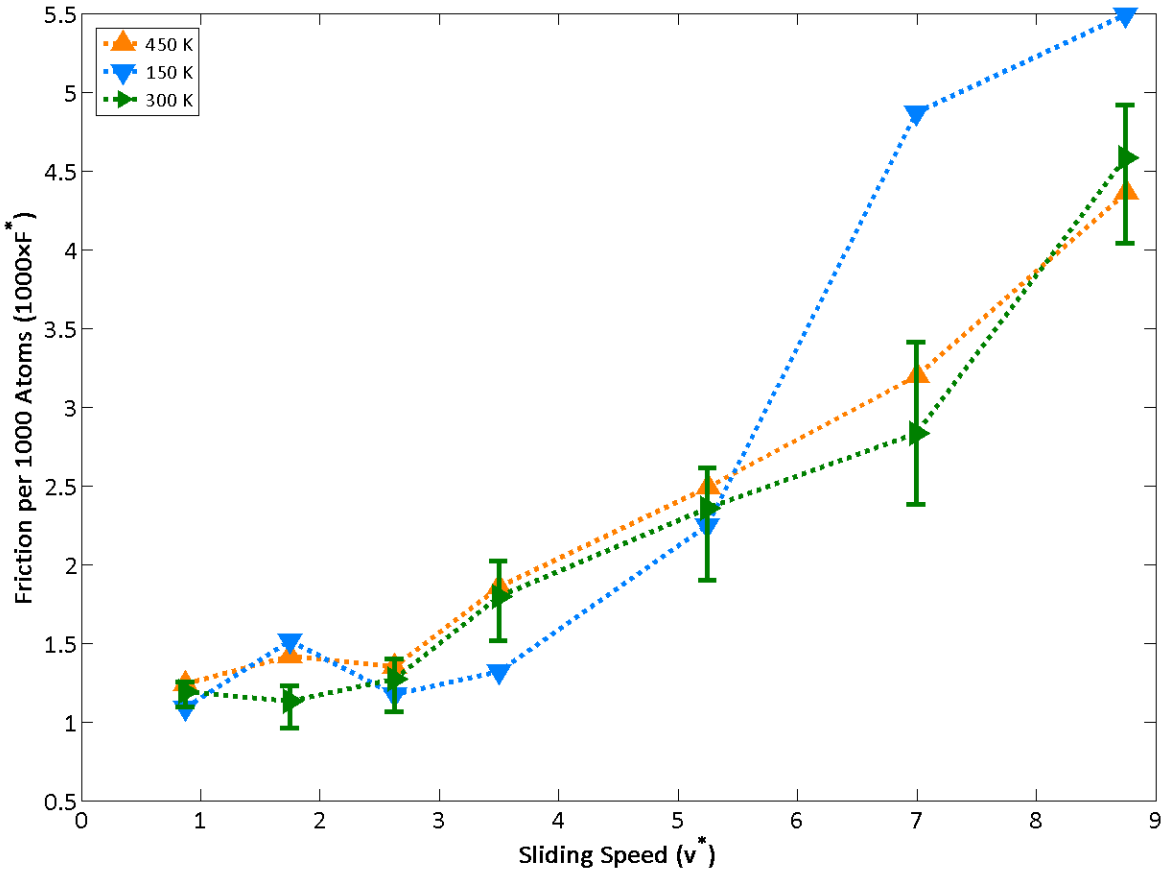

Figure 5-24: Non-dimensionalization of the friction by the thermal energy captures the linear dependence of friction on temperature, allowing simulations at different temperatures to be collapsed onto a single resulting trend.

collide during rotation, transferring their orderly kinetic energy into increased temperature. Based on the plot, the dependence of friction on temperature appears approximately linear. This linear dependence of friction on the temperature is the reason that friction has been non-dimensionalized by a factor that varies linearly with temperature (specifically the thermal energy, see section 5.3.1); doing so allows results from different temperatures to collapse onto a single trend. Indeed, this is illustrated in figure 5-24, where the same data has been plotted as a function of speed, with the non-dimensionalization applied.

5.3.3.4 Length Effects

Length can also be a factor in determining the friction in the CNT bearing. Of course, increased length will lead to increased overall friction torque because the contact area is increased; however, the data here are reported as friction per atom, so since the number of atoms is also proportional to the length we would not expect a change in friction for CNTs of different lengths.

When thinking about the length of the tube, it is useful to non-dimensionalize by the persistence length. The persistence length is a measure of the stiffness of the CNT in bending; tubes longer than the persistence length behave more like strings – they are very compliant and cannot be treated with beam theory. On the other hand, tubes shorter than the persistence length will tend to be stiffer and more

amenable to beam theory. (For example, a typical construction girder, having American Society for Testing and Materials (ASTM) A6 standard cross-section S20x96 and made of steel with modulus Y = 200 GPa [153], has a persistence length of 3×10^{28} m at room temperature, and realistically long construction beams are well modeled by beam theory.) The persistence length is given by:

$$\ell_{\mathrm{p}} = \frac{YI_{yy}}{k_{\mathrm{B}}T}$$

For our nanotubes, we take Y = 1.2 TPa [122] and

$$I_{yy} = \frac{\pi}{4}\left[\left(r_2 + \frac{h}{2}\right)^4 - \left(r_2 + \frac{h}{2}\right)^4\right]$$

where h is the inter-wall spacing of 0.34 nm. For the baseline geometry of a (9,9) tube inside a (14,14) nanotube, this works out to I_{yy} = 1.16×10^{-36} m^4 and p_ℓ = 337 μm. Note that none of the nanotubes studied here approach the persistence length, so the beam approximation should always be valid. Nevertheless, as the length increases, the stiffness of the beam decreases and deflections in the transverse direction can be expected to be larger.

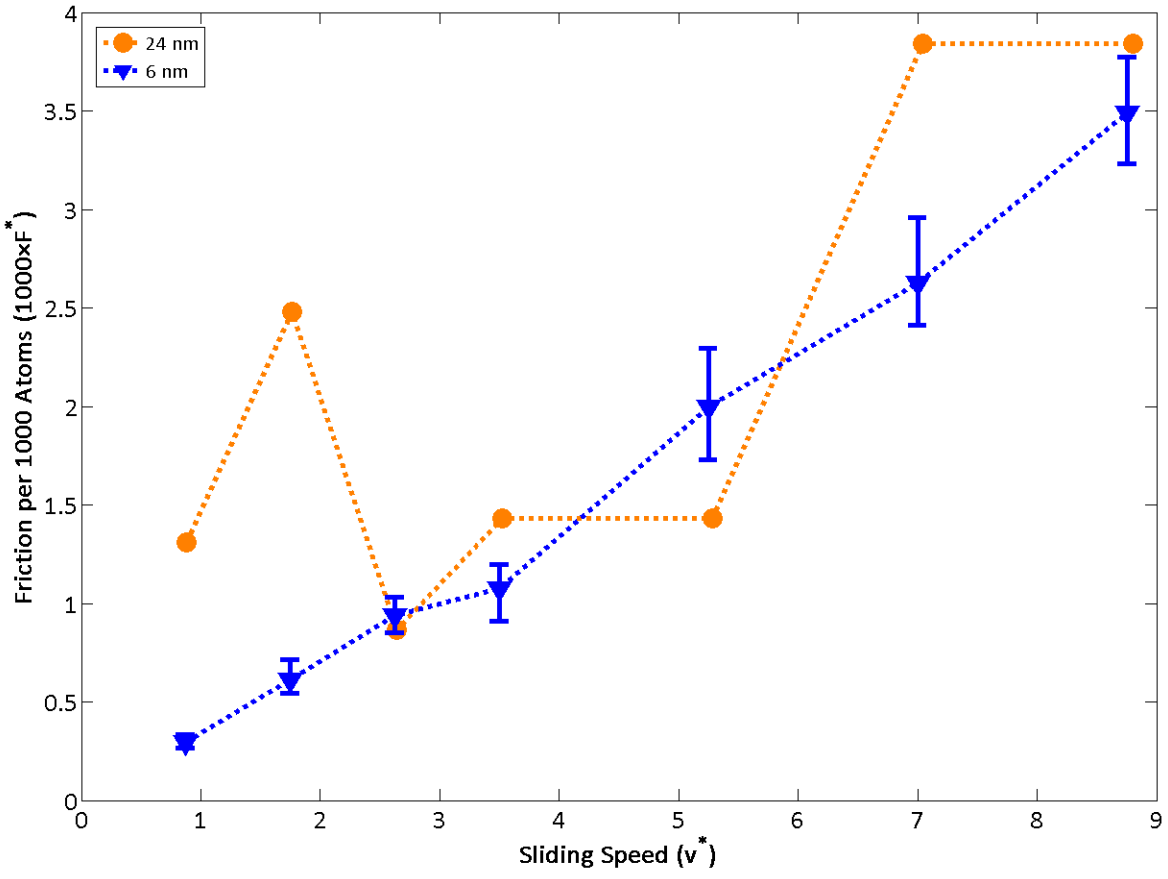

Figure 5-25: Tubes of two different lengths are shown. The Baseline tubes are approximately 1.7×10^{-4} times the persistence length, and the longer tubes are and 7.1×10^{-4} times the persistence length.

As expected, the data in figure 5-25 show that the length does not substantially affect the mean friction value. However, the variability from run to run is drastically increased, as a direct consequence of the reduced stiffness of the beam as its length increases. The more compliant beam can deflect more, and its bending modes (which are randomly excited by the thermal fluctuations) make up a more significant contribution to the friction.

For applications of the CNT bearing, the desired CNT will need to be orders of magnitude longer than those used in simulation, as discussed in section 6.2.2. This might initially seem to indicate that the CNTs would cross over the persistence length threshold and be untenably flexible. However, it is important to recognize that these CNTs will also likely be much thicker than the simulated tubes, with many more walls, drastically improving bending stiffness, and hence increasing the persistence length. Furthermore, in applications, the CNTs will need to be attached to other materials; in the example of the rotor discussed here, the CNT is encased in a thick polysilicon rotor, and unable to bend for a large portion of its length.

5.3.3.5 Chirality Effects

Chirality is a unique property of CNTs, which describes the helical angle at which a graphene sheet must be rolled in order to produce a given CNT. The chirality can be completely described by two numbers, called the chiral indices, denoted (m, n). Detailed descriptions of how the chiral indices determine the CNT geometry are readily available [3, 139]. It has been hypothesized that the chirality may affect CNT friction [13, 20, 24], because the ridges in the energy landscape (visualized in figure 5-3) may interlock more easily when the threads of the two tubes align. Additionally, the chirality of tubes tested has varied amongst the friction reports in the literature, and may contribute to the variation in reported friction values. For that reason, the friction in CNT systems of different chiralities was simulated. Four different chiralities were chosen, based on the four chiralities used in the literature studies [20, 21, 24, 27] selected as most relevant (see section 5.1.) These four chiralities are listed in table 5-5, and the results of the corresponding friction simulations are illustrated in figure 5-26.

When considering chirality, however, there are two complicating factors that must be considered. Because the chirality completely specifies the CNT geometry, the radius of a given CNT is also known based on the chirality, and can be estimated directly from the chiral indices (see section 5.2.5.1). For a DWNT, that means that both the interface radius $\bar{r}$ and the inter-tube spacing are determined by the chirality. Care must therefore be taken to isolate the effect of chirality alone from the effects of CNT interface radius and spacing. The interface radius and spacing for the chiralities used are recorded in table 5-5, based on measurements from the simulations (as described in section 5.2.5.1).

Table 5-5: Comparison of CNT geometries used in the literature

Inner Tube	Outer Tube	Inner Tube Radius (nm)	Outer Tube Radius (nm)	Interface Radius (nm)	Spacing (nm)	Investigated By
(4,4)	(9,9)	0.2733	0.6055	0.4394	0.3322	[21, 24]
(15,0)	(23,0)	0.5795	0.8984	0.7390	0.3189	[27]
(9,9)	(14,14)	0.6034	0.9398	0.7716	0.3363	[20]
(9,9)	(22,4)	0.6035	0.9404	0.7719	0.3370	[20]

Radii were measured from the simulations, not estimated from chiral indices, or taken from literature.

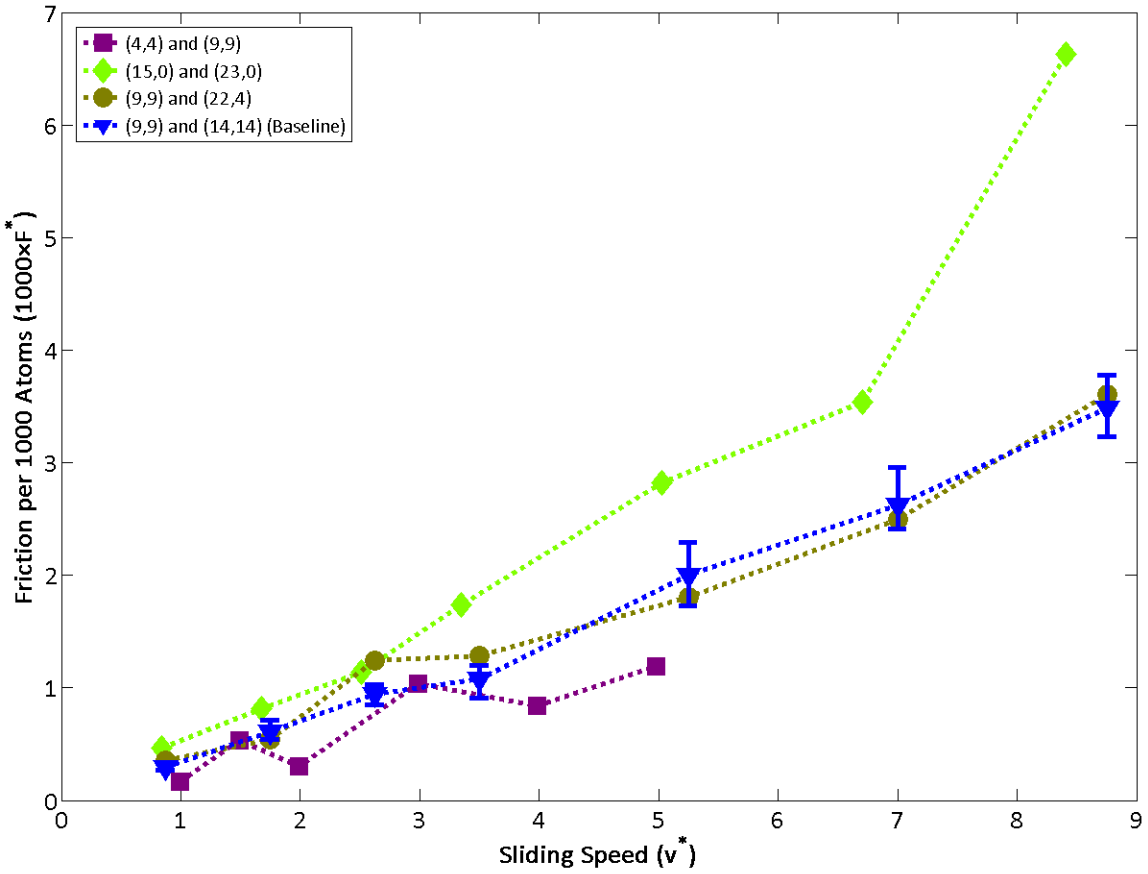

Figure 5-26: Effect of different CNT chiralities is investigated, using steady adiabatic simulations. Each chirality has an associated interface radius (characteristic of the overall tube size) and spacing (between the two tubes) which are listed in table 5-5. Chirality does not have a strong effect at lower speeds, and the data agree well for different CNTs. However, at higher speeds, the tube with tighter spacing tends to experience increased friction, likely due to the increased strength of the interaction between tubes when the spacing is reduced.

The interface radius, which is half of the average diameter between the two CNTs, might be expected to have an effect on the friction in the CNT system. Large diameter CNTs have a lower curvature than smaller diameter, which means that less bending energy is required per atom in the tube to maintain that curve. Additionally, the greater number of atoms around the circumference means that larger deflections are possible. These two factors contribute to a softer CNT, and it might be expected that this reduced stiffness could cause an increase in friction, by encouraging the transfer of kinetic energy into thermal vibrations of the atoms.

The spacing also might be expected to influence the friction; for tighter spacings, the energy minimum at the equilibrium spacing is shallower, and the energy gradient is steeper (and hence the forces are stronger.) This stronger interaction would be expected to increase friction for tighter spacings.

In fact, however, the data (figure 5-26) show that these two effects, along with any effect that might be present due to chirality alone, are only present at higher rotational speeds. For sliding speeds lower than $v^* = 3$ (about 5 Å/ps), the friction for CNTs of all four chiralities agree quite well, whereas the

friction diverges for higher speeds. The deviations at higher speeds are might be explained by the spacing variations; the configuration showing the highest friction (the (15,0)/(23,0) system), has 4% less spacing than the next tightest system, and likewise the other three tubes (with very similar spacings, within 1%) do not show as much variation. The interface radius, on the other hand, does not appear to correlate with the friction results. It is also interesting to note that the interface radius dependence is consistent with simulations of friction in graphene (which is the equivalent of an infinite interface radius), as discussed in section 5.3.4. Furthermore, there is strong evidence that the chirality may not be important to the friction: for the (9,9)/(14,14) and (9,9)/(22,4) geometries, which are nearly identical in interface radius and spacing (less than 0.2% difference), there is no marked difference outside of the error bars for the entire speed range.

These results are important in establishing the basic relationships between the geometry (as described by the chiral indices) and the friction. Still, as mentioned previously, the interactions between chirality, interface radius, and spacing effects are complex, and an exhaustive probing of this parameter space was outside the scope of the thesis. Further work is necessary to fully characterize the individual influences of each of these effects, as well as how they interact with each other.

5.3.3.6 Summary of Parametric Studies

The dependence of friction on a variety of parameters has been investigated. First, the effect of system physical parameters has been investigated. Friction appears to depend linearly on the speed of the relative motion (section 5.3.1) and on the temperature (section 5.3.3.3). Non-dimensionalization of the friction work by the measured thermal energy captures this dependence and allows friction versus speed curves to be collapsed into a single trend, both for simulations with controlled temperatures and for adiabatic simulations. CNT geometry was also probed; tube length did not affect the friction, although the variability in friction from simulation to simulation increased due to the increased flexibility of the longer CNT. Interface radius and CNT chirality also appear to have little or no influence, while decreased inter-wall spacing increases the friction. However, the complex interactions between chirality, interface radius, and spacing were not completely covered, and further work is necessary to confidently isolate these effects.

Second, parameters of the simulation implementation were investigated. The averaging implementation (downsampling rate) was shown to have no impact (section 5.3.3.1) on the friction for downsampling factors between 50 and 500, showing that the averaging is unlikely to cause discrepancies in friction estimates. However, the choice of thermostat (section 5.3.3.2) can be a factor; the Langevin thermostat was shown to give inflated friction estimates compared to the Nosé-Hoover and Berendsen thermostats, attributed to its inclusion of an artificial damping term. Most importantly, the friction predictions of completely independent friction simulation strategies were compared (section 5.3.1) and shown to agree well, particularly at low speeds. At higher speeds, the inherent temperature rise caused by the adiabatic boundary condition caused reported friction to be higher, because of the proportional dependence of friction on temperature.

In summary, friction depends linearly on sliding speed and temperature, and increases with decreasing inter-tube spacing. Friction does not depend or depends only weakly on the interface radius and the chirality. The reported friction value is not sensitive to downsampling, or simulation method, but can be altered by the system thermostat, and for adiabatic simulations, by the thermal energy accumulation.

5.3.4 Comparison with Graphene

Another interesting question pertaining to the friction in the CNT is how that friction compares to friction in graphene, the planar analogue of CNTS. In the limit of increasing tube diameter, the CNT bearing system becomes equivalent to a graphene system, wherein two infinite sheets of graphene are translating relative to each other. This situation was also simulated, for comparison. The geometry (shown in figure 5-27) consisted of two graphene sheets, corresponding to unwrapped (5,5) CNTs with a length of 10 hexagons, or a rectangle of dimensions 21.2 Å by 24.5 Å, with periodic boundary conditions to simulate an infinite sheet. A coast-down experiment was performed, where the top sheet was given an initial translational velocity, and the bottom sheet is held fixed. Again, the time rate of change of the momentum (translational momentum, in this case) is equal to the friction force.

The resulting friction data, from the graphene simulation (shown in figure 5-28) illustrates that the friction in graphene is in quantitative agreement with that measured for CNTs; although there is a very large variability in the measurements (likely caused by the small simulation domain used to reduce computational cost), the results fall within the error bars of the CNT friction for most cases, the general trend can be inferred to be the same. This observation reinforces the findings from the simulations of CNTs of different diameters (see section 5.3.3.5), that the friction does not depend strongly on the CNT diameter. Indeed, graphene corresponds to a CNT of infinite diameter, which is the limiting case.

While it has been expected that graphene friction should behave in the same way as CNT friction, this novel result demonstrates that it does agree quantitatively. The implications of such a finding are important for several reasons. First, the graphene simulations are much simpler to set up and implement, because they do not incorporate rotation but only translation. It is therefore unnecessary to decompose individual atom velocities based on their position in order to derive the tangential components, as is necessary in the CNT simulation to compute the temperature correctly and to measure the angular momentum and kinetic energy. The graphene simulation also runs more quickly as a result of doing away with these extra per-atom computations. It would therefore be beneficial to use graphene simulations to gather a large dataset on friction instead of CNT simulations, to save computational cost.

More importantly, use of graphene may aid in developing a better understanding of the mechanisms driving the friction. The mode shapes in graphene are simpler, corresponding to waves in two dimensions, instead of complex, fully three-dimensional shapes. If the modes contributing to friction in graphene can be established, it would be straightforward to visualize the same of these modes, which could show exactly what atomic motions cause the friction. For example, is there a stick-slip interaction in which atoms transfer their in-plane kinetic energy, or does energy transfer occur by coupling of out-of-plane vibrations? Removing the complicating factors due to the cylindrical nature of the CNT should make it easier to see the mechanisms at work. Future research on friction in carbon systems, particularly research aimed at developing a better understanding of the mechanisms, should take advantage of the simpler graphene system to gain better insight.

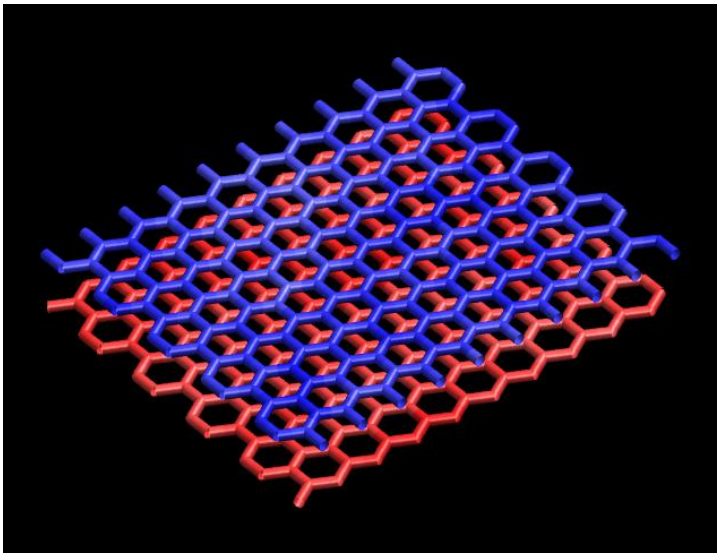

Figure 5-27 Geometry for the graphene simulations consisted of two rectangular graphene sheets with a periodic boundary condition in both in-plane directions.

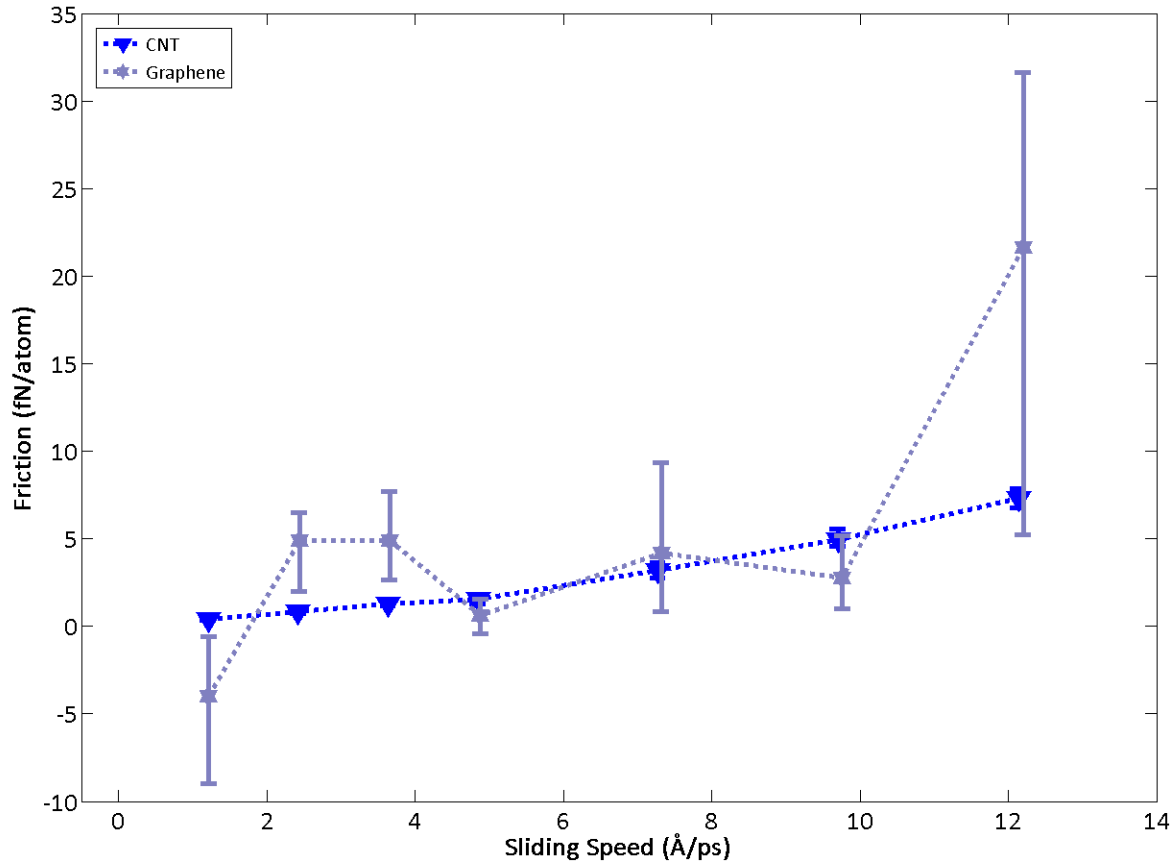

Figure 5-28: Friction in the graphene system, as a function of relative sliding speed. The baseline CNT simulations are also shown for comparison. The larger error bars are likely due to the small size of the simulated graphene system, which does not provide for as many atoms across which to average the data.

[This page intentionally left blank.]

6 Conclusions

6.1 Accomplishments, Contributions, and Lessons Learned

6.1.1 Practice

A substantial accomplishment of this work is the development of the fabrication process for the prototype CNT rotor device. Demonstrating this fabrication process has shown that it is possible to fabricate CNT bearing-based rotors that use a vertically oriented CNT. The vertical orientation of the CNT provides for superior geometric flexibility, since both dimensions of the rotor plane become accessible to the lithography. This enables axisymmetric rotors to be fabricated, with arbitrarily many evenly spaced components (*e.g.* electrodes or vanes) for superior interaction with the environment as well as improved rotor balance and hence higher operational speeds. Furthermore, the concept of using CVD grown CNTs provides a pathway to eventual batch-fabrication of CNT bearing devices, by illustrating a mechanism whereby CNTs can be placed at arbitrary locations without manual interaction.

In developing the fabrication process, many lessons were learned. One important discovery was the trade-off between high and low temperature CVD growth of CNTs (which suffer from diffusion of the catalyst, and defect-ridden CNTs, respectively). It was also discovered that the connections between the CNT and the substrate, as well as the CNT and the rotor, can be susceptible to failure during the release step, and methods to correct that deficiency were corrected.

Besides demonstrating the feasibility of such a CNT rotor, the prototype fabrication process represents a template, on which subsequent CNT bearing device designs might be based. Many fabrication challenges that can be expected to surface in any follow-on work were addressed during the fabrication process development. These included methods for attaching a rotor directly to the CNT without attaching it to the substrate (by stripping the sacrificial layer from the CNT with the aid of a non-conformal photoresist mask), for overcoming issues with tube placement precision (by mapping tube locations with the e-beam tool prior to fabrication of the rest of the device), and for achieving high resolution lithography over a high-topography substrate (via the additional thick resist lithography step). The testing protocol developed herein will also be of immediate utility for measuring the friction in the test device, once sufficiently high quality CNTs are available.

In addition, in the course of developing the fabrication process, knowledge of the effects of a suite of commonly used MEMS processes on CNTs was gained. In particular, it was shown that depositions and chemical etches tend not to damage the CNTs, while ion-based etches do. Furthermore, a consistent and broad assessment was conducted on these processes, generating a reference that will be useful for future CNT device designers deciding which materials and process to use for their fabrication.

Finally, a method for manipulating CNTs into place with a vertical orientation was developed. Since placement of CNTs is critical to the success of any CNT MEMS device, and since herding individual CNTs into position has been a non-trivial challenge for some time, this method will become an option for solving this problem. While involving time-consuming manual interaction, this technique could be particularly useful in an experimental setting. Engineers developing devices will get instant feedback on their CNT manipulation attempts, and furthermore may benefit from the familiar paradigm of looking at and moving an object directly, compared with the indirect fabrication methods typifying MEMS. In

developing the pick-and-place procedure, it was learned that vision and degrees of freedom in the manipulation system can be significant limitations on the performance of the pick-and place routine; poor vision makes it difficult to assess the work, and poor movement capabilities make it difficult to correct errors that are discovered. Furthermore, the difficulty in manipulating loose CNTs (as opposed to substrate-attached CVD CNTs) is compounded by difficulty of extracting them from the dense tangles in which they are obtained.

6.1.2 Theory

On the simulation side, this work has addressed the discrepancies among friction estimates reported in the literature. By conducting many different types of simulations with carefully controlled parameters, it has been shown that the independent simulations types can produce results within each other's error bars (and average values differing by a factor of two or three), and need not differ by several orders of magnitude. In establishing the simulation protocols, the challenges in conducting those simulations became clear. One main challenge is addressing systems of comparable length and time scale to the experiments; current computational capability curtails the cases that can be contemplated to speeds several orders higher and sizes several orders lower than the experiments. Another challenge, the difficulty in controlling all the myriad parameters that influence simulations, including thermostat implementation and settings, averaging techniques, boundary conditions, has been described.

In addition, the effects of an array of parameters on the CNT friction have been investigated. While the friction does not depend on the simulation mode (and should not, since friction is a property of the system and not of the particular simulation designed to probe that system), friction has been found to depend on other parameters. Friction appears to vary linearly with sliding speed, for the range of speeds considered. This was consistent across all types of simulations considered, when accounting for the temperature increase inherent in adiabatic simulations. Friction also depends linearly on temperature, as seen not only in steady state simulations with controlled temperature, but also in adiabatic simulations where the temperature increases because kinetic energy is dissipated into thermal energy. Geometric considerations were found to have weaker effects; the tube interface radius and chirality did not cause deviations in friction larger than the measurement error, although friction was found to increase with decreasing inter-tube spacing. Because of the complex inter-relationship between chirality, interface radius, and spacing, the exact nature of these dependencies could not be determined from the limited data acquired here; further study on this point is required. The other geometric parameter, tube length, which is independent of the other three, also did not appear to influence the value of friction, although longer tubes experienced higher variability from run to run (a tube four times longer shows error bars two to three times larger), because of the increased tube flexibility, which makes excitation of bending modes easier.

Finally, the mechanisms behind the friction have been investigated by studying the phonons that make up the motion in the CNT bearing system. It has been found that stationary CNTs display little difference in phonon spectra (the difference between spectra is everywhere less than half of the amplitude of the original spectra, and does not exhibit any clear peaks, valleys, or plateaus) depending on whether an inner or outer tube is present and exerting van der Waals interactions on it. When comparing the spectrum of a rotating tube to the still tube, the difference of the spectra exhibit some plateaus of activity in the range of 10-14 THz and 20-25 THz, but no specific frequency peaks, indicating that the mechanisms for dissipating orderly kinetic energy into disorderly thermal energy are broadband, and not linked to any one particular mode strongly. It may therefore difficult to "engineer" the friction by controlling the CNT geometry in order to modify certain phonons.

Overall, this work has improved the state of knowledge about carbon nanotube friction, by creating a test device that demonstrates the bearing, and could be used to measure friction, and by in parallel conducting simulations that estimate the friction in a consistent manner, building confidence in the simulation accuracy.

6.2 Recommendations for Future Work

While this project has made significant contributions to the state of the art of carbon nanotube bearings, there remains much work to be done. The fabrication process has been successful at constructing CNT bearing test rotors, but these rotors have not worked. Further process refinements, and particularly development of high quality CNTs, will be necessary to make the prototype fully successful. Additionally, while the simulation work reported here has addressed the underlying reasons for the discrepancies amongst friction reported in the literature, room for improvement remains, particularly in the areas of validation, expansion of the simulation spatially and temporally, as well as addressing defects in CNTs.

6.2.1 CNT Bearing Prototype

The prototype fabrication process developed here is capable of constructing a rotor with drive vanes supported on a vertically aligned, isolated CNT. However, much work needs to be done to enable these devices to function, in large part because the CNTs used here were highly defective and did not exhibit the nested-tube structure that is critical to their success as a bearing. The details of these defects were reported in section 4.2.1; in summary, the tubes were so rife with inter-wall bonding, amorphous carbon regions, split, misaligned, and crooked graphitic planes that the CNT structure was difficult to discern.

One of the approaches used here to address the issue of CNT quality, namely manipulation of CNTs in to place, has exhibited promise, yet development remains. For this work, CVD grown CNTs were used as targets for manipulation, because of their availability and vertical orientation. This choice made the initial development of the pick-and-place process more straightforward, but does nothing to address the CNT quality. The vision for this process is to use it with high quality loose CNTs, such as those produced by the arc-discharge method, which are the type used in previous CNT bearing demonstrations [1, 2] and which exhibit few or no inter-wall defects for their entire extent. Making the jump from the CVD CNTs to loose CNTs will require practice at changing the orientation of tubes using the manipulation system, since loose tubes can have arbitrary orientation.

Additionally, further development of the CNT manipulation technique will need to address the issue of separating loose CNTs from each other, to enable placement of a single CNT. Loose CNTs tend to aggregate into bundles, held together by the van der Waals interactions between neighboring tubes. Separating these tubes can be quite difficult with the manipulator, so ideally one could use some physical or chemical process to disperse the CNTs broadly across a substrate before introduction to the manipulation system. Such techniques have been used by prior researchers in constructing horizontally oriented CNT rotors [1, 2]; it would be beneficial to enhance this process with a mechanism for giving the tubes a vertical alignment as they are dispersed, easing the requirements for the subsequent manipulation. This might be achieved by dispersing the CNTs on a substrate with some features like walls or trenches that provide vertical areas to which the CNTs might adhere. It might also be possible to use a dielectrophoretic approach to orient the tubes properly.

In the long term, however, manipulation is not a viable approach, because it frustrates one of the purposes of going to a vertically oriented CNT in the first place, namely, improving manufacturability by

placing CNTs via batch processing. Any successful application device will need to be batch fabricatable in order to be produced at reasonable cost. Therefore, improvement of the crystalline quality of CVD grown CNTs is necessary for the long-term success of the bearing technology. At the very least, CNT quality will need to be improved to the point where rotation can be achieved, and friction comparable to existing arc-discharge-CNT-based demonstrations (about 0.85 MPa [2], or about 100 fN/atom) can be obtained, and for the bearing technology to compete with existing bearings (discussed in section 2.1), it must also provide similar friction (torque constants of about 10^{-9} to 10^{-12} N-m/rpm [58, 78]).

There are several possible approaches to improving CNT quality. Most of them involve high temperatures, which allow defects to be annealed out by granting additional mobility to the atoms. Simply annealing CNTs after the fact has been proven effective at improving tube quality [126], but theses high temperatures are incompatible with the rest of the fabrication, because they are higher even than the melting temperature of silicon, of which the substrate is comprised.

One other approach that has been successful in the literature is localized annealing of individual tubes via Joule heating [127, 128, 130]; this method works by passing a current through each tube, heating it due to its electrical resistance. It has also been shown that any remaining catalyst can further improve the CNT quality when subjected to this type of annealing [129]. The current could be applied via AFM or SEM manipulators (which would still hamper manufacturability) or via electrical contacts fabricated into the device (potentially increasing complexity.)

Another way to reduce the number of defects would be to simply increase the growth temperature. The temperature at the growth stage is more effective in improving quality than at the anneal stage, since the tubes are still being built up using atoms from the surrounding gas or plasma; the increased temperature allows each atom a better chance to diffuse into a low-energy (non-defective) site before bonding. Therefore, it might be possible to achieve similar results to a later anneal step with lower, usable temperatures. However, as discussed in section 4.2.1.1, heightened growth temperature has caused unwanted side effects, in particular diffusion of the catalyst particles from their intended locations. This challenge might be overcome by investing in understanding precisely the surface interactions between the substrate and the catalyst, and engineering an adhesion-promotion layer to hold the catalyst in place during growth. However, this layer would have to not interfere with the catalysis and growth of the CNTs themselves. An alternative strategy might be to use physical barriers to restrain the catalyst, such as depositing catalyst regions at the bottom of etched cavities. At any rate, in order for the CVD CNT approach to succeed, a method for annealing defects or preventing their formation during growth will be necessary.

6.2.2 CNT Friction Simulations

The simulations conducted here have made strides by demonstrating that simulated friction estimates can agree when the simulations are consistent, and by identifying the dependencies of CNT friction on many important parameters. Nevertheless, much work remains to be done on these simulations.

First, the simulations must be validated with experimental data. This notion is of critical importance, since the simulations will only have utility as predictive tools if their results can be trusted. Gathering such validation data should be a top priority. Because of the difficulty of conducting CNT friction experiments, the true value of friction remains unknown, particularly in the rotating configuration, for which no dynamic friction measurements have yet been made. Although obtaining the same friction estimate from multiple simulations builds confidence in these simulations,

experimental data is still the best way to truly anchor the simulations to physical reality. The prototype device, once constructed using a sufficiently high quality CNT to allow rotation, will be able to provide useful validation data. In this way, further development of the experimental work presented here will also advance the credibility of the simulation work. Once the simulations have been proven accurate, they will be more useful as a tool in predicting friction for future application work.

Another main area in which the simulations should be further investigated is in their scale. Experiments to date have used tubes comprising tens of walls and millions to billions of atoms, whereas the simulations have focused on only two walls, and systems of a few thousand atoms. Although this work has shown that diameter does not appear to be a significant factor in CNT friction, and that length only has an effect to the degree that it reduces the bending stiffness, it would still be advantageous to be able to simulate CNTs that are more comparable to the experimental case. This is mainly a computational power limitation; MD codes are capable of splitting their geometric domain into segments, and simulating each in parallel, so that large systems can be more readily accommodated. As processor cores become cheaper, simulatable system size will grow.

The scale issue extends also to the temporal dimension. Simulation speeds thus far have not been able to probe rotation speeds lower than 10^8 revolutions per second, while experiments have been limited to the order of a few revolutions per second. As the experimental capabilities are improved, and once the prototype developed here is operational, the experimentally accessible speed limit will increase. Decreasing the lower limit of the simulations will also be useful in bridging the gap between experiment and theory, and eventually may allow for direct comparison. With the straightforward MD methods used here, it is difficult to simulate long times, since the simulation cannot easily be parallelized in time as it can in space. Therefore, the time limit depends more on processor speed than number of processors, and processor speed is evolving more slowly. However, there are advanced techniques that can be used to simulate longer times. One possibility is temperature-accelerated dynamics [154]. This approach raises the simulation temperature, which causes events in the simulation to occur faster. The original time that the event would have taken to occur can then be inferred from the time at the elevated temperature and the height of the energy barrier for the event.

The last major issue that needs to be addressed in simulation is defects; this is also an important priority, because while simulations have thus far concentrated on simulating perfect, defect-free CNTs, the experiments indicate that defects are in fact the dominant contributor to friction [2, 9, 12]. Only one simulation has addressed defects to date [17], and it only considered Stone-Wales type defects, which are arguably the defect type with the least impact, since they only cause a small local change to the wall curvature. In the future, simulations should thoroughly address the dependence of friction on CNT defects, in order to be as applicable as possible to the experiments. A first step could be to introduce randomly distributed point defects, such as vacancies, interstitials, or erroneous species into the CNT structure; the friction could then be characterized as a function of both defect density (number of defects per tube wall area) and distribution (concentrated in clumps, spread evenly, etc). Eventually it would be interesting to simulate larger-scale defects such as scroll regions, dislocation faults, and topological changes in the CNT; these area likely the main contributors to real CNT friction, and although implementation would require some effort to define their precise atomic geometry, the results would be useful.

[This page intentionally left blank.]

REFERENCES

[1] A. M. Fennimore, T. D. Yuzvinsky, Wei-Qiang Han, M. S. Fuhrer, J. Cumings, and A. Zettl, "Rotational actuators based on carbon nanotubes," *Nature,* vol. 424, no. 6947, pp. 408-410, 2003. http://dx.doi.org/10.1038/nature01823

[2] Bertrand Bourlon, D. Christian Glattli, Csilla Miko, Laszlo Forro, and Adrian Bachtold, "Carbon Nanotube Based Bearing for Rotational Motions," *Nano Letters,* vol. 4, no. 4, pp. 709-712, 2004. http://dx.doi.org/10.1021/nl035217g

[3] Eugene Hightower Cook, "A carbon nanotube bearing and Stodola rotor," Master of Science Thesis in Aeronautics and Astronautics, *Massachusetts Institute of Technology,* 2008. http://dspace.mit.edu/handle/1721.1/46796

[4] A. D. Romig, Michael T. Dugger, and Paul J. McWhorter, "Materials issues in microelectromechanical devices: science, engineering, manufacturability and reliability," *Acta Materialia,* vol. 51, no. 19, pp. 5837-5866, 2003. http://dx.doi.org/10.1016/S1359-6454(03)00440-3

[5] Erin E. Flater, Alex D. Corwin, Maarten P. de Boer, and Robert W. Carpick, "In situ wear studies of surface micromachined interfaces subject to controlled loading," *Wear,* vol. 260, no. 6, pp. 580-593, 2006. http://dx.doi.org/10.1016/j.wear.2005.02.070

[6] J.-C. Charlier and J.-P. Michenaud, "Energetics of multilayered carbon tubules," *Physical Review Letters,* vol. 70, no. 12, pp. 1858-1861, 1993. http://dx.doi.org/10.1103/PhysRevLett.70.1858

[7] John Cumings and A. Zettl, "Low-Friction Nanoscale Linear Bearing Realized from Multiwall Carbon Nanotubes," *Science,* vol. 289, no. 5479, pp. 602-604, 2000. http://dx.doi.org/10.1126/science.289.5479.602

[8] Alexander K. Zettl, Adam M. Fennimore, and Thomas D. Yuzvinsky, "Rotational actuator or motor based on carbon nanotubes," United States Patent 7,053,520, 2004. http://patft.uspto.gov/netacgi/nph-Parser?patentnumber=7053520

[9] Min-Feng Yu, Boris I. Yakobson, and Rodney S. Ruoff, "Controlled Sliding and Pullout of Nested Shells in Individual Multiwalled Carbon Nanotubes," *Journal of Physical Chemistry B,* vol. 104, pp. 8764-8767, 2000. http://dx.doi.org/10.1021/jp002828d

[10] Seiji Akita and Yoshikazu Nakayama, "Mechanical and Electrical Properties of Multiwall Nanotube under Interlayer Sliding," *e-Journal of Surface Science and Nanotechnology,* vol. 3, pp. 86-93, 2005. http://dx.doi.org/10.1380/ejssnt.2005.86

[11] Seiji Akita and Yoshikazu Nakayama, "Interlayer Sliding Force of Individual Multiwall Carbon Nanotubes," *Japanese Journal of Applied Physics,* vol. 42, pp. 4830-4833, 2003. http://dx.doi.org/10.1143/JJAP.42.4830

[12] A. Kis, K. Jensen, S. Aloni, W. Mickelson, and A. Zettl, "Interlayer Forces and Ultralow Sliding Friction in Multiwalled Carbon Nanotubes," *Physical Review Letters,* vol. 97, no. 2, pp. 025501-4, 2006. http://dx.doi.org/10.1103/PhysRevLett.97.025501

[13] Wanlin Guo and Huajian Gao, "Optimized Bearing and Interlayer Friction in Multiwalled Carbon Nanotubes," *Computer Modeling in Engineering & Sciences* vol. 7, no. 1, pp. 19-34, 2005. http://dx.doi.org/10.3970/cmes.2005.007.019

[14] Jose L. Rivera, Clare McCabe, and Peter T. Cummings, "The oscillatory damped behaviour of incommensurate double-walled carbon nanotubes," *Nanotechnology,* vol. 16, no. 2, pp. 186-198, 2005. http://dx.doi.org/10.1088/0957-4484/16/2/003

[15] J. L. Rivera, C. McCabe, and P. T. Cummings, "Oscillatory Behavior of Double Nanotubes under Extension: A Simple Nanoscale Damped Spring," *Nano Lett.,* vol. 3, no. 8, pp. 1001-1005, 2003. http://dx.doi.org/10.1021/nl034171o

[16] Wanlin Guo, Yufeng Guo, Huajian Gao, Quanshui Zheng, and Wenyu Zhong, "Energy Dissipation in Gigahertz Oscillators from Multiwalled Carbon Nanotubes," *Physical Review Letters,* vol. 91, no. 12, p. 125501, 2003. http://dx.doi.org/10.1103/PhysRevLett.91.125501

[17] Wanlin Guo, Wenyu Zhong, Yitao Dai, and Sunan Li, "Coupled defect-size effects on interlayer friction in multiwalled carbon nanotubes," *Physical Review B: Condensed Matter and Materials Physics,* vol. 72, no. 7, pp. 075409-075410, 2005. http://dx.doi.org/10.1103/PhysRevB.72.075409

[18] Haibin Su, W.A. Goddard, III, and Yang Zhao, "Dynamic friction force in a carbon peapod oscillator," *Nanotechnology,* vol. 17, no. 22, pp. 5691-5695, 2006. http://dx.doi.org/10.1088/0957-4484/17/22/026

[19] Xiao-Hua Zhang, Ugo Tartaglino, Giuseppe E. Santoro, and Erio Tosatti, "Velocity plateaus and jumps in carbon nanotube sliding," *Surface Science,* vol. 601, no. 18, pp. 3693-3696, 2007. http://dx.doi.org/10.1016/j.susc.2007.05.034

[20] S. Zhang, W. K. Liu, and R. S. Ruoff, "Atomistic Simulations of Double-Walled Carbon Nanotubes (DWCNTs) as Rotational Bearings," *Nano Lett.,* vol. 4, no. 2, pp. 293-297, 2004. http://dx.doi.org/10.1021/nl0350276

[21] Yasuaki Omata, Yuichiro Yamagami, Kotaro Tadano, Takashi Miyake, and Susumu Saito, "Nanotube nanoscience: A molecular-dynamics study," *Physica E: Low-dimensional Systems and Nanostructures,* vol. 29, no. 3-4, pp. 454-468, 2005. http://dx.doi.org/10.1016/j.physe.2005.06.009

[22] S.S. Kuznetsov, Yu. E. Lozovik, and A.M. Popov, "The nanoactuator based on a carbon nanotube," *Physics of the Solid State,* vol. 49, no. 5, pp. 1004-1012, 2007. http://dx.doi.org/10.1134/S1063783407050320

[23] Iman. Salehinia and Sergey.N. Medyanik, "Transmission Between Translational and Rotational Motions in Double-Walled Carbon Nanotubes," *Journal of Computational and Theoretical Nanoscience,* vol. 8, no. 2, pp. 179-188, 2011. http://dx.doi.org/10.1166/jctn.2011.1674

[24] J. Servantie and P. Gaspard, "Rotational Dynamics and Friction in Double-Walled Carbon Nanotubes," *Physical Review Letters,* vol. 97, no. 18, pp. 186106-4, 2006. http://dx.doi.org/10.1103/PhysRevLett.97.186106

[25] J. Servantie and P. Gaspard, "Methods of Calculation of a Friction Coefficient: Application to Nanotubes," *Physical Review Letters,* vol. 91, no. 18, p. 185503, 2003. http://dx.doi.org/10.1103/PhysRevLett.91.185503

[26] J. Servantie and P. Gaspard, "Translational dynamics and friction in double-walled carbon nanotubes," *Physical Review B,* vol. 73, no. 12, p. 125428, 2006. http://dx.doi.org/10.1103/PhysRevB.73.125428

[27] B. E. Zhu and et al., "Thermal effect on DWCNTs as rotational bearings," *Nanotechnology,* vol. 19, no. 49, p. 495708, 2008. http://dx.doi.org/10.1088/0957-4484/19/49/495708

[28] M. A. Guillorn, M. L. Simpson, G. J. Bordonaro, V. I. Merkulov, L. R. Baylor, and D. H. Lowndes, "Fabrication of gated cathode structures using an in situ grown vertically aligned carbon nanofiber as a field emission element," *Journal of Vacuum Science & Technology B: Microelectronics and Nanometer Structures,* vol. 19, no. 2, pp. 573-578, 2001. http://dx.doi.org/10.1116/1.1358855

[29] M. A. Guillorn, T. E. McKnight, A. Melechko, V. I. Merkulov, P. F. Britt, D. W. Austin, D. H. Lowndes, and M. L. Simpson, "Individually addressable vertically aligned carbon nanofiber-based electrochemical probes," *Journal of Applied Physics,* vol. 91, no. 6, pp. 3824-3828, 2002. http://dx.doi.org/10.1063/1.1448671

[30] J. Li, H. T. Ng, A. Cassell, W. Fan, H. Chen, Q. Ye, J. Koehne, J. Han, and M. Meyyappan, "Carbon Nanotube Nanoelectrode Array for Ultrasensitive DNA Detection," *Nano Letters,* vol. 3, no. 5, pp. 597-602, 2003. http://dx.doi.org/10.1021/nl0340677

[31] X. Yang, M. A. Guillorn, D. Austin, A. V. Melechko, H. Cui, H. M. Meyer, V. I. Merkulov, J. B. O. Caughman, D. H. Lowndes, and M. L. Simpson, "Fabrication and Characterization of Carbon Nanofiber-Based Vertically Integrated Schottky Barrier Junction Diodes," *Nano Letters,* vol. 3, no. 12, pp. 1751-1755, 2003. http://dx.doi.org/10.1021/nl0346631

[32] Takashi Ikuno, Mitsuhiro Katayama, Kuei-Yi Lee, Takashi Kuzuoka, Jung-Goo Lee, Shin-ichi Honda, Hirotaro Mori, and Kenjiro Oura, "Local Etching of Insulator-Coated Carbon Nanotubes towards Passivated Nanoprobes " *Japanese Journal of Applied Physics,* vol. 43, no. 7B, pp. L987-L989, 2004. http://dx.doi.org/10.1143/JJAP.43.L987

[33] J. Koehne, J. Li, A. M. Cassell, H. Chen, Q. Ye, H. T. Ng, J. Han, and M. Meyyappan, "The fabrication and electrochemical characterization of carbon nanotube nanoelectrode arrays," *Journal of Materials Chemistry,* vol. 14, no. 4, pp. 676-684, 2004. http://dx.doi.org/10.1039/b311728f

[34] H. B. Peng and J. A. Golovchenko, "Coulomb blockade in suspended Si3N4-coated single-walled carbon nanotubes," *Applied Physics Letters,* vol. 84, no. 26, pp. 5428-5430, 2004. http://dx.doi.org/10.1063/1.1765733

[35] A. Subramanian, L. X. Dong, J. Tharian, U. Sennhauser, and B. J. Nelson, "Batch fabrication of carbon nanotube bearings," *Nanotechnology,* vol. 18, no. 7, p. 075703, 2007. http://dx.doi.org/10.1088/0957-4484/18/7/075703

[36] Q. Ye, A. M. Cassell, H. Liu, K. J. Chao, J. Han, and M. Meyyappan, "Large-Scale Fabrication of Carbon Nanotube Probe Tips for Atomic Force Microscopy Critical Dimension Imaging Applications," *Nano Lett.,* vol. 4, no. 7, pp. 1301-1308, 2004. http://dx.doi.org/10.1021/nl049341r

[37] L. Zhang, A. V. Melechko, V. I. Merkulov, M. A. Guillorn, M. L. Simpson, D. H. Lowndes, and M. J. Doktycz, "Controlled transport of latex beads through vertically aligned carbon nanofiber membranes," *Applied Physics Letters,* vol. 81, no. 1, p. 135, 2002. http://dx.doi.org/10.1063/1.1490142

[38] A. V. Melechko, T. E. McKnight, M. A. Guillorn, V. I. Merkulov, B. Ilic, M. J. Doktycz, D. H. Lowndes, and M. L. Simpson, "Vertically aligned carbon nanofibers as sacrificial templates for nanofluidic structures," *Applied Physics Letters,* vol. 82, no. 6, pp. 976-978, 2003. http://dx.doi.org/10.1063/1.1544058

[39] Bruce J. Hinds, Nitin Chopra, Terry Rantell, Rodney Andrews, Vasilis Gavalas, and Leonidas G. Bachas, "Aligned Multiwalled Carbon Nanotube Membranes," *Science,* vol. 303, no. 5654, pp. 62-65, 2004. http://dx.doi.org/10.1126/science.1092048

[40] Aleksandr Noy, Hyung Gyu Park, Francesco Fornasiero, Jason K. Holt, Costas P. Grigoropoulos, and Olgica Bakajin, "Nanofluidics in Carbon Nanotubes," *Nano Today,* vol. 2, no. 6, pp. 22-29, 2007. http://dx.doi.org/10.1016/S1748-0132(07)70170-6

[41] Kirt R. Williams and Richard S. Muller, "Etch Rates for Micromachining Processing," *Journal of Microelectromechanical Systems,* vol. 5, no. 4, pp. 256-269, 1996. http://dx.doi.org/10.1109/84.546406

[42] K. R. Williams, K. Gupta, and M. Wasilik, "Etch rates for micromachining processing-Part II," *Journal of Microelectromechanical Systems,* vol. 12, no. 6, pp. 761-778, 2003. http://dx.doi.org/10.1109/JMEMS.2003.820936

[43] S. F. Bart, M. Mehregany, L. S. Tavrow, J. H. Lang, and S. D. Senturia, "Electric micromotor dynamics," *Electron Devices, IEEE Transactions on,* vol. 39, no. 3, pp. 566-575, 1992. http://dx.doi.org/10.1109/16.123479

[44] M. A. Guillorn, M. D. Hale, V. I. Merkulov, M. L. Simpson, G. Y. Eres, H. Cui, A. A. Puretzky, and D. B. Geohegan, "Operation of individual integrally gated carbon nanotube field emitter cells," *Applied Physics Letters,* vol. 81, no. 15, pp. 2860-2862, 2002. http://dx.doi.org/10.1063/1.1512955

[45] J. S. Moon, P. S. Alegaonkar, J. H. Han, T. Y. Lee, J. B. Yoo, and J. M. Kim, "Enhanced field emission properties of thin-multiwalled carbon nanotubes: Role of SiOx coating," *Journal of Applied Physics,* vol. 100, 2006. http://dx.doi.org/10.1063/1.2384795

[46] Walt A. de Heer, A. ChÃ¢telain, and D. Ugarte, "A Carbon Nanotube Field-Emission Electron Source," *Science,* vol. 270, no. 5239, pp. 1179-1180, 1995. http://dx.doi.org/10.1126/science.270.5239.1179

[47] J. Martinez, T. D. Yuzvinsky, A. M. Fennimore, A. Zettl, R. Garcia, and C. Bustamante, "Length control and sharpening of atomic force microscope carbon nanotube tips assisted by and electron beam," *Nanotechnology,* vol. 16, no. 11, pp. 2493-2496, 2005. http://dx.doi.org/10.1088/0957-4484/16/11/004

[48] R. A. Miller, E. G. Nazarov, G. A. Eiceman, and A. Thomas King, "A MEMS radio-frequency ion mobility spectrometer for chemical vapor detection," *Sensors & Actuators: A. Physical,* vol. 91, no. 3, pp. 301-312, 2001. http://dx.doi.org/10.1016/S0924-4247(01)00600-8

[49] S. C. Terry, J. H. Jerman, and J. B. Angell, "A gas chromatographic air analyzer fabricated on a silicon wafer," *IEEE Transactions on Electron Devices,* vol. 26, no. 12, pp. 1880-1886, 1979. http://dx.doi.org/10.1109/T-ED.1979.19791

[50] C. C. Wong, J. H. Flemming, D. R. Adkins, M. A. Plowman, and M. Center, "Evaluation of mini/micro-pumps for Micro-Chem-Lab™," in *Proceedings of the Fluids Engineering Division, ASME International Mechanical Engineering Congress and Exposition*, San Francisco, CA, 1995. http://catalog.asme.org/ConferencePublications/PrintBook/1995_Proceedings_Fluids.cfm

[51] C. B. Freidhoff, R. M. Young, S. Sriram, T. T. Braggins, T. W. O'Keefe, J. D. Adam, H. C. Nathanson, R. R. A. Syms, T. J. Tate, M. M. Ahmad, S. Taylor, and J. Tunstall, "Chemical sensing using nonoptical microelectromechanical systems," *Journal of Vacuum Science & Technology A: Vacuum, Surfaces, and Films,* vol. 17, p. 2300, 1999. http://dx.doi.org/10.1116/1.581764

[52] S. Taylor, R. F. Tindall, and R. R. A. Syms, "Silicon based quadrupole mass spectrometry using microelectromechanical systems," *Journal of Vacuum Science & Technology B: Microelectronics and Nanometer Structures,* vol. 19, p. 557, 2001. http://dx.doi.org/10.1116/1.1359172

[53] C. G. Wilson and Y. B. Gianchandani, "Spectral detection of metal contaminants in water using an on-chip microglow discharge," *Electron Devices, IEEE Transactions on,* vol. 49, no. 12, pp. 2317-2322, 2002. http://dx.doi.org/10.1109/TED.2002.805608

[54] H. Zhou, H. Q. Li, V. Sharma, and M. A. Schmidt, "A single-stage micromachined vacuum pump achieving 164 torr absolute pressure," in *Micro Electro Mechanical Systems (MEMS), 2011 IEEE 24th International Conference on*, pp. 1095-1098.

[55] Marc Weinberg, "Nanotube Spinning Gyro Performance," Cambridge, MA, 2006.

[56] A. H. Epstein, S. D. Senturia, G. Anathasuresh, A. Ayon, K. Breuer, K. S. Chen, F. Ehrich, G. Gauba, R. Ghodssi, C. Groshenry, S. Jacobson, J. H. Lang, C.-C. Mehra, J. Mur Miranda, S. Nagle, D. Orr, E. Piekos, M. A. Schmidt, G. Shirley, S. Spearing, C. Tan, Y.-S. Tzeng, and I. Waitz, "Power MEMS and microengines," in *International Conference on Solid State Sensors and Actuators (TRANSDUCERS'97),* Chicago, IL, 1997. http://dx.doi.org/10.1109/SENSOR.1997.635209

[57] C. L. Tsai and A. K. Henning, "Surface micromachined turbines," in *International Conference on Solid State Sensors and Actuators (TRANSDUCERS'97),* Chicago, IL, 1997. http://dx.doi.org/10.1109/SENSOR.1997.635229

[58] M. McCarthy, C. M. Waits, and R. Ghodssi, "Dynamic Friction and Wear in a Planar-Contact Encapsulated Microball Bearing Using an Integrated Microturbine," *Journal of Microelectromechanical Systems,* vol. 18, no. 2, pp. 263-273, 2009. http://dx.doi.org/10.1109/JMEMS.2009.2013407

[59] M. Mehregany, S. F. Bart, L. S. Tavrow, J. H. Lang, S. D. Senturia, and M. F. Schlecht, "A study of three microfabricated variable-capacitance motors," *Sensors & Actuators: A. Physical,* vol. 21, no. 1, pp. 173-179, 1990. http://dx.doi.org/10.1016/0924-4247(90)85033-Z

[60] L. S. Tavrow, S. F. Bart, and J. H. Lang, "Operational characteristics of microfabricated electric motors," in *International Conference on Solid-State Sensors and Actuators (TRANSDUCERS'91),* San Francisco, CA, USA, pp. 877-881, 1991. http://dx.doi.org/10.1109/SENSOR.1991.149026

[61] R. T. Howe, J. H. Lang, M. F. Schlecht, M. A. Schmidt, S. D. Senturia, M. Mehregany, and L. S. Tavrow, "Method for fabricating side drive electrostatic micromotor," United States Patent 5,043,043, 1991. http://v3.espacenet.com/textdoc?DB=EPODOC&IDX=US5043043&F=0

[62] Mehran Mehregany, Stephen F. Bart, Lee S. Tavrow, Jeffrey H. Lang, and Stephen D. Senturia, "Principles in design and microfabrication of variable-capacitance side-drive motors," *Journal of Vacuum Science & Technology A: Vacuum, Surfaces, and Films,* vol. 8, no. 4, 1990. http://dx.doi.org/10.1116/1.576515

[63] V. R. Dhuler, M. Mehregany, and S. M. Phillips, "An experimental technique and a model for studying the operation of harmonic side-drive micrometers," *IEEE Transactions on Electron Devices,* vol. 40, no. 11, pp. 1977-1984, 1993. http://dx.doi.org/10.1109/16.239737

[64] V. R. Dhuler, M. Mehregany, and S. M. Phillips, "A comparative study of bearing designs and operational environments for harmonic side-drive micromotors," *IEEE Transactions on Electron Devices,* vol. 40, no. 11, pp. 1985-1989, 1993. http://dx.doi.org/10.1109/16.239738

[65] M. Mehregany, S. D. Senturia, and J. H. Lang, "Measurement of wear in polysilicon micromotors," *IEEE Transactions on Electron Devices,* vol. 39, no. 5, pp. 1136-1143, 1992. http://dx.doi.org/10.1109/16.129094

[66] T. M. Mayer, J. W. Elam, S. M. George, P. G. Kotula, and R. S. Goeke, "Atomic-layer deposition of wear-resistant coatings for microelectromechanical devices," *Applied Physics Letters,* vol. 82, p. 2883, 2003. http://dx.doi.org/10.1063/1.1570926

[67] T. W. Scharf, P. G. Kotula, and S. V. Prasad, "Friction and wear mechanisms in MoS2/Sb2O3/Au nanocomposite coatings," *Acta Materialia,* vol. 58, no. 12, pp. 4100-4109, 2010. http://dx.doi.org/10.1016/j.actamat.2010.03.040

[68] T. W. Scharf, J. A. Ohlhausen, D. R. Tallant, and S. V. Prasad, "Mechnisms of friction in diamondlike nanocomposite coatings," *Journal of Applied Physics,* vol. 101, p. 063521, 2006. http://dx.doi.org/10.1063/1.2711147

[69] Nima Ghalichechian, Alireza Modafe, Mustafa Ilker Beyaz, and Reza Ghodssi, "Design, Fabrication, and Characterization of a Rotary Micromotor Supported on Microball Bearings," *Journal of Microelectromechanical Systems,* vol. 17, no. 3, pp. 632-642, 2008. http://dx.doi.org/10.1109/JMEMS.2008.916346

[70] C. M. Waits, M. McCarthy, and R. Ghodssi, "A Microfabricated Spiral-Groove Turbopump Supported on Microball Bearings," *Journal of Microelectromechanical Systems,* vol. 19, no. 1, pp. 99-109, 2010. http://dx.doi.org/10.1109/JMEMS.2009.2035525

[71] C. C. Wong, D. Chu, S. L. Liu, M. R. Tuck, Z. Mahmud, and V. A. Amatucci, "Rapid prototyping of a micro pump with laser micromachining," *Proceedings of SPIE,* vol. 2642, p. 156, 1995. http://dx.doi.org/10.1117/12.221164

[72] Jasper Lodewyk Steyn, "A Microfabricated ElectroQuasiStatic Induction Turbine-Generator," Doctor of Philosophy Thesis in Aeronautics and Astronautics, *Massachusetts Institute of Technology,* 2005. http://dspace.mit.edu/handle/1721.1/32463

[73] Chiang Juay Teo, "MEMS Turbomachinery Rotordynamics: Modeling, Design, and Testing," Doctor of Philosophy Thesis in Aeronautics and Astronautics, *Massachusetts Institute of Technology,* 2006. http://dspace.mit.edu/handle/1721.1/36180

[74] Z. S. Spakovszky and L. X. Liu, "Scaling Laws for Ultra-Short Hydrostatic Gas Journal Bearings," *Journal of Vibration and Acoustics,* vol. 127, no. 3, pp. 254-261, 2005. http://dx.doi.org/10.1115/1.1897739

[75] Lixian Lui, "Theory for Hydrostatic Gas Journal Bearings for Micro-Electro-Mechanical Systems," Doctor of Philosophy Thesis in Aeronautics and Astronautics, *Massachusetts Institute of Technology,* 2005. http://dspace.mit.edu/handle/1721.1/33921

[76] Bernard Yen, "A Fully-Integrated Multi-Watt Permanent Magnet Turbine Generator," Doctor of Philosophy Thesis in Electrical Engineering, *Massachusetts Institute of Technology,* 2008. http://dspace.mit.edu/handle/1721.1/45860

[77] Jeffrey H. Lang, *Multi-Wafer Rotating MEMS Machines.* From series *MEMS Reference Shelf.* New York: Springer, 2009. http://dx.doi.org/10.1007/978-0-387-77747-4

[78] C. Livermore, A. R. Forte, T. Lyszczarz, S. D. Umans, A. A. Ayon, and J. H. Lang, "A high-power MEMS electric induction motor," *Journal of Microelectromechanical Systems,* vol. 13, no. 3, pp. 465-471, 2004. http://dx.doi.org/10.1109/JMEMS.2004.828736

[79] E. S. Piekos, D. J. Orr, S. A. Jacobson, F. F. Ehrich, and K. S. Breuer, "Design and Analysis of Microfabricated High Speed Gas Journal Bearings," in *28th AIAA Fluid Dynamics Conference*, Snowmass Village, Colorado, 1997.

[80] Mei Lin Chan, Brian Yoxall, Hyunkyu Park, Zhaoyi Kang, Igor Izyumin, Jeffrey Chou, Mischa M. Megens, Ming C. Wu, Bernhard E. Boser, and David A. Horsley, "Low friction liquid bearing MEMS micromotor," in *IEEE 24th International Conference on Micro Electro Mechanical Systems (MEMS),* Cancún, Mexico, pp. 1237-1240, 2011. http://dx.doi.org/10.1109/MEMSYS.2011.5734656

[81] Sumio Iijima, "Helical microtubules of graphitic carbon," *Nature,* vol. 354, no. 6348, pp. 56-58, 1991. http://dx.doi.org/10.1038/354056a0

[82] Mildred S. Dresselhaus, Gene Dresselhaus, and Phaedon Avouris, *Carbon Nanotubes: Synthesis, Structure, Properties, and Applications.* From series *Topics in Applied Physics.* vol. 80 Berlin: Springer, 2001. http://dx.doi.org/10.1007/3-540-39947-X

[83] M. F. Yu, M. J. Dyer, G. D. Skidmore, H. W. Rohrs, X. K. Lu, K. D. Ausman, J. R. Von Ehr, and R. S. Ruoff, "Three-dimensional manipulation of carbon nanotubes under a scanning electron microscope," *Nanotechnology,* vol. 10, no. 3, pp. 244-252, 1999. http://dx.doi.org/10.1088/0957-4484/10/3/304

[84] Min-Feng Yu, Oleg Lourie, Mark J. Dyer, Katerina Moloni, Thomas F. Kelly, and Rodney S. Ruoff, "Strength and Breaking Mechanism of Multiwalled Carbon Nanotubes Under Tensile Load," *Science,* vol. 287, no. 5453, pp. 637-640, 2000. http://dx.doi.org/10.1126/science.287.5453.637

[85] Philip G. Collins, Michael S. Arnold, and Phaedon Avouris, "Engineering Carbon Nanotubes and Nanotube Circuits Using Electrical Breakdown," *Science,* vol. 292, pp. 706-709, 2001. http://dx.doi.org/10.1126/science.1058782

[86] John P. Cumings, Alex K. Zettl, Steven G. Louie, and Marvin L. Cohen, "Telescoped multiwall nanotube and manufacture thereof," USA Patent 6,874,668, 2005. http://v3.espacenet.com/textdoc?DB=EPODOC&IDX=EP0664438&F=0

[87] A. Zettl and J. Cumings, "Sharpened Nanotubes, Nanobearings, and Nanosprings," in *Electronic Properties of Novel Materials-Molecular Nanostructures: XIV International Winterschool/Euroconference.*, 2000, pp. 526-532.

[88] John Cumings, Philip G. Collins, and A. Zettl, "Peeling and sharpening multiwall nanotubes," *Nature,* vol. 406, no. 6796, p. 586, 2000. http://dx.doi.org/10.1038/35020698

[89] T. D. Yuzvinsky, A. M. Fennimore, A. Kis, and A. Zettl, "Controlled placement of highly aligned carbon nanotubes for the manufacture of arrays of nanoscale torsional actuators," *Nanotechnology,* vol. 17, no. 2, pp. 434-438, 2006. http://dx.doi.org/10.1088/0957-4484/17/2/015

[90] M. L. Allinger, F. Li, and L. Yan, "Molecular mechanics. The MM3 force field for alkenes," *Journal of Computational Chemistry,* vol. 11, no. 7, pp. 848-867, 1990. http://dx.doi.org/10.1002/jcc.540110708

[91] Y. Guo, N. Karasawa, and W. Goddard, "Prediction of fullerene packing in C 60 and C 70 crystals," *Nature,* vol. 351, no. 6326, pp. 464-467, 1991. http://dx.doi.org/10.1038/351464a0

[92] J. E. Lennard-Jones, "Cohesion," *Proceedings of the Physical Society,* vol. 43, pp. 461-482, 1931. http://dx.doi.org/10.1088/0959-5309/43/5/301

[93] Aleksey N. Kolmogorov and Vincent H. Crespi, "Smoothest Bearings: Interlayer Sliding in Multiwalled Carbon Nanotubes," *Physical Review Letters,* vol. 85, no. 22, pp. 4727-4730, 2000. http://dx.doi.org/10.1103/PhysRevLett.85.4727

[94] Donald W. Brenner, "Empirical potential for hydrocarbons for use in simulating the chemical vapor deposition of diamond films," *Physical Review B,* vol. 42, no. 15, p. 9458, 1990. http://dx.doi.org/10.1103/PhysRevB.42.9458

[95] J. Tersoff, "New empirical approach for the structure and energy of covalent systems," *Physical Review B,* vol. 37, no. 12, p. 6991, 1988. http://dx.doi.org/10.1103/PhysRevB.37.6991

[96] Steven J. Stuart, Alan B. Tutein, and Judith A. Harrison, "A reactive potential for hydrocarbons with intermolecular interactions," *Journal of Chemical Physics,* vol. 112, p. 6472, 2000. http://dx.doi.org/10.1063/1.481208

[97] "LAMMPS WWW Site," Webpage (accessed in 2010): http://lammps.sandia.gov

[98] A. V. Melechko, V. I. Merkulov, T. E. McKnight, M. A. Guillorn, K. L. Klein, D. H. Lowndes, and M. L. Simpson, "Vertically aligned carbon nanofibers and related structures: Controlled synthesis and directed assembly," *Journal of Applied Physics,* vol. 97, no. 4, pp. 041301-39, 2005. http://dx.doi.org/10.1063/1.1857591

[99] "NanoLab Website," Webpage (accessed in 2011): www.nano-lab.com

[100] "Materials and Electrochemical Research (MER) Corporation," Tuscon, AZ, USA. Webpage (accessed in 2011): http://www.mercorp.com

[101] "TEMwindows.com," West Henrietta, NY, USA. Webpage (accessed in 2011): http://www.temwindows.com

[102] Elizabeth A. Whitsitt, Valerie C. Moore, Richard E. Smalley, and Andrew R. Barron, "LPD silica coating of individual single walled carbon nanotubes," *Journal of Materials Chemistry,* vol. 15, pp. 4678-4687, 2005. http://dx.doi.org/10.1039/b509869f

[103] Atsuhiko Kojima, Mitsuyasu Shimizu, Chan Kyeong Hyon, Takafumi Kamimura, Masatoshi Maeda, and Kazuhiko Matsumoto, "Air Stable n-type Top Gate Carbon Nanotube Filed Effect Transistors with Silicon Nitride Insulator Deposited by Thermal Chemical Vapor Deposition," *Japanese Journal of Applied Physics,* vol. 44, pp. L328-L330, 2005. http://dx.doi.org/10.1143/JJAP.44.L328

[104] Jason K. Holt, Aleksandr Noy, Thomas Huser, David Eaglesham, and Olgica Bakajin, "Fabrication of a Carbon Nanotube-Embedded Silicon Nitride Membrane for Studies of Nanometer-Scale Mass Transport," *Nano Letters,* vol. 4, no. 11, pp. 2245-2250, 2004. http://dx.doi.org/10.1021/nl048876h

[105] E. Raymundo-Piñero, P. Azaïs, T. Cacciaguerra, D. Cazorla-Amorós, A. Linares-Solano, and F. Béguin, "KOH and NaOH activation mechanisms of multiwalled carbon nanotubes with different structural organisation," *Carbon,* vol. 43, no. 4, pp. 786-795, 2005. http://dx.doi.org/10.1016/j.carbon.2004.11.005

[106] Chien-Hung Chen and Chen-Chia Huang, "Hydrogen storage by KOH-modified multi-walled carbon nanotubes," *International Journal of Hydrogen Energy,* vol. 32, no. 2, pp. 237-246, 2007. http://dx.doi.org/10.1016/j.ijhydene.2006.03.010

[107] Sang Moon Lee, Soon Chang Lee, Jong Hwa Jung, and Hae Jin Kim, "Pore characterization of multi-walled carbon nanotubes modified by KOH," *Chemical Physics Letters,* vol. 416, no. 4-6, pp. 251-255, 2005. http://dx.doi.org/10.1016/j.cplett.2005.09.107

[108] S. Costa, C. Tripisciano, E. Borowiak-Palen, and R. J. Kalenczuk, "Comparative study on purity evaluation of singlewall carbon nanotubes," *Energy Conversion and Management,* vol. 49, no. 9, pp. 2490-2493, 2008. http://dx.doi.org/10.1016/j.enconman.2008.01.037

[109] Nirupama Chakrapani, Yiming M. Zhang, Saroj K. Nayak, James A. Moore, David L. Carroll, Yoon Y. Choi, and Pulickel M. Ajayan, "Chemisorption of Acetone on Carbon Nanotubes," *The Journal of Physical Chemistry B,* vol. 107, no. 35, pp. 9308-9311, 2003. http://dx.doi.org/doi:10.1021/jp034970v

[110] Dmitry Kazachkin, Yoshifumi Nishimura, Stephan Irle, Keiji Morokuma, Radisav D. Vidic, and Eric Borguet, "Interaction of Acetone with Single Wall Carbon Nanotubes at Cryogenic Temperatures: A Combined Temperature Programmed Desorption and Theoretical Study," *Langmuir,* vol. 24, no. 15, pp. 7848-7856, 2008. http://dx.doi.org/doi:10.1021/la800030y

[111] Poornendu Chaturvedi, Preeti Verma, Anand Singh, P.K.Chaudhary, Harsh, and P.K. Basu, "Carbon Nanotube–Purification and Sorting Protocols," *Defence Science Journal,* vol. 58, no. 5, pp. 591-599, 2008.

[112] Naiqin Zhao, Chunnian He, Jiajun Li, Zhaoyang Jiang, and Yongdan Li, "Study on purification and tip-opening of CNTs fabricated by CVD," *Materials Research Bulletin,* vol. 41, no. 12, pp. 2204-2209, 2006. http://dx.doi.org/10.1016/j.materresbull.2006.04.029

[113] A. Jungen, C. Stampfer, J. Hoetzel, and C. Hierold, "Novel process flow for the integration of carbon nanotubes into MEMS," in *13th International Conference on Solid-State Sensors, Actuators and Microsystems (TRANSDUCERS '05),* Seoul, Korea, vol. 1, pp. 105-108, 2005. http://dx.doi.org/10.1109/SENSOR.2005.1496370

[114] Alain Jungen, Christoph Stampfer, Jochen Hoetzel, Victor M. Bright, and Christofer Hierold, "Process integration of carbon nanotubes into microelectromechanical systems," *Sensors and Actuators A: Physical,* vol. 130-131, pp. 588-594, 2006. http://dx.doi.org/10.1016/j.sna.2005.12.019

[115] Christoph Stampfer, Alain Jungen, and Christofer Hierold, "Fabrication of discrete nanoscaled force sensors based on single-walled carbon nanotubes," *IEEE Sensors Journal,* vol. 6, no. 3, p. 613, 2006. http://dx.doi.org/10.1109/JSEN.2006.874490

[116] Xihong Chen, Yongqin Chang, Zhe Wang, and Dapeng Yu, "Effect of ion beam etching on the field emission of carbon nanotube arrays," *Solid State Communications,* vol. 149, no. 13-14, pp. 523-526, 2009. http://dx.doi.org/10.1016/j.ssc.2009.01.011

[117] S. H. Lee, C. H. Lin, J. M. Chiou, and C. T. Kuo, "Effects of post treatment on the field emission properties of CNTs grown by ECR-CVD," *Diamond and Related Materials,* vol. 15, no. 4-8, pp. 854-858, 2006. http://dx.doi.org/10.1016/j.diamond.2005.11.032

[118] H. H. Jeffcott, "The lateral vibration of loaded shafts in the neighbourhood of a whirling speed–the effect of want of balance," *Philosophical Magazine,* vol. 37, no. 6, p. 304, 1919.

[119] Aurel Stodola, *Steam and Gas Turbines*. New York: McGraw-Hill Book Co., Inc, 1927.

[120] Dara W. Childs, *Turbomachinery Rotordynamics: Phenomena, Modeling, and Analysis*. New York: Wiley-Interscience, 1993.

[121] Boris Yakobson and Phaedon Avouris, "Mechanical Properties of Carbon Nanotubes," in *Carbon Nanotubes: Synthesis, Structure, Properties, and Applications*, M. S. Dresselhaus, G. Dresselhaus, and P. Avouris, Eds. New York: Springer-Verlag, 2001, pp. 287-327. http://dx.doi.org/10.1007/3-540-39947-X_12

[122] E. W. Wong, P. E. Sheehan, and C. M. Lieber, "Nanobeam Mechanics: Elasticity, Strength, and Toughness of Nanorods and Nanotubes," *Science,* vol. 277, no. 5334, p. 1971, 1997. http://dx.doi.org/10.1126/science.277.5334.1971

[123] Z. F. Ren, Z. P. Huang, D. Z. Wang, J. G. Wen, J. W. Xu, J. H. Wang, L. E. Calvet, J. Chen, J. F. Klemic, and M. A. Reed, "Growth of a single freestanding multiwall carbon nanotube on each nanonickel dot," *Applied Physics Letters,* vol. 75, no. 8, pp. 1086-1088, 1999. http://dx.doi.org/10.1063/1.124605

[124] Z. F. Ren, Z. P. Huang, J. W. Xu, J. H. Wang, P. Bush, M. P. Siegal, and P. N. Provencio, "Synthesis of Large Arrays of Well-Aligned Carbon Nanotubes on Glass," *Science,* vol. 282, no. 5391, pp. 1105-1107, 1998. http://dx.doi.org/10.1126/science.282.5391.1105

[125] Y. Tu, Z. P. Huang, D. Z. Wang, J. G. Wen, and Z. F. Ren, "Growth of aligned carbon nanotubes with controlled site density," *Applied Physics Letters,* vol. 80, no. 21, pp. 4018-4020, 2002. http://dx.doi.org/10.1063/1.1482790

[126] K. Behler, S. Osswald, H. Ye, S. Dimovski, and Y. Gogotsi, "Effect of Thermal Treatment on the Structure of Multi-walled Carbon Nanotubes," *Journal of Nanoparticle Research,* vol. 8, no. 5, pp. 615-625, 2006. http://dx.doi.org/10.1007/s11051-006-9113-6

[127] J. Y. Huang, S. Chen, S. H. Jo, Z. Wang, D. X. Han, G. Chen, M. S. Dresselhaus, and Z. F. Ren, "Atomic-Scale Imaging of Wall-by-Wall Breakdown and Concurrent Transport Measurements in Multiwall Carbon Nanotubes," *Physical Review Letters,* vol. 94, no. 23, pp. 236802-4, 2005. http://dx.doi.org/10.1103/PhysRevLett.94.236802

[128] J. Y. Huang, S. Chen, Z. F. Ren, G. Chen, and M. S. Dresselhaus, "Real-Time Observation of Tubule Formation from Amorphous Carbon Nanowires under High-Bias Joule Heating," *Nano Letters,* vol. 6, no. 8, pp. 1699-1705, 2006. http://dx.doi.org/10.1021/nl0609910

[129] K. Jensen, W. Mickelson, W. Han, and A. Zettl, "Current-controlled nanotube growth and zone refinement," *Applied Physics Letters,* vol. 86, no. 17, pp. 173107-3, 2005. http://dx.doi.org/10.1063/1.1920427

[130] S. Chen, J. Y. Huang, Z. Wang, K. Kempa, G. Chen, and Z. F. Ren, "High-bias-induced structure and the corresponding electronic property changes in carbon nanotubes," *Applied Physics Letters,* vol. 87, no. 26, pp. 263107-3, 2005. http://dx.doi.org/10.1063/1.2155116

[131] "Kleindiek Nanotechnik, GmbH," Reutlingen, Germany. Webpage (accessed in 2011): http://www.nanotechnik.com/

[132] Z. P. Huang, D. L. Carnahan, J. Rybczynski, M. Giersig, M. Sennett, D. Z. Wang, J. G. Wen, K. Kempa, and Z. F. Ren, "Growth of large periodic arrays of carbon nanotubes," *Applied Physics Letters,* vol. 82, no. 3, pp. 460-462, 2003. http://dx.doi.org/DOI:10.1063/1.1539299

[133] "Kleindiek Nanotechnik Web Page," Webpage (accessed in 2011): http://www.nanotechnik.com/

[134] "Philtec, Inc.," Annapolis, MD, USA. Webpage (accessed in 2011): http://www.philtec.com/

[135] Steve Plimpton, "Fast Parallel Algorithms for Short Range Molecular Dyanmics," *Journal of Computational Physics,* vol. 117, pp. 1-19, 1995. http://dx.doi.org/10.1006/jcph.1995.1039

[136] Sulin Zhang, Roopam Khare, Ted Belytschko, K. Jimmy Hsia, Steven L. Mielke, and George C. Schatz, "Transition states and minimum energy pathways for the collapse of carbon nanotubes," *Physical Review B,* vol. 73, no. 7, p. 075423, 2006. http://dx.doi.org/10.1103/PhysRevB.73.075423

[137] Shuichi Nosé, "A unified formulation of the constant temperature molecular dynamics methods," *Journal of Chemical Physics,* vol. 81, no. 1, p. 511, 1984. http://dx.doi.org/10.1063/1.447334

[138] William G. Hoover, "Canonical dynamics: Equilibrium phase-space distributions," *Physical Review A,* vol. 31, no. 3, p. 1695, 1985. http://dx.doi.org/10.1103/PhysRevA.31.1695

[139] Mildred Dresselhaus and Phaedon Avouris, "Introduction to Carbon Materials Research," in *Carbon Nanotubes: Synthesis, Structure, Properties, and Applications*, M. S. Dresselhaus, G. Dresselhaus, and P. Avouris, Eds. New York: Springer-Verlag, 2001, pp. 1-9. http://dx.doi.org/10.1007/3-540-39947-X_1

[140] Julian D. Gale and Andrew L. Rohl, "The General Utility Lattice Program (GULP)," *Molecular Simulation,* vol. 29, no. 5, pp. 291 - 341, 2003. http://dx.doi.org/10.1080/0892702031000104887

[141] J. D. Gale, "The General Utility Lattice Program (GULP)," Webpage (accessed in 2011): http://projects.ivec.org/gulp/

[142] John A. Thomas, Joseph E. Turney, Ryan M. Iutzi, Cristina H. Amon, and Alan J. H. McGaughey, "Predicting phonon dispersion relations and lifetimes from the spectral energy density," *Physical Review B,* vol. 81, no. 8, p. 081411, 2010.

[143] Ling Ti Kong, "Phonon dispersion measured directly from molecular dynamics simulations," *Computer Physics Communications (to be published),* 2011.

[144] Ling Ti Kong, Guido Bartels, Carlos Campañá, Colin Denniston, and Martin H. Müser, "Implementation of Green's function molecular dynamics: An extension to LAMMPS," *Computer Physics Communications,* vol. 180, no. 6, pp. 1004-1010, 2009.

[145] "FixPhonon webpage," Webpage (accessed in 2011): http://code.google.com/p/fix-phonon

[146] L. A. Girifalco, Miroslav Hodak, and Roland S. Lee, "Carbon nanotubes, buckyballs, ropes, and a universal graphitic potential," *Physical Review B,* vol. 62, no. 19, p. 13104, 2000. http://dx.doi.org/10.1103/PhysRevB.62.13104

[147] Kidong Park, Jaesung Jang, Daniel Irimia, Jennifer Sturgis, James Lee, J. Paul Robinson, Mehmet Toner, and Rashid Bashir, "'Living cantilever arrays' for characterization of mass of single live cells in fluids," *Lab on a Chip,* vol. 8, no. 7, pp. 1034-1041, 2008. http://dx.doi.org/10.1039/B803601B

[148] H. J. C. Berendsen, J. P. M. Postma, W. F. van Gunsteren, A. DiNola, and J. R. Haak, "Molecular dynamics with coupling to an external bath," *Journal of Chemical Physics,* vol. 81, no. 8, p. 3684, 1984. http://dx.doi.org/10.1063/1.448118

[149] Paul Langevin, "On the Theory of Brownian Motion," *Comptes rendus de l'Académie des sciences,* vol. 146, pp. 530-533, 1908.

[150] T. Schneider, E. P. Stoll, and R. Morf, "Brownian motion of interacting and noninteracting particles subject to a periodic potential and driven by an external field," *Physical Review B,* vol. 18, no. 3, p. 1417, 1978. http://dx.doi.org/10.1103/PhysRevB.18.1417

[151] Wataru Shinoda, Motoyuki Shiga, and Masuhiro Mikami, "Rapid estimation of elastic constants by molecular dynamics simulation under constant stress," *Physical Review B,* vol. 69, no. 13, p. 134103, 2004. http://dx.doi.org/10.1103/PhysRevB.69.134103

[152] Philippe H. Hünenberger, "Thermostat Algorithms for Molecular Dynamics Simulations," in *Advanced Computer Simulation*. vol. 173: Springer Berlin / Heidelberg, 2005, pp. 130-130. http://dx.doi.org/10.1007/b99427

[153] James W. Dally and Robert J. Bonenberger, *Design Analysis of Structural Elements*, 3rd ed. Knoxville, TN: College House Enterprises, LLC., 2003.

[154] Mads R. Sørensen and Arthur F. Voter, "Temperature-accelerated dynamics for simulation of infrequent events," *The Journal of Chemical Physics,* vol. 112, no. 21, pp. 9599-9606, 2000. http://dx.doi.org/10.1063/1.481576